

NOVEL TSPO LIGANDS TO FACILITATE RAPID TRACER DISCOVERY AND AS
PRECISION IMAGING DIAGNOSTICS OF CANCER

By

Jun Li

Dissertation

Submitted to the Faculty of the
Graduate School of Vanderbilt University
in partial fulfillment of the requirements
for the degree of

DOCTOR OF PHILOSOPHY

in

Interdisciplinary Materials Science

August, 2016

Nashville, Tennessee

Approved:

Professor H. Charles Manning

Professor Scott A. Guelcher

Professor Craig L. Duvall

Professor Robert J. Coffey

Professor John C. Gore

To my parents, Mr. Zhiqiang Li and Ms. Jianmei Gao
and my girlfriend, Rongxin Shi

ACKNOWLEDGEMENTS

The work presented in this thesis would not have been possible without the support of a number of people. They enabled me to chase and fulfill my dream over the past several years.

First and foremost, I want to express my gratitude to my advisor, Professor H. Charles Manning, for his guidance during the entire project. I am so grateful for his patience and endless help whenever I encountered a problem. I am thankful that I was able to have delicious homemade food at Charles house and share memorable experiences with his family and group members all together. I will never forget how he supports me and celebrates every tiny success I made throughout my graduate career.

I would like to acknowledge the members of my committee: Dr. Scott Guelcher, Dr. Craig Duvall, Dr. Robert Coffey, and Dr. John Gore. I really appreciate their guidance. Their advice and questions always allow me to dive deeper into the problem or think differently.

I would like to acknowledge my fellow members and dear friends of the Manning lab: Dr. Michael Schulte, Dr. Michael Nickels, Dr. Jason Buck, Dr. Matthew Hight, Dr. Dewei Tang, Dr. Yiu-Yin Cheung, Dr. Adam Rosenberg, Dr. Gina Kavanaugh, Dr. Fei Liu, Allie Fu, Ping Zhao, Ling Geng, and Sam Saleh. Special thanks to Dr. Dewei Tang for his assistance on TSPO projects. Special thanks to Allie Fu, Ping Zhao, and Ling Geng for helping me with the mouse model and biological sample preparation. Special thanks to Dr. Michael Schulte, Dr. Michael Nickels, Dr. Matthew Hight, Dr. Jason Buck, Dr. Yiu-Yin Cheung, and Sam Saleh not only for their professional guidance on research, but also for sharing so many wonderful experiences outside of lab. I will never forget all the happiness and memorable moments in Friday happy hour, golfing, Hawaii trip, and etc.

I would like to acknowledge several individuals at VUIIS, VUMC, and VU for their contribution to this dissertation, including but not limited to Dr. Jarrod Smith, Dr. Eric Dawson, Dr. Paige Vinson, Dr. Daniel Colvin, Aaron Greenfield, Dr. Mohammed Tantawy, Jarrod True, Kevin Wilson, and Fuxue Xin. I want to thank Dr. Jarrod Smith and Dr. Eric Dawson for all the modeling work in this thesis. I want to thank Dr. Paige Vinson for plasma protein binding experiment on the *N*-acetamide pyrazolopyrimidines project. I want to thank Aaron Greenfield and Fuxue Xin for running PET and MRI imaging.

I would like to thank Sarah Satterwhite for her support throughout my graduate career. I still remember she bought all the textbooks for me on my first day of arrival because she realized I had a tight budget before I got my first paycheck. She made my experience at IMS program a pleasant one. I want to thank Dr. Kane Jennings, Dr. Scott Guelcher, and Dr. Eva Harth for their guidance during my first year research rotation.

I would like to acknowledge Dr. Xiaoni Yang, my master's advisor at the Chinese Academy of Sciences. He introduced me to the real world of scientific research and supported me to study abroad.

I would like to thank Dr. Gongzhen Cheng, Dr. Lin Zhuang, Dr. Baizhao Zeng, and Dr. Hua Hou at Wuhan University. They are all great teachers and mentors. Their support during my undergraduate career allowed me to pursue a higher degree and more professional training.

I would like to thank Mr. Defu Lu and Ms. Fengping Yuan in my middle school, and Ms. Zhangfeng Ye in my elementary school. I have known them since my childhood, and keep contact for almost two decades. Without their guidance, I will not be able to go to a good high school, college, and finally come to Vanderbilt.

I would especially like to thank my girlfriend. I feel so fortunate to meet her at Vanderbilt. Our love encouraged us to achieve our goals and allowed us to enjoy a better life in a foreign country far away from home. She makes me a better and happier person.

Finally, I would like to thank my parents for their never-ending love and care. They have always supported and encouraged me to pursue my dreams, and taught me to be a good person and take responsibility for myself. I never imagined I would go to the United States for a graduate career when I was sitting in front of an old desk in our dark 200 square foot house without fan, heater, or air conditioner twenty years ago. It is their love and support that make things happen.

TABLE OF CONTENTS

	Page
DEDICATION.....	ii
ACKNOWLEDGEMENTS.....	iii
LIST OF TABLES	viii
LIST OF FIGURES	ix
LIST OF SCHEMES.....	xiii
LIST OF EQUATIONS.....	xiv
LIST OF ABBREVIATIONS.....	xv
Chapter	
I. INTRODUCTION	1
II. TSPO MOLECULAR IMAGING PROBES	4
2.1 Modalities of Molecular Imaging	4
2.2 Molecular Imaging Tracer ¹⁸ F-FDG	8
2.3 TSPO PET Tracers.....	11
2.4 TSPO Optical Imaging Probes	14
III. NEW STRUCTURE-ACTIVITY RELATIONSHIPS OF <i>N</i> -ACETAMIDE SUBSTITUTED PYRAZOLOPYRIMIDINES AS PHARMACOLOGICAL LIGANDS OF TSPO.....	16
3.1 Introduction	16
3.2 Chemistry	17
3.3 Ligand Affinity	20
3.4 Lipophilicity	24
3.5 Plasma Protein Binding.....	27
3.6 Conclusion.....	29
3.7 Method and Materials	31
IV. NOVEL TSPO FLUORESCENT LIGANDS FOR OPTICAL IMAGING	45
4.1 Introduction	45
4.2 Chemistry	45
4.3 Binding Affinity and Spectroscopic Characterization	47

4.4 Computational Modeling.....	50
4.5 Molar Extinction Coefficient and Quantum Yield	52
4.6 Cell Imaging	53
4.7 Conclusion.....	55
4.8 Method and Materials	57
V. DEVELOPMENT OF A HIGH-THROUGHPUT SCREENING METHOD USING A NOVEL TSPO OPTICAL LIGAND	80
5.1 Introduction	80
5.2 Ligand Saturation Curve and Displacement Experiments	83
5.3 Fluorescent Ligand in Screening Assay	84
5.4 Screening a Novel Library of Chemical Probe Candidates.....	85
5.5 Conclusion.....	89
5.6 Methods.....	90
VI. TSPO NEAR-INFRARED-BASED LIGAND AND PET TRACER AS PRECISION IMAGING DIAGNOSIS AND TREATMENT OF PANCREATIC CANCER.....	91
6.1 Introduction	91
6.1.1 Pancreatic Cancer	91
6.1.2 Near-infrared (NIR) Ligands for Optical Imaging.....	91
6.1.3 Zr-89 PET Tracer	94
6.2 TSPO in Pancreatic Tumor.....	95
6.3 TSPO NIR Ligand Development.....	97
6.4 NIR Probe (VUIIS-1520) Characterization.....	99
6.5 Genetically Engineered Mouse Models of Pancreatic Cancer	101
6.6 Experimental Design.....	102
6.7 Optical Imaging	103
6.8 Free Dye Imaging	109
6.9 Displacement	112
6.10 Optical Surgical Navigation	113
6.11 Chemistry and Radiochemistry of Zr-89 PET Tracer	114
6.12 Binding Affinity and Computational Modeling	116
6.13 Autoradiography	117
6.14 PET Imaging.....	119
6.15 Conclusion.....	119
6.16 Method and Materials	120
VII. CONCLUSION.....	122
Appendix	125
REFERENCES	127
ORIGINAL DATA	

LIST OF TABLES

Table	Page
3.3.1 Structure, molecular weight, yield, and affinity of pyrazolopyrimidines	22
3.4.1 Lipophilicity of pyrazolopyrimidines	25
3.5.1 Plasma protein binding of selected compounds	29
4.3.1 Binding affinity to TSPO of fluorescent ligands 4.23-4.29.....	48
5.3.1 Ligand binding affinity screened with optical probe and ³ H-PK11195	85
5.4.1 Inhibition of new compounds screened with optical probe and ³ H-PK11195.....	86
6.1.3.1 Half-life of isotopes.....	94
A.1.1 Isotopes used in SPECT.....	125

LIST OF FIGURES

Figure	Page
2.1.1 Simplified workflow for PET imaging tracer development	6
2.1.2 Simplified workflow for optical imaging probe development.....	8
2.2.1 Chemical structure of glucose and ¹⁸ F-FDG.....	9
2.2.2 First four steps of glycolysis	10
2.2.3 Beta decay of Fluorine-18.....	10
2.3.1 Common chemical scaffolds of TSPO ligands	12
2.3.2 Structure of Aplidem and DPA-713	13
2.3.3 Pyrazolopyrimidine ring numbering, and 2-(5,7-diethyl-2-(4-methoxyphenyl)pyrazolo[1,5- <i>a</i>]pyrimidin-3-yl)- <i>N,N</i> -diethylacetamide, previously reported by our group.....	13
2.4.1 TSPO fluorescent probes previously reported in literature.	14
3.1.1 Structure of DPA-713 (3.1), 2-(5,7-diethyl-2-(4-methoxyphenyl)pyrazolo[1,5- <i>a</i>]pyrimidin-3-yl)- <i>N,N</i> -diethylacetamide, previously reported by our group (3.2) and indicated substituents of new pyrazolopyrimidine-based ligands.....	17
3.2.1 Comparison of different synthetic routes.	18
4.2.1 Generalized structure of TSPO fluorescent ligands.	46
4.3.1 Fluorescent probe aqueous spectroscopy.....	49
4.4.1 12 modeling poses of probe 4.29 and TSPO.....	51
4.4.2 Best score modeling structure of probe 4.29 interaction with TSPO.....	51
4.5.1 Molar extinction coefficient of probe 4.29.	52
4.6.1 Confocal microscopy images of C6 rat glioma cells incubated with optical probe. (A, D) fluorescent images of optical probe; (B, E) fluorescent images of Mito Tracker Red; (C, F) merged images of optical probe and Mito Tracker Red. (D, E, F) fluorescent images of the chosen area in (A).	54

4.6.2 Displacement experiment of 4.29 with its parent ligand. (G, H, I) images of displacement experiment. C6 cells were co-incubated with 0.1 μ M optical probe and 10 μ M 2-(5,7-diethyl-2-(4-methoxyphenyl)pyrazolo[1,5- <i>a</i>]pyrimidin-3-yl)- <i>N,N</i> -diethylacetamide; (J, K, L) images of C6 glioma cells dosed with Mito Tracker Red only.....	55
5.1.1 Chemical structure of PK 11195.....	80
5.1.2 Competitive binding assay using 3 H-PK11195 to detect the ligand binding affinity.	81
5.1.3 Screening assay using TSPO fluorescent ligand to replace 3 H-PK 11195.....	82
5.1.4 TSPO fluorescent probe 4.29 used for screening.....	82
5.2.1 Saturation curve of fluorescent probe binding to C6 glioma cell lysate (left, black curve) and displacement experiments (left, red curve). C6 glioma cell lysates were co-incubated with 0.50-100 nM fluorescent probe and 100 nM 2-(5,7-diethyl-2-(4-methoxyphenyl)pyrazolo[1,5- <i>a</i>]pyrimidin-3-yl)- <i>N,N</i> -diethylacetamide.	84
5.4.1 SSR- and phrazolopyrimidine-based TSPO ligand series.....	85
6.1.2.1 Electromagnetic spectrum from ultraviolet to near-infrared.....	92
6.1.2.2 Penetration depth of various wavelengths of light.....	93
6.1.3.1 Antibody labeling with Zr-89.....	95
6.2.1 TSPO immunostaining of human normal and neoplastic pancreas.....	96
6.2.2 TSPO expression of specimens collected from 155 VUMC patients.	97
6.3.1 TSPO NIR ligand (VUIIS-1520) structure.....	98
6.4.1 Binding affinity of VUIIS-1520.....	100
6.4.2 Computational modeling of VUIIS-1520.....	101
6.5.1 Advanced PDA of <i>Ptfla-Cre;LSL-Kras^{G12D/+};Smad4^{fl/fl}</i> mouse model.....	102
6.6.1 Experimental design of optical imaging and surgical navigation.....	102
6.7.1 Excised tissue imaging by Odyssey of genetically engineered tumor mouse and control mouse aged at four weeks. The ratio of signal intensity was averaged of tissue samples collected from three tumor and three control mice.....	103
6.7.2 H&E (A and D), trichrome (B and E), and TSPO IHC (C and F) stain of pancreas from the control mouse. The magnification of A, B, and C was 5x, of D, E, and F was 10x.....	104

6.7.3 H&E (A and D), trichrome (B and E), and TSPO IHC (C and F) stain of pancreas from the four week genetically engineered tumor mouse. The magnification of A, B, and C was 5x, of D, E, and F was 10x.	105
6.7.4 Excised pancreatic imaging by Odyssey of genetically engineered tumor mouse and control mouse aged at four (left) and nine (right) weeks.	105
6.7.5 H&E (A and D), trichrome (B and E), and TSPO IHC (C and F) stain of pancreas from the nine week genetically engineered tumor mouse. The magnification of A, B, and C was 5x, of D, E, and F was 10x.	106
6.7.6 Excised tissue imaging by Odyssey of genetically engineered tumor mouse and control mouse aged at fifteen weeks. The ratio of signal intensity was averaged of tissue samples collected from three tumor and three control mice.	107
6.7.7 H&E (A and D), trichrome (B and E), and TSPO IHC (C and F) stain of pancreas from the fifteen week genetically engineered tumor mouse. The magnification of A, B, and C was 5x, of D, E, and F was 10x.	108
6.7.8 Ratio of signal intensity between tumor mice and control mice at different age.....	109
6.8.1 Specificity of conjugated TSPO NIR probe. Images of excised tissues from tumor mice injected with VUIIS-1520 (left), unconjugated LI-COR IRDye 800CW (middle), and the ratio of signal intensity (right).	110
6.8.2 Images of excised tissues of free dye injection into the control mouse (left) and tumor mouse (middle). The right image compared the ratio of signal intensity from injection of VUIIS-1520 and free dye.....	111
6.8.3 Images of excised tissues from control mice injected with VUIIS-1520 (left), unconjugated LI-COR IRDye 800CW (middle), and the ratio of signal intensity (right).....	112
6.9.1 Displacement of VUIIS-1520 with its parent ligand (left). Images of excised tissues with (middle) or without (right) displacement.	113
6.10.1 Optical surgical navigation of pancreatic tumor by using VUIIS-1520.....	114
6.12.1 Binding affinity of VUIIS-1530.....	116
6.12.2 Computational modeling of VUIIS-1530 interaction with TSPO.....	117
6.13.1 Autoradiograph of pancreas. six week tumor mouse (A), twelve week tumor mouse (B), and control mouse (D) with retro orbital injection of VUIIS-1530; 6-week tumor mouse with intraperitoneal injection of VUIIS-1530 (C).	118

6.13.2 Autoradiography of cross section of tumor mouse.	118
6.14.1 PET imaging of VUIIS-1530. Transverse (left) and sagittal (right) slices of a representative tumor mouse are shown.	119

LIST OF SCHEMES

Scheme	Page
3.2.1 Reported synthetic route to pyrazolopyrimidine-based TSPO ligands	18
3.2.2 Synthetic route to <i>N,N</i> -acetamide disubstituted pyrazolopyrimidines.	20
4.2.1 Synthesis of TSPO fluorescent ligands.	47
6.3.1 Synthetic pathway to TSPO NIR ligand (VUIIS-1520).	99
6.11.1 Radiosynthesis of TSPO probe VUIIS-1530.....	115
A.1.1 Synthetic route to TSPO SPECT probe	126

LIST OF EQUATIONS

Equation	Page
2.1.1 Electron excitation.....	7
2.1.2 Electron emission	7
3.4.1 Lipophilicity.....	24
3.4.2 log P and log K relationship.....	25
3.5.1 Plasma protein binding	28
4.5.1 Beer's law	52
4.5.2 Quantum yield.....	53
5.2.1 Binding affinity	83
5.2.2 Dissociation constant.....	83

LIST OF ABBREVIATIONS

AcOH	acetic acid
Bu	butyl
Bz	benzoyl
c	concentration
°C	degrees Celsius
CBR	central benzodiazepine receptor
CH ₂ Cl ₂	dichloromethane
CNS	central nervous system
CP	chronic pancreatitis
CT	computed tomography
d	day
d	doublet
DCM	dichloromethane
DIEPA	<i>N,N</i> -diisopropylethylamine
DMF	dimethylformamide
DMSO	dimethyl sulfoxide
Et	ethyl
Et ₃ N	triethyl amine
EtOAc	ethyl acetate
EtOH	ethanol
FITC	fluorescein isothiocyanate

eq	equivalent
^{18}F -FDG	2-deoxy-2-(^{18}F)fluoro-D-glucose
g	gram
h	hour
H&E	Hematoxylin and eosin stain
HRMS	High-resolution Mass Spectrometry
HATU	1-[Bis(dimethylamino)methylene]-1 <i>H</i> -1,2,3-triazolo[4,5- <i>b</i>]pyridinium 3-oxid hexafluorophosphate
HPLC	high performance liquid chromatography
IC ₅₀	half maximal inhibitory concentration
IHC	Immunohistochemistry
<i>i</i> -Pr	isopropyl
IPMNs	intraductal papillary mucinous neoplasms
K_i	absolute inhibition constant
K_d	dissociation constant
LC-MS	liquid chromatography-mass spectrometry
m	minute
m	multiplet
M	molar
MAOS	microwave-assisted organic synthesis
Me	methyl
MeOH	methanol

mg	milligram
mL	milliliter
mol	mole
MRI	magnetic resonance imaging
MW	microwave
nM	nanomolar
NMR	nuclear magnetic resonance spectroscopy
NIR	near-infrared
O/N	overnight
PBS	phosphate-buffered saline
PET	positron emission tomography
Ph	phenyl
R	organic substituent
RRT	relative retention time
PanIN	pancreatic intraepithelial neoplasia
PDA	pancreatic ductal adenocarcinoma
rt	room temperature
s	second
s	singlet
SAR	structure activity relationship
<i>t</i>	tert
t	triplet
TFA	trifluoroacetic acid

THF	tetrahydrofuran
TLC	thin layer chromatography
TMA	tissue microarray
Ts	tosyl
TSPO	translocator protein
UV-vis	ultraviolet–visible
VUIIS	Vanderbilt University Institute of Imaging Science
μg	microgram
μM	micromolar

CHAPTER 1

INTRODUCTION

Molecular imaging plays an essential role in non-invasive disease detection, staging, response to therapy, and drug development due to its ability to visualize, characterize, and measure biological processes at the cellular and molecular level in humans and other living systems. The sensitivity and quantitative nature of molecular imaging coupled with the ability to design tracers to target very specific biological processes and molecular events renders molecular imaging uniquely capable of detecting tumors and other diseases. Several modalities are approved for molecular imaging, including positron emission tomography (PET), single-photon emission computed tomography (SPECT), optical imaging, and sometimes magnetic resonance imaging (MRI) and ultrasound (US).

The basis of molecular imaging relies upon probes or tracers with high specificity and affinity for targets relevant to particular molecular events. Though molecular imaging is applicable to many human diseases, this thesis will focus mainly upon molecular imaging of cancer. By far, the most widely used molecular imaging probe in oncology is 2-deoxy-2- (^{18}F) fluoro-D-glucose (FDG) for PET, which accumulates in tissues as a function of glucose uptake. Many tumors utilize glycolysis to at least partially fuel their growth, which has led to FDG PET becoming a mainstream tool for cancer detection and assessment. However, FDG has several limitations. FDG uptake in tumors can be confounded by accumulation in surrounding tissues possessing increased glycolytic metabolism such as the brain. Conversely, not all tumors exhibit high metabolic rates, such as prostate cancer. These issues highlight a currently unmet need to explore and validate additional molecular targets for cancer imaging.

The main molecular imaging target explored in this thesis is the translocator protein, TSPO. Previously termed as peripheral benzodiazepine receptor (PBR), TSPO is an 18 kDa protein typically localized to the outer mitochondrial membrane whose primary role is to facilitate cholesterol metabolism. TSPO expression and function is shown to be linked with steroid biosynthesis, cellular proliferation, and apoptosis.^[1-2] In oncology, TSPO overexpression has been reported in many human cancers, including glioma, colon cancer, and breast cancer.^[3-13]

This dissertation seeks to develop, evaluate, and validate novel TSPO ligands to facilitate tracer discovery and as precision imaging diagnostics of cancer. The major objective of this project is three-fold:

1) To further elucidate structure activity relationship (SAR) around pyrazolopyrimidine TSPO ligands scaffold;

Our group's previous research has evaluated the 5, 6, and 7 positions on the pyrazolopyrimidine scaffold, which led to the discovery of a novel TSPO ligand exhibiting a 36-fold enhancement in affinity compared to DPA-713.^[14] To continue our evaluation of the pyrazolopyrimidine scaffold as a lead for molecular imaging probes for TSPO in cancer, **Chapter 3** elucidates new SARs related to *N,N*-disubstitutions of the terminal acetamide and explores the impacts of substituents on lipophilicity and plasma protein binding.

2) To develop an improved tool that allows rapid discovery of new molecular imaging tracers for TSPO;

Screening is a necessary step to discover new TSPO chemical probes and to evaluate the binding affinity of newly developed ligands. Presently, ³H-PK 11195, a long half-life radioactive

material, is routinely used in competitive binding assay. However, the current method is not only slow and expensive, but also requires caution due to the use of radioactive materials. Leveraging the existence of fluorescent unit within the optical ligand, **Chapter 4** and **5** develops a fast tracer screening assay using a novel TSPO fluorescent probe to replace ^3H -PK 11195.

3) To explore the utility of novel TSPO ligands as precision imaging diagnostics and for optical surgical navigation in the treatment of pancreatic cancer.

Pancreatic cancer is the fourth leading cause of cancer-related deaths in the United States, and seventh worldwide. Despite improvement and progress in diagnosis, surgery, and other treatment, the overall five-year survival rate remains only 5%. **Chapter 6** establishes and highlights a clear connection between pancreatic cancer and TSPO expression: TSPO elevation was found not only in invasive and highly advanced pancreatic cancer, such as pancreatic ductal adenocarcinoma (PDA), it was also observed in pre-malignant pancreatic lesions, such as pancreatic intraepithelial neoplasia (PanIN), and cystic lesions, such as intraductal papillary mucinous neoplasm (IPMN). TSPO near-infrared (NIR) probe was developed for pancreatic cancer imaging and to aid in optical surgical navigation. Further, a small molecular TSPO PET tracer functionalized with Zirconium-89 was reported for the first time and utilized in the tumor imaging, which is ideal for the long circulation time required to enter high grade dense stromal.

CHAPTER 2

TSPO MOLECULAR IMAGING PROBES

2.1 Modalities of Molecular Imaging

Modalities approval for molecular imaging include PET, SPECT, optical imaging, and sometimes MRI and ultrasound. This dissertation mainly focused on the development of PET and optical imaging probes. In the Appendix, a SPECT probe was also reported.

PET and SPECT are broadly applied in both clinical imaging and preclinical research. PET and SPECT can offer good spatial resolution, high sensitivity, and easy quantitative measurements. However, both require using radioactive materials for imaging. Optical imaging typically uses dyes or quantum dots, which can avoid radiation. Optical imaging can also have a low background. However, optical imaging may not be applicable for deep tissues because of the strong attenuation of the signal. Due to the scattering of photons, it is difficult to generate tomographic images with optical imaging methods. Optical imaging can play an active role in imaging the disease close to the surface or by using together with endoscopy. Another area that optical imaging is applicable is surgical navigation to assist the surgeon in locating the tumor, and determining the extent of spread. The use of contrast agents in MRI is considered as molecular imaging. MRI has very good spatial resolution, but it requires to have a large amount of contrast agents attaching to the target. Another drawback of using contrast agents is the difficulty to work on quantitative measurement, since it needs to analyze the influence of contrast agents on the signal. Ultrasound can use microbubbles as a contrast agent. Microbubbles are much larger than small molecules, and the application is limited in vascular targets.

PET imaging utilizes tracers labeled with typically short-lived radioactive isotopes, which emit positrons after undergoing beta decay. The positron travels a short distance and then interacts with an electron. The annihilation produces a pair of coincident photons traveling in approximately opposite directions. When the photons interact with the scintillator, light will be created, which can be further detected by photomultiplier tubes.^[15-16] These phenomena form the basis of positron emission tomography.

The PET tracer itself plays the central role in molecular imaging of disease. To visualize and measure biologic processes in tumors, we first need to identify a process that behaves differently in tumor tissues versus normal tissues, such as proliferation, apoptosis, hypoxia, and angiogenesis. The ability to distinguish abnormal biologic processes in tumors allows us to further develop tracers to image the tumor. A good tracer should bind specifically to the target and generate signal strong enough to be separated from the background.

Assuming a target or phenotype of interest is known, a typical starting point for probe development starts with medicinal chemistry. As shown in **Figure 2.1.1**, starting from the selective of an appropriate chemical scaffold, a library of hundreds or thousands of chemical compounds of similar or diverse structure will be accomplished. Screening will then be performed to identify possible hits and to, subsequently, examine the affinity of the compounds and find the ones with high-affinity. Quite often, structure activity relationship (SAR) and computational modeling will be introduced to analyze the influence of chemical structure on interaction with the target. Thus, depending on the binding affinity of chemical probes, it might be necessary to start over to choose another scaffold or synthesize more probes bearing the same scaffold and screen again. After several rounds of library development and screening, potential probes with high binding affinity, good stability, suitable lipophilicity and plasma protein

binding will be chosen to move forward to radiosynthesis to develop PET tracers for imaging. Further screening and *in vivo* imaging studies can help to evaluate the tracer performance in disease imaging. Tracers which exhibit exceptional *in vivo* performance in small animal imaging studies may have the opportunity to go to the clinic.

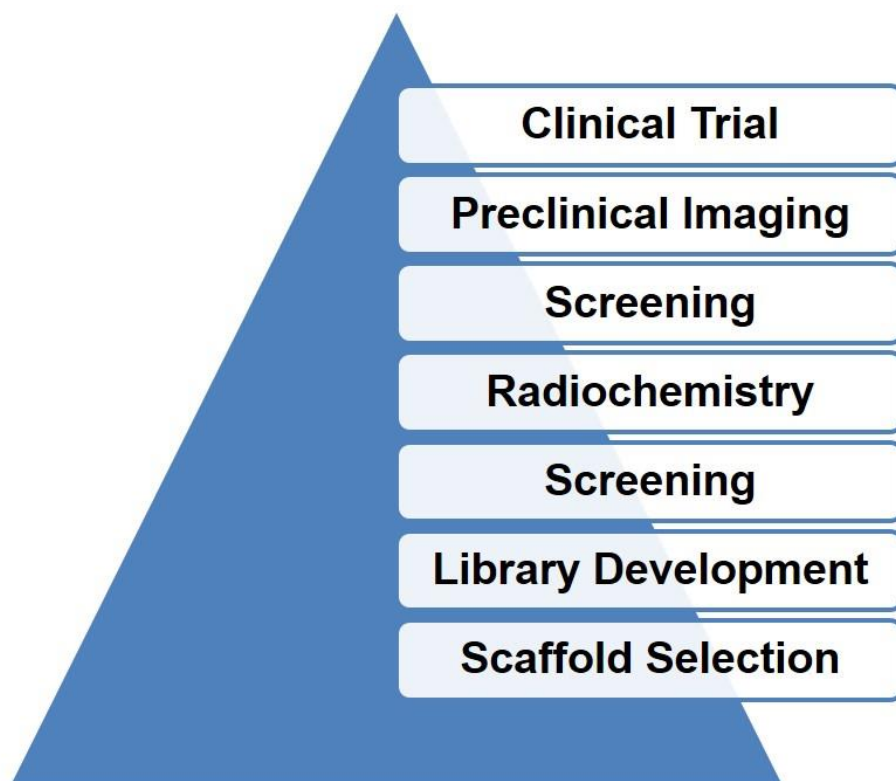


Figure 2.1.1 Simplified workflow for PET imaging tracer development.

As another modality of noninvasive molecular imaging, optical imaging offers an alternative approach to PET and offers several unique advantages. Optical imaging utilizes inexpensive and much simpler instrumentation, making it more affordable and accessible for preclinical testing in research and to small hospitals or healthcare centers for clinical imaging.^{[17-}

^{18]} Optical imaging relies upon the use of optical probes that will emit photons following

excitation, which significantly reduces the radiation exposure to the subject and workers as seen in PET or CT imaging. Given the long half-lives of optical probes, they are easier to store, deliver, and use, and suitable for large scale manufacturing. Taking advantage of long half-lives probes, optical imaging can be used in lengthy procedures or for tracking disease progression. One can also utilize several probes that emit a diversity of colors and measure the signals from different channels simultaneously, which allows the investigation of a series of molecular properties at the same time.

When an orbital electron absorbs photon energy, it can be excited to a higher energy state. Fluorescence occurs when the electrons relax from excited singlet state to ground state. Subsequent the emitted fluorescence can be detected by the instrumentation, which may include a PMT or CCD camera.



The procedure to generate optical imaging probes is quite similar to PET tracer. However, due to the existence of fluorescent unit within the probe, there is no need to replace certain atoms with its isotope to emit the signal. As a result, it may take fewer steps to develop optical imaging probes. However, the presence of the fluorophores, which may be bulky, exhibit high lipophilicity, or a significantly charged character, can dominate the biological properties of the tracer.

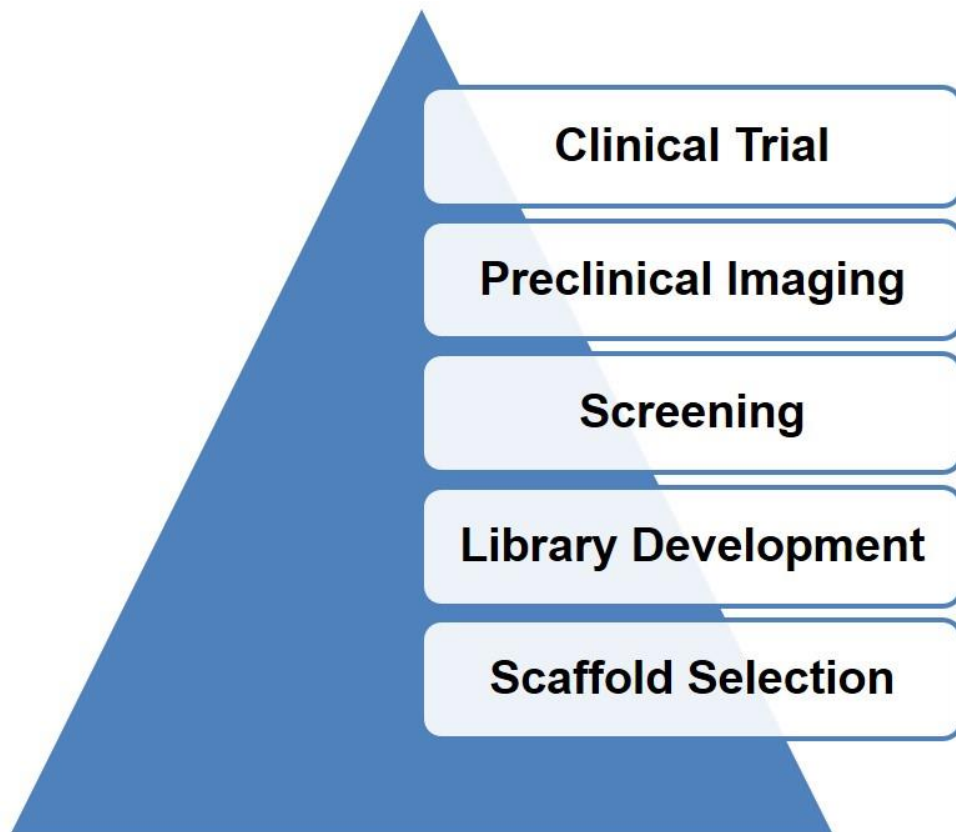


Figure 2.1.2 Simplified workflow for optical imaging probe development.

2.2 Molecular Imaging Tracer ^{18}F -FDG

Currently, the most widely used molecular imaging tracer in the clinic is 2-deoxy-2- (^{18}F) fluoro-D-glucose (^{18}F -FDG), a glucose analog (**Figure 2.2.1**). FDG is distinct from glucose due to its substitution of the hydroxyl group at the 2' position with fluorine-18.

The synthesis of FDG was firstly reported by Josef Pacak *et al.* (Charles University, Czech Republic) in *Chemical Communications* in 1969.^[19] Later, Tatsuo Ido and Al Wolf *et al.* (Brookhaven National Laboratory, NY) labeled FDG with both Fluorine-18 and Carbon-14.^[20] In 1976, ^{18}F -FDG was first administered to human by Abass Alavi (University of Pennsylvania, PA). Interestingly, a prototype of the PET imaging camera was invented almost at the same time.

In 1961, the first single plane PET scan was constructed by James Roberson (Brookhaven National Laboratory, NY).^[21] The development of ^{18}F -FDG greatly helped the expansion of PET imaging.

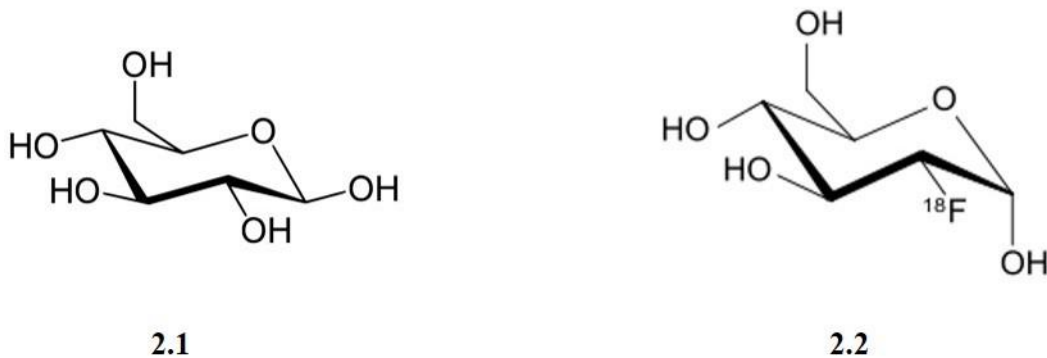


Figure 2.2.1 Chemical structure of glucose and ^{18}F -FDG.

As a glucose analog, ^{18}F -FDG accumulates in tissues as a function of glucose uptake. In normal glycolysis (**Figure 2.2.2**), the hydroxyl group at the 2' position is needed to convert G6P to F6P. However, 2' hydroxyl group is replaced with ^{18}F in ^{18}F -FDG, which terminates further metabolism of ^{18}F -FDG. Thus, ^{18}F -FDG can enter cells like glucose but cannot move out after forming ^{18}F -FDG-6-phosphate and is trapped in the cell.

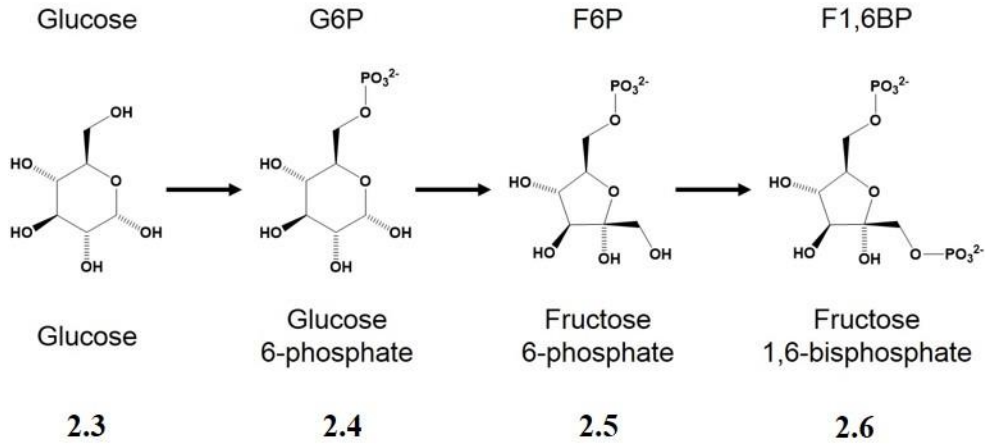


Figure 2.2.2 First four steps of glycolysis.

After undergoing beta decay (**Figure 2.2.3**), ^{18}F will be converted to ^{18}O and capture H^+ from the surrounding environment to regenerate hydroxyl group at the 2' position, which allows further glycolysis to take place. In general, after being absorbed by the cell, ^{18}F -FDG will not be released until it decays, which makes it ideal to reflect glucose uptake and distribution.



Figure 2.2.3 Beta decay of Fluorine-18.

^{18}F -FDG was firstly applied in the neuroscience field. In 1980, Som P. *et al.* (Brookhaven National Laboratory, NY) described the application of ^{18}F -FDG as a nontoxic tracer for rapid tumor diagnosis and utilized in the detection of seminoma in dogs.^[22]

However, FDG has several limitations. FDG uptake in tumors can be confounded by accumulation in tissues possessing increased glycolytic metabolism such as the brain. Conversely, not all tumors exhibit high metabolic rates, such as prostate cancer.^[14, 23] These issues highlight a currently unmet need to explore and validate additional molecular targets for cancer imaging. Molecular imaging relies on using personalized tracers designed to target very specific biological processes and molecular events. Despite its potential, a lack of specific and biologically validated tracers that are capable of providing detailed molecular information about individual tumors limits the breadth of biological questions addressable with molecular imaging.

2.3 TSPO PET Tracers

TSPO, previously known as peripheral benzodiazepine receptor (PBR),^[1, 24] is an 18 kDa protein typically localized to the outer mitochondrial membrane whose primary role is to facilitate cholesterol metabolism. Within that context, TSPO expression and function tend to be linked with steroid biosynthesis, cellular proliferation, and apoptosis.^[25-27] Prompting our interest in TSPO as a target for non-invasive imaging, elevated levels of TSPO are observed in many human cancers,^[6-8, 28-33] where it is reportedly associated with progression and diminished survival.

As a promising target for cancer imaging, TSPO ligands have been synthesized based upon a diversity of core scaffolds, including benzodiazepines, isoquinoline carboxamides, phenoxyphenylacetamide, indolacetamides, *N,N*-dialkyl-2-phenylindol-3-ylglyoxyamides, and pyrazolopyrimides (**Figure 2.3.1**).^[34-37] Some of the most widely imaged TSPO probes include PK 11195, DAA 1097, DAA 1106, and Ro 5-4864.^[35-36, 38-42]

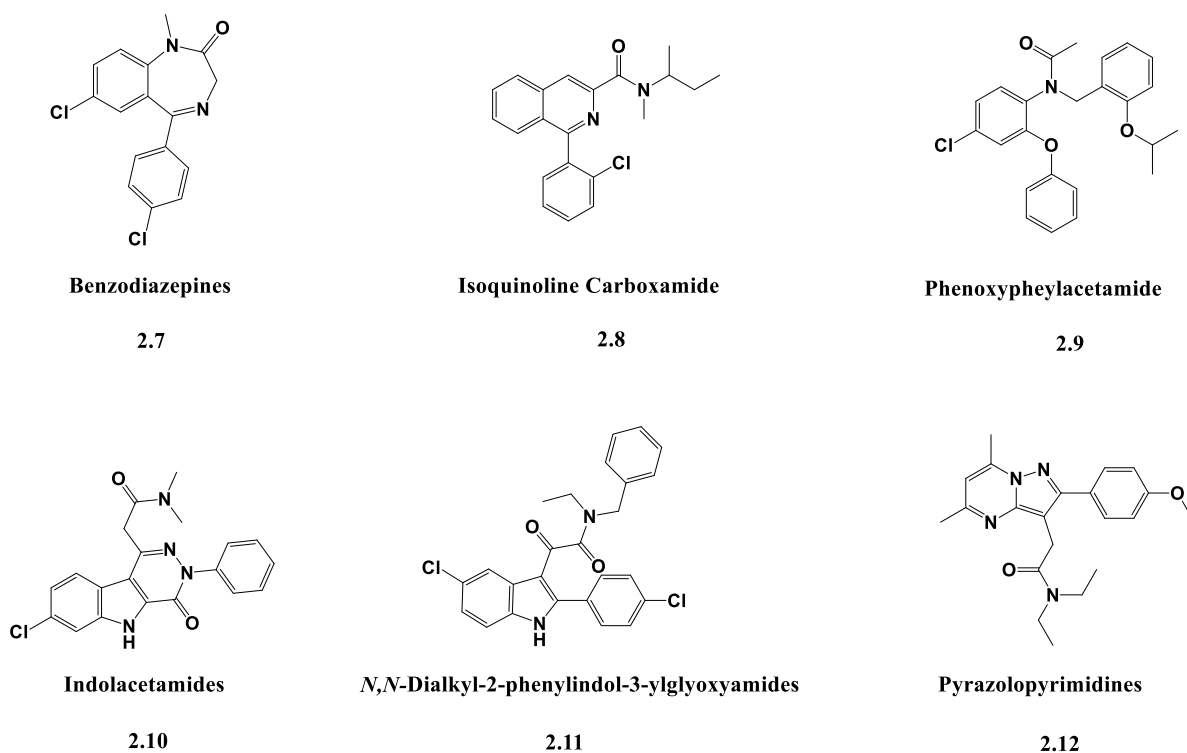
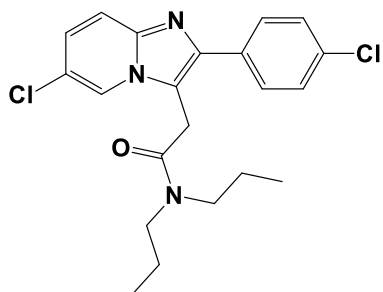


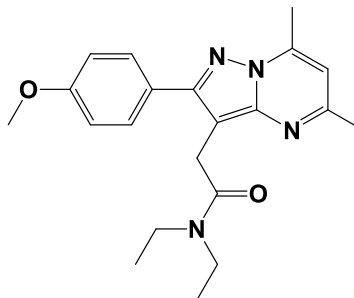
Figure 2.3.1 Common chemical scaffolds of TSPO ligands.

Alpidem (**Figure 2.3.2**) was among the first TSPO ligands that exhibit nanomolar binding affinity to TSPO ($K_i=0.5-7$ nM).^[43-45] However, further research illustrated that it also exhibited high binding affinity to central benzodiazepine receptor (CBR, $K_i=1-28$ nM).^[45] Starting from this highly potent but non-selective ligand, Selleri S *et al.* reported a novel ligand which can selectively bind to TSPO and maintain nanomolar affinity ($K_i=4.7$ nM) through structural optimization.^[45-46] This ligand was later named DPA-713 (**Figure 2.3.2**).^[36]



Aplidem

2.13

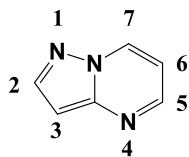


DPA-713

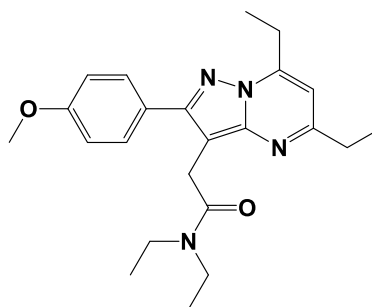
2.14

Figure 2.3.2 Structure of Aplidem and DPA-713.

Based upon the structure of DPA-713, our group previously optimized the 5, 6, and 7 positions of the pyrazolopyrimidine scaffold, and reported a novel PET tracer with improved affinity and pharmacokinetic properties for cancer imaging (**Figure 2.3.3**).^[14, 47]



2.15



2.16

Figure 2.3.3 Pyrazolopyrimidine ring numbering, and 2-(5,7-diethyl-2-(4-methoxyphenyl)pyrazolo[1,5-a]pyrimidin-3-yl)-*N,N*-diethylacetamide, previously reported by our group.

2.4 TSPO Optical Imaging Probes

Several TSPO fluorescence probes have been reported for cancer imaging (**Figure 2.4.1**). PK 11195 is among the earliest discovered TSPO selective ligands. By conjugating PK 11195 with Lissamine-Rhodamine B sulfonyl chloride dye, Manning *et al.* described a TSPO fluorescent probe and utilized the reagent for glioma cell imaging.^[13,48] Further, Bai *et al.* found that Lissamine-Rhodamine B sulfonyl chloride conjugated probe had two isomers with different molar extinction coefficients ($\epsilon_1 = 88\,000\text{ L/mol cm}$, $\epsilon_2 = 350\,000\text{ L/mol cm}$).^[49] By separating the one with a higher molar extinction coefficient, the signal intensity was significantly increased. This author also linked another TSPO ligand DAA 1106 with IR Dye 800CW and accomplished a probe with high affinity to TSPO ($K_i = 42\text{ nM}$).^[50] In a separate study by Denora N *et al.*, green dye FITC was applied and used to image Ra2 immortalized microglial clone.^[37]

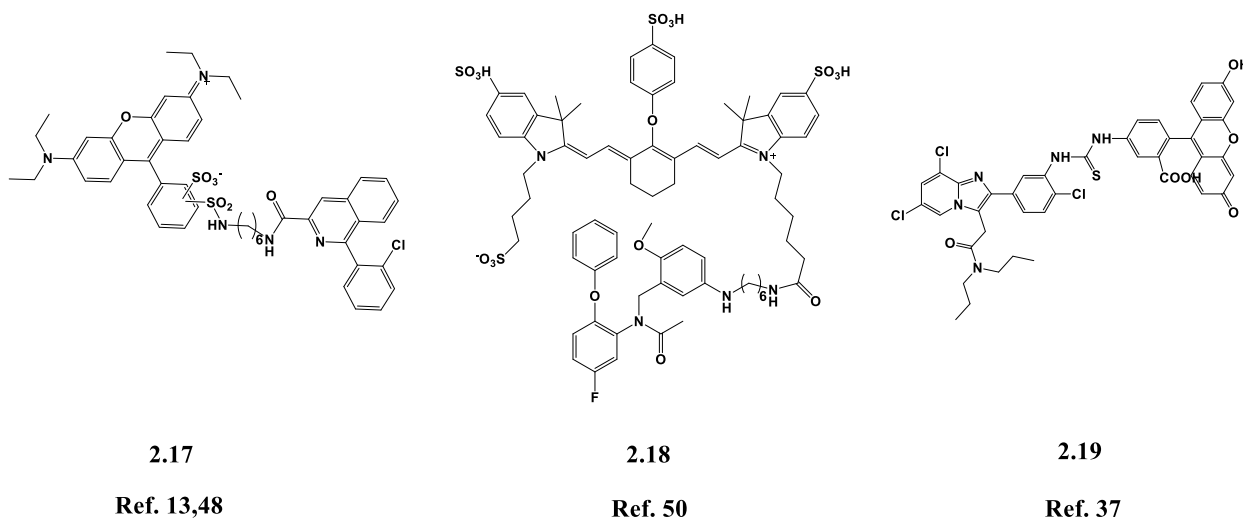


Figure 2.4.1 TSPO fluorescent probes previously reported in literature.

Beyond simple fluorescent imaging, it has been shown that multimodal imaging is feasible. Most molecular imaging probes can only provide one type of signal. However, by

integrating several signatures into one probe, a multimodal probe allows one to diagnose disease using multiple imaging methods. By introducing Eu^{3+} and Gd^{3+} into TSPO fluorescent probe Ln-PK11195, Manning HC *et al.* developed the first TSPO fluorescent/MRI probe, which can be used in both disease diagnosis and surgical navigation. ^[13]

In summary, given the important role of TSPO in many human diseases, especially in cancer, many TSPO tracers or probes have been discovered. This thesis will further develop several novel molecular imaging probes to target TSPO to aid in cancer diagnosis and treatment.

CHAPTER 3

NEW STRUCTURE-ACTIVITY RELATIONSHIPS OF *N*-ACETAMIDE SUBSTITUTED PYRAZOLOPYRIMIDINES AS PHARMACOLOGICAL LIGANDS OF TSPO

3.1 Introduction

Imaging now plays a critical role in cancer diagnosis and molecular characterization of actionable lesions. Thus, imaging is central in the successful deployment of precision cancer medicine. Among clinical modalities available for cancer imaging, the sensitivity and quantitative nature of positron emission tomography (PET), coupled with the ability to produce biologically active tracers bearing positron-emitting isotopes, renders PET imaging uniquely capable of detecting tumors and profiling their molecular features.

As a promising target for cancer imaging, TSPO ligands have been synthesized based upon a diversity of core scaffolds. Many TSPO ligands were previously developed to image CNS disorders and thus, have sub-optimal pharmacokinetic properties for peripheral organ sites.^[24, 51] Our lab has focused on the development and characterization of high-affinity TSPO ligands applicable to a wide variety of imaging modalities, especially in tumors that arise outside of the central nervous system.^[14, 47, 52-56]

Based upon the structure of DPA-713, our group previously optimized the 5, 6, and 7 positions of a pyrazolopyrimidine, and reported a novel PET tracer exhibiting over 30-fold enhancement in affinity (**Figure 3.1.1**).^[14, 47] Based upon our prior work and motivated by the work of Selleri *et al.*,^[45-46] we further elaborated on the pyrazolopyrimidine structure activity relationships related to *N,N*-disubstitutions of the terminal acetamide. Herein, we report a variety

of novel pyrazolopyrimidine TSPO candidate ligands ($n = 16$), bearing alkyl, alicyclic, aryl, and heterocyclic pendant acetamides. In doing so, we also report the development of a novel synthetic route to these compounds that allows for a rapid library expansion approach.

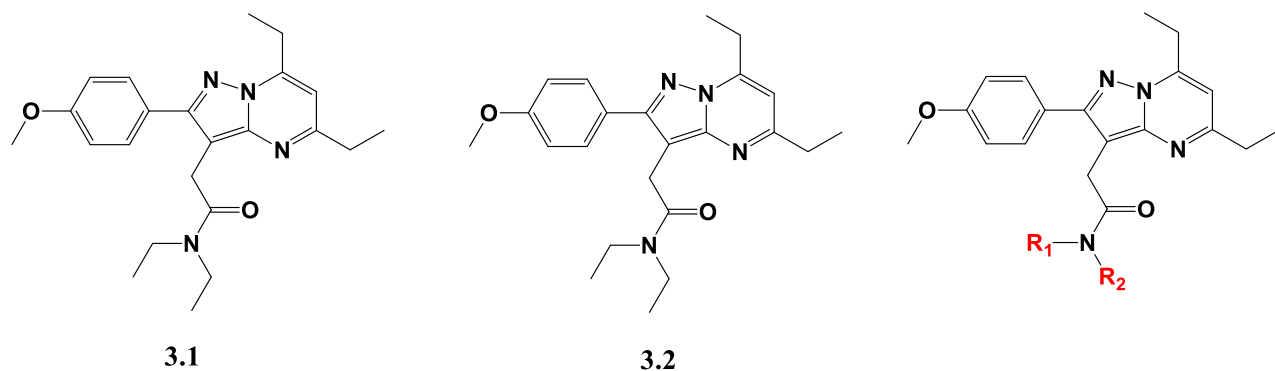
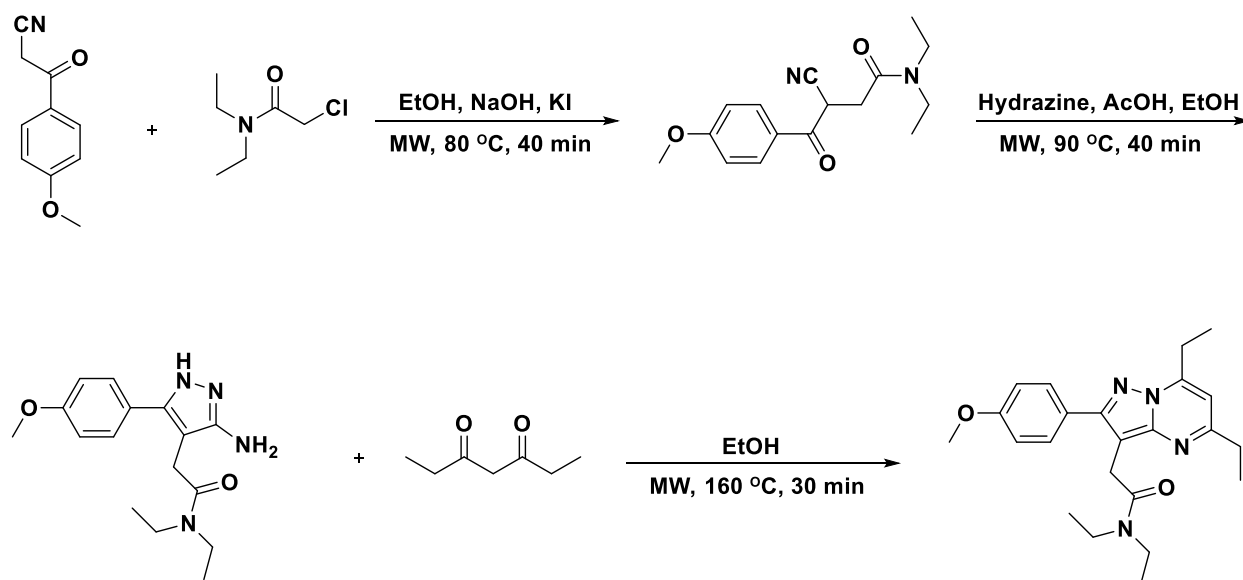


Figure 3.1.1 Structure of DPA-713 (**3.1**), 2-(5,7-diethyl-2-(4-methoxyphenyl)pyrazolo[1,5-*a*]pyrimidin-3-yl)-*N,N*-diethylacetamide, previously reported by our group (**3.2**) and indicated substituents of new pyrazolopyrimidine-based ligands.

3.2 Chemistry

Scheme 3.2.1 showed previously reported synthetic route to pyrazolopyrimidine-based TSPO ligands.^[36, 45, 52, 57] Starting from the reaction of 3-(4-methoxyphenyl)-3-oxopropanenitrile and 2-chloro-*N,N*-diethylacetamide, compound **3** was formed and further reacted with hydrazine to form pyrazolo ring. TSPO ligand DPA-713 was further synthesized through the reaction of **4** and 2,4-pentanedione.



Scheme 3.2.1 Reported synthetic route to pyrazolopyrimidine-based TSPO ligands.

Our prior synthetic route to pyrazolopyrimidine-based libraries required a divergent synthesis at the first step (**Figure 3.2.1**, left), which reduced the efficiency of producing products with various substituents. To achieve a more efficient pathway, we needed to develop a new route which allows diversification in the final step, providing a facile approach to generating a diverse library. (**Figure 3.2.1**, right).

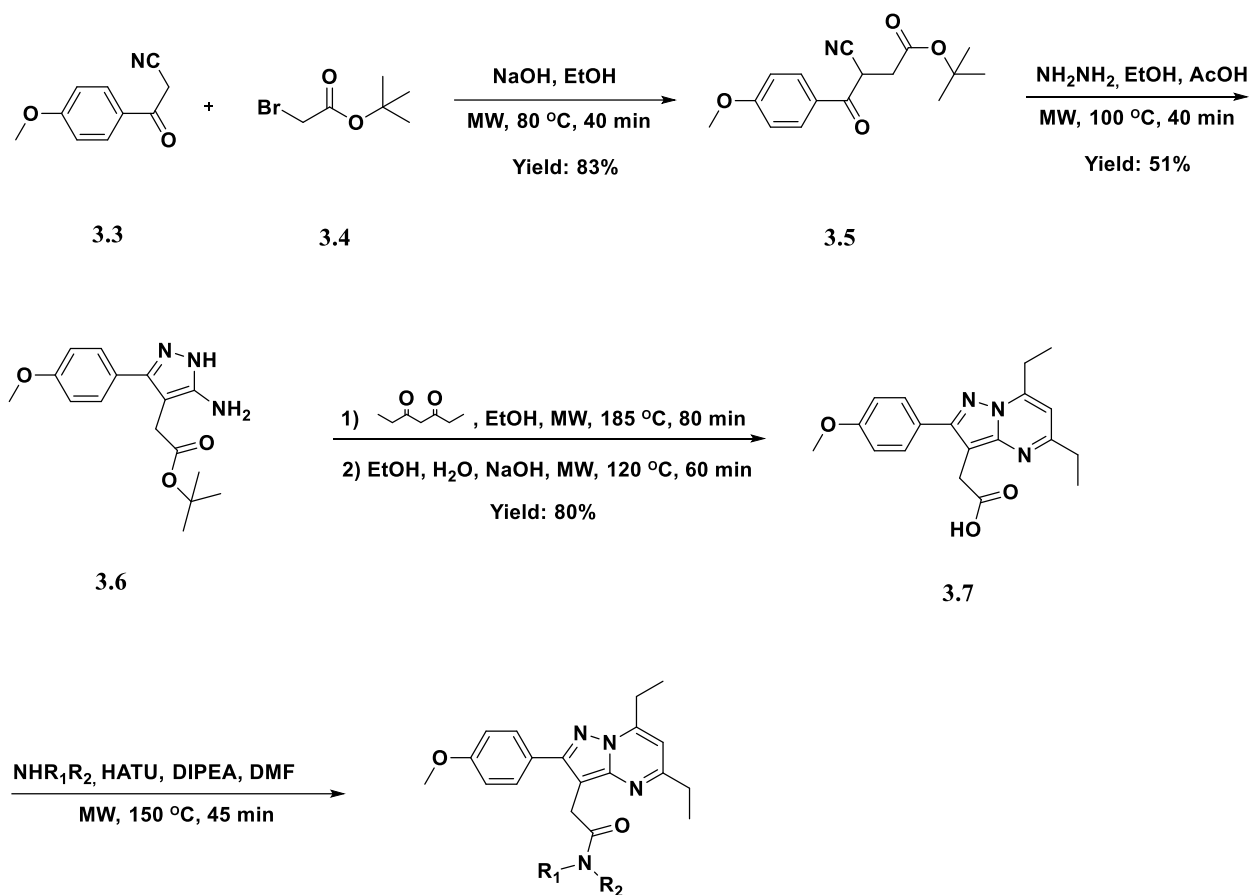


Figure 3.2.1 Comparison of different synthetic routes.

To further accelerate the library generation, we utilized microwave-assisted organic synthesis (MAOS). Featuring a high-speed synthesis approach, MAOS uses microwave heating to accelerate organic reactions. The ability of materials to convert the microwave to heat is dependent on dielectric properties.^[58-60] MAOS is less effective or useless to treat materials without permanent dipole moment. However, since either the reactants or solvents used in organic synthesis mostly have some polarity, most reaction systems can absorb and convert microwave efficiently.

Though some early research claimed MAOS had “specific” effects and the reaction under microwave behaved differently from conventional heating,^[61-62] most current researchers believe its ability to accelerate the reaction representing a pure thermal/kinetic effect. In conventional heating, the heat transfer from the heat source to reaction system is inefficient because it needs to penetrate and be absorbed through several layers of medium, including air and vessel. Typically, the vessel has a higher temperature than the reaction system, which is called wall effect. In MAOS, however, since most vessels are microwave transparent, the microwave can interact directly with the reaction with little energy loss from penetration.

The new synthetic route was shown in **Scheme 3.2.2**. Starting from commercially available compounds **3.3** and **3.4**, compound **3.5** was synthesized in a single step. Subsequently, the pyrazolo ring of compound **3.6** was formed by the reaction of compound **3.5** with hydrazine in ethanol, in the presence of acetic acid. Preparation of compound **3.7** was accomplished in a one-pot reaction procedure, combining compound **3.6** with 3,5-heptanedione to close pyrimidine ring, followed by deprotection to reveal the free carboxylic acid. Finally, a variety of secondary amines were subsequently reacted with carboxylic acid **3.7** to generate the final chemical probes evaluated here. In total, 16 probes were synthesized with a diversity of *N*-acetamide substituents.



Scheme 3.2.2 Synthetic route to *N,N*-acetamide disubstituted pyrazolopyrimidines.

3.3 Ligand Affinity

TSPO affinities of the chemical probes were determined using a C6 glioma cell lysate binding assay previously described.^[14]

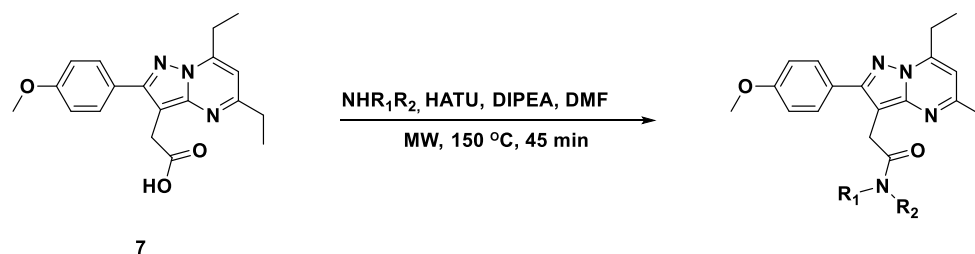
Previous investigation of 5/7 substitutions illuminated that TSPO affinity was highly sensitive to alkyl substitutions and intolerant of steric bulk. For example, when changing the ethyl group to isopropyl, the binding affinity was diminished from 0.18 nM to over 500 nM.^[14]

However, we found the acetamide position particularly tolerant to *N*-alkyl substitution, with entries of differentially substituted alkyl groups exhibiting affinities in the nano molar to sub-nano molar range with the chain length ranging from one to six carbons. Among them, *N*-alkyl substitutions of up to 5 carbon length exhibited affinities analogous or better than DPA-713.

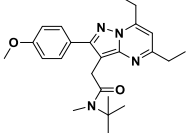
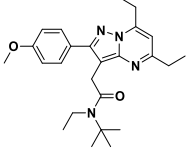
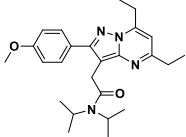
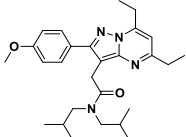
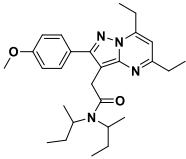
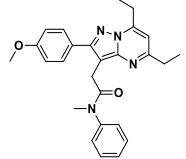
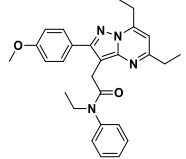
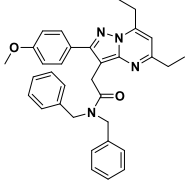
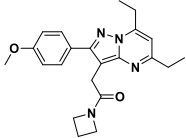
Chemical probes possessing branched alkane substituents typically maintained reasonably high affinity, yet branching generally diminished affinities relative to straight chain alkyl groups of similar carbon number. It was noted that the bulky *t*-butyl group significantly decreased binding affinity. When substituting ethyl groups with *t*-butyls, the affinity decreased by over 300-fold, from 0.18 nM (compound **3.10**) to 59.12 nM (compound **3.16**).

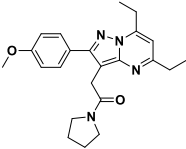
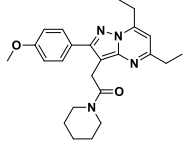
Interestingly, the introduction of a phenyl ring rescued the binding affinity. We observed the heterozygous phenyl-ethyl substitution pattern to be particularly favorable, resulting in a novel ligand with pico-molar activity ($K_i = 0.28$ nM), which is among the highest binding affinity for TSPO ligands reported to date. In contrast, when both *N*-acetamide substitutions were homologated to benzyl groups, affinity was decreased significantly ($K_i = 397.29$ nM). It was also found that acetamide substitution with ethyl group was generally well-tolerated in combination with many other *N*-substitutions on the acetamide. For example, mixed ethyl acetamides gained better than other substituents of similar structure, e.g. **3.15** ($K_i = 94.79$ nM) vs **3.16** ($K_i = 59.12$ nM), **3.20** ($K_i = 6.44$ nM) vs **3.21** ($K_i = 0.28$ nM). In contrast to acyclic derivatives, alicyclic constrained derivatives (**3.23**, **3.24** and **3.25**) exhibited very poor binding affinity.

Table 3.3.1 Structure, molecular weight, yield, and affinity of pyrazolopyrimidines.



Compound	Structure	MW	Yield	K_i (Nm) ^{c,d}
3.8^a (DPA-713)		366.46	---	4.7
3.9		366.46	97%	37.59±5.96
3.10^b		394.52	86%	0.18
3.11		422.57	82%	5.57±2.98
3.12		450.63	82%	7.34±0.89
3.13		478.68	80%	2.17±0.74
3.14		506.74	79%	18.57±10.27

3.15		408.55	64%	94.79±43.05
3.16		422.57	70%	59.12±16.12
3.17		422.57	67%	20.03±1.56
3.18		450.63	85%	13.25±1.76
3.19		450.63	76%	14.40±8.07
3.20		428.54	51%	6.44±1.44
3.21		442.56	49%	0.28±0.14
3.22		518.66	76%	397.29±69.39
3.23		378.48	96%	87.75±37.96

3.24		392.50	83%	127.20±13.13
3.25		406.53	84%	49.22±9.24

^aDPA-713, see ref 6. ^bProbe 5b, see ref 1. ^c K_i versus ³H-flunitrazepam > 10000 Nm. ^dAll K_i values were averaged from triple runs with corresponding standard derivation.

3.4 Lipophilicity

Recognizing acetamide substitution as an opportunity to diversify the binding affinity of novel TSPO ligands, we further evaluated the lipophilicity, which is an important factor that dictates biodistribution and clearance.^[63-64] For example, to pass the blood brain barrier to reach the target in the brain, the lipophilicity needs to be in the range of 2 to 3.5.

Lipophilicity is measured by log P, the partition coefficient of a drug between an aqueous (water) and lipophilic (octanol) phases.^[64]

$$\log P = \log \left(\frac{[\text{drug}] \text{ in octanol}}{[\text{drug}] \text{ in water}} \right) \quad \text{Equation 3.4.1}$$

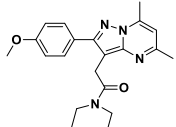
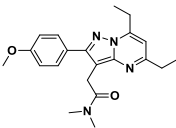
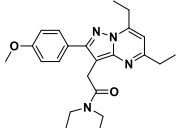
Lipophilicity (log $P_{7.5}$) was determined using analytical reverse phase HPLC as previously reported. Briefly, standard samples with known log $P_{7.5}$ were examined firstly by HPLC to determine the relative retention times (RRT). log K was then calculated from RRT and

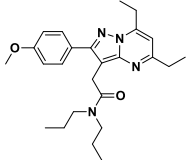
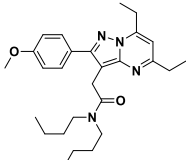
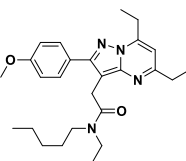
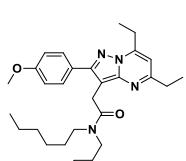
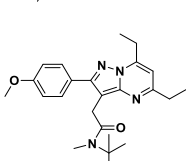
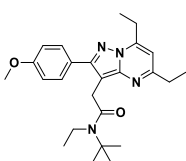
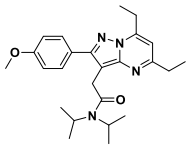
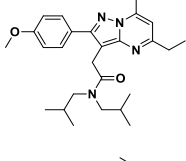
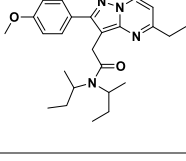
built relationship with $\log P_{7.5}$. Subsequently, the RRT and $\log K$ of the ligands were measured and compared with the calibration equation to find out the $\log P_{7.5}$.

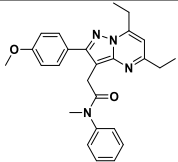
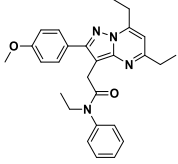
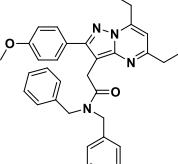
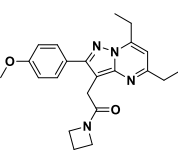
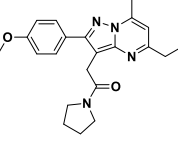
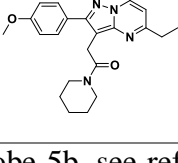
$$\log P = 1.72 \times \log K + 2.59 \quad \text{Equation 3.4.2}$$

As shown in **Table 3.4.1**, chain length was a critical determinant of lipophilicity within the *N*-alkyl series. Long carbon chain substitutions, such as **3.12** (n=4), **3.13** (n=5) and **3.14** (n=6), were extremely lipophilic as expected. Compared to straight chain alkyl groups of similar carbon number, branched alkyl substituents tended to exhibit more moderate lower lipophilicity. The lipophilicity of phenyl substitution compounds (**3.20** and **3.21**, **3.11** and **3.27** respectively) appeared to represent a compromise between longer alkyl chains and bulky branched substituents.

Table 3.4.1 Lipophilicity of pyrazolopyrimidines

Compound	Structure	Retention Time (min) ^c	$\log K$	$\log P_{7.5}$
3.8^a (DPA-713)		---	---	2.40
3.9		4.794	-0.068	2.47
3.10^b		---	---	2.84

3.11		9.787	0.445	3.35
3.12		15.831	0.709	3.81
3.13		27.645	0.987	4.29
3.14		50.788	1.271	4.78
3.15		7.933	0.316	3.13
3.16		9.509	0.428	3.32
3.17		8.958	0.392	3.26
3.18		15.08	0.684	3.77
3.19		14.753	0.673	3.75

3.20		7.742	0.300	3.11
3.21		9.051	0.398	3.27
3.22		14.495	0.664	3.73
3.23		5.153	-0.0273	2.58
3.24		5.675	0.078	2.72
3.25		6.807	0.213	2.96

^a DPA-713, see ref 6. ^b Probe 5b, see ref 1. ^c Retention time was averaged from triple runs with 1% or less standard deviation for each sample.

3.5 Plasma Protein Binding

Plasma protein binding is another important factor to determine the efficiency of a drug to reach the target. It measures the degree of a drug binds to the proteins in the plasma.

After injecting the drug (tracer in PET imaging) into the blood, it exists in both bound and unbound states. These two states exist together and interchange in an equilibrium when the binding is reversible.

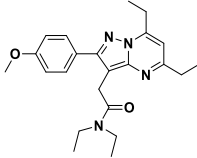
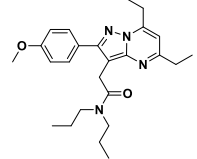
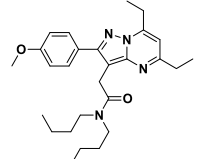
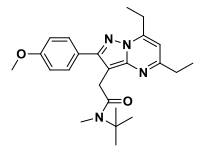
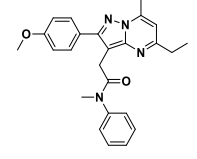
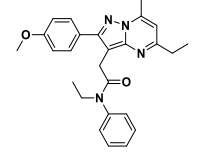


However, the bound fraction stays in the blood and cannot reach the target. Only the unbound fraction diffuses through the membranes and binds to the target. To be a more efficient tracer, it should have a higher unbound fraction.

Briefly, plasma protein binding was performed using the equilibrium dialysis method. A vessel was separated by a semipermeable membrane into two compartments. One compartment contained plasma, while the other only had buffer solution. The ligand was added into the vessel and shake for a few hours. After extraction, the buffer and plasma fractions were analyzed using standard LC-MS methods.^[65]

The majority of the compounds reported here exhibited unbound fractions of approximately 1%, including phenyl substituents (**Table 3.5.1**). It was noted that chemical probes exhibited higher lipophilicity tended to also exhibit lower unbound fraction. For example, the unbound fraction of compound **12** (n=4, log P_{7.5}=3.81) was 0.3%, the lowest among the examined library members.

Table 3.5.1 Plasma protein binding of selected compounds.

Compound	Structure	Fraction Unbound
3.10		1.1%
3.11		0.7%
3.12		0.3%
3.15		1.3%
3.20		1.1%
3.21		0.6%

3.6 Conclusion

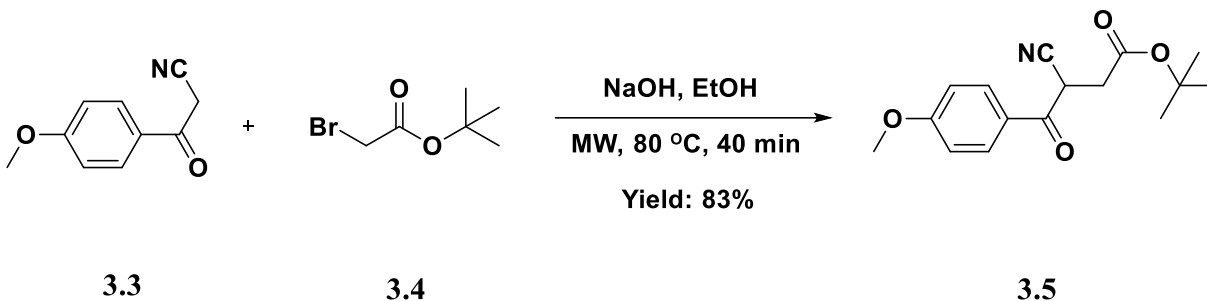
In summary, we illustrate here that the pendant acetamide represents an opportunity to diversify the chemical and physical properties of pyrazolopyrimidine-based TSPO ligands. Several new chemical probes exhibited suitable binding properties, lipophilicity and protein

binding to serve as TSPO imaging tracers when functionalized with an appropriate positron emitter such as Carbon-11. We anticipate that these results may expand opportunities of using TSPO ligands to image disease relevant to peripheral tissues.

3.7 Method and Materials

General Procedure for Ligand Synthesis

MAOS of Compound 3.5.

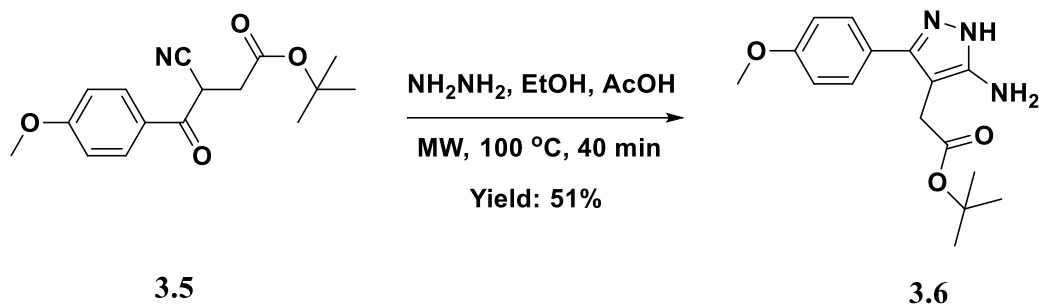


tert-butyl 3-cyano-4-(4-methoxyphenyl)-4-oxobutanoate (Compound 3.5)

To a solution of 3-(4-methoxyphenyl)-3-oxopropanenitrile (Compound 3.3, 1 g, 1 eq) and *tert*-butyl 2-bromoacetate (Compound 3.4, 1.672 g, 1.5 eq) in ethanol (EtOH, 20 mL) was added NaOH (274.3 mg, 1.2 eq). The reaction mixture was microwaved at 80 °C for 40 min. The reaction was monitored by LCMS. When completed, the mixture was concentrated and purified by Teledyne Isco CombiFlash Purification Systems on 40 g silica gel (DCM/methanol = 90/10, v/v) to yield compound 3.5 as a yellow solid.

¹H-NMR (CDCl₃, 400 MHz) δ 8.02 (d, 2H, *J* = 8.6 Hz), 7.0 (d, 2H, *J* = 8.6 Hz), 4.67 (t, 1H, *J* = 6.88 Hz), 3.90 (s, 3H), 3.20-3.14 (m, 1H), 2.87-2.82 (m, 1H), 1.45 (s, 9H); ¹³C-NMR (CDCl₃, 100 MHz) δ 186.9, 168.6, 164.7, 131.3, 126.8, 116.8, 114.3, 82.3, 55.6, 33.9, 33.8, 27.9. HRMS calc'd for C₁₆H₁₉NO₄ *m/z* = 290.1387 (M+H⁺), found 290.1393.

MAOS of Compound 3.6.

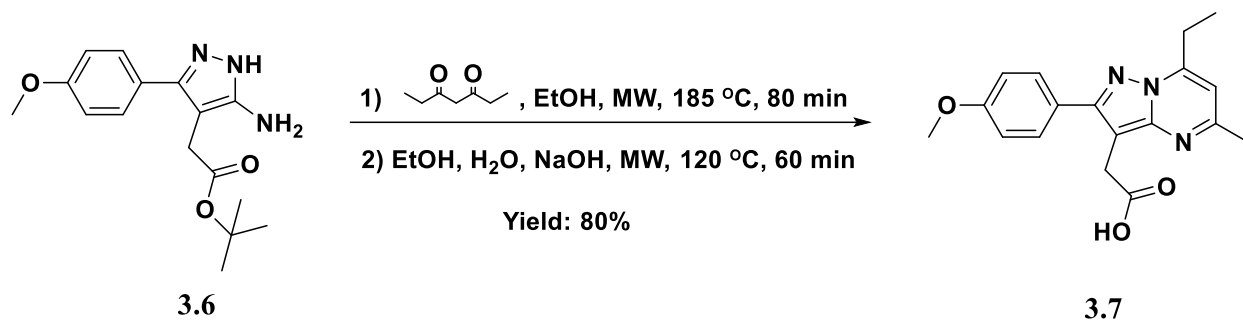


tert-butyl 2-(5-amino-3-(4-methoxyphenyl)-1*H*-pyrazol-4-yl)acetate (Compound 3.6)

To a solution of *tert*-butyl 3-cyano-4-(4-methoxyphenyl)-4-oxobutanoate (Compound **3.5**, 1 g, 1 eq) in ethanol (EtOH, 18 mL) was added hydrazine (110.7 mg, 1 eq) and acetic acid (0.25 mL). The reaction mixture was microwaved at 100 °C for 40 min. The reaction was monitored by LCMS. When completed, the mixture was concentrated and purified by Teledyne Isco CombiFlash Purification Systems on 40 g silica gel (DCM/methanol = 90/10, v/v) to yield compound **3.6** as a yellow solid.

¹H-NMR (CDCl₃, 400 MHz) δ 7.47 (d, 2H, *J* = 8.7 Hz), 6.97 (d, 2H, *J* = 8.6 Hz), 3.84 (s, 3H), 3.31 (s, 2H), 1.47 (s, 9H); ¹³C-NMR (CDCl₃, 100 MHz) δ 171.3, 159.8, 154.2, 142.6, 128.9, 122.6, 114.3, 97.1, 81.3, 55.3, 30.9, 28.0. HRMS calc'd for C₁₆H₂₁N₃O₃ *m/z* = 304.1656 (M+H⁺), found 304.1660.

MAOS of Compound 3.7.

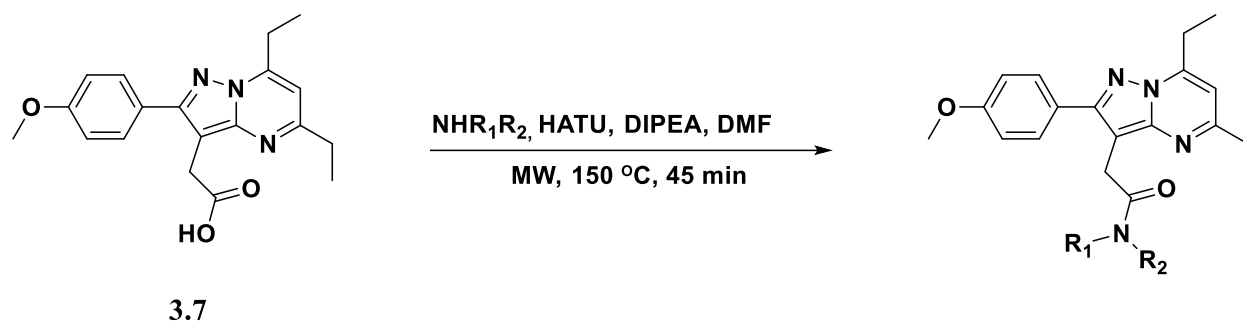


2-(5,7-diethyl-2-(4-methoxyphenyl)pyrazolo[1,5-*a*]pyrimidin-3-yl)acetic acid (Compound 3.7)

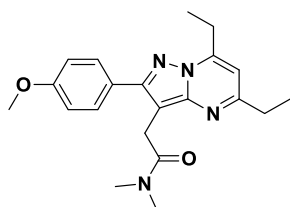
To a solution of *tert*-butyl 2-(5-amino-3-(4-methoxyphenyl)-1*H*-pyrazol-4-yl)acetate (Compound 3.6, 0.5 g, 1 eq) in ethanol (10 mL) was added heptane-3,5-dione (232.3 mg, 1.1 eq). The reaction mixture was microwaved at 185 °C for 80 min. After that, NaOH (132 mg, 2 eq) and water (3 mL) were added into the vial and the mixture was irradiated at 120 °C for another 60 min. The reaction was monitored by LCMS. When completed, the ethanol solvent was dried with rotary evaporator and then the reaction was acidified with 1.0 M aqueous HCl and extracted with 20 mL dichloromethane (DCM) three times. The organic solutions were then collected, dried over magnesium sulfate, and concentrated to dryness. The residue was purified by Teledyne Isco CombiFlash Purification Systems on 40 g silica gel (DCM/methanol = 90/10, v/v) to yield compound 3.7.

¹H-NMR (CDCl₃, 400 MHz) δ 7.7 (d, 2H, *J* = 8.7 Hz), 7.02 (d, 2H, *J* = 8.7 Hz), 6.59 (s, 1H), 3.99 (s, 2H), 3.86 (s, 3H), 3.26-3.20 (m, 2H), 2.94-2.88 (m, 2H), 1.46 (t, 3H, *J* = 7.48 Hz), 1.37 (t, 3H, *J* = 7.6 Hz); ¹³C-NMR (CDCl₃, 100 MHz) δ 173.6, 163.0, 160.0, 154.9, 151.0, 146.8, 129.9, 125.3, 114.2, 105.2, 97.9, 55.3, 30.9, 28.0, 23.3, 12.7, 10.2. HRMS calc'd for C₁₉H₂₁N₃O₃ *m/z* = 340.1656 (M+H⁺), found 340.1660.

General Procedure for MAOS of the Library.



To a solution of 2-(5,7-diethyl-2-(4-methoxyphenyl)pyrazolo[1,5-*a*]pyrimidin-3-yl)acetic acid (Compound **7**, 15 mg, 1 eq) in DMF (1 mL) was added HATU (15.4 mg, 1 eq), *N,N*-Diisopropylethylamine (DIPEA, 10.4 mg, 2 eq), and 1 eq of a variety of secondary amine. The reaction mixture was then microwaved at 150 °C for 45 min. The reaction was monitored by LCMS. When completed, the mixture was then purified with Gilson (C18 column, acetonitrile/water, 5% to 95%).

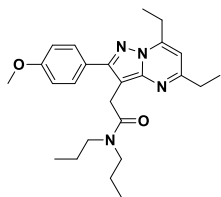


2-(5,7-diethyl-2-(4-methoxyphenyl)pyrazolo[1,5-*a*]pyrimidin-3-yl)-*N,N*-dimethylacetamide (Compound **3.9**)

Prepared according to general procedure, 97% yield.

¹H-NMR (CDCl₃, 400 MHz) δ 7.73 (d, 2H, *J* = 8.8 Hz), 7.01 (d, 2H, *J* = 8.8 Hz), 6.58 (s, 1H), 3.98 (s, 2H), 3.86 (s, 3H), 3.27-3.21 (m, 2H), 3.17 (s, 3H), 2.99 (s, 3H), 2.94-2.88 (m, 2H), 1.47 (t, 3H, *J* = 7.5 Hz), 1.36 (t, 3H, *J* = 7.6 Hz); ¹³C-NMR (CDCl₃, 100 MHz) δ 173.6, 163.0, 160.0,

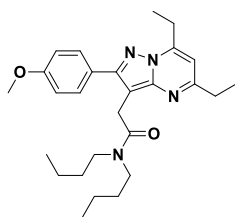
154.9, 151.0, 146.8, 129.9, 125.3, 114.2, 105.2, 97.9, 55.3, 30.9, 28.0, 23.3, 12.7, 10.2. HRMS calc'd for C₂₁H₂₆N₄O₂ m/z = 367.2129 (M+H⁺), found 367.2131.



**2-(5,7-diethyl-2-(4-methoxyphenyl)pyrazolo[1,5-*a*]pyrimidin-3-yl)-*N,N*-dipropylacetamide
(Compound 3.11)**

Prepared according to general procedure, 82% yield.

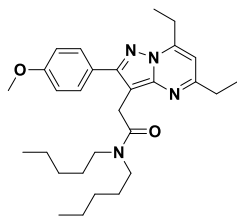
¹H-NMR (CDCl₃, 400 MHz) δ 7.81 (d, 2H, *J* = 8.8 Hz), 6.98 (d, 2H, *J* = 8.8 Hz), 6.52 (s, 1H), 3.95 (s, 2H), 3.86 (s, 3H), 3.43 (t, 2H, *J* = 7.8 Hz), 3.31 (t, 2H, *J* = 7.6 Hz), 3.23-3.17 (m, 2H), 2.87-2.81 (m, 3H), 1.67-1.61 (m, 2H), 1.57-1.51 (m, 2H), 1.45 (t, 3H, *J* = 7.5 Hz), 1.34 (t, 3H, *J* = 7.6 Hz), 0.9 (t, 3H, *J* = 7.4 Hz), 0.86 (t, 3H, *J* = 7.4 Hz); ¹³C-NMR (CDCl₃, 100 MHz) δ 170.8, 162.2, 159.7, 154.9, 149.9, 147.2, 129.9, 126.3, 113.9, 104.8, 100.7, 55.2, 50.0, 48.1, 31.2, 28.1, 23.3, 22.2, 20.8, 12.8, 11.3, 11.2, 10.2. HRMS calc'd for C₂₅H₃₄N₄O₂ m/z = 423.2755 (M+H⁺), found 427.2763.



***N,N*-dibutyl-2-(5,7-diethyl-2-(4-methoxyphenyl)pyrazolo[1,5-*a*]pyrimidin-3-yl)acetamide
(Compound 3.12)**

Prepared according to general procedure, 82% yield.

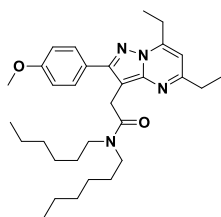
$^1\text{H-NMR}$ (CDCl_3 , 400 MHz) δ 7.82 (d, 2H, $J = 8.8$ Hz), 6.99 (d, 2H, $J = 8.8$ Hz), 6.51 (s, 1H), 3.94 (s, 2H), 3.85 (s, 3H), 3.44 (t, 2H, $J = 7.8$ Hz), 3.33 (t, 2H, $J = 7.6$ Hz), 3.23-3.17 (m, 2H), 2.86-2.80 (m, 2H), 1.62-1.54 (m, 2H), 1.50-1.47 (m, 2H), 1.45 (t, 3H, $J = 7.5$ Hz), 1.34 (t, 3H, $J = 7.6$ Hz), 1.30-1.25 (m, 4H), 0.92 (t, 3H, $J = 7.3$ Hz), 0.89 (t, 3H, $J = 7.3$ Hz); $^{13}\text{C-NMR}$ (CDCl_3 , 100 MHz) δ 170.7, 162.2, 159.7, 154.8, 149.8, 147.4, 130.0, 126.3, 113.9, 104.8, 100.8, 55.2, 48.1, 46.2, 31.3, 31.2, 29.8, 28.2, 23.2, 20.1, 20.0, 13.8, 13.7, 12.8, 10.3. HRMS calc'd for $\text{C}_{27}\text{H}_{38}\text{N}_4\text{O}_2$ $m/z = 451.3068$ ($\text{M}+\text{H}^+$), found 451.3074.



**2-(5,7-diethyl-2-(4-methoxyphenyl)pyrazolo[1,5-*a*]pyrimidin-3-yl)-*N,N*-dipentylacetamide
(Compound 3.13)**

Prepared according to general procedure, 80% yield.

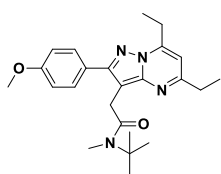
$^1\text{H-NMR}$ (CDCl_3 , 400 MHz) δ 7.76 (d, 2H), 6.99 (d, 2H, $J = 8.2$ Hz), 6.58 (s, 1H), 4.14 (s, 2H), 3.86 (s, 3H), 3.51-3.18 (m, 6H), 3.07-2.98 (m, 2H), 1.82-1.60 (m, 2H), 1.56-1.49 (m, 2H), 1.47 (t, 3H, $J = 7.4$ Hz), 1.39 (t, 3H, $J = 7.6$ Hz), 1.26-0.84 (m, 14H); $^{13}\text{C-NMR}$ (CDCl_3 , 100 MHz) δ 170.4, 169.9, 162.3, 160.1, 156.5, 151.0, 130.0, 125.3, 113.9, 104.1, 101.0, 55.2, 52.0, 48.7, 34.3, 33.2, 29.1, 28.5, 27.0, 23.8, 22.4, 16.9, 13.9, 12.9, 11.5, 11.3, 10.2. HRMS calc'd for $\text{C}_{29}\text{H}_{42}\text{N}_4\text{O}_2$ $m/z = 479.3381$ ($\text{M}+\text{H}^+$), found 479.3385.



**2-(5,7-diethyl-2-(4-methoxyphenyl)pyrazolo[1,5-*a*]pyrimidin-3-yl)-*N,N*-dihexylacetamide
(Compound 3.14)**

Prepared according to general procedure, 79% yield.

$^1\text{H-NMR}$ (CDCl_3 , 400 MHz) δ 7.82 (d, 2H, $J = 8.8$ Hz), 6.99 (d, 2H, $J = 8.8$ Hz), 6.52 (s, 1H), 3.94 (s, 2H), 3.85 (s, 3H), 3.42 (t, 2H, $J = 7.8$ Hz), 3.32 (t, 2H, $J = 7.6$ Hz), 3.23-3.17 (m, 2H), 2.87-2.81 (m, 2H), 1.58-1.53 (m, 2H), 1.51-1.46 (m, 2H), 1.45 (t, 3H, $J = 7.5$ Hz), 1.34 (t, 3H, $J = 7.6$ Hz), 1.28-1.22 (m, 12H), 0.88 (t, 3H, $J = 6.7$ Hz), 0.86 (t, 3H, $J = 6.8$ Hz); $^{13}\text{C-NMR}$ (CDCl_3 , 100 MHz) δ 170.6, 162.2, 159.7, 154.9, 149.8, 147.3, 129.9, 126.3, 113.9, 104.7, 100.8, 55.2, 48.4, 46.5, 31.6, 31.5, 31.2, 29.0, 28.3, 27.6, 26.6, 26.5, 23.3, 22.5, 14.0, 13.9, 12.8, 10.2. HRMS calc'd for $\text{C}_{31}\text{H}_{46}\text{N}_4\text{O}_2$ $m/z = 507.3694$ ($\text{M}+\text{H}^+$), found 507.3697.

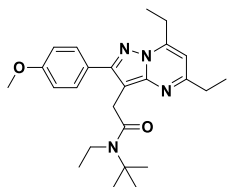


***N*-(*tert*-butyl)-2-(5,7-diethyl-2-(4-methoxyphenyl)pyrazolo[1,5-*a*]pyrimidin-3-yl)-*N*-methylacetamide (Compound 3.15)**

Prepared according to general procedure, 64% yield.

$^1\text{H-NMR}$ (CDCl_3 , 400 MHz) δ 7.73 (d, 2H, $J = 8.8$ Hz), 6.98 (d, 2H, $J = 8.8$ Hz), 6.53 (s, 1H), 3.94 (s, 2H), 3.86 (s, 3H), 3.23-3.18 (m, 2H), 2.99 (s, 3H), 2.88-2.83 (m, 2H), 1.45 (t, 3H, $J = 7.5$

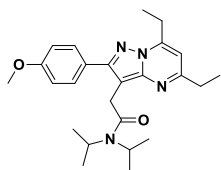
Hz), 1.38 (s, 9H), 1.35 (t, 3H, $J = 7.6$ Hz); $^{13}\text{C-NMR}$ (CDCl_3 , 100 MHz) δ 171.6, 162.4, 159.7, 154.9, 150.4, 146.9, 129.8, 126.3, 113.9, 104.6, 101.0, 56.9, 55.3, 32.2, 31.7, 31.1, 28.1, 23.3, 13.1, 10.2. HRMS calc'd for $\text{C}_{24}\text{H}_{32}\text{N}_4\text{O}_2$ $m/z = 409.2598$ ($\text{M}+\text{H}^+$), found 409.2603.



***N*-(*tert*-butyl)-2-(5,7-diethyl-2-(4-methoxyphenyl)pyrazolo[1,5-*a*]pyrimidin-3-yl)-*N*-ethylacetamide (Compound 3.16)**

Prepared according to general procedure, 70% yield.

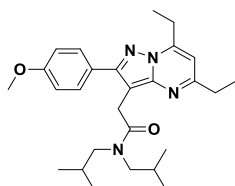
$^1\text{H-NMR}$ (CDCl_3 , 400 MHz) δ 7.67 (d, 2H, $J = 8.8$ Hz), 6.99 (d, 2H, $J = 8.8$ Hz), 6.58 (s, 1H), 4.01 (s, 2H), 3.86 (s, 3H), 3.57-3.52 (m, 2H), 3.27-3.22 (m, 2H), 2.96-2.90 (m, 2H), 1.49-1.45 (m, 12H), 1.37 (t, 3H, $J = 7.6$ Hz), 1.25 (t, 3H, $J = 7.1$ Hz); $^{13}\text{C-NMR}$ (CDCl_3 , 100 MHz) δ 171.1, 162.6, 159.9, 155.9, 152.3, 145.4, 130.0, 125.6, 113.9, 104.4, 100.9, 57.6, 55.3, 39.6, 30.4, 30.1, 28.8, 23.6, 16.9, 13.0, 10.2. HRMS calc'd for $\text{C}_{25}\text{H}_{34}\text{N}_4\text{O}_2$ $m/z = 423.2755$ ($\text{M}+\text{H}^+$), found 423.2757.



2-(5,7-diethyl-2-(4-methoxyphenyl)pyrazolo[1,5-*a*]pyrimidin-3-yl)-*N,N*-diisopropylacetamide (Compound 3.17)

Prepared according to general procedure, 67% yield.

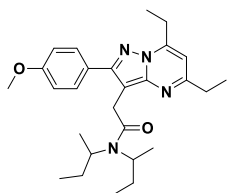
¹H-NMR (CDCl₃, 400 MHz) δ 7.71 (d, 2H, *J* = 8.7 Hz), 6.99 (d, 2H, *J* = 8.8 Hz), 6.61 (s, 1H), 4.28-4.23 (m, 1H), 4.2 (s, 2H), 3.86 (s, 3H), 3.49-3.43 (m, 1H), 3.31-3.26 (m, 2H), 3.13-3.06 (m, 2H), 1.48 (t, 3H, *J* = 7.5 Hz), 1.41 (t, 3H, *J* = 7.6 Hz); ¹³C-NMR (CDCl₃, 100 MHz) δ 169.9, 167.9, 162.6, 160.8, 158.9, 138.8, 130.0, 123.9, 114.1, 103.1, 101.1, 55.3, 48.9, 46.1, 30.3, 26.7, 24.5, 20.8, 20.5, 13.3, 10.2. HRMS calc'd for C₂₅H₃₄N₄O₂ *m/z* = 423.2755 (M+H⁺), found 423.2760.



**2-(5,7-diethyl-2-(4-methoxyphenyl)pyrazolo[1,5-*a*]pyrimidin-3-yl)-*N,N*-diisobutylacetamide
(Compound 3.18)**

Prepared according to general procedure, 85% yield.

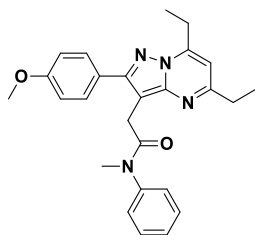
¹H-NMR (CDCl₃, 400 MHz) δ 7.82 (d, 2H, *J* = 8.8 Hz), 6.99 (d, 2H, *J* = 8.8 Hz), 6.52 (s, 1H), 3.97 (s, 2H), 3.85 (s, 3H), 3.34 (d, 2H, *J* = 7.6 Hz), 3.24-3.17 (m, 4H), 2.87-2.82 (m, 2H), 2.11-1.88 (m, 2H), 1.45 (t, 3H, *J* = 7.5 Hz), 1.34 (t, 3H, *J* = 7.6 Hz), 0.95 (d, 6H, *J* = 6.6 Hz), 0.83 (d, 6H, *J* = 6.7 Hz); ¹³C-NMR (CDCl₃, 100 MHz) 171.6, 162.2, 159.8, 155.0, 150.2, 147.0, 130.0, 126.2, 113.9, 104.7, 100.9, 56.0, 55.2, 53.9, 31.0, 28.3, 28.0, 26.5, 23.3, 20.1, 20.0, 12.7, 10.2. HRMS calc'd for C₂₇H₃₈N₄O₂ *m/z* = 451.3068 (M+H⁺), found 451.3069.



***N,N*-di-*sec*-butyl-2-(5,7-diethyl-2-(4-methoxyphenyl)pyrazolo[1,5-*a*]pyrimidin-3-yl)acetamide (Compound 3.19)**

Prepared according to general procedure, 76% yield.

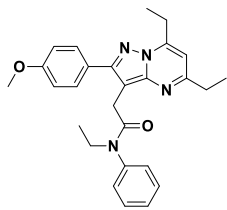
¹H-NMR (CDCl₃, 400 MHz) δ 7.75 (dd, 2H, *J*₁ = 8.8 Hz, *J*₂ = 8.8 Hz 3 Hz), 6.98 (d, 2H, *J* = 8Hz), 6.54 (s, 1H), 4.04-3.92 (m, 2H), 3.86 (s, 3H), 3.57 (s, 2H), 3.24-3.22 (m, 2H), 2.89-2.84 (m, 2H), 1.71-1.58 (m, 3H), 1.45 (t, 3H, *J* = 7.5 Hz), 1.36-1.33 (m, 6H), 1.11-1.02 (m, 3H), 0.90-0.78 (m, 6H); ¹³C-NMR (CDCl₃, 100 MHz) 170.6, 162.4, 159.8, 155.1, 150.1, 146.6, 129.9, 125.9, 113.8, 104.6, 100.6, 55.3, 52.9, 30.9, 30.2, 27.5, 27.4, 23.4, 17.8, 17.7, 12.9, 12.1, 11.9, 10.2. HRMS calc'd for C₂₇H₃₈N₄O₂ *m/z* = 451.3068 (M+H⁺), found 451.3070.



2-(5,7-diethyl-2-(4-methoxyphenyl)pyrazolo[1,5-*a*]pyrimidin-3-yl)-*N*-methyl-*N*-phenylacetamide (Compound 3.20)

Prepared according to general procedure, 51% yield.

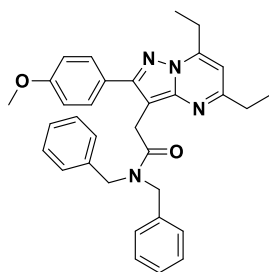
H-NMR (CDCl₃, 400 MHz) δ 7.66 (d, 2H, *J* = 8.6 Hz), 7.41-7.29 (m, 5H), 7.0 (d, 2H, *J* = 8.8 Hz), 6.53 (s, 1H), 3.88 (s, 3H), 3.75 (s, 2H), 3.29 (s, 3H), 3.22-3.16 (m, 2H), 2.92-2.86 (m, 2H), 1.44 (t, 3H, *J* = 7.5 Hz), 1.38 (t, 3H, *J* = 7.6 Hz); ¹³C-NMR (CDCl₃, 100 MHz) 171.2, 162.4, 159.8, 155.1, 150.9, 146.5, 143.9, 129.8, 129.6, 127.6, 127.3, 125.9, 113.9, 104.7, 100.4, 55.3, 37.7, 30.7, 29.1, 23.4, 12.9, 10.2. HRMS calc'd for C₂₆H₂₈N₄O₂ *m/z* = 429.2285 (M+H⁺), found 429.2289.



2-(5,7-diethyl-2-(4-methoxyphenyl)pyrazolo[1,5-*a*]pyrimidin-3-yl)-*N*-ethyl-*N*-phenylacetamide (Compound 3.21)

Prepared according to general procedure, 49% yield.

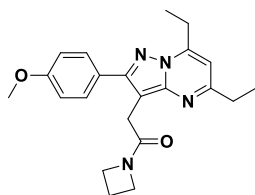
$^1\text{H-NMR}$ (CDCl_3 , 400 MHz) δ 7.66 (d, 2H, $J = 8.6$ Hz), 7.39-7.35 (m, 2H), 7.31-7.29 (m, 3H), 7.0 (d, 2H, $J = 8.8$ Hz), 6.52 (s, 1H), 3.88 (s, 3H), 3.78-3.72 (m, 2H), 3.7 (s, 2H), 3.21-3.16 (m, 2H), 2.91-2.86 (m, 2H), 1.44 (t, 3H, $J = 7.5$ Hz), 1.38 (t, 3H, $J = 7.6$ Hz), 1.11 (t, 3H, $J = 7.1$ Hz); $^{13}\text{C-NMR}$ (CDCl_3 , 100 MHz) 170.5, 162.3, 159.8, 155.0, 150.7, 142.3, 129.8, 129.5, 128.4, 127.6, 126.0, 113.9, 104.7, 100.6, 55.3, 44.5, 30.8, 29.5, 23.4, 13.0, 12.9, 10.2. HRMS calc'd for $\text{C}_{27}\text{H}_{30}\text{N}_4\text{O}_2$ $m/z = 443.2442$ ($\text{M}+\text{H}^+$), found 443.2444.



***N,N*-dibenzyl-2-(5,7-diethyl-2-(4-methoxyphenyl)pyrazolo[1,5-*a*]pyrimidin-3-yl)acetamide (Compound 3.22)**

Prepared according to general procedure, 76% yield.

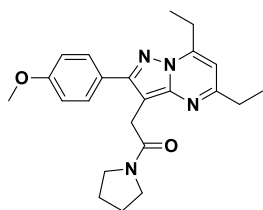
¹H-NMR (CDCl₃, 400 MHz) δ 7.85 (d, 2H, *J* = 8.8 Hz), 7.31-7.24 (m, 10H), 7.0 (d, 2H, *J* = 8.8 Hz), 6.49 (s, 1H), 4.71 (s, 2H), 4.62 (s, 2H), 4.11 (s, 2H), 3.88 (s, 3H), 3.18-3.13 (m, 2H), 2.86-2.80 (m, 2H), 1.43 (t, 3H, *J* = 7.5 Hz), 1.33 (t, 3H, *J* = 7.6 Hz); ¹³C-NMR (CDCl₃, 100 MHz) 171.9, 162.3, 159.8, 154.8, 149.9, 147.2, 137.4, 136.6, 130.0, 128.5, 128.4, 128.3, 127.2, 126.2, 126.1, 113.9, 104.8, 100.1, 55.2, 50.2, 48.6, 31.2, 28.6, 23.2, 12.8, 10.2. HRMS calc'd for C₃₃H₃₄N₄O₂ *m/z* = 519.2755 (M+H⁺), found 519.2760.



**1-(azetidin-1-yl)-2-(5,7-diethyl-2-(4-methoxyphenyl)pyrazolo[1,5-*a*]pyrimidin-3-yl)ethanone
(Compound 3.23)**

Prepared according to general procedure, 96% yield.

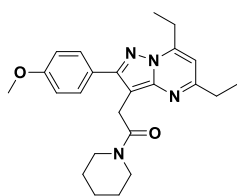
¹H-NMR (CDCl₃, 400 MHz) δ 7.76 (d, 2H, *J* = 8.8 Hz), 7.02 (d, 2H, *J* = 8.8 Hz), 6.61 (s, 1H), 4.3 (t, 2H, *J* = 7.6 Hz), 4.09 (t, 2H, *J* = 7.6 Hz), 3.87 (s, 3H), 3.76 (s, 2H), 3.27-3.21 (m, 2H), 2.97-2.91 (m, 2H), 2.32-2.25 (m, 2H), 1.47 (t, 3H, *J* = 7.5 Hz), 1.39 (t, 3H, *J* = 7.6 Hz); ¹³C-NMR (CDCl₃, 100 MHz) 171.3, 162.8, 160.1, 155.9, 152.1, 145.6, 130.1, 125.3, 114.1, 104.8, 98.9, 55.3, 50.9, 48.6, 30.4, 26.2, 23.5, 15.1, 12.9, 10.1. HRMS calc'd for C₂₂H₂₆N₄O₂ *m/z* = 379.2129 (M+H⁺), found 379.2131.



2-(5,7-diethyl-2-(4-methoxyphenyl)pyrazolo[1,5-*a*]pyrimidin-3-yl)-1-(pyrrolidin-1-yl)ethanone (Compound 3.24)

Prepared according to general procedure, 83% yield.

$^1\text{H-NMR}$ (CDCl_3 , 400 MHz) δ 7.69 (d, 2H, $J = 8.8$ Hz), 7.01 (d, 2H, $J = 8.8$ Hz), 6.68 (s, 1H), 4.15 (s, 2H), 3.86 (s, 3H), 3.7 (t, 2H, $J = 6.8$ Hz), 3.52 (t, 2H, $J = 6.9$ Hz), 3.34-3.28 (m, 2H), 3.18-3.12 (m, 2H), 2.04-1.98 (m, 2H), 1.93-1.88 (m, 2H), 1.49 (t, 3H, $J = 7.5$ Hz), 1.42 (t, 3H, $J = 7.6$ Hz); $^{13}\text{C-NMR}$ (CDCl_3 , 100 MHz) 169.1, 162.7, 160.4, 159.4, 158.9, 130.1, 124.5, 116.3, 114.2, 103.9, 99.8, 55.3, 46.9, 46.4, 29.5, 28.5, 25.9, 24.2, 24.0, 13.1, 10.1. HRMS calc'd for $\text{C}_{23}\text{H}_{28}\text{N}_4\text{O}_2$ $m/z = 393.2285$ ($\text{M}+\text{H}^+$), found 393.2288.



2-(5,7-diethyl-2-(4-methoxyphenyl)pyrazolo[1,5-*a*]pyrimidin-3-yl)-1-(piperidin-1-yl)ethanone (Compound 3.25)

Prepared according to general procedure, 84% yield.

$^1\text{H-NMR}$ (CDCl_3 , 400 MHz) δ 7.77 (d, 2H, $J = 8.8$ Hz), 7.0 (d, 2H, $J = 8.8$ Hz), 6.56 (s, 1H), 3.99 (s, 2H), 3.86 (s, 3H), 3.57 (t, 4H, $J = 5.1$ Hz), 3.26-3.20 (m, 2H), 2.90-2.85 (m, 2H), 1.66-1.61 (m, 2H), 1.56-1.49 (m, 4H), 1.46 (t, 3H, $J = 7.5$ Hz), 1.35 (t, 3H, $J = 7.6$ Hz); $^{13}\text{C-NMR}$ (CDCl_3 , 100 MHz) 169.4, 162.5, 159.9, 155.3, 151.0, 146.3, 129.9, 125.9, 113.9, 104.6, 100.2, 55.3, 46.9, 43.3, 30.8, 28.2, 26.3, 25.6, 24.5, 23.4, 13.0, 10.2. HRMS calc'd for $\text{C}_{24}\text{H}_{30}\text{N}_4\text{O}_2$ $m/z = 407.2442$ ($\text{M}+\text{H}^+$), found 407.2444.

General Experimental

In vitro TSPO Binding Assay.

C6 cells were washed with phosphate-buffered saline (PBS), frozen, and then thawed in lysis buffer to generate C6 cell lysate. The cell lysate was then incubated with ^3H -PK 11195 (final concentration: 0.6 nM) and synthesized ligands (final concentration 10^{-5} to 10^{-12} M) at 4 °C for 2 hrs in 24 well plate. The solution was washed and filtered with Brandel harvester and collected on filter paper. Scintillation buffer was then added into the vial with filter paper and liquid scintillation counter (Beckman LS 6000 Scintillation Counter) was applied to measure residual radioactive on the paper. Binding affinity was further calculated using Prism GraphPad software.

Lipophilicity.

Lipophilicity was measured using HPLC method with a C18 Dynamax column and a mobile phase of phosphate buffer (85/15, v/v, pH = 7.5) and methanol. A group of standard samples with known log $P_{7.5}$ was measured first to find the retention time. The standards included catechol, aniline, benzene, bromobenzene, toluene, ethylbenzene, 2-chlorobiphenyl, biphenyl, 1-chloronaphthalene, 1,2,3-trimethylbenzene, 1,2,3,4-tetrachlorobenzene, 1,2,4,5-tetrabromobenzene, pentachlorobenzene, and 4-nitrophenol. log K was further calculated from relative retention time and built working curve verse log $P_{7.5}$. The function between log $P_{7.5}$ and log K was found to be $\log P_{7.5} = 1.72 \cdot \log K + 2.59$. TSPO ligands were further measured their relative retention times to achieve corresponding log K values. log $P_{7.5}$ was calculated subsequently by using the above function.

CHAPTER 4

NOVEL TSPO FLUORESCENT LIGANDS FOR OPTICAL IMAGING

4.1 Introduction

Molecular imaging plays an important role in disease detection, staging, and drug development through the visualization, characterization, and measurement of biological processes at the cellular and molecular level in humans and other living systems. **Chapter 3** focused on the development and characterization of high-affinity ligands for PET imaging. This chapter will further explore the utility of fluorescent probes for optical imaging.

Herein, we developed a series of new TSPO ligands with appended fluorescein isothiocyanate (FITC) easily detectable by conventional optical imaging and microscopy based upon our optimized pyrazolopyrimidine structure. A library of candidate ligands were expanded and subjected to competitive binding assays that explored the effects of linker length (n= 2-8). The prioritized fluorescent probe exhibited exceptional TSPO affinity and negligible central benzodiazepine receptor (CBR) activity, had suitable *in vitro* imaging characteristics, and further demonstrated specific binding to mitochondria in live cells.

4.2 Chemistry

In our prior work, from optimizing the 5, 6, and 7 positions of the pyrazolopyrimidine DPA-713, we reported a novel TSPO PET tracer with improved affinity and pharmacokinetic properties. Based upon its structure, fluorescent ligands were synthesized through conjugating the TSPO ligand unit with FITC by various linker length (2-8 carbons, **Figure 4.2.1**). The ligand unit was used to identify target TSPO, and the dye unit was used to emit the signal.

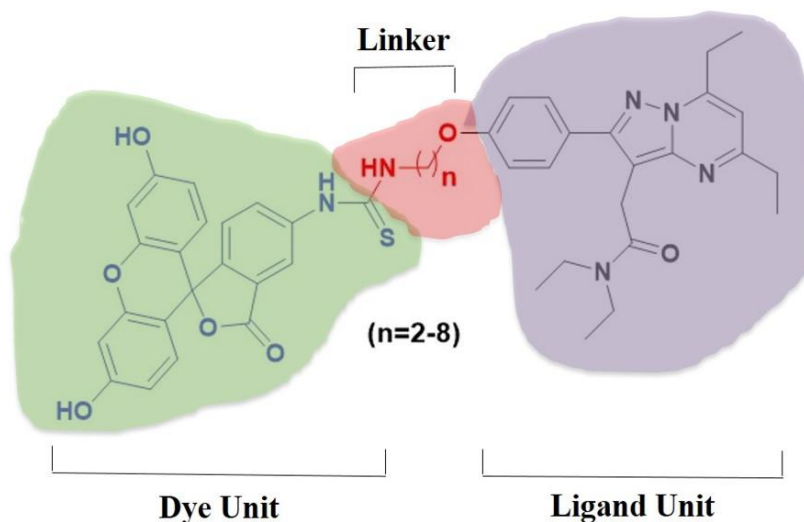
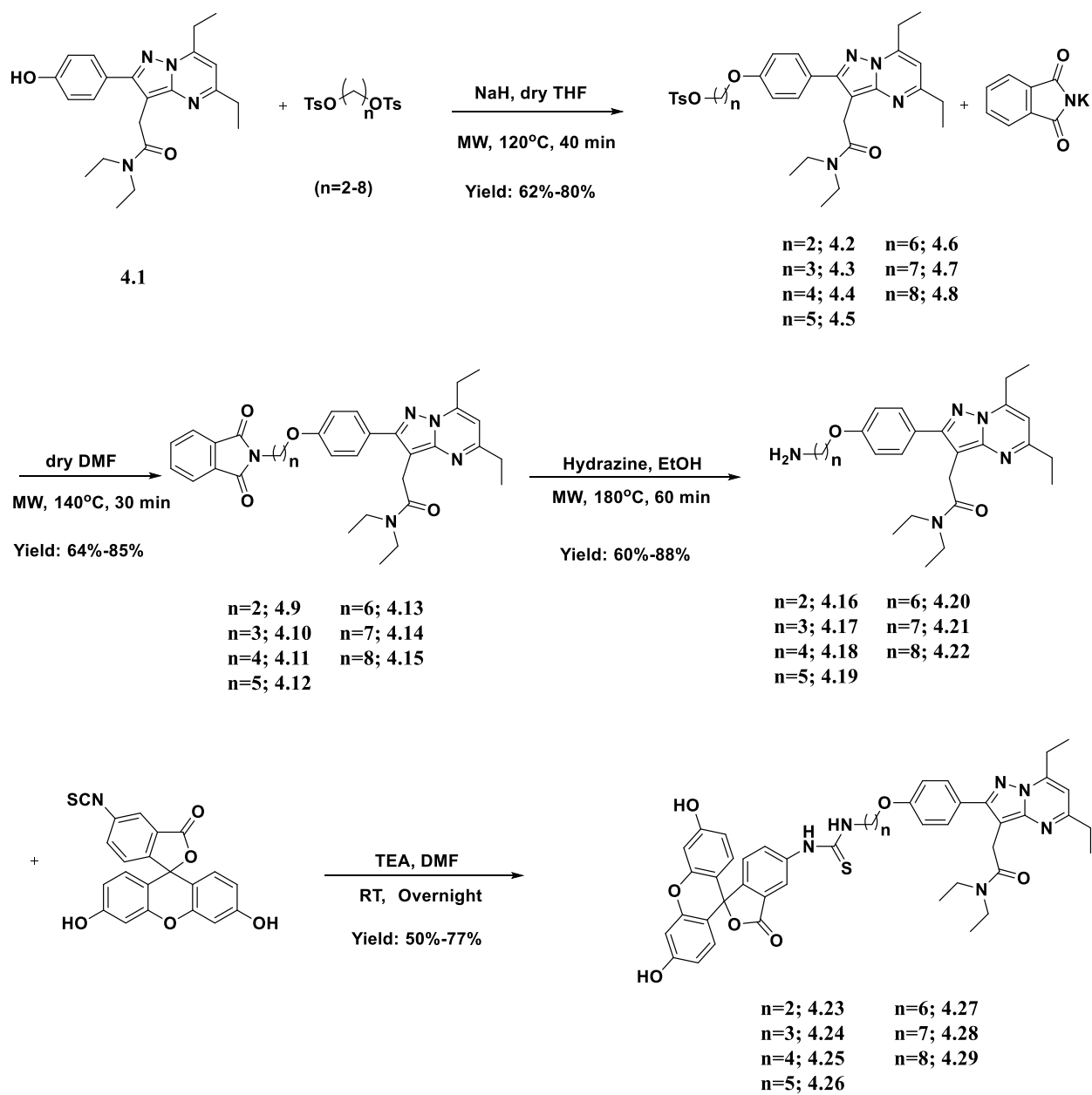


Figure 4.2.1 Generalized structure of TSPO fluorescent ligands.

As shown in **Scheme 4.2.1**, a consecutive four-step synthesis started from **4.1**, which was synthesized based upon previously reported pathway.^[14] In the first step, **4.2-4.8** were synthesized by reacting of the hydroxyl group in **1** with a diversity of ditosylate,^[66] which was formed by the reaction of diol with tosyl chloride at room temperature. After adding the linker to the ligand unit, compounds **4.9-4.15** were formed by reaction of corresponding **4.2-4.8** with phthalimide potassium salt in dry DMF. The third step in the synthesis of precursor **4.16-4.22** features the formation of amine group, generated using hydrazine to treat **4.9-4.15** in ethanol. After that, the final product was accomplished by the reaction of the amine group with isothiocyanate of the FITC dye in the presence of basic environment providing by triethylamine in DMF overnight at room temperature. The dye unit was conjugated to the opposite end of the linker.



Scheme 4.2.1 Synthesis of TSPO fluorescent ligands.

4.3 Binding Affinity and Spectroscopic Characterization

TSPO affinities of the synthesized optical probes were calculated, using a C6 glioma cell lysate binding assay previously described.^[14, 55] The binding affinity data are shown in **Table**

4.3.1. The K_i values of the synthesized probes varied from submicromolar to subnanomolar. The probe bearing an 8-carbon linker (**4.29**) had the highest binding affinity ($K_i = 0.31$ nM), which was 590-fold higher than **4.26** ($K_i = 184.86$ nM). Notably, the affinity of **4.29** was almost the same as its parent TSPO ligand, 2-(5,7-diethyl-2-(4-(2-fluoroethoxy)phenyl)pyrazolo[1,5-a]pyrimidin-3-yl)-N,N-diethylacetamide ($K_i = 0.27$ nM). As far as the author is aware, this is the lowest reported K_i value for a fluorescent TSPO probe and as such, makes **4.29** a very promising candidate as a tumor-imaging agent.

In our group's previous studies, the 4-position of the 2-phenyl group of the pyrazolopyrimidine core scaffold bore minimal influence on the binding affinity, as demonstrated by the structure-activity relationships when replacing the 4-methoxy (DPA-713) with 4-(2-fluoroethoxy) (DPA-714) group.^[14] However, when connecting the bulky FITC fluorescent unit at the same position of the scaffold, the small difference in the linker length had a surprising impact upon affinity. For example, **4.24**, whose linker was only one carbon greater than **4.23**, exhibited an 8-fold decrease in binding affinity.

Table 4.3.1 Binding affinity to TSPO of fluorescent ligands **4.23-4.29**.

Entry	K_i (nM)
4.23 (n= 2)	13.84 ± 4.99
4.24 (n=3)	110.88±25.63
4.25 (n=4)	155.47±8.94
4.26 (n=5)	184.86±15.39
4.27 (n=6)	11.67±4.86
4.28 (n=7)	16.29±5.01
4.29 (n=8)	0.31±0.02

It was also observed that the binding affinity did not change correspondingly with the linker length. Given the size of the fluorescent unit, the longer linker was expected to benefit the interaction between TSPO and probe. However, **4.23** had a much higher affinity than **4.24-4.26**, even though with shorter linker length. The trend was similar to the previous research done by M. Bai *et al.*,^[50] which suggested that the linker length might not be the only factor having an impact on binding affinity, and the fluorescent unit may also influence binding.

After coupling with the FITC, the probes exhibited similar aqueous spectroscopy (**Figure 4.3.1**), with the maximum absorption wavelength at approximately 500 nm and the maximum emission wavelength at approximately 522 nm. Compared to FITC itself, whose maximum absorption centers at 492 nm and maximum emission at 518 nm, a small red-shift in signal was discovered after connecting with the ligand unit, which come from the lowering in separation between energy level after conjugation.

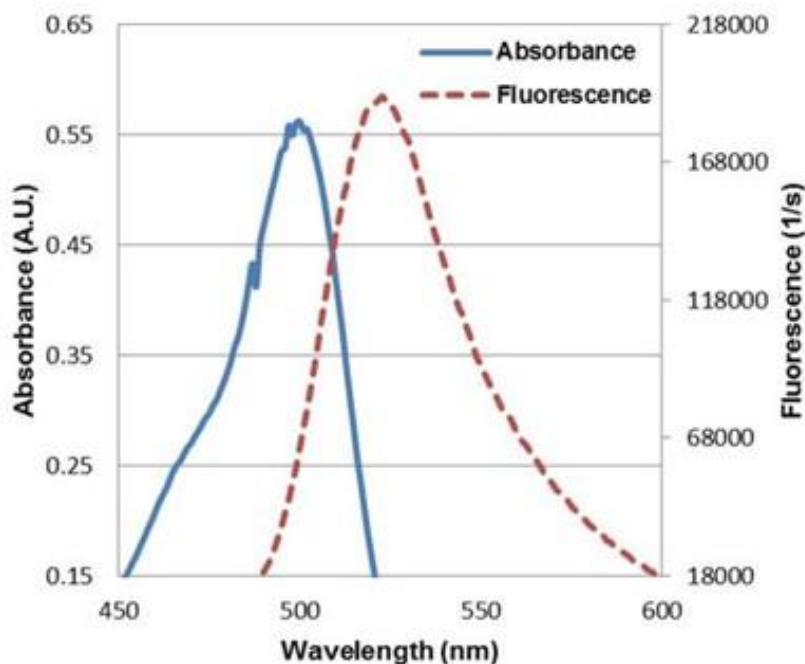


Figure 4.3.1 Fluorescent probe aqueous spectroscopy.

4.4 Computational Modeling

Computational modeling allows us to understand how the drug interacts with the target. To perform computational modeling, we first need to know the TSPO protein structure.

However, as a membrane protein located on the mitochondria, it is extremely difficult to get the TSPO crystal. In a recent study by Li F *et al.*, the authors described the structural study of TSPO protein and mutation from bacteria (*RsTSPO*). Since 34% of *RsTSPO* sequence is identical to the human protein, it can serve as a good model system to investigate human TSPO.^[67]

It was found that TSPO was formed from two identical monomers. Each composed of five transmembrane α helices.^[67-68] The dimer had a tight interface, which was unaltered by mutation and devoid of any hydrogen bond. The mutation caused movement and closer association of helices TM-II and TM-V.

Based upon a model built by our group, probe **4.29**, the fluorescent probe with the highest affinity in the library, was further evaluated computationally (**Figure 4.4.1**) with TSPO protein. The protein structure we used here was modeled from previous structure modeling using NMR. **Figure 4.4.1** showed 12 poses from the modeling of interaction between TSPO and probe **4.29**, which all described that the ligand unit fit with the TSPO hydrophobic pocket forming by the five transmembrane α helices, while the fluorescent unit protruded outside the pocket. The pose helped to diminish the negative influence on binding affinity from bulky dye unit.

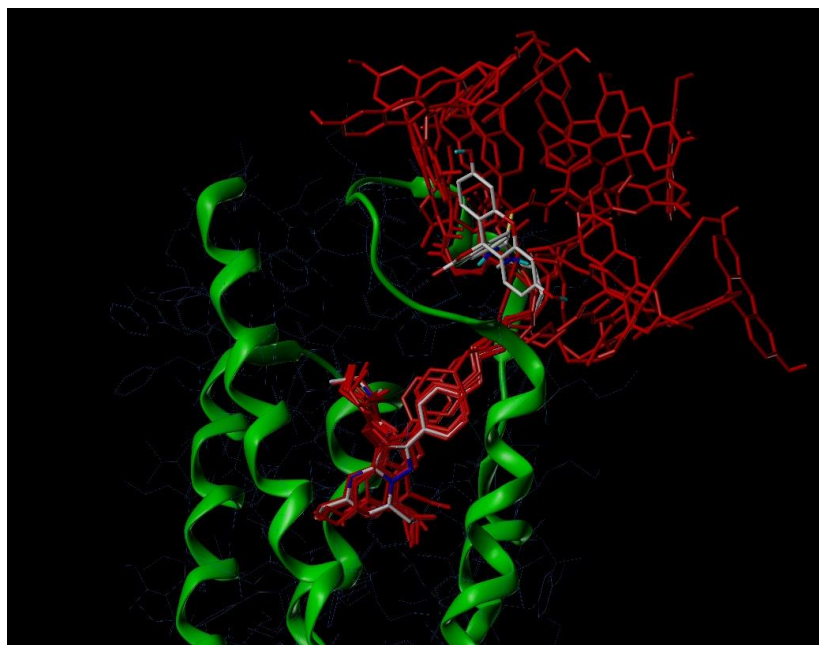


Figure 4.4.1 12 modeling poses of probe **4.29** and TSPO.

The different view of the best scoring pose was shown in **Figure 4.4.2**. The two side chains shown near the bottom of the pocket in the left picture were from tryptophan TRP51 and phenylalanine PHE90 of TSPO. They were stacking with the pyrazolo ring of the probe through π - π conjugation.

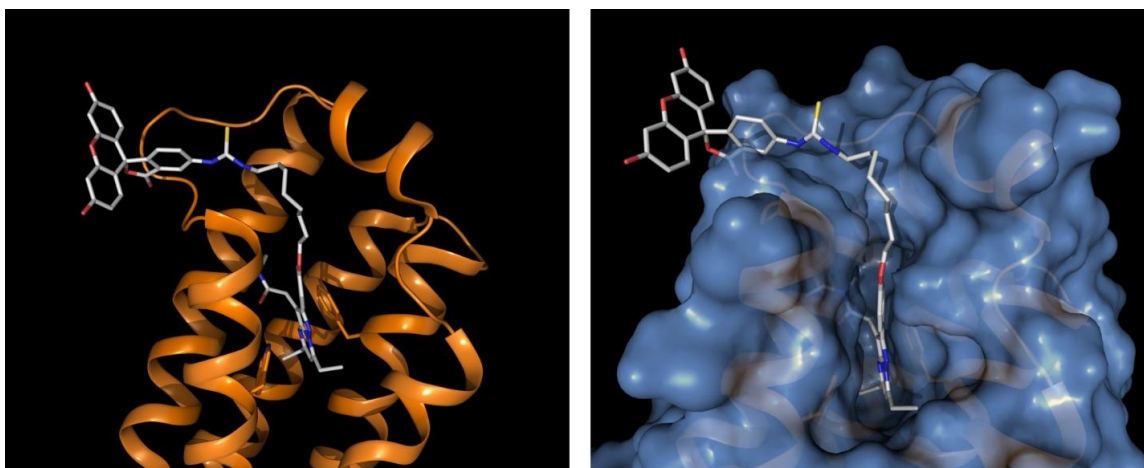


Figure 4.4.2 Best score modeling structure of probe **4.29** interaction with TSPO.

4.5 Molar Extinction Coefficient and Quantum Yield

According to Beer's law (or Beer-Lambert law), the absorption of light depends on material and the path through which light travels.

$$A = \epsilon bc \quad \text{Equation 4.5.1}$$

A is the absorbance, ϵ is the molar extinction coefficient, b is the path length, and c is the concentration.

The thickness of the cuvette we used for UV-vis was 1 cm, which was the path length. If we put absorbance on y-axis, and concentration on x-axis, and tested the absorbance at different concentration, the slope of the curve was the molar extinction coefficient.

The absorbance at a different probe concentrations fit a linear curve. The molar extinction coefficient of **4.29** was calculated following Beer's Law and was found to be $13913.04 \text{ L}\cdot\text{mol}^{-1}\cdot\text{cm}^{-1}$ (**Figure 4.5.1**).

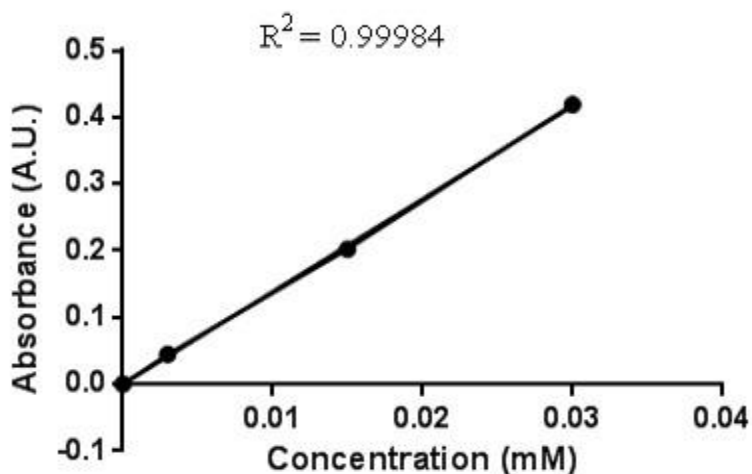


Figure 4.5.1 Molar extinction coefficient of probe **4.29**.

Quantum yield in fluorescence measures the number of photons emitted per photon absorbed by the dye. The dye with higher quantum yield is more efficient to generate fluorescence.

$$\phi = \frac{\# \text{ photons emitted}}{\# \text{ photons absorbed}} \quad \text{Equation 4.5.2}$$

Quantum yield was calculated from the ratio of integration of the area under the fluorescent curves (AUC) of FITC dye and optical probe, which were found to be 0.36. Since the quantum yield of FITC is known to be 0.92, the yield of **4.29** was 0.33.

4.6 Cell Imaging

We further studied the use of TSPO fluorescent probe for tumor cell imaging. C6 rat glioma cell line was chosen and **4.29** was utilized to stain the cell. We also used another dye, Mito Tracker Red, to stain the cell. Mito Tracker Red is a commercialized red-fluorescent dye to label mitochondria.^[17, 69-71] Since **4.29** and Mito Tracker Red has a different color, we can co-incubate C6 cells with two dyes together and perform imaging under confocal imaging.

As shown in **Figure 4.6.1**, the novel fluorescent probe **4.29** could label the cells very effectively. An intense fluorescent signal was found to be perinuclear with little signal appearing in the nucleus itself. The large-scale and magnified merged images also indicated optical signal from two dyes can match very well, which further illustrated that **4.29** binds specifically to the mitochondria, where TSPO is located.

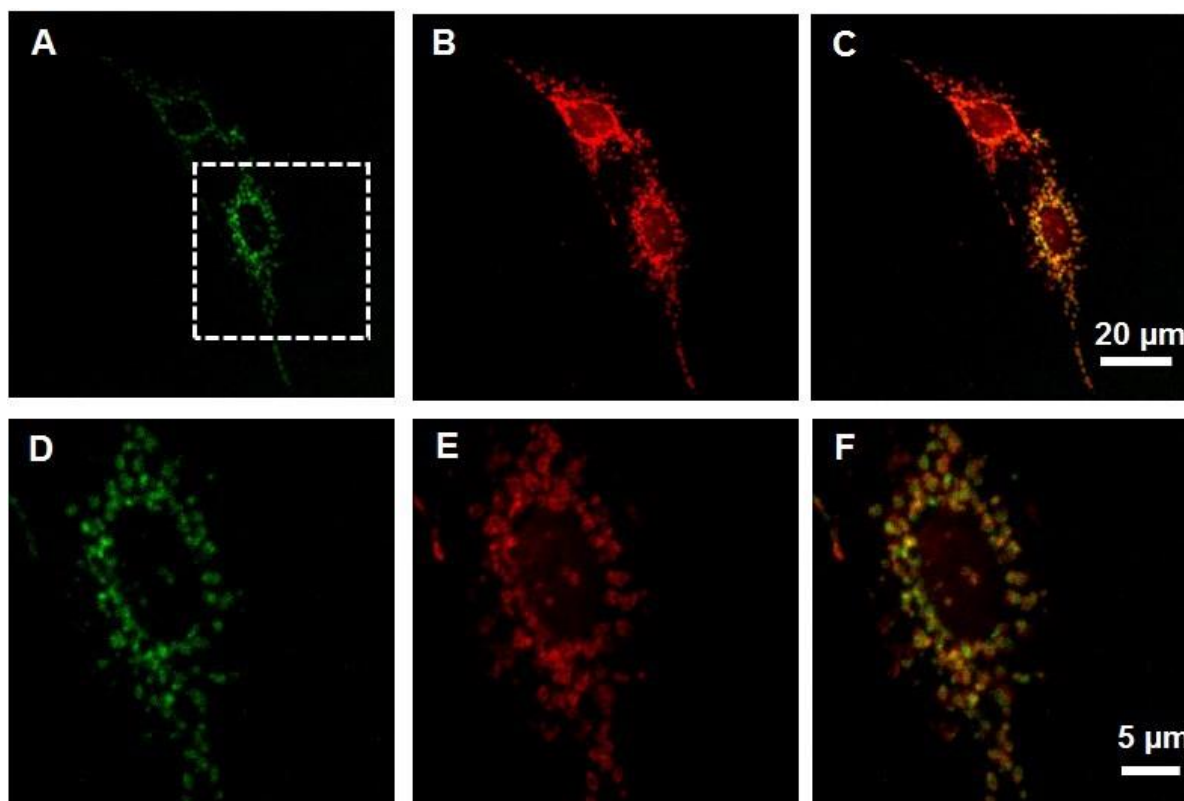


Figure 4.6.1 Confocal microscopy images of C6 rat glioma cells incubated with optical probe. (A, D) fluorescent images of optical probe; (B, E) fluorescent images of Mito Tracker Red; (C, F) merged images of optical probe and Mito Tracker Red. (D, E, F) fluorescent images of the chosen area in (A).

Displacement experiment was further performed to identify if the fluorescent probe and its parent ligand attached to the same target. C6 glioma cells were treated with fluorescent probe **4.29** and 100-fold higher concentration of its parent ligand 2-(5,7-diethyl-2-(4-methoxyphenyl)pyrazolo[1,5-*a*]pyrimidin-3-yl)-*N,N*-diethylacetamide (ligand unit of the fluorescent probe), and as well as Mito Tracker Red. Since the parent ligand cannot emit optical signal, the signal will be decreased if it can displace fluorescent probe from the target. As shown in **Figure 4.6.2**, the parent ligand totally replaced fluorescent probe and left no signal in the green channel, only the red signal channel from Mito Tracker Red can be seen in the confocal

imaging, which further confirmed that fluorescent probe bind the same target as its parent ligand, which was TSPO protein.

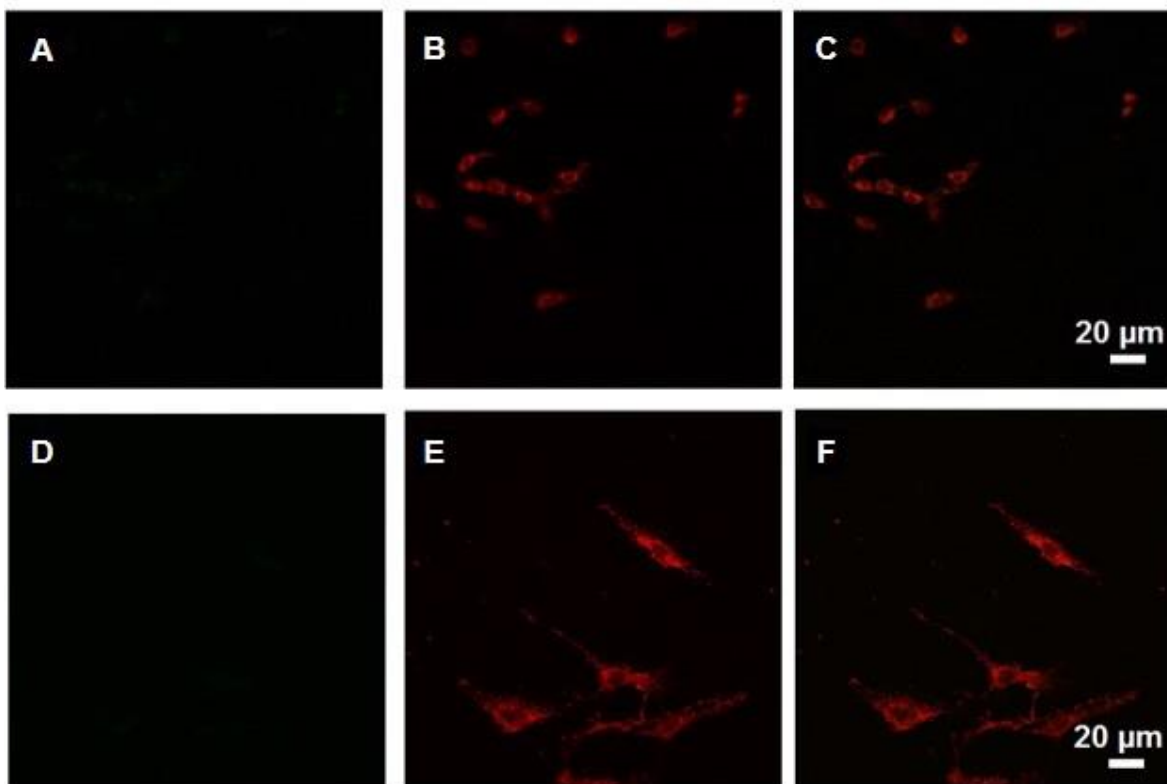


Figure 4.6.2 Displacement experiment of **4.29** with its parent ligand. (G, H, I) images of displacement experiment. C6 cells were co-incubated with 0.1 μM optical probe and 10 μM 2-(5,7-diethyl-2-(4-methoxyphenyl)pyrazolo[1,5-*a*]pyrimidin-3-yl)-*N,N*-diethylacetamide; (J, K, L) images of C6 glioma cells dosed with Mito Tracker Red only.

4.7 Conclusion

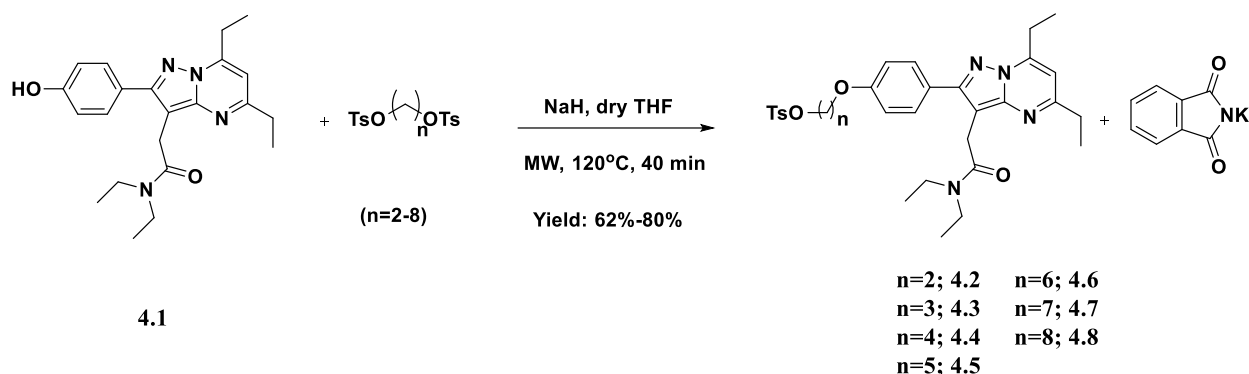
We developed a series of novel TSPO fluorescent probes through connecting our previously reported TSPO ligand with a fluorescent unit (FITC). By changing the linker length from two to eight carbons, optical properties of the probes remained similar, while TSPO binding affinities varied greatly. This led to the discovery of a new TSPO optical probe with a K_i value of 0.31 nM, the highest binding affinity amongst TSPO fluorescent probes reported to date.

Subsequent saturation curve determination, displacement experiment and cell imaging illustrated the specific binding to TSPO.

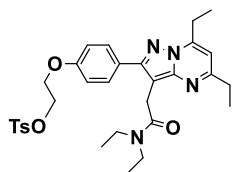
This work lays the foundation for the development of a battery fluorescence-based TSPO ligands that could potentially be translated to *in vivo* studies, especially with further refining of the fluorescent properties. In addition, we envision a role for these probes as precision, point-of-care diagnostics, given the important role of TSPO in many human diseases.

4.8 Method and Materials

General Procedure for Ligand Synthesis



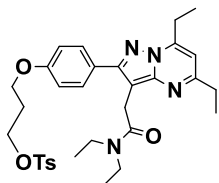
General Procedure of Compound 4.2-4.8. To a solution of 2-(5,7-diethyl-2-(4-hydroxyphenyl)pyrazolo[1,5-a]pyrimidin-3-yl)-N,N-diethylacetamide (Compound 4.1, 100 mg, 1 eq) in dry tetrahydrofuran (THF, 7 mL) was added NaH (18.9 mg, 3 eq). The reaction mixture was then stirred at 0 °C for 10 min and allowed to warm up to room temperature before adding ditosylate (3 eq). The reaction mixture was then irradiated in a Biotage Initiator at 120 °C for 40 min. After that, the reaction was acidified with 1.0 M aqueous HCl and extracted with dichloromethane (DCM) three times. The organic solutions were then collected, dried over magnesium sulfate, and concentrated to dryness. The residue was purified by flash chromatography using 19:1 DCM/methanol to yield compound 4.2-4.8 as a yellow solid.



2-(4-(3-(2-(diethylamino)-2-oxoethyl)-5,7-diethylpyrazolo[1,5-a]pyrimidin-2-yl)phenoxy)ethyl 4-methylbenzenesulfonate (Compound 4.2)

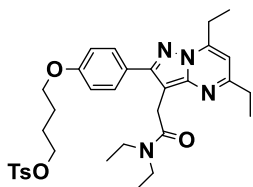
¹H-NMR (CDCl₃, 400 MHz) δ 7.84-7.79 (m, 4H), 7.35 (d, 2H, *J* = 8 Hz), 6.87 (d, 2H, *J* = 8.8 Hz), 6.51 (s, 1H), 4.39 (t, 2H, *J* = 4.76 Hz), 4.19 (t, 2H, *J* = 4.76 Hz), 3.91 (s, 2H), 3.54-3.59 (m,

2H), 3.43-3.38 (m, 2H), 3.21-3.16 (m, 2H), 2.85-2.79 (m, 2H), 2.45 (s, 3H), 1.44 (t, 3H, $J = 7.5\text{Hz}$), 1.34 (t, 3H, $J = 7.5\text{Hz}$), 1.21 (t, 3H, $J = 7.1\text{ Hz}$), 1.1 (t, 3H, $J = 7.1\text{ Hz}$). ^{13}C -NMR (CDCl_3 , 100 MHz) δ 170.3, 162.2, 158.1, 154.5, 149.6, 147.5, 144.9, 132.8, 130.0, 129.8, 127.9, 127.2, 114.5, 104.9, 100.8, 68.0, 65.3, 42.4, 40.6, 31.3, 27.9, 23.2, 21.6, 14.3, 13.0, 12.8, 10.2. HRMS calc'd for $\text{C}_{31}\text{H}_{38}\text{N}_4\text{O}_5\text{S}$ $m/z = 579.2636$ ($\text{M}+\text{H}^+$), found 579.2635.



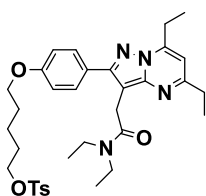
3-(4-(3-(2-(diethylamino)-2-oxoethyl)-5,7-diethylpyrazolo[1,5-*a*]pyrimidin-2-yl)phenoxy)propyl 4-methylbenzenesulfonate (Compound 4.3)

^1H -NMR (CDCl_3 , 400 MHz) δ 7.81-7.75 (m, 4H), 7.25 (d, 2H, $J = 7.8\text{ Hz}$), 6.83 (d, 2H, $J = 8.8\text{ Hz}$), 6.51 (s, 1H), 4.25 (t, 2H, $J = 6.0\text{ Hz}$), 3.98 (t, 2H, $J = 5.8\text{ Hz}$), 3.93 (s, 2H), 3.60-3.54 (m, 2H), 3.43-3.38 (m, 2H), 3.21-3.15 (m, 2H), 2.85-2.79 (m, 2H), 2.38 (s, 3H), 2.16-2.10 (m, 2H), 1.44 (t, 3H, $J = 7.5\text{ Hz}$), 1.33 (t, 3H, $J = 7.5\text{Hz}$), 1.22 (t, 3H, $J = 7.1\text{ Hz}$), 1.11 (t, 3H, $J = 7.1\text{ Hz}$). ^{13}C -NMR (CDCl_3 , 100 MHz) δ 170.3, 162.2, 158.5, 154.6, 149.7, 147.5, 144.8, 132.6, 129.9, 129.8, 127.7, 126.7, 114.3, 104.9, 100.6, 67.0, 62.9, 42.4, 40.6, 31.3, 28.8, 28.0, 23.2, 21.6, 14.3, 13.0, 12.8, 10.3. HRMS calc'd for $\text{C}_{32}\text{H}_{40}\text{N}_4\text{O}_5\text{S}$ $m/z = 593.2792$ ($\text{M}+\text{H}^+$), found 593.2791.



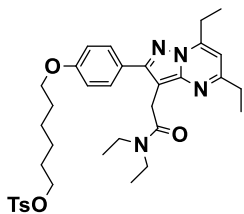
4-(4-(3-(2-(diethylamino)-2-oxoethyl)-5,7-diethylpyrazolo[1,5-*a*]pyrimidin-2-yl)phenoxy)butyl 4-methylbenzenesulfonate (Compound 4.4)

¹H-NMR (CDCl₃, 400 MHz) δ 7.82-7.78 (m, 4H), 7.35 (d, 2H, *J* = 8.0 Hz), 6.91 (d, 2H, *J* = 8.8 Hz), 6.52 (s, 1H), 4.13 (t, 2H, *J* = 6 Hz), 3.96 (t, 2H, *J* = 5.7 Hz), 3.93 (s, 2H), 3.58-3.52 (m, 2H), 3.43-3.38 (m, 2H), 3.23-3.17 (m, 2H), 2.87-2.82 (m, 2H), 2.45 (s, 3H), 1.87-1.85 (m, 4H), 1.45 (t, 3H, *J* = 7.5 Hz), 1.34 (t, 3H, *J* = 7.5 Hz), 1.21 (t, 3H, *J* = 7.1 Hz), 1.11 (t, 3H, *J* = 7.1 Hz).
¹³C-NMR (CDCl₃, 100 MHz) δ 170.3, 162.3, 158.9, 154.9, 149.9, 147.2, 144.7, 133.0, 129.9, 129.8, 127.8, 126.4, 114.3, 104.7, 100.6, 70.0, 66.7, 42.4, 40.6, 31.2, 28.0, 25.7, 25.2, 23.3, 21.6, 14.3, 12.9, 12.8, 10.2. HRMS calc'd for C₃₃H₄₂N₄O₅S *m/z* = 607.2949 (M+H⁺), found 607.2949.



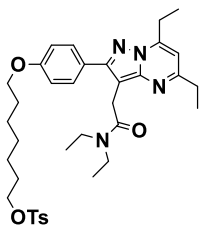
5-(4-(3-(2-(diethylamino)-2-oxoethyl)-5,7-diethylpyrazolo[1,5-*a*]pyrimidin-2-yl)phenoxy)pentyl 4-methylbenzenesulfonate (Compound 4.5)

¹H-NMR (CDCl₃, 400 MHz) δ 7.82-7.79 (m, 4H), 7.35 (d, 2H, *J* = 8 Hz), 6.94 (d, 2H, *J* = 8.8 Hz), 6.52 (s, 1H), 4.07 (t, 2H, *J* = 6.4 Hz), 3.95 (t, 2H, *J* = 6 Hz), 3.93 (s, 2H), 3.58-3.53 (m, 2H), 3.43-3.38 (m, 2H), 3.23-3.17 (m, 2H), 2.86-2.80 (m, 2H), 2.44 (s, 3H), 1.79-1.70 (m, 4H), 1.55-1.4 (m, 2H), 1.45 (t, 3H, *J* = 7.5 Hz), 1.34 (t, 3H, *J* = 7.5 Hz), 1.21 (t, 3H, *J* = 7.1 Hz), 1.11 (t, 3H, *J* = 7.1 Hz). ¹³C-NMR (CDCl₃, 100 MHz) δ 170.3, 162.2, 159.0, 154.9, 149.9, 147.3, 144.7, 133.0, 129.9, 129.7, 127.8, 126.3, 114.4, 104.8, 100.6, 70.3, 67.4, 42.4, 40.6, 31.2, 28.5, 28.5, 28.0, 23.3, 22.0, 21.6, 14.3, 13.0, 12.8, 10.2. HRMS calc'd for C₃₄H₄₄N₄O₅S *m/z* = 621.3105 (M+H⁺), found 621.3108.



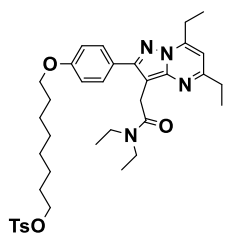
6-(4-(3-(2-(diethylamino)-2-oxoethyl)-5,7-diethylpyrazolo[1,5-*a*]pyrimidin-2-yl)phenoxy)hexyl 4-methylbenzenesulfonate (Compound 4.6)

¹H-NMR (CDCl₃, 400 MHz) δ 7.81-7.79 (m, 4H), 7.36-7.34 (d, 2H, *J* = 8 Hz), 6.95 (d, 2H, *J* = 8.8 Hz), 6.51 (s, 1H), 4.05 (t, 2H, *J* = 6.4 Hz), 3.96 (t, 2H, *J* = 6.4 Hz), 3.9 (s, 2H), 3.58-3.53 (m, 2H), 3.44-3.38 (m, 2H), 3.23-3.17 (m, 2H), 2.86-2.81 (m, 2H), 2.45 (s, 3H), 1.79-1.66 (m, 4H), 1.45 (t, 3H, *J* = 7.5 Hz), 1.41-1.39 (m, 4H), 1.34 (t, 3H, *J* = 7.5 Hz), 1.21 (t, 3H, *J* = 7.1 Hz), 1.11 (t, 3H, *J* = 7.1 Hz). ¹³C-NMR (CDCl₃, 100 MHz) δ 170.3, 162.2, 159.1, 164.9, 149.8, 147.4, 144.6, 133.1, 129.9, 129.7, 127.8, 126.2, 114.4, 104.7, 100.6, 70.4, 67.6, 42.4, 40.6, 31.2, 28.9, 28.7, 28.0, 25.4, 25.1, 23.2, 21.6, 14.3, 13.0, 12.8, 10.2. HRMS calc'd for C₃₅H₄₆N₄O₅S *m/z* = 635.3262 (M+H⁺), found 635.3264.



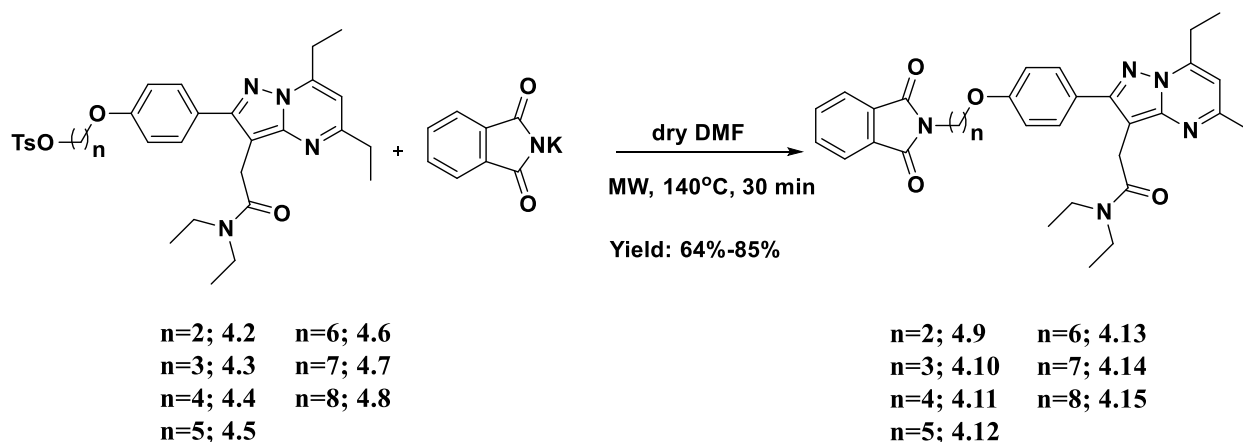
7-(4-(3-(2-(diethylamino)-2-oxoethyl)-5,7-diethylpyrazolo[1,5-*a*]pyrimidin-2-yl)phenoxy)heptyl 4-methylbenzenesulfonate (Compound 4.7)

¹H-NMR (CDCl₃, 400 MHz) δ 7.81-7.79 (m, 4H), 7.35 (d, 2H, *J* = 8 Hz), 6.96 (d, 2H, *J* = 8.7 Hz), 6.51 (s, 1H), 4.03 (t, 2H, *J* = 6.4 Hz), 3.98 (t, 2H, *J* = 6.3 Hz), 3.93 (s, 2H), 3.58-3.53 (m, 2H), 3.44-3.38 (m, 2H), 3.23-3.17 (m, 2H), 2.87-2.81 (m, 2H), 2.45 (s, 3H), 1.72-1.64 (m, 4H), 1.47 (t, 3H, *J* = 7.5 Hz), 1.43-1.31 (m, 6H), 1.34 (t, 3H, *J* = 7.5 Hz), 1.21 (t, 3H, *J* = 7.1 Hz), 1.11 (t, 3H, *J* = 7.1 Hz). ¹³C-NMR (CDCl₃, 100 MHz) δ 170.3, 162.2, 159.2, 154.9, 147.4, 144.6, 133.1, 129.9, 129.7, 127.8, 126.2, 114.4, 104.7, 100.6, 70.5, 67.7, 42.4, 40.6, 31.3, 29.0, 28.7, 28.6, 28.0, 25.7, 25.2, 23.2, 21.6, 14.3, 13.0, 12.8, 10.2. HRMS calc'd for C₃₆H₄₈N₄O₅S *m/z* = 649.3418 (M+H⁺), found 649.3421.

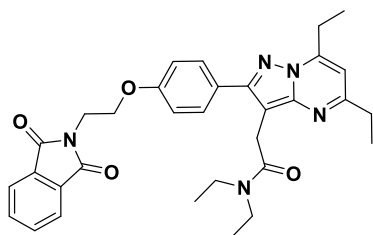


8-(4-(3-(2-(diethylamino)-2-oxoethyl)-5,7-diethylpyrazolo[1,5-*a*]pyrimidin-2-yl)phenoxy)octyl 4-methylbenzenesulfonate (Compound 4.8)

$^1\text{H-NMR}$ (CDCl_3 , 400 MHz) δ 7.82-7.79 (m, 4H), 7.35 (d, 2H, $J = 8$ Hz), 6.97 (d, 2H, $J = 8.8$ Hz), 6.51 (s, 1H), 4.04 (t, 2H, $J = 6.5$ Hz), 3.99 (t, 2H, $J = 6.5$ Hz), 3.93 (s, 2H), 3.58-3.53 (m, 2H), 3.44-3.38 (m, 2H), 3.23-3.17 (m, 2H), 2.87-2.81 (m, 2H), 2.45 (s, 3H), 1.77-1.64 (m, 4H), 1.45 (t, 3H, $J = 7.5$ Hz), 1.36-1.27 (m, 8H), 1.34 (t, 3H, $J = 7.5$ Hz), 1.21 (t, 3H, $J = 7.1$ Hz), 1.11 (t, 3H, $J = 7.1$ Hz). $^{13}\text{C-NMR}$ (CDCl_3 , 100 MHz) δ 170.3, 162.2, 159.2, 154.9, 149.7, 147.5, 144.6, 133.2, 129.9, 129.7, 127.8, 126.2, 114.4, 104.7, 100.7, 70.6, 67.8, 42.4, 40.6, 31.3, 29.1, 29.0, 28.8, 28.7, 28.1, 25.8, 25.2, 23.2, 21.6, 14.3, 13.0, 12.8, 10.2. HRMS calc'd for $\text{C}_{37}\text{H}_{50}\text{N}_4\text{O}_5\text{S}$ $m/z = 663.3575$ ($\text{M}+\text{H}^+$), found 663.3580.



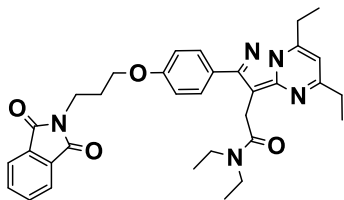
General Procedure of Compound 4.9-4.15. To a solution of compound 4.2-4.8 (100 mg, 1 eq) in 6 mL dry dimethylformamide (DMF) was added potassium 1,3-dioxoisindolin-2-ide (2 eq). The reaction mixture was irradiated in a Biotage Initiator at 140 °C for 30 min. The mixture was then concentrated and purified by flash chromatography using 19:1 DCM/methanol to yield compound 4.9-4.15 as a yellow solid.



2-(2-(4-(2-(1,3-dioxoisindolin-2-yl)ethoxy)phenyl)-5,7-diethylpyrazolo[1,5-a]pyrimidin-3-yl)-N,N-diethylacetamide (Compound 4.9)

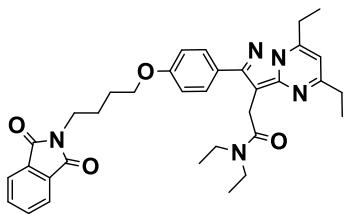
¹H-NMR (CDCl₃, 400 MHz) δ 7.89-7.72 (m, 4H), 7.77 (d, 2H, *J* = 8.8 Hz), 6.96 (d, 2H, *J* = 8.8 Hz), 6.5 (s, 1H), 4.27 (t, 2H, *J* = 5.8 Hz), 4.14 (t, 2H, *J* = 5.8 Hz), 3.89 (s, 2H), 3.56-3.51 (m, 2H), 3.42-3.37 (m, 2H), 3.21-3.15 (m, 2H), 2.85-2.79 (m, 2H), 1.43 (t, 3H, *J* = 7.5 Hz), 1.33 (t, 3H, *J* = 7.5 Hz), 1.2 (t, 3H, *J* = 7.1 Hz), 1.1 (t, 3H, *J* = 7.1 Hz). ¹³C-NMR (CDCl₃, 100 MHz) δ 170.2, 168.1, 162.2, 158.4, 154.7, 149.7, 147.5, 134, 132, 130, 126.8, 123.3, 114.5, 104.8, 100.7,

64.7, 42.3, 40.6, 37.3, 31.3, 27, 23.2, 14.3, 13.0, 12.8, 10.2. HRMS calc'd for C₃₂H₃₅N₅O₄ m/z = 554.2762 (M+H⁺), found 554.2767.



2-(2-(4-(3-(1,3-dioxisoindolin-2-yl)propoxy)phenyl)-5,7-diethylpyrazolo[1,5-*a*]pyrimidin-3-yl)-*N,N*-diethylacetamide (Compound 4.10)

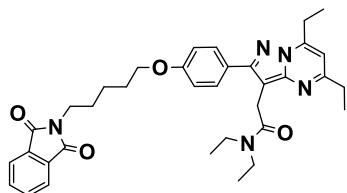
¹H-NMR (CDCl₃, 400 MHz) δ 7.86-7.721 (m, 4H), 7.73 (d, 2H, *J* = 8.8 Hz), 6.89 (d, 2H, *J* = 8.8 Hz), 6.52 (s, 1H), 4.08 (t, 2H, *J* = 6 Hz), 3.94 (t, 2H, *J* = 6.8 Hz), 3.92 (s, 2H), 3.56-3.50 (m, 2H), 3.44-3.38 (m, 2H), 3.23-3.17 (m, 2H), 2.87-2.82 (m, 2H), 2.25-2.18 (m, 2H), 1.45 (t, 3H, *J* = 7.5 Hz), 1.34 (t, 3H, *J* = 7.5 Hz), 1.21 (t, 3H, *J* = 7.1 Hz), 1.11 (t, 3H, *J* = 7.1 Hz). ¹³C-NMR (CDCl₃, 100 MHz) δ 170.3, 168.3, 162.3, 158.9, 155.0, 150.2, 147.1, 133.9, 132.1, 129.9, 126.3, 123.2, 114.4, 104.7, 100.6, 65.6, 42.4, 40.7, 35.4, 31.1, 28.2, 27.99, 23.3, 14.2, 13.0, 12.9, 10.2. HRMS calc'd for C₃₃H₃₇N₅O₄ m/z = 568.2918 (M+H⁺), found 568.2916.



2-(2-(4-(4-(1,3-dioxisoindolin-2-yl)butoxy)phenyl)-5,7-diethylpyrazolo[1,5-*a*]pyrimidin-3-yl)-*N,N*-diethylacetamide (Compound 4.11)

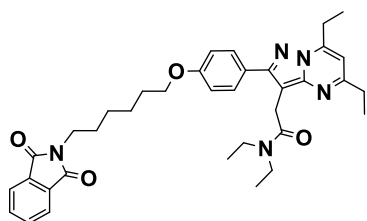
¹H-NMR (CDCl₃, 400 MHz) δ 7.87-7.71 (m, 4H), 7.76 (d, 2H, *J* = 8.8 Hz), 6.96 (d, 2H, *J* = 8.8 Hz), 6.52 (s, 1H), 4.04 (t, 2H, *J* = 5.8 Hz), 3.93 (s, 2H), 3.79 (t, 2H, *J* = 6.6 Hz), 3.56-3.51 (m, 2H), 3.44-3.38 (m, 2H), 3.23-3.17 (m, 2H), 2.87-2.81 (m, 2H), 1.96-1.82 (m, 4H), 1.44 (t, 3H, *J* = 7.5 Hz), 1.34 (t, 3H, *J* = 7.5 Hz), 1.21 (t, 3H, *J* = 7.1 Hz), 1.11 (t, 3H, *J* = 7.1 Hz). ¹³C-NMR

(CDCl₃, 100 MHz) δ 170.3, 168.4, 162.2, 159.0, 155.0, 150.1, 147.2, 133.9, 132.1, 129.9, 126.2, 123.2, 114.5, 104.7, 100.6, 67.2, 42.4, 40.7, 37.6, 31.1, 28.0, 26.6, 25.3, 23.3, 14.3, 13.0, 12.9, 10.2. HRMS calc'd for C₃₄H₃₉N₅O₄ m/z = 582.3075 (M+H⁺), found 582.3076.



2-(2-(4-((5-(1,3-dioxisoindolin-2-yl)pentyl)oxy)phenyl)-5,7-diethylpyrazolo[1,5-*a*]pyrimidin-3-yl)-*N,N*-diethylacetamide (Compound 4.12)

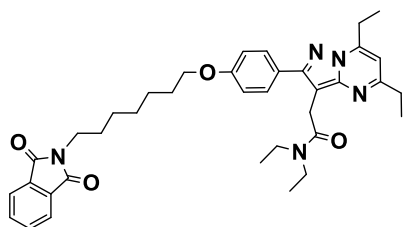
¹H-NMR (CDCl₃, 400 MHz) δ 7.86-7.71 (m, 4H), 7.76 (d, 2H, *J* = 8.8 Hz), 6.95 (d, 2H, *J* = 8.8 Hz), 6.52 (s, 1H), 3.99 (t, 2H, *J* = 6.4 Hz), 3.93 (s, 2H), 3.74 (t, 2H, *J* = 7.2 Hz), 3.56-3.51 (m, 2H), 3.44-3.38 (m, 2H), 3.23-3.17 (m, 2H), 2.87-2.82 (m, 2H), 1.89-1.82 (m, 2H), 1.82-1.74 (m, 2H), 1.59-1.51 (m, 2H), 1.45 (t, 3H, *J* = 7.5 Hz), 1.34 (t, 3H, *J* = 7.5 Hz), 1.21 (t, 3H, *J* = 7.1 Hz), 1.11 (t, 3H, *J* = 7.1 Hz). ¹³C-NMR (CDCl₃, 100 MHz) δ 170.4, 168.4, 162.3, 159.2, 155.0, 150.2, 147.1, 133.8, 132.1, 129.6, 126.0, 123.1, 114.4, 104.7, 100.5, 67.5, 42.4, 40.7, 37.8, 31.1, 28.7, 28.3, 28.0, 23.3, 23.2, 14.2, 13.0, 12.9, 10.2. HRMS calc'd for C₃₅H₄₁N₅O₄ m/z = 596.3231 (M+H⁺), found 596.3234.



2-(2-(4-((6-(1,3-dioxisoindolin-2-yl)hexyl)oxy)phenyl)-5,7-diethylpyrazolo[1,5-*a*]pyrimidin-3-yl)-*N,N*-diethylacetamide (Compound 4.13)

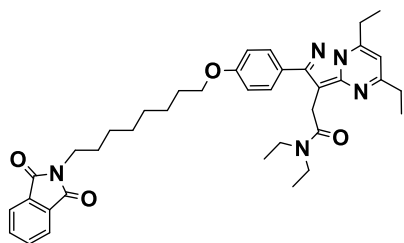
¹H-NMR (CDCl₃, 400 MHz) δ 7.86-7.70 (m, 4H), 7.77 (d, 2H, *J* = 8.8 Hz), 6.96 (d, 2H, *J* = 8.8 Hz), 6.51 (s, 1H), 3.99 (t, 2H, *J* = 6.5 Hz), 3.92 (s, 2H), 3.71 (t, 2H, *J* = 7.2 Hz), 3.57-3.52 (m,

2H), 3.44-3.38 (m, 2H), 3.22-3.17 (m, 2H), 2.86-2.80 (m, 2H), 1.85-1.77 (m, 2H), 1.77-1.68 (m, 2H), 1.58-1.49 (m, 2H), 1.44 (t, 3H, $J = 7.5$ Hz), 1.45-1.41 (m, 2H), 1.34 (t, 3H, $J = 7.5$ Hz), 1.21 (t, 3H, $J = 7.1$ Hz), 1.11 (t, 3H, $J = 7.1$ Hz). ^{13}C -NMR (CDCl_3 , 100 MHz) δ 170.3, 168.4, 162.2, 159.2, 154.9, 149.8, 147.4, 133.8, 132.1, 129.9, 126.1, 123.1, 114.4, 104.7, 100.6, 67.7, 42.4, 40.6, 37.9, 31.3, 29.0, 28.5, 28.0, 26.6, 25.6, 23.2, 14.3, 13.0, 12.8, 10.2. HRMS calc'd for $\text{C}_{36}\text{H}_{43}\text{N}_5\text{O}_4$ $m/z = 610.3388$ ($\text{M}+\text{H}^+$), found 610.3389.



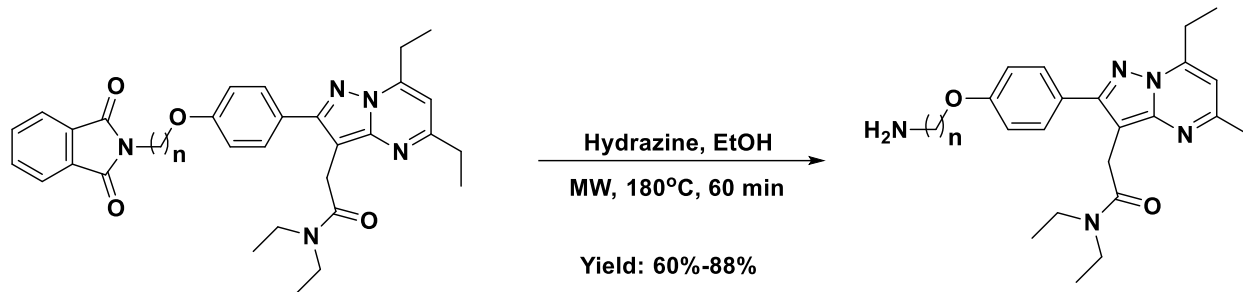
2-(2-(4-((7-(1,3-dioxoisindolin-2-yl)heptyl)oxy)phenyl)-5,7-diethylpyrazolo[1,5-*a*]pyrimidin-3-yl)-*N,N*-diethylacetamide (Compound 4.14)

^1H -NMR (CDCl_3 , 400 MHz) δ 7.86-7.70 (m, 4H), 7.77 (d, 2H, $J = 8.8$ Hz), 6.96 (d, 2H, $J = 8.8$ Hz), 6.51 (s, 1H), 3.99 (t, 2H, $J = 6.5$ Hz), 3.93 (s, 2H), 3.7 (t, 2H, $J = 7.2$ Hz), 3.57-3.51 (m, 2H), 3.44-3.38 (m, 2H), 3.23-3.17 (m, 2H), 2.86-2.80 (m, 2H), 1.76-1.66 (m, 4H), 1.44 (t, 3H, $J = 7.5$ Hz), 1.49-1.38 (m, 6H), 1.34 (t, 3H, $J = 7.5$ Hz), 1.21 (t, 3H, $J = 7.1$ Hz), 1.11 (t, 3H, $J = 7.1$ Hz). ^{13}C -NMR (CDCl_3 , 100 MHz) δ 170.3, 168.4, 162.4, 159.2, 155.0, 149.8, 147.5, 133.8, 132.0, 129.9, 126.1, 123.1, 114.5, 104.7, 100.6, 67.8, 42.4, 40.6, 37.9, 31.3, 29.1, 28.9, 28.5, 28.0, 26.7, 25.9, 23.2, 14.3, 13.0, 12.8, 10.2. HRMS calc'd for $\text{C}_{37}\text{H}_{45}\text{N}_5\text{O}_4$ $m/z = 624.3544$ ($\text{M}+\text{H}^+$), found 624.3544.



2-(2-(4-((8-(1,3-dioxisoindolin-2-yl)octyl)oxy)phenyl)-5,7-diethylpyrazolo[1,5-*a*]pyrimidin-3-yl)-*N,N*-diethylacetamide (Compound 4.15)

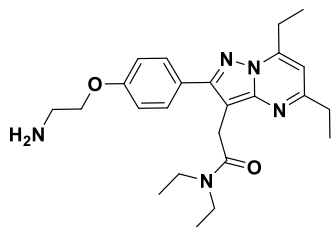
$^1\text{H-NMR}$ (CDCl_3 , 400 MHz) δ 7.86-7.70 (m, 4H), 7.76 (d, 2H, $J = 8.8$ Hz), 6.97 (d, 2H, $J = 8.8$ Hz), 6.53 (s, 1H), 3.99 (t, 2H, $J = 6.6$ Hz), 3.94 (s, 2H), 3.69 (t, 2H, $J = 7.2$ Hz), 3.56-3.50 (m, 2H), 3.44-2.38 (m, 2H), 3.23-3.17 (m, 2H), 2.88-2.82 (m, 2H), 1.87-1.74 (m, 2H), 1.73-1.64 (m, 2H), 1.46-1.32 (t, 3H, $J = 7.5$ Hz), 1.37 (m, 8H), 1.34 (t, 3H, $J = 7.5$ Hz), 1.2 (t, 3H, $J = 7.1$ Hz), 1.11 (t, 3H, $J = 7.1$ Hz). $^{13}\text{C-NMR}$ (CDCl_3 , 100 MHz) δ 170.4, 168.4, 162.3, 159.3, 155.1, 150.3, 147, 133.8, 132.1, 129.9, 125.9, 123.1, 114.5, 104.7, 100.5, 67.9, 42.4, 40.7, 38, 31, 29.2, 29.1, 29, 28.5, 28, 26.7, 25.9, 23.3, 14.2, 13, 12.9, 10.2. HRMS calc'd for $\text{C}_{38}\text{H}_{47}\text{N}_5\text{O}_4$ $m/z = 638.3701$ ($\text{M}+\text{H}^+$), found 638.3703.



n=2; 4.9 n=6; 4.13
 n=3; 4.10 n=7; 4.14
 n=4; 4.11 n=8; 4.15
 n=5; 4.12

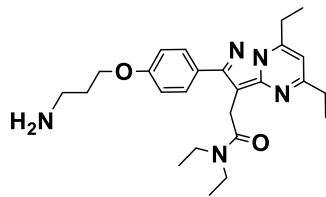
n=2; 4.16 n=6; 4.20
 n=3; 4.17 n=7; 4.21
 n=4; 4.18 n=8; 4.22
 n=5; 4.19

General Procedure of Compound 4.16-4.22. To a solution of compound 4.9-4.15 (50 mg, 1 eq) in 4 mL of ethanol was added hydrazine (5 eq). The reaction mixture was irradiated in a Biotage Initiator at 180 °C for 60 min. The mixture was then concentrated and purified by flash chromatography using 6:4 DCM/methanol to yield compound 4.16-4.22 as a yellow crystal.



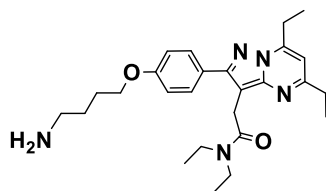
2-(2-(4-(2-aminoethoxy)phenyl)-5,7-diethylpyrazolo[1,5-a]pyrimidin-3-yl)-N,N-diethylacetamide (Compound 4.16)

¹H-NMR (CDCl₃, 600 MHz) δ 7.85 (s, 2H), 7.5 (d, 2H, *J* = 8.6 Hz), 6.81 (d, 2H, *J* = 8.6 Hz), 6.59 (s, 1H), 4.04 (t, 2H), 3.93 (s, 2H), 3.10-3.36 (m, 2H), 3.31-3.27 (m, 2H), 3.19-3.15 (m, 4H), 2.90-2.87 (m, 2H), 1.38 (t, 3H, *J* = 7.5 Hz), 1.29 (t, 3H, *J* = 7.5 Hz), 1.11 (t, 3H, *J* = 7.1 Hz), 1.01 (t, 3H, *J* = 7.1 Hz). ¹³C-NMR (CDCl₃, 150 MHz) δ 170.4, 163.4, 158.5, 156, 154.7, 143.8, 129.9, 125.5, 116.6, 114.8, 114.7, 104.9, 99.5, 63.5, 42.7, 41.3, 39.4, 29.7, 27.9, 23.7, 13.7, 12.7, 12.5, 9.9. HRMS calc'd for C₂₄H₃₃N₅O₂ m/z = 424.2707 (M+H⁺), found 424.2706.



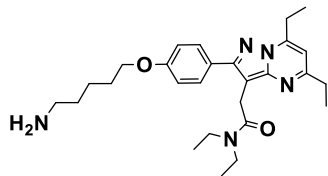
2-(2-(4-(3-aminopropoxy)phenyl)-5,7-diethylpyrazolo[1,5-a]pyrimidin-3-yl)-N,N-diethylacetamide (Compound 4.17)

$^1\text{H-NMR}$ (CDCl_3 , 600 MHz) δ 7.82 (s, 2H), 7.56 (d, 2H, $J = 8.5$ Hz), 6.82 (d, 2H, $J = 8.5$ Hz), 6.51 (s, 2H), 3.90-3.88 (m, 4H), 3.42-3.39 (m, 2H), 3.29-2.25 (m, 2H), 3.15-3.11 (m, 2H), 3.00-2.91 (m, 2H), 2.84-2.79 (m, 2H), 2.01-1.90 (m, 2H), 1.36 (t, 3H, $J = 7.6$ Hz), 1.26 (t, 3H, $J = 7.6$ Hz), 1.11 (t, 3H, $J = 7.1$ Hz), 1 (t, 3H, $J = 7.1$ Hz). $^{13}\text{C-NMR}$ (CDCl_3 , 150 MHz) δ 170.5, 163.0, 158.9, 155.4, 152.5, 145.5, 129.8, 125.7, 117, 115.1, 114.7, 104.9, 99.9, 65.2, 42.6, 41.1, 37.8, 30.2, 28.1, 26.7, 23.5, 13.9, 12.8, 12.7, 10. HRMS calc'd for $\text{C}_{25}\text{H}_{35}\text{N}_5\text{O}_2$ $m/z = 438.2864$ ($\text{M}+\text{H}^+$), found 438.2870.



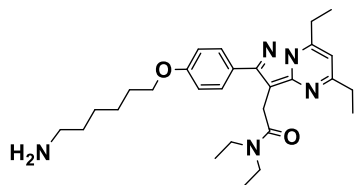
2-(2-(4-(4-aminobutoxy)phenyl)-5,7-diethylpyrazolo[1,5-a]pyrimidin-3-yl)-N,N-diethylacetamide (Compound 4.18)

$^1\text{H-NMR}$ (CDCl_3 , 600 MHz) δ 7.74 (s, 2H), 7.62 (d, 2H, $J = 8.4$ Hz), 6.85 (d, 2H, $J = 8.4$ Hz), 6.49 (s, 1H), 3.97-3.76 (m, 4H), 3.45-3.41 (m, 2H), 3.31-3.27 (m, 2H), 3.15-3.10 (m, 2H), 2.85-2.74 (m, 8H), 1.37 (t, 3H, $J = 7.5$ Hz), 1.27 (t, 3H, $J = 7.5$ Hz), 1.13 (t, 3H, $J = 7.1$ Hz), 1.01 (t, 3H, $J = 7.1$ Hz). $^{13}\text{C-NMR}$ (CDCl_3 , 600 MHz) δ 170.6, 162.9, 159.1, 155.1, 151.5, 146.3, 129.8, 125.8, 114.7, 105, 100.1, 67.1, 42.6, 41.0, 39.7, 30.7, 28.1, 25.9, 24.3, 23.4, 14.1, 12.9, 12.8, 10.1. HRMS calc'd for $\text{C}_{26}\text{H}_{37}\text{N}_5\text{O}_2$ $m/z = 452.3020$ ($\text{M}+\text{H}^+$), found 452.3024.



2-(2-(4-((5-aminopentyl)oxy)phenyl)-5,7-diethylpyrazolo[1,5-a]pyrimidin-3-yl)-N,N-diethylacetamide (Compound 4.19)

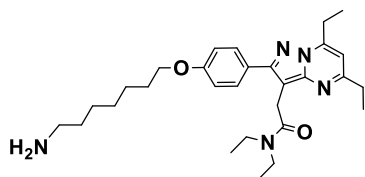
$^1\text{H-NMR}$ (CDCl_3 , 600 MHz) δ 7.75 (s, 2H), 7.69 (d, 2H, $J = 8.3$ Hz), 6.89 (d, 2H, $J = 8.4$ Hz), 6.46 (s, 1H), 3.99-3.81 (m, 4H), 3.49-3.44 (m, 2H), 3.34-3.27 (m, 2H), 3.15-3.10 (m, 2H), 2.81-2.70 (m, 4H), 1.71-1.61 (m, 2H), 1.59-1.51 (m, 2H), 1.41-1.38 (m, 2H), 1.37 (t, 3H, $J = 7.4$ Hz), 1.27 (t, 3H, $J = 7.5$ Hz), 1.14 (t, 3H, $J = 7.1$ Hz), 1.02 (t, 3H, $J = 7$ Hz). $^{13}\text{C-NMR}$ (CDCl_3 , 150 MHz) δ 170.5, 162.6, 159.3, 154.8, 150.2, 147.3, 129.8, 126, 114.7, 105, 100.4, 67.3, 42.6, 40.9, 39.7, 31.2, 28.3, 28.2, 26.8, 23.3, 22.8, 14.2, 12.9, 12.8, 10.2. HRMS calc'd for $\text{C}_{27}\text{H}_{39}\text{N}_5\text{O}_2$ $m/z = 466.3177$ ($\text{M}+\text{H}^+$), found 466.3183.



2-(2-(4-((6-aminohexyl)oxy)phenyl)-5,7-diethylpyrazolo[1,5-a]pyrimidin-3-yl)-N,N-diethylacetamide (Compound 4.20)

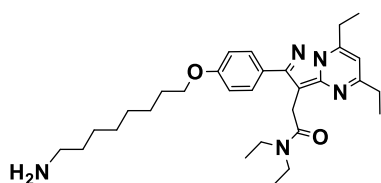
$^1\text{H-NMR}$ (CDCl_3 , 600 MHz) δ 7.7 (s, 2H), 7.63 (d, 2H, $J = 8.7$ Hz), 6.87 (d, 2H, $J = 8.7$ Hz), 6.47 (s, 1H), 3.88-3.84 (m, 4H), 3.45-3.41 (m, 2H), 3.31-3.26 (m, 2H), 3.13-3.09 (m, 2H), 2.79-2.75 (m, 2H), 2.70-2.63 (m, 2H), 1.67-1.62 (m, 2H), 1.49-1.44 (m, 2H), 1.35 (t, 3H, $J = 7.5$ Hz), 1.35-1.30 (m, 2H), 1.25 (t, 3H, $J = 7.6$ Hz), 1.26-1.21 (m, 2H), 1.12 (t, 3H, $J = 7.1$ Hz), 1.01 (t, 3H, $J = 7.1$ Hz). $^{13}\text{C-NMR}$ (CDCl_3 , 150 MHz) 170.6, 162.7, 159.5, 155.2, 151.2, 146.6, 129.8, 125.6, 117.3, 115.3, 114.7, 104.9, 100.2, 67.6, 42.6, 40.9, 39.7, 30.8, 28.7, 28.1, 27.2, 25.8, 25.3,

23.4, 14.1, 12.9, 10.2, 8.4. HRMS calc'd for C₂₈H₄₁N₅O₂ m/z = 480.3333 (M+H⁺), found 480.3339.



2-(2-(4-((7-aminoheptyl)oxy)phenyl)-5,7-diethylpyrazolo[1,5-a]pyrimidin-3-yl)-N,N-diethylacetamide (Compound 4.21)

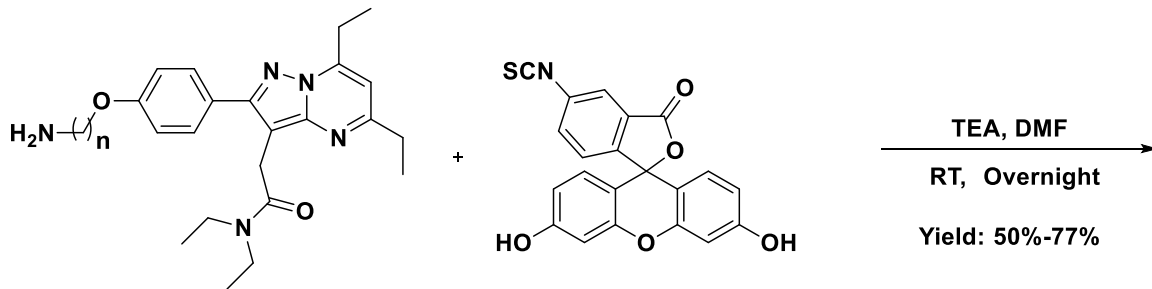
¹H-NMR (CDCl₃, 600 MHz) δ 7.7 (s, 2H), 7.61 (d, 2H, *J* = 8.7 Hz), 6.89 (d, 2H, *J* = 8.7 Hz), 6.5 (s, 1H), 3.91-3.88 (m, 4H), 3.44-3.40 (m, 2H), 3.32-3.28 (m, 2H), 3.16-3.11 (m, 2H), 2.83-2.78 (m, 2H), 2.71-2.64 (m, 2H), 1.71-1.63 (m, 2H), 1.50-1.42 (m, 2H), 1.37 (t, 3H, *J* = 7.5 Hz), 1.36-1.31 (m, 2H), 1.27 (t, 3H, *J* = 7.5 Hz), 1.23-1.15 (m, 4H), 1.12 (t, 3H, *J* = 7.1 Hz), 1.02 (t, 3H, *J* = 7.1 Hz). ¹³C-NMR (CDCl₃, 150 MHz) 170.5, 162.8, 159.7, 155.5, 151.9, 145.9, 129.9, 125.3, 117.2, 115.2, 114.7, 104.8, 100.1, 67.8, 42.6, 41.0, 39.8, 30.5, 28.9, 28.5, 28.1, 27.2, 26.1, 25.6, 23.5, 14.1, 12.9, 12.8, 10.1. HRMS calc'd for C₂₉H₄₃N₅O₂ m/z = 494.3490 (M+H⁺), found 494.3492.



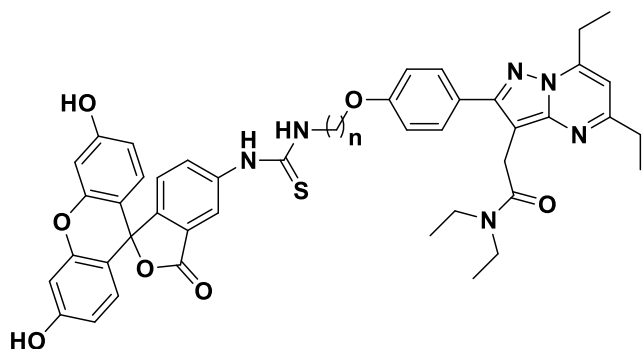
2-(2-(4-((8-amino-octyl)oxy)phenyl)-5,7-diethylpyrazolo[1,5-a]pyrimidin-3-yl)-N,N-diethylacetamide (Compound 4.22)

¹H-NMR (CDCl₃, 600 MHz) δ 7.74 (d, 2H, *J* = 8.5 Hz), 7.67 (s, 2H), 7.0 (d, 2H, *J* = 8.6 Hz), 6.59 (s, 1H), 4.05-3.99 (m, 4H), 3.55-3.52 (m, 2H), 3.42-3.37 (m, 2H), 3.25-3.21 (m, 2H), 2.92-2.87 (m, 2H), 2.77-2.70 (m, 2H), 1.80-1.76 (m, 2H), 1.47 (t, 3H, *J* = 7.4 Hz), 1.54-1.48 (m, 2H), 1.46-1.42 (m, 2H), 1.37 (t, 3H, *J* = 7.5 Hz), 1.35-1.29 (m, 2H), 1.28-1.23 (m, 4H), 1.23 (t, 3H, *J*

= 7.1 Hz), 1.11 (t, 3H, $J = 7.1$ Hz). ^{13}C -NMR (CDCl_3 , 150 MHz) 162.5, 159.4, 154.9, 150.2, 147.3, 129.8, 125.9, 114.7, 114.6, 104.9, 100.4, 67.8, 42.6, 40.8, 39.9, 31.2, 28.9, 28.7, 28.6, 28.2, 27.2, 26.1, 25.6, 23.3, 14.2, 12.9, 12.8, 10.2. HRMS calc'd for $\text{C}_{30}\text{H}_{45}\text{N}_5\text{O}_2$ $m/z = 508.3646$ ($\text{M}+\text{H}^+$), found 508.3651.

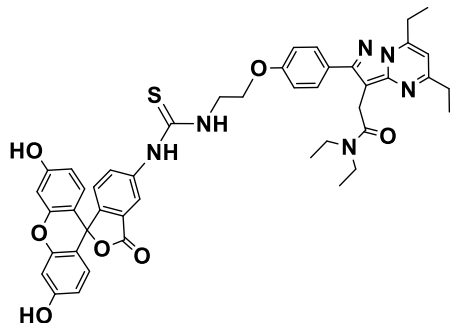


n=2; 4.16 n=6; 4.20
 n=3; 4.17 n=7; 4.21
 n=4; 4.18 n=8; 4.22
 n=5; 4.19



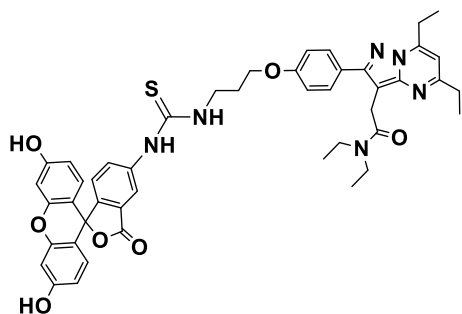
n=2; 4.23 n=6; 4.27
 n=3; 4.24 n=7; 4.28
 n=4; 4.25 n=8; 4.29
 n=5; 4.26

General Procedure of Fluorescent Compound 4.23-4.29. To a solution of compound 4.16-4.22 (20 mg, 1 eq) and fluorescent compound FITC (2 eq) in 3 mL DMF was added triethylamine (TEA, 4 eq). The reaction mixture was stirred in the dark at room temperature overnight. The mixture was then purified with a Gilson to yield compound 4.23-4.29 as an orange solid.



2-(2-(4-(2-(3-(3',6'-dihydroxy-3-oxo-3*H*-spiro[isobenzofuran-1,9'-xanthen]-5-yl)thioureido)ethoxy)phenyl)-5,7-diethylpyrazolo[1,5-*a*]pyrimidin-3-yl)-*N,N*-diethylacetamide (Compound 4.23)

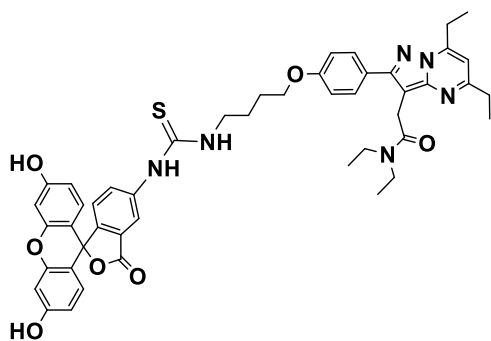
¹H-NMR (CD₃OD, 600 MHz) δ 8.16 (s, 1H), 7.72 (d, 1H, *J* = 6.9 Hz), 7.66 (d, 2H, *J* = 8.8 Hz), 7.12 (d, 1H, *J* = 8.3 Hz), 7.09 (d, 2H, *J* = 8.8 Hz), 6.77 (s, 1H), 6.72-6.65 (m, 4H), 6.56 (d, 1H, *J* = 2.3 Hz), 6.54 (d, 1H, *J* = 2.3 Hz), 4.29 (t, 2H, *J* = 5.2 Hz), 4.05 (t, 2H, *J* = 5.2 Hz), 3.95 (s, 2H), 3.55-3.52 (m, 2H), 3.39-3.36 (m, 2H), 3.18-3.14 (m, 2H), 2.86-2.82 (m, 2H), 1.45 (t, 2H, *J* = 7.5 Hz), 1.35 (t, 3H, *J* = 7.6 Hz), 1.21 (t, 3H, *J* = 7.1 Hz), 1.09 (t, 3H, *J* = 7.1 Hz). HRMS calc'd for C₄₅H₄₄N₆O₇S *m/z* = 813.3065 (M+H⁺), found 813.3049.



2-(2-(4-(3-(3-(3',6'-dihydroxy-3-oxo-3*H*-spiro[isobenzofuran-1,9'-xanthen]-5-yl)thioureido)propoxy)phenyl)-5,7-diethylpyrazolo[1,5-*a*]pyrimidin-3-yl)-*N,N*-diethylacetamide (Compound 4.24)

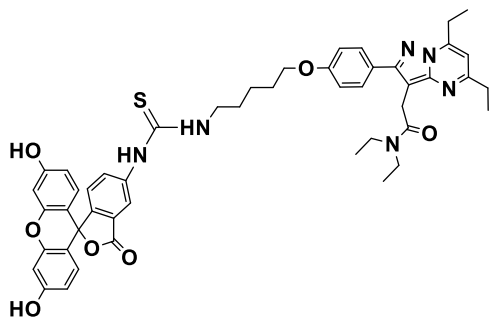
¹H-NMR (CD₃OD, 600 MHz) δ 8.19 (s, 1H), 7.76 (d, 1H, *J* = 7.0 Hz), 7.61 (d, 2H, *J* = 8.6 Hz), 7.11 (d, 1H, *J* = 8.3 Hz), 7.02 (d, 2H, *J* = 8.7 Hz), 6.91-6.77 (m, 5H), 6.70-6.68 (m, 2H), 4.15 (t,

2H, $J = 5.9$ Hz), 3.91 (s, 2H), 3.84 (t, 2H, $J = 5.7$ Hz), 3.54-3.51 (m, 2H), 3.39-3.36 (m, 2H), 3.18-3.11 (m, 2H), 2.87-2.83 (m, 2H), 2.18-2.15 (m, 2H), 1.42 (t, 3H, $J = 7.4$ Hz), 1.35 (t, 3H, $J = 7.6$ Hz), 1.21 (t, 3H, $J = 7.1$ Hz), 1.1 (t, 3H, $J = 7.1$ Hz). HRMS calc'd for $C_{46}H_{46}N_6O_7S$ $m/z = 827.3221$ ($M+H^+$), found 827.3197.



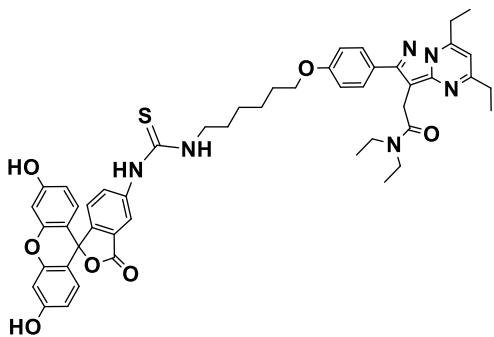
2-(2-(4-(4-(3-(3',6'-dihydroxy-3-oxo-3*H*-spiro[isobenzofuran-1,9'-xanthen]-5-yl)thioureido)butoxy)phenyl)-5,7-diethylpyrazolo[1,5-*a*]pyrimidin-3-yl)-*N,N*-diethylacetamide (Compound 4.25)

1H -NMR (CD_3OD , 600 MHz) δ 8.05 (s, 1H), 7.65 (d, 1H, $J = 8$ Hz), 7.53 (d, 2H, $J = 8.7$ Hz), 7.03 (d, 1H, $J = 8.2$ Hz), 6.92 (d, 2H, $J = 8.8$ Hz), 6.67-6.62 (m, 5H), 6.51 (d, 1H, $J = 2.1$ Hz), 6.49 (d, 1H, $J = 2.1$ Hz), 4.01 (t, 2H, $J = 5.8$ Hz), 3.85 (s, 2H), 3.62 (t, 2H), 3.45-3.42 (m, 2H), 3.30-3.26 (m, 2H), 3.07-3.04 (m, 2H), 2.76-2.72 (m, 2H), 1.81-1.74 (m, 4H), 1.33 (t, 3H, $J = 7.5$ Hz), 1.25 (t, 3H, $J = 7.6$ Hz), 1.12 (t, 3H, $J = 7.1$ Hz), 1.0 (t, 3H, $J = 7.1$ Hz). HRMS calc'd for $C_{47}H_{48}N_6O_7S$ $m/z = 841.3378$ ($M+H^+$), found 841.3354.



2-(2-(4-((5-(3-(3',6'-dihydroxy-3-oxo-3*H*-spiro[isobenzofuran-1,9'-xanthen]-5-yl)thioureido)pentyl)oxy)phenyl)-5,7-diethylpyrazolo[1,5-*a*]pyrimidin-3-yl)-*N,N*-diethylacetamide (Compound 4.26)

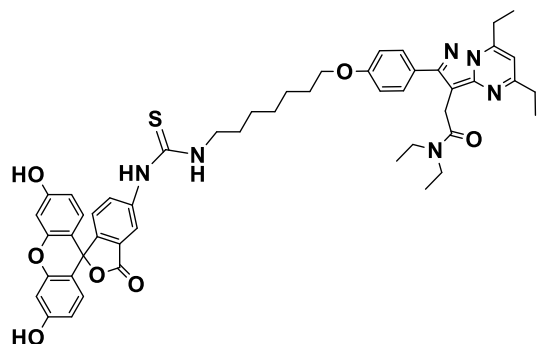
¹H-NMR (CD₃OD, 600 MHz) δ 8.0 (s, 1H), 7.61 (d, 1H, *J* = 8.2 Hz), 7.52 (d, 2H, *J* = 8.7 Hz), 6.99 (d, 1H, *J* = 7.6 Hz), 6.91 (d, 2H, *J* = 8.8 Hz), 6.68 (s, 1H), 6.57-6.53 (m, 4H), 6.43 (d, 1H, *J* = 2.3 Hz), 6.42 (d, 1H, *J* = 2.4 Hz), 3.99 (t, 2H, *J* = 6.2 Hz), 3.84 (s, 2H), 3.55 (t, 2H, *J* = 6.5 Hz), 3.46-3.41 (m, 2H), 3.30-3.26 (m, 2H), 3.10-3.05 (m, 2H), 2.78-2.74 (m, 2H), 1.81-1.76 (m, 2H), 1.69-1.64 (m, 2H), 1.54-1.50 (m, 2H), 1.35 (t, 3H, *J* = 7.5 Hz), 1.26 (t, 3H, *J* = 7.6 Hz), 1.11 (t, 3H, *J* = 7.1 Hz), 0.99 (t, 3H, *J* = 7.1 Hz). HRMS calc'd for C₄₈H₅₀N₆O₇S *m/z* = 855.3534 (M+H⁺), found 855.3516.



2-(2-(4-((6-(3-(3',6'-dihydroxy-3-oxo-3*H*-spiro[isobenzofuran-1,9'-xanthen]-5-yl)thioureido)hexyl)oxy)phenyl)-5,7-diethylpyrazolo[1,5-*a*]pyrimidin-3-yl)-*N,N*-diethylacetamide (Compound 4.27)

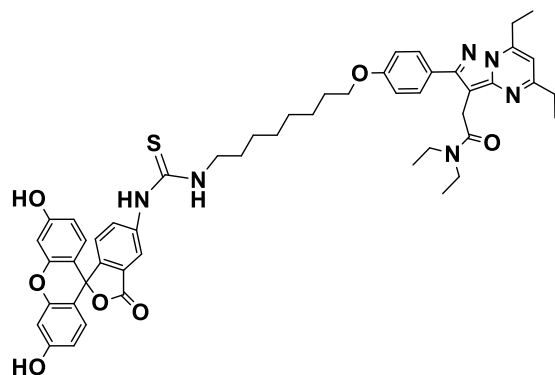
¹H-NMR (CD₃OD, 600 MHz) δ 8.20 (s, 1H), 7.75 (d, 1H, *J* = 8 Hz), 7.63 (d, 2H, *J* = 8.7 Hz), 7.14 (d, 1H, *J* = 8.2 Hz), 7.01 (d, 2H, *J* = 8.8 Hz), 6.80-6.71 (m, 5H), 6.65-6.59 (m, 2H), 4.07 (t, 2H, *J* = 6.4 Hz), 3.95 (s, 2H), 3.65 (t, 2H, *J* = 5.6 Hz), 3.57-3.53 (m, 2H), 3.41-3.37 (m, 2H), 3.18-3.14 (m, 2H), 2.88-2.84 (m, 2H), 1.88-1.82 (m, 2H), 1.75-1.69 (m, 2H), 1.63-1.57 (m, 2H), 1.54-1.49 (m, 2H), 1.44 (t, 3H, *J* = 7.5 Hz), 1.36 (t, 3H, *J* = 7.6 Hz), 1.22 (t, 3H, *J* = 7.1 Hz),

1.10 (t, 3H, $J = 7.1$ Hz). HRMS calc'd for $C_{49}H_{52}N_6O_7S$ $m/z = 869.3691(M+H^+)$, found 869.3670.



2-(2-(4-((7-(3-(3',6'-dihydroxy-3-oxo-3*H*-spiro[isobenzofuran-1,9'-xanthen]-5-yl)thioureido)heptyl)oxy)phenyl)-5,7-diethylpyrazolo[1,5-*a*]pyrimidin-3-yl)-*N,N*-diethylacetamide (Compound 4.28)

1H -NMR (CD_3OD , 600 MHz) δ 8.16 (s, 1H), 7.71 (d, 1H, $J = 8.2$ Hz), 7.62 (d, 2H, $J = 8.8$ Hz), 7.08 (d, 1H, $J = 8.2$ Hz), 6.99 (d, 2H, $J = 8.8$ Hz), 6.76 (s, 1H), 6.70-6.64 (m, 4H), 6.54 (d, 1H, $J = 2.3$ Hz), 6.53 (d, 1H, $J = 2.2$ Hz), 4.03 (t, 2H, $J = 6.3$ Hz), 3.94 (s, 2H), 3.61 (t, 2H, $J = 5.5$ Hz), 3.55-3.53 (m, 2H), 3.41-3.37 (m, 2H), 3.17-3.13 (m, 2H), 2.87-2.82 (m, 2H), 1.84-1.78 (m, 2H), 1.69-1.65 (m, 2H), 1.57-1.51 (m, 2H), 1.47-1.44 (m, 2H), 1.43 (t, 3H, $J = 7.4$ Hz), 1.34 (t, 3H, $J = 7.6$ Hz), 1.32-1.28 (m, 2H), 1.21 (t, 3H, $J = 7.1$ Hz), 1.1 (t, 3H, $J = 7.1$ Hz). HRMS calc'd for $C_{50}H_{54}N_6O_7S$ $m/z = 883.3847 (M+H^+)$, found 883.3828.



2-(2-(4-((8-(3-(3',6'-dihydroxy-3-oxo-3*H*-spiro[isobenzofuran-1,9'-xanthen]-5-yl)thioureido)octyl)oxy)phenyl)-5,7-diethylpyrazolo[1,5-*a*]pyrimidin-3-yl)-*N,N*-diethylacetamide (Compound 4.29)

¹H-NMR (CD₃OD, 600 MHz) δ 8.08 (s, 1H), 7.66 (d, 1H, *J* = 7.6 Hz), 7.51 (d, 2H, *J* = 8.8 Hz), 7.02 (d, 1H, *J* = 8.2 Hz), 6.88 (d, 2H, *J* = 8.8 Hz), 6.73-6.65 (m, 5H), 6.54 (d, 1H, *J* = 2.2 Hz), 6.53 (d, 1H, *J* = 2.2 Hz), 3.92 (t, 2H, *J* = 6.3 Hz), 3.84 (s, 2H), 3.5 (t, 2H, *J* = 5.8 Hz), 3.46-3.42 (m, 2H), 3.31-3.27 (m, 2H), 3.08-3.03 (m, 2H), 2.76-2.72 (m, 2H), 1.72-1.66 (m, 2H), 1.59-1.51 (m, 2H), 1.45-1.38 (m, 2H), 1.33 (t, 3H, *J* = 7.5 Hz), 1.36-1.31 (m, 6H), 1.24 (t, 3H, *J* = 7.6 Hz), 1.12 (t, 3H, *J* = 7.1 Hz), 0.99 (t, 3H, *J* = 7.1 Hz). HRMS calc'd for C₅₁H₅₆N₆O₇S *m/z* = 897.4004 (M+H⁺), found 897.3985.

General Experimental

Spectroscopic Characterization

After preparing 20 μM of 23-29 aqueous solutions in 25 mM phosphate buffer (pH 7.2), absorption and emission spectra were measured with an Agilent 8453 UV-visible spectrophotometer and PTI 814 photomultiplier detection system at room temperature, respectively.

Receptor Binding Assay

Binding affinity of the fluorescent probes using C6 glioma cell lysates were carried out as previously reported. All experiments were conducted in triplicate. Binding affinities (IC_{50}) were calculated with GraphPad Prism 6. K_i was calculated using the Cheng and Prusoff equation: $K_i = \text{IC}_{50}/(1+[\text{L}]/K_d)$. [L] is the concentration of [3H]PK 11195, which was 6 nM in our experiment; the K_d for PK 11195 was 5 nM.

Displacement Experiments

Displacement experiments using C6 glioma cell lysate were performed by co-incubating 0.50-100 nM optical probe and 100 nM 2-(5,7-diethyl-2-(4-methoxyphenyl)pyrazolo[1,5-*a*]pyrimidin-3-yl)-*N,N*-diethylacetamide for 2 hours. The solutions were then filtered with a Brandel harvester and imaging carried out in a Maestro imaging system (CRi) with the same exposure time for each sample. Image J was applied to measure signal intensity.

Cell Culture

C6 glioma cells were cultured in Dulbecco's modified Eagle medium (DMEM), supplemented with 10% fetal bovine serum and 1% penicillin streptomycin. Cells were maintained at 37 °C, 5% CO_2 in a tissue culture incubator (Forma Scientific).

Cell Imaging

C6 cells were incubated with 0.1 μM optical probe in DMEM medium for 2 h in a tissue culture incubator at 37 $^{\circ}\text{C}$, at 5% CO_2 . At the end of the incubation, the cells were rinsed with PBS three times, before addition of 50 nM Mito Tracker red in serum-free DMEM medium, with incubation for another 20 min. After that, cells were rinsed with PBS three times, fixed, and imaged by Zeiss LSM 510 inverted confocal microscope. In the displacement experiments, C6 cells were co-incubated with 0.1 μM probe and 10 μM 2-(5,7-diethyl-2-(4-methoxyphenyl)pyrazolo[1,5-*a*]pyrimidin-3-yl)-*N,N*-diethylacetamide in DMEM medium for 2h.

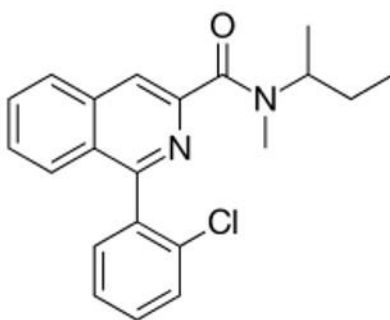
CHAPTER 5

DEVELOPMENT OF A HIGH-THROUGHPUT SCREENING METHOD USING A NOVEL TSPO OPTICAL LIGAND

5.1 Introduction

There is a critical need to discover ligands with high target affinity to aid in molecular imaging, tumor diagnosis, and therapy. Following the target validation and library development, screening is necessary to identify molecular hits. An inexpensive and rapid screening method can greatly advance the discovery and application of new molecular imaging probes for the clinic.

Presently, ^3H -PK 11195 (**Figure 5.1.1**), a radioactive material and also a TSPO ligand, is routinely used to screen newly developed TSPO ligands. The screening method using here is called competitive binding assay. The competition curve is accomplished by plotting percentage of total binding against the concentration of the new ligand. Since the concentration of ^3H -PK 11195 and cell lysate is kept the same, higher concentration of new ligand will result in lower ^3H -PK 11195 binding to the protein. We can use the competition curve to calculate IC_{50} and K_i values of a new ligand.



5.1

Figure 5.1.1 Chemical structure of PK 11195.

In a standard screening assay (**Figure 5.1.2**), C6 cell lysate is treated with newly synthesized ligand and ^3H -PK 11195 together in a 24-well plate. The cell lysate will be incubated at 4 °C for about 2 hrs to allow the ligand and ^3H -PK 11195 to compete binding with TSPO protein. Brandel Harvester is then used to wash the cell lysate with phosphate-buffered saline (PBS buffer), and the protein is trapped in the filter paper. Filters are further punched into vials with scintillation buffer. Liquid scintillation counter (Beckman LS 6000SC) will finally be applied to measure the residual radioactivity on the filters. [14, 55, 72]

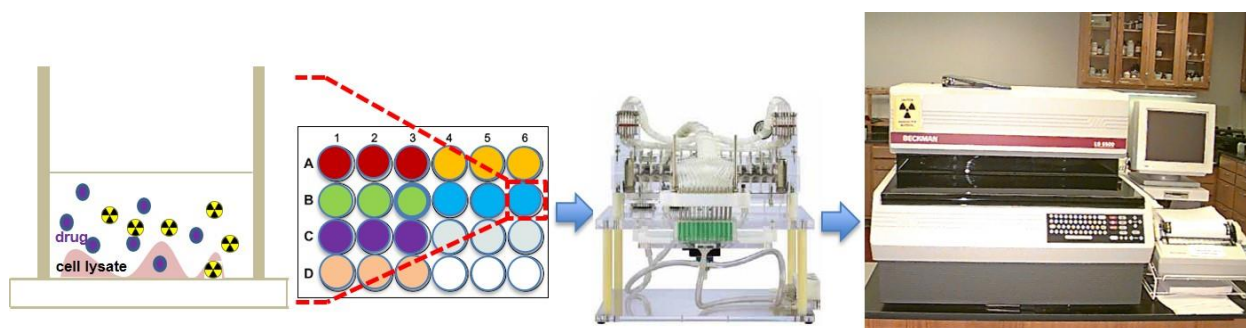


Figure 5.1.2 Competitive binding assay using ^3H -PK11195 to detect the ligand binding affinity.

However, current screening assay has several limitations. Tritium (^3H) is a radioactive isotope of hydrogen with the half-life of 12.32 years. It is quite risky and expensive to use ^3H -PK11195 in the screening assay. In addition, it requires to prepare lots of paperwork and follow complex regulatory process to perform the assay. It also takes long time to read the counts by using a liquid scintillation counter.

Another alternative choice is to use optical ligand. By leveraging the existence of fluorescent unit within the ligand to measure the signal, TSPO optical ligands can be utilized to develop a fast screening method to replace ^3H -PK 11195 (**Figure 5.1.3**).

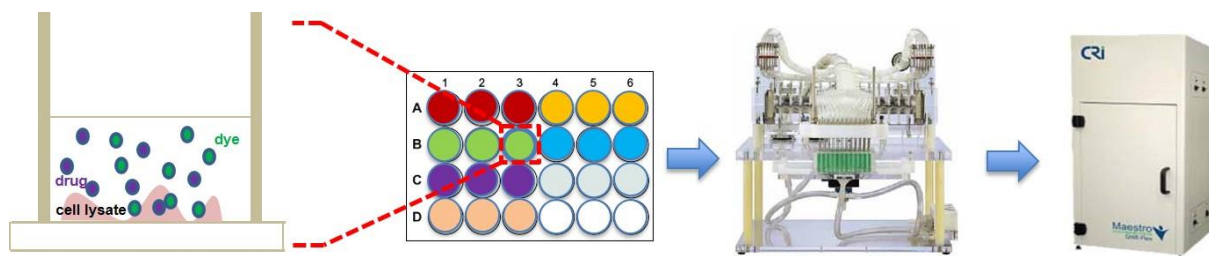


Figure 5.1.3 Screening assay using TSPO fluorescent ligand to replace ^3H -PK 11195.

Herein, we used the fluorescent probe **4.29** described in **Chapter 4** to replace ^3H -PK 11195 and developed a new fast, inexpensive, and non-radioactive screening assay. A three-dimensional pharmacophore model was built through ensembles of highly potent TSPO compounds in the SSR and pyrazolopyrimidines series. The composite model was used to calculate and select a library of novel chemotypes. The high-throughput screening assay using TSPO fluorescent probe was further applied to screen the library. Several new scaffolds were discovered and can be very promising with further structural optimization.

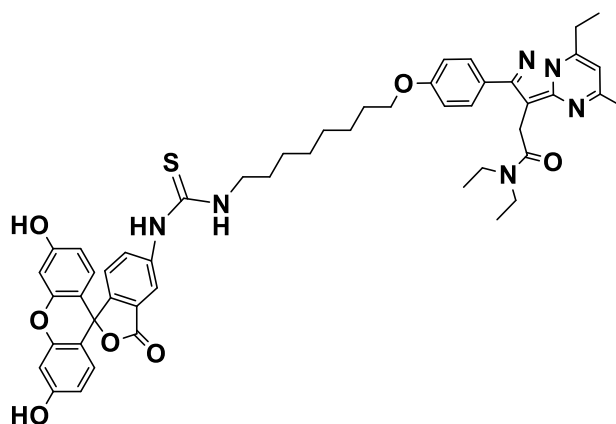


Figure 5.1.4 TSPO fluorescent probe **4.29** used for screening.

5.2 Ligand Saturation Curve and Displacement Experiments

In the previous chapter, we have demonstrated that the fluorescent probe **4.29** had very high binding affinity to TSPO ($K_i = 0.31$ nM) and further confirmed its specificity by co-incubating the C6 cell lysate with both **4.29** and Mitro Tracker Red. However, to further utilize **4.29** in the screening assay, we need to measure additional parameters of the probe.

In the competitive binding assay, after generating a competition curve, the coefficient we can calculate from the curve is the half maximal inhibitory concentration, *i.e.* IC_{50} . IC_{50} measures the concentration of the drug (newly developed ligand) required to inhibit the binding from competing ligand (3H-PK 11195 or TSPO fluorescent probe) by half. However, IC_{50} is not an absolute constant of affinity. It depends on the concentration and type of competing ligand used in the assay. IC_{50} can be converted to absolute inhibition constant K_i by using the Cheng and Prusoff equation^[73]:

$$K_i = \frac{IC_{50}[L]}{1 + \frac{[L]}{K_d}} \quad \text{Equation 5.2.1}$$

Here, IC_{50} can be calculated from the competition curve; $[L]$ is the concentration and K_d is the dissociation constant of the competing ligand.

From the binding equilibrium, K_d was found to be:

$$K_d = \frac{[ligand][protein]}{[protein-ligand complex]} \quad \text{Equation 5.2.2}$$

Obviously, K_d equals the ligand concentration when half of the receptor sites are occupied.

Leveraging the existence of the fluorescent unit within the probe, we can measure the optical signal with a Maestro imaging system (CRi) and calculate the saturation curves (**Figure 5.2.1**, left, black curve). It was noted that specific binding dominated up to a concentration of 10

nM. Upon further increasing the probe concentration, while maintaining the same amount of TSPO, non-specific binding was observed. The K_d value of probe **4.29** was found to be 0.22 nM by calculating from the saturation curve (**Figure 5.2.1**, right).

For displacement experiment, probe **4.29** was co-incubated with its parent ligand. (**Figure 5.2.1**, left, red curve). It was shown that at low probe concentration, it was nearly totally blocked by the addition of its parent ligand, only with minor fluctuations. However, when the probe concentration exceeded 10 nM, the increase in the fluorescent signal was observed. As highlighted in the saturation curve, non-specific binding began to dominate above a concentration of 10 nM, which made the blocking less effective. The results from the saturation curve and displacement experiment match very well with each other.

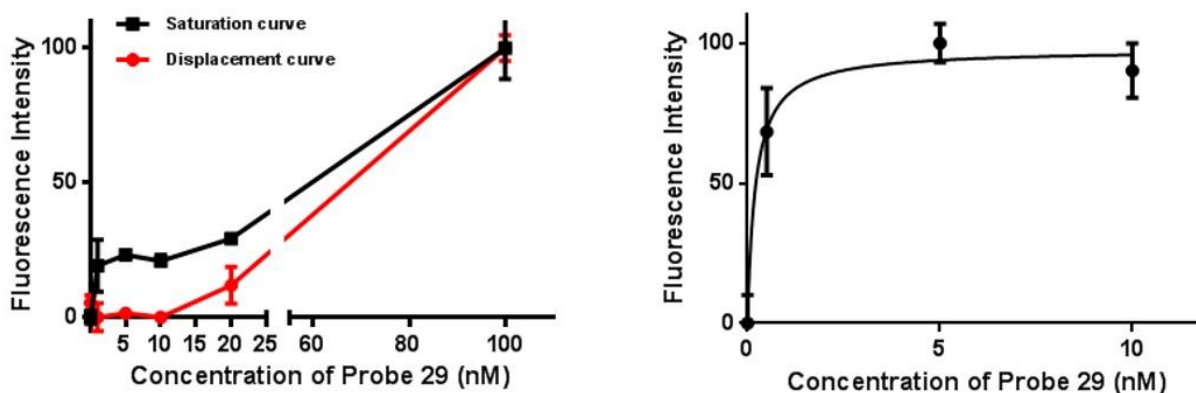


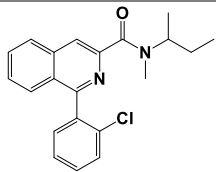
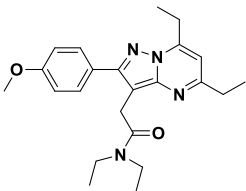
Figure 5.2.1 Saturation curve of fluorescent probe binding to C6 glioma cell lysate (left, black curve) and displacement experiments (left, red curve). C6 glioma cell lysates were co-incubated with 0.50-100 nM fluorescent probe and 100 nM 2-(5,7-diethyl-2-(4-methoxyphenyl)pyrazolo[1,5-a]pyrimidin-3-yl)-N,N-diethylacetamide.

5.3 Fluorescent Ligand in Screening Assay

Current screening assay features using radioactive materials ^3H -PK 11195. To assess if our new assay using TSPO fluorescent ligand is comparable with the current method, some well-studied TSPO ligands were screened with both the optical probe and ^3H -PK 11195. As shown in

Table 5.3.1, the K_i values calculated from two methods matched with each other, which demonstrated that we can use the optical probe to replace the radioactive material in the screening.

Table 5.3.1 Ligand binding affinity screened with optical probe and ^3H -PK11195.

Compound	Optical Probe (nM)	^3H -PK11195 (nM)
	2.43	1.90
	0.11	0.18

5.4 Screening a Novel Library of Chemical Probe Candidates

We further utilized the new assay to screen a library of chemical probes to find some possible new scaffold for TSPO ligand. By doing so, SSR- and phrazolopyrimidine-based TSPO ligand series^[14, 52, 54] (**Figure 5.4.1**) were used to generate a three-dimensional pharmacophore model.

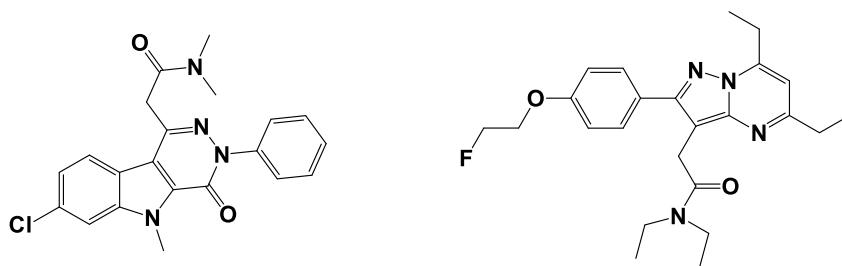


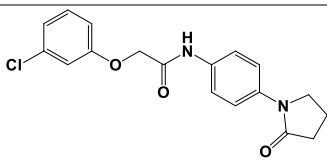
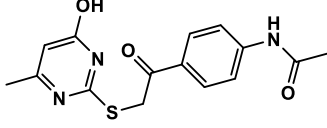
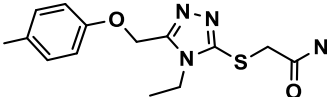
Figure 5.4.1 SSR- and phrazolopyrimidine-based TSPO ligand series.

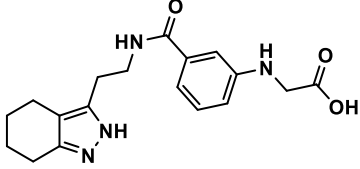
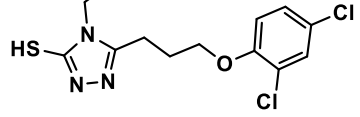
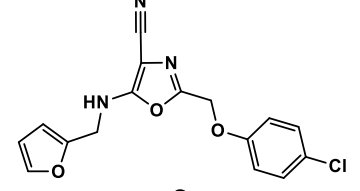
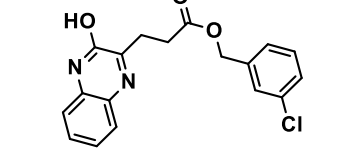
The model generated using the SurflexSim algorithm, based upon highly potent compounds in the SSR-based series and was further flexibly aligned with phrazolopyrimidines and other validated TSPO chemical scaffolds including aryloxyanilines. SurflexSim scores used both minimization of non-overlapping molecular surface and alignment of pharmacophore points for positive (Hbond donor), negative (Hbond acceptor), and hydrophobic (neutral) moieties.

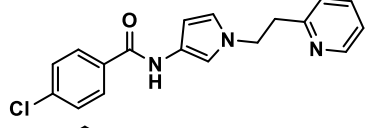
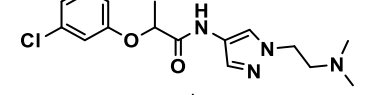
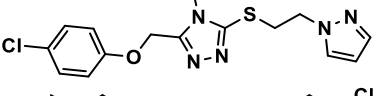
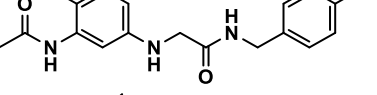
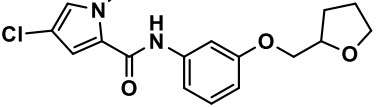
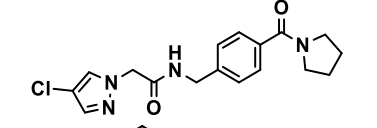
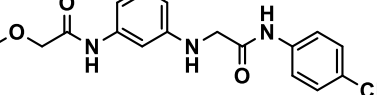
The validated model was utilized in an initial virtual screen of the ZINC library of 2.5 million compounds. The top scoring compounds generated from SAR-by-catalog experimental screen were performed with the new screening method to discover novel chemical scaffold that may be applicable for future TSPO ligand development.

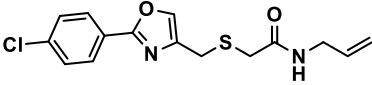
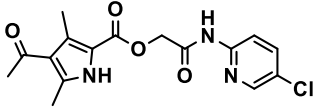
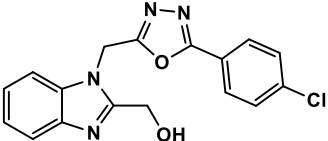
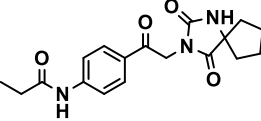
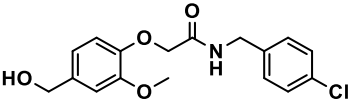
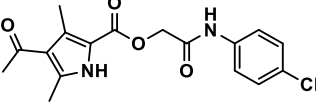
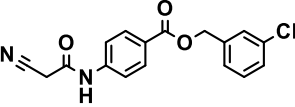
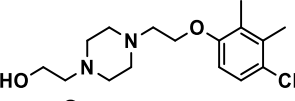
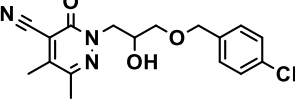
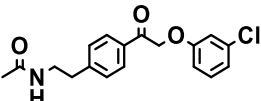
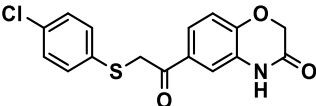
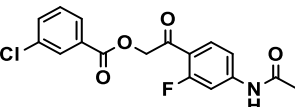
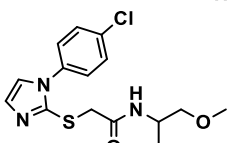
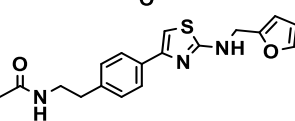
For some of the compounds, we also measured with both optical probe and ^3H -PK 11195 assays, and it showed again that two screening assays matched well. After screening the entire selected compound library, several novel TSPO chemical scaffolds were discovered. We anticipate that the new scaffolds can play an active role in TSPO ligand development with further structural optimization.

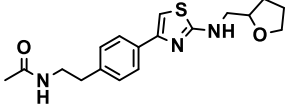
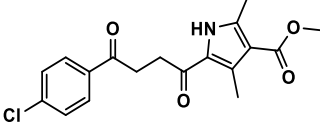
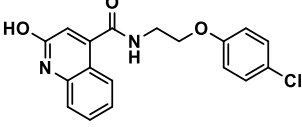
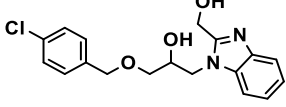
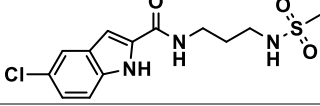
Table 5.4.1 Inhibition of new compounds screened with optical probe and ^3H -PK11195.

Entry	Structure	Optical Probe	^3H -PK11195
1		inactive	inactive
2		inactive	inactive
3		inactive	inactive

4		30%	29%
5		inactive	inactive
6		19%	18%
7		inactive	inactive

Entry	Structure	Optical Probe
8		20%
9		inactive
10		20%
11		inactive
12		15%
13		inactive
14		inactive

15		inactive
16		10%
17		inactive
18		inactive
19		inactive
20		inactive
21		22%
22		inactive
23		inactive
24		inactive
25		inactive
26		inactive
27		inactive
28		inactive

29		inactive
30		inactive
31		inactive
32		inactive
33		inactive

5.5 Conclusion

We further examined properties of fluorescent probe **4.29** developed in **Chapter 4** and demonstrated that optical probe can also play an important role in the competitive binding assay by replacing currently used radioactive materials. A library of potent compounds assessed through our computational model was screened with the new assay and some of them were very promising with further structural optimization. We anticipate the new assay can help with TSPO ligand development and discovery.

5.6 Methods

Saturation Curves

The saturation curves for K_d were determined utilizing 0.50-100 nM of optical probe, followed by incubation with C6 glioma cell lysates. All experiments were conducted in triplicate and imaging was carried out in a Maestro imaging system (CRi) with the same exposure time for each sample. Image J was applied to measure the signal intensity and the saturation curve (K_d) was normalized and calculated with GraphPad Prism 6.

TSPO Binding Assay using Fluorescent Probe

The C6 cell lysate was then incubated with fluorescent probe 4.29 (final concentration: 0.6 nM) and new ligands (final concentration 10^{-5} to 10^{-12} M) at 4 °C for 2 hrs in 24 well plate. The plate was covered with aluminium foil to avoid exposure to the light.

The solution was washed and filtered with Brandel harvester and collected on filter paper. The filter paper was imaged with Maestro Imaging System (CRi). The background was subtracted using the unmix function of the Maestro software. The signal intensity was measured with Image J by integrating the intensity within the filter paper. Binding affinity was further calculated using Prism GraphPad software.

CHAPTER 6

TSPO NEAR-INFRARED-BASED LIGAND AND PET TRACER AS PRECISION IMAGING DIAGNOSIS AND TREATMENT OF PANCREATIC CANCER

6.1 Introduction

6.1.1 Pancreatic Cancer

Pancreatic cancer is among the most aggressive types of cancer. Pancreatic cancer is currently the fourth leading cause of cancer-related deaths in the United States, and seventh worldwide. Despite significant improvements and progress in diagnosis, surgery, and other treatment, the overall five-year survival rate remains a dismal 5%. Even if diagnosed and treated early, the five-year survival rate is still roughly 20%.

According to a recent report by Lola Rahib *et al.*, pancreatic cancer is projected to be the second most common cause of death from cancer by 2030, surpassing breast, colorectal, and prostate cancers.^[74] Pancreatic ductal adenocarcinoma (PDA) accounts for the most common type of pancreatic cancer. Due to the lack of therapeutic options for highly advanced PDA, the early detection, especially the identification of precursor lesions such as pancreatic intraepithelial neoplasia (PanIN) and intraductal papillary mucinous neoplasms (IPMNs) can effectively aid in cancer treatment. Given the limited accessibility of the pancreas, it is imperative to develop noninvasive imaging modalities capable of detecting small tumors or precursor lesions.

6.1.2 Near-infrared (NIR) Ligands for Optical Imaging

In **Chapter 4**, we successfully developed a series of TSPO fluorescent ligands, featuring compound **4.29**, the highest affinity of TSPO fluorescent probes that have been reported.

However, this probe may not be suitable for *in vivo* imaging. Tissues and organs can be regarded as a homogenous biological system. The majority of the light attenuation in a homogeneous system is caused by Mie scattering, which is proportional to $1/\lambda^4$. This means that for the probe that emits a shorter wavelength of light, it will have stronger scattering and more signal attenuation, which makes it difficult for the light to penetrate the tissue.

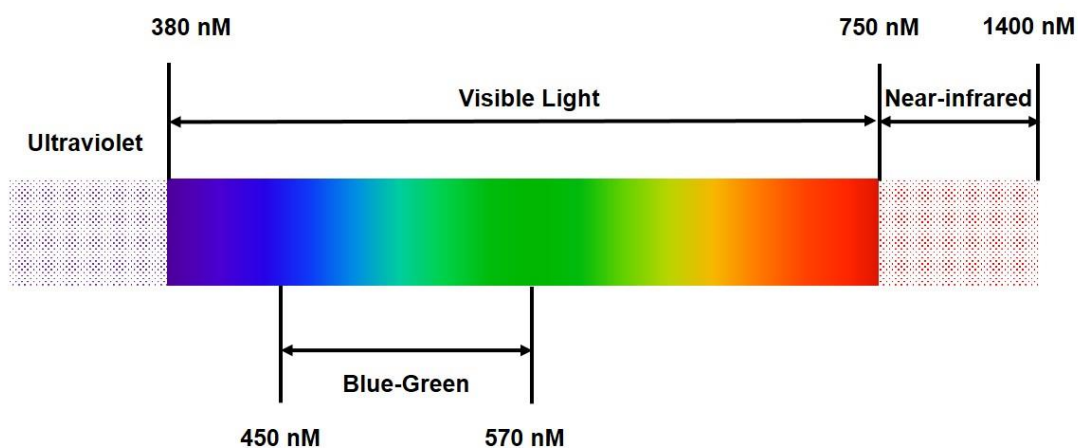


Figure 6.1.2.1 Electromagnetic spectrum from ultraviolet to near-infrared.

The fluorescent probes we developed in **Chapter 4** had the maximum emission wavelength at 520 nm, which was the blue-green light range and was too short to penetrate the organ. To solve this problem, red or near-infrared ligands were prepared for *in vivo* imaging and optical surgical navigation. [18, 75]

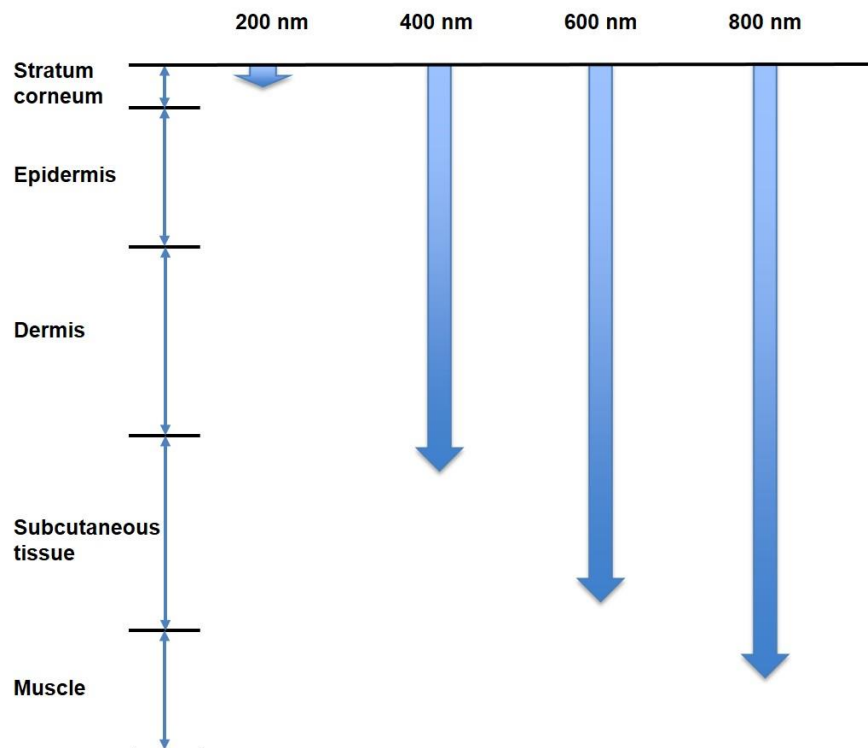


Figure 6.1.2.2 Penetration depth of various wavelengths of light.

Several small molecular near-infrared probes targeting TSPO have been reported for tumor imaging. Bai *et al.* reported a DAA1106 conjugated near-infrared dye for C6 glioma cell imaging.^[50] By connecting LI-COR 800CW with PK 11195, Deane *et al.* developed a novel TSPO targeted molecular imaging probe and studied its application in colonic adenomas and carcinomas in Smad3^{-/-} mice.^[4] Wyatt *et al.* further utilized the same probe and evaluated its performance in human breast adenocarcinoma cells (MDA-MA-231) and athymic nude mice bearing the same type of xenografts.^[12]

Near-infrared ligands can also be developed by labeling monoclonal antibodies. Jacob Houghton *et al.* labeled 5B1, a human monoclonal antibody targeting pancreatic cancer biomarker CA19.9, with a near-infrared 800-nm emission dye, and found it valuable to image CA 19.9 positive pancreatic tumor.^[76]

6.1.3 Zr-89 PET Tracer

FDG, the most commonly used PET tracer in clinic, utilize the isotope F-18. Our group previously used F-18 as a major source of isotope for PET tracer. The advantage of using a short half-life isotope is that the material will not be radioactive for a long time. However, it may not be a suitable choice if the tracer needs an extended time to reach the target.

Table 6.1.3.1 Half-life of isotopes

Isotope	Half-life
C-11	20.4 mins
N-13	9.97 mins
O-15	122 seconds
F-18	109.8 mins
Cu-62	9.74 mins
Zr-89	78.4 hours
I-124	4.18 days

Table 6.1.3.1 showed half-life of commonly used radioisotopes. In our pancreatic cancer study, it was observed that the probe needed about 18-24 hrs to reach and accumulate in the pancreas, making Zr-89 ideal to be used in the PET imaging. Unlike short half-life isotopes, Zr-89 is more commonly used to label antibodies of interest; ^[77] thus a novel synthetic and radiochemical labeling procedure for incorporation of Zr-89 into small molecule TSPO ligands was developed. So far as we know, this is the first time a small molecule Zr-89 tracer has been developed.

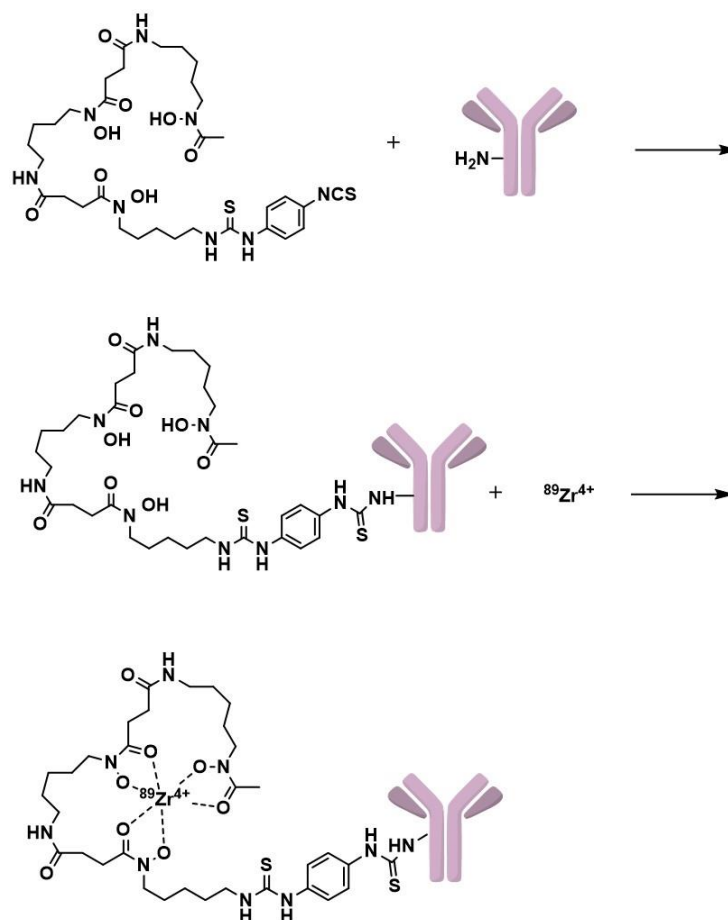


Figure 6.1.3.1 Antibody labeling with Zr-89.

6.2 TSPO in Pancreatic Tumor

A few years ago, we developed a TSPO near-infrared probe which can detect early intestinal lesions in the *Apc^{Min/+}* mouse model and advanced colon cancers in the *Smad3^{-/-}* model. Herein, we further explored TSPO expression in pancreatic tumors.

TSPO levels in normal pancreas, PanIN, and PDA were assessed by immunostaining. As shown in **Figure 6.2.1**, TSPO expression was low in normal pancreatic ductal and centroacinar cells. However, a high level immunoreactivity was observed in pancreatic precursor lesions and PDA. TSPO expression was slightly elevated in low-grade PanIN lesions, and significantly elevated in high-grade PanIN lesions.

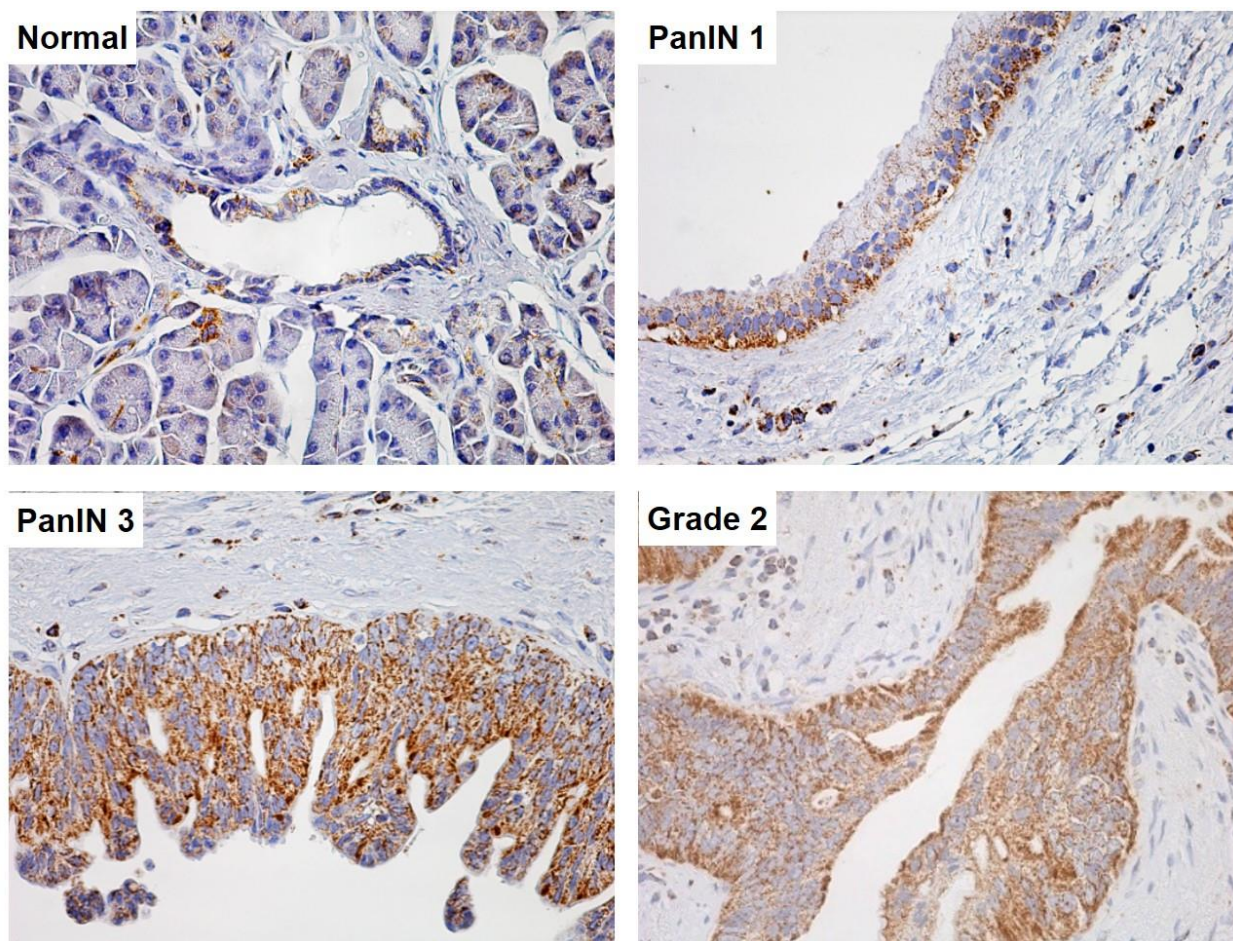


Figure 6.2.1 TSPO immunostaining of human normal and neoplastic pancreas.

Using pancreatic cancer tissue microarrays (TMAs) collected from 155 patients at Vanderbilt University Medical Center (VUMC), TSPO expression was further evaluated using an intensity score-derived methodology, which defined none or weak expression as score one, modest as two, and strong as three.

As shown in **Figure 6.2.2**, TSPO expression was low in the normal pancreas with the mean IHC score found to be 1.025. Modest expression was found in chronic pancreatitis (CP), an inflammatory condition of pancreas. The mean score was 1.385, slightly higher compared to normal pancreas. However, TSPO was significantly overexpressed in both precursor lesions

(PanIN) and all grades of invasive PDA, with the mean score of 2.500 (PanIN), 2.625(Grade 1), 2.576 (Grade 2), and 1.923 (Grade 3) respectively.

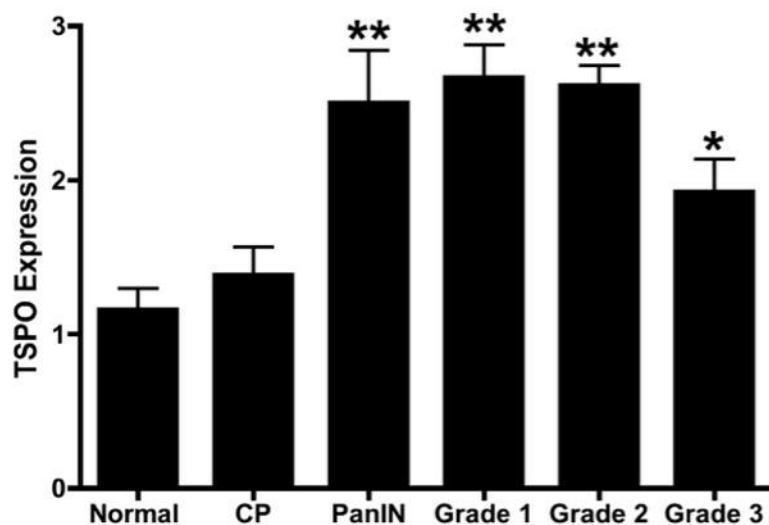


Figure 6.2.2 TSPO expression of specimens collected from 155 VUMC patients.

This finding further confirmed a clear connection between pancreatic cancer and TSPO expression. Elevated TSPO levels were found not only in invasive and highly advanced pancreatic cancer, such as PDA, but also observed in pre-malignant pancreatic lesions. This finding allows us to develop molecular imaging probes that can target TSPO to identify pancreatic precursor and advanced lesions.

6.3 TSPO NIR Ligand Development

In **Chapter 4**, it was found that the probe with 8-carbon linker had the highest affinity to TSPO. Since the FITC dye was not ideal for *in vivo* imaging, near-infrared dye LI-COR IRDye 800CW was chosen to replace FITC but to attach TSPO ligand unit using the same linker (**Figure 6.3.1**).

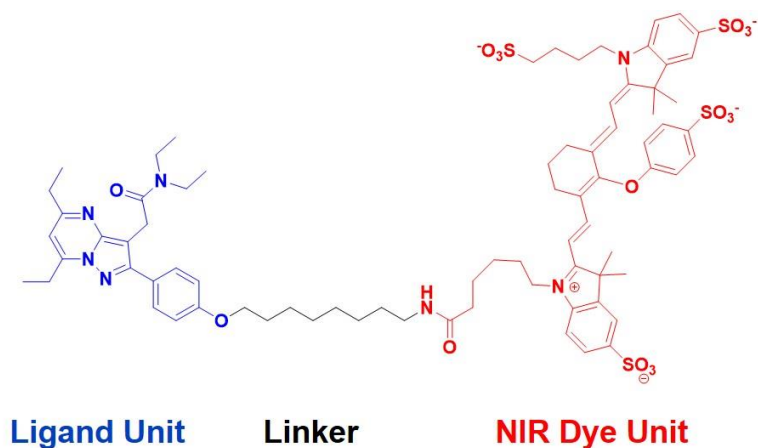
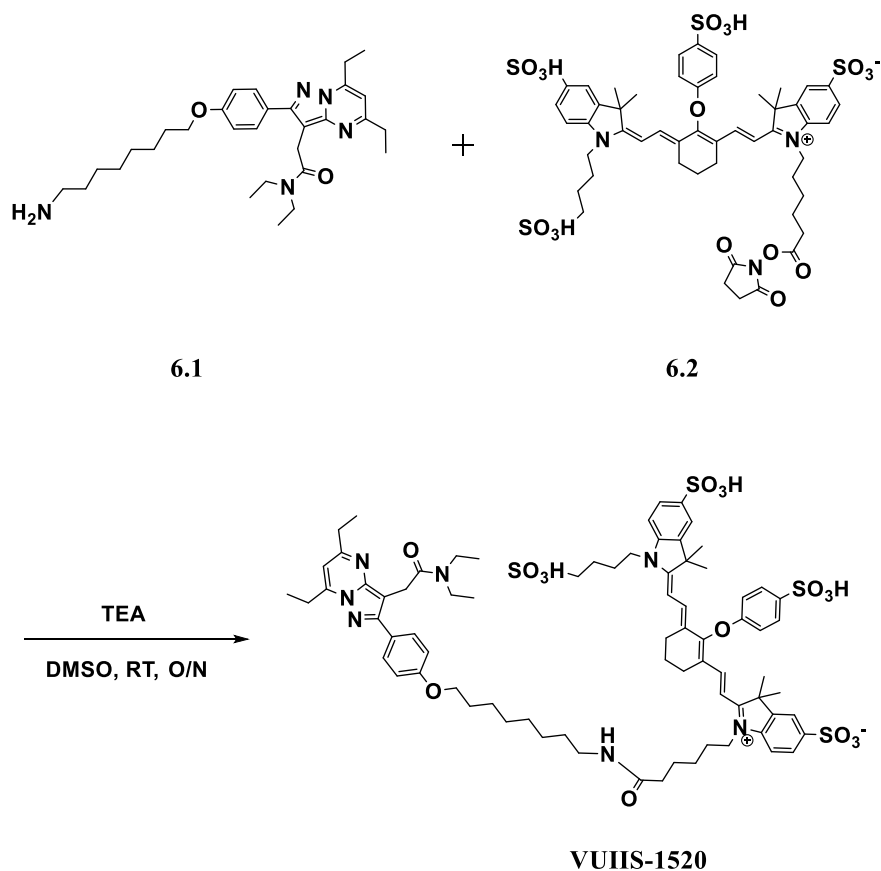


Figure 6.3.1 TSPO NIR ligand (VUIIS-1520) structure.

As shown in **Scheme 6.3.1**, compound **6.1** was accomplished following the synthetic route reported in **Chapter 4, 6.2** (LI-COR IRDye 800CW) was purchased from LI-COR Biosciences. Briefly, **6.1** and **6.2** were firstly dissolved in DMSO; TEA was subsequently added into the mixture. The reaction was protected from light, and stirred overnight at room temperature. The product was purified by HPLC and concentrated using rotary evaporation.



Scheme 6.3.1 Synthetic pathway to TSPO NIR ligand (VUIIS-1520).

6.4 NIR Probe (VUIIS-1520) Characterization

TSPO binding affinity was measured using a C6 glioma cell lysate assay previously reported (**Figure 6.4.1**). The IC_{50} value was found to be 9.83 nM, and its K_i was calculated to be 4.47 nM using Cheng and Prusoff equation: $K_i = \text{IC}_{50}/(1+[L]/K_d)$ ([L] is the concentration of ^3H -PK 11195, which was 6 nM in our experiment; the K_d for ^3H -PK 11195 was 5 nM). To our knowledge, this is the highest affinity for any TSPO NIR probe that has been reported. With the extremely large dye unit, most of the imaging probes appending NIR dye exhibit affinity in the micro-mole range. The novel probe we developed exhibits at least 60 fold higher affinity.

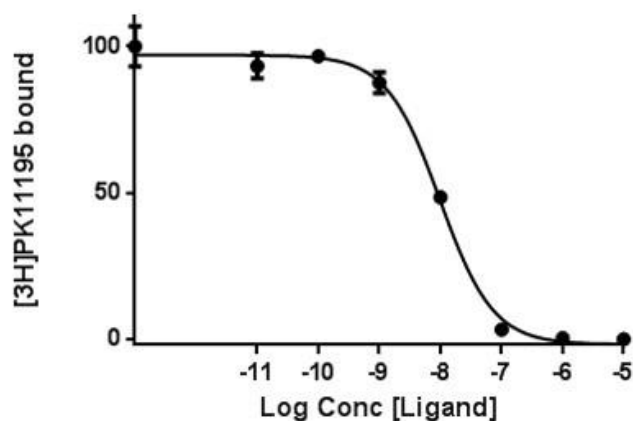


Figure 6.4.1 Binding affinity of VUIIS-1520.

Computational modeling was further applied to understand the interaction between VUIIS-1520 and TSPO. Similar to what we learned in **Chapter 4**, the TSPO ligand unit sat inside the TSPO protein pocket, which was formed by five α -helices, while the NIR dye unit protruded outside the pocket. It indicated that 8-carbon linker length was ideal to diminish the negative influence on affinity from introducing the dye unit. However, comparing with TSPO fluorescent probe **4.29**, the affinity of NIR probe was decreased by over 14-fold, which showed that the bulky NIR dye unit had a negative impact on affinity.

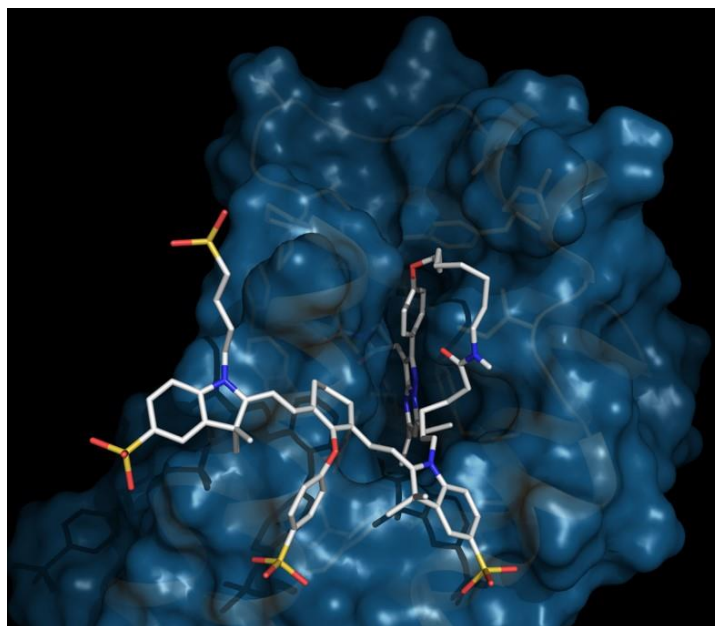


Figure 6.4.2 Computational modeling of VUIIS-1520.

6.5 Genetically Engineered Mouse Models of Pancreatic Cancer

All pancreatic cancer studies involving animals were using *Ptf1a-Cre;LSL-Kras^{G12D/+};Smad4^{fl/fl}* model. Ptf1a (Pancreas transcription factor 1 subunit alpha) is a protein which plays an essential role in the mammalian pancreatic development and differentiation. The stop codon between two *loxP* was excised using Cre-Lox recombination to activate the *Kras* mutation (*Kras^{G12D}*). It was found that the *Kras* mutation can only initiate and accelerate tumor events. *Kras* mutation generated only pancreatic intraepithelial neoplasia in ~1 year and developed very slowly to PDA.^[78-79] To develop a more aggressive mouse model, it was further combined with *Smad4^{fl/fl}* knockout,^[80] whose inactivation has been observed in invasive human PDA. The *Ptf1a-Cre;LSL-Kras^{G12D/+};Smad4^{fl/fl}* mouse model was found to develop PDA rapidly (**Figure 6.5.1**) and mouse survival of ~20 weeks.

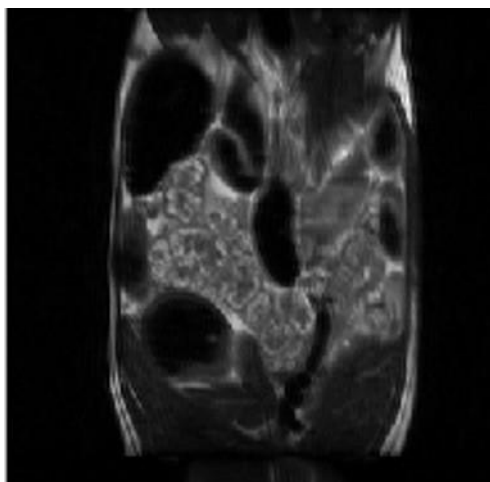


Figure 6.5.1 Advanced PDA of *Ptf1a-Cre;LSL-Kras^{G12D/+};Smad4^{fl/fl}* mouse model.

6.6 Experimental Design

The NIR probe VUIIS-1520 was dissolved in phosphate-buffered saline (PBS) and then delivered through retro-orbital injection. The mouse was imaged 18-24 hrs later.

Excised tissues were imaged using Odyssey Imaging Systems (LI-COR Biosciences) with 800 nm filter. The Maestro imaging system (CRi) was utilized to mimic optical surgical navigation.

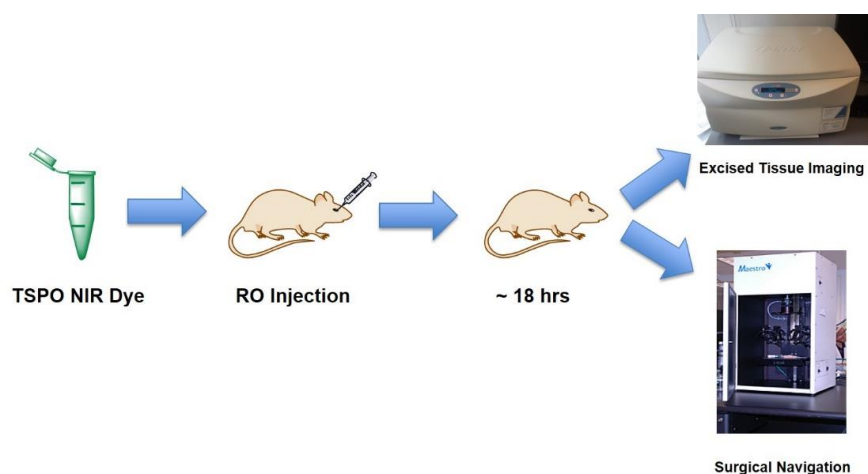


Figure 6.6.1 Experimental design of optical imaging and surgical navigation.

6.7 Optical Imaging

A group of genetically engineered mice at different age (aged 4-15 weeks) were sacrificed at certain time after probe injection, and excised tissues were imaged together with the control mice of the same age.

The signal intensity from different organs of tumor and control mice at four weeks was shown in **Figure 6.7.1**. Liver and kidney generally exhibited high optical signal intensity in both the tumor and control mouse. Lung, colon, and spleen expressed minor signal, while the heart and brain had the lowest intensity. However, the pancreas exhibited different signal intensity in tumor and control mouse. Pancreas was among the lowest signal intensity tissues in the control mouse, while exhibiting significantly strong signal in the tumor mouse.

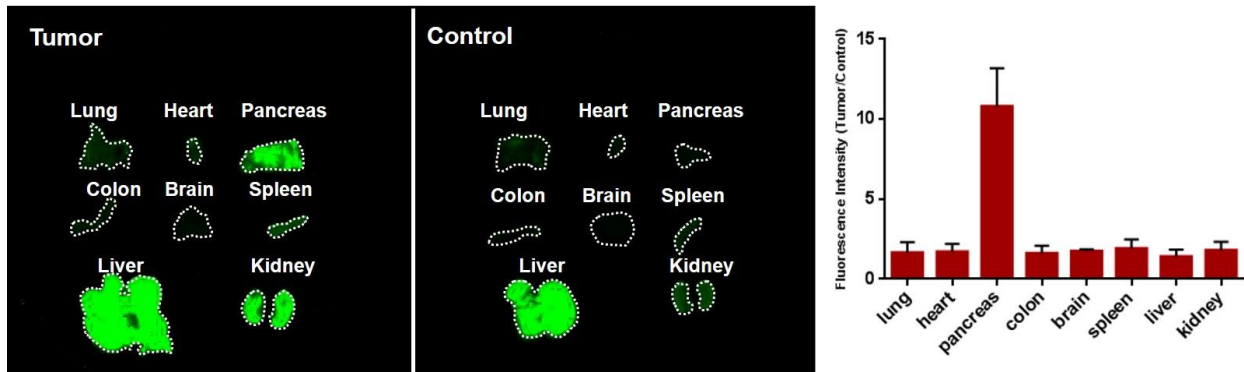


Figure 6.7.1 Excised tissue imaging by Odyssey of genetically engineered tumor mouse and control mouse aged at four weeks. The ratio of signal intensity was averaged of tissue samples collected from three tumor and three control mice.

Figure 6.7.2 showed H&E and trichrome staining, as well as immunoreactivity of pancreas from the control mouse. Similar to what we found in normal human pancreas, TSPO had low expression in the normal mouse pancreas.

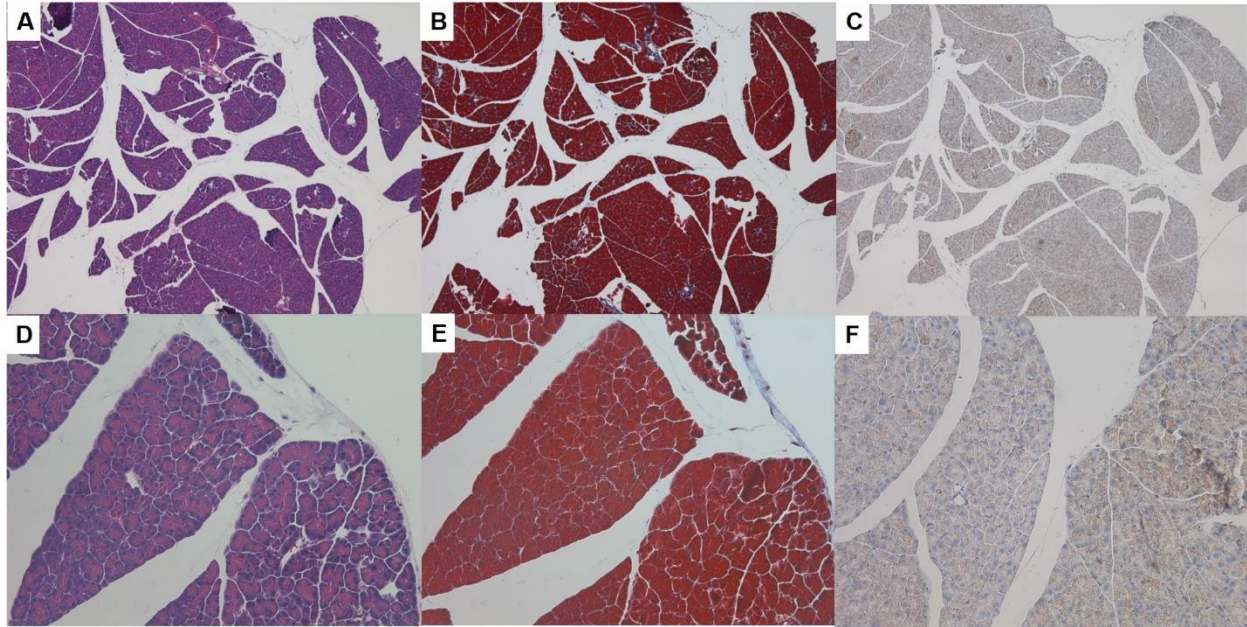


Figure 6.7.2 H&E (A and D), trichrome (B and E), and TSPO IHC (C and F) stain of pancreas from the control mouse. The magnification of A, B, and C was 5x, of D, E, and F was 10x.

Figure 6.7.3 showed the pancreatic tissue collected from four-week old *Ptf1a-Cre;LSL-Kras^{G12D/+};Smad4^{fl/fl}* genetically engineered mice treated with tamoxifen. Cystic lesions and early stage invasive tumors were observed in tissues from the pancreas, although there are surrounding histologically normal pancreas. The existence of normal cells may cause the comparably lower signal intensity in some particular areas in **Figure 6.7.1**. From TSPO immunohistochemistry staining, we found that both the cystic and early invasive lesions exhibited high signal compared with the normal cells, which confirmed the TSPO expression in early stage pancreatic cancer and the utility of *Ptf1a-Cre;LSL-Kras^{G12D/+};Smad4^{fl/fl}* mouse model. It also proved that the optical imaging can efficiently distinguish precursor lesions from normal pancreas.

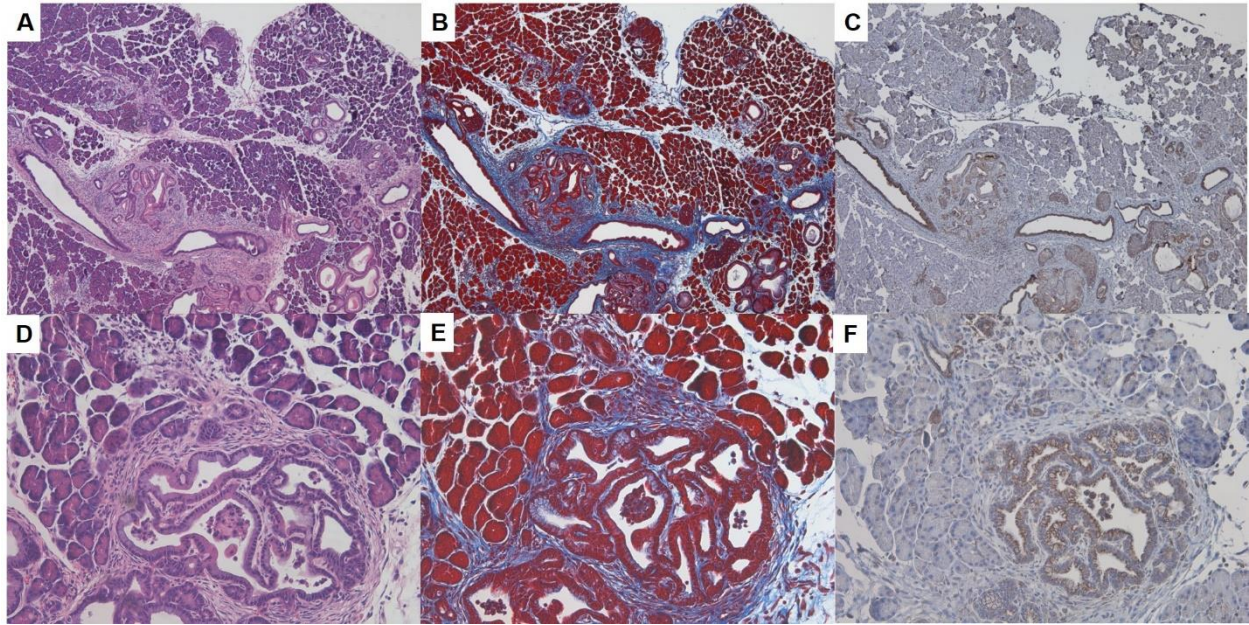


Figure 6.7.3 H&E (A and D), trichrome (B and E), and TSPO IHC (C and F) stain of pancreas from the four week genetically engineered tumor mouse. The magnification of A, B, and C was 5x, of D, E, and F was 10x.

Similar to what we found out in the four week old mice, pancreas of nine week old genetically engineered mouse also showed elevated signal intensity (**Figure 6.7.4**). Moreover, the signal intensity from the pancreas of nine week old genetically engineered mouse was not only stronger but also more uniform.

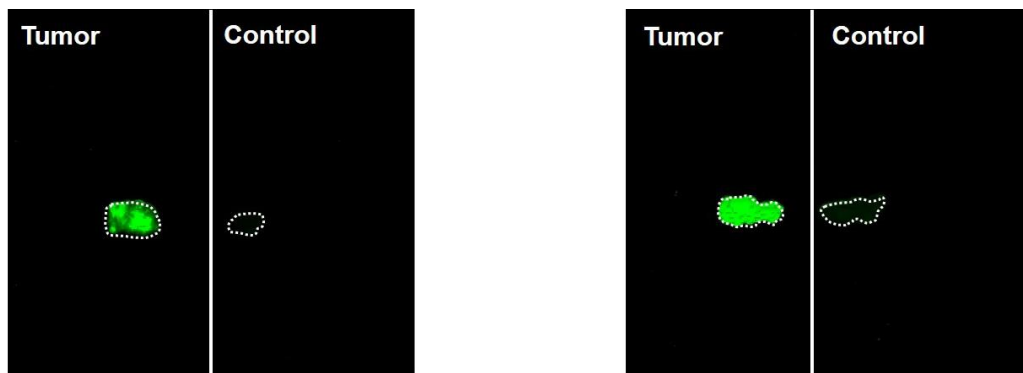


Figure 6.7.4 Excised pancreatic imaging by Odyssey of genetically engineered tumor mouse and control mouse aged at four (left) and nine (right) weeks.

Some interesting findings can be seen in the tissue staining from the pancreas of nine week old genetically engineered mouse. Fewer normal cells can be observed as the lesions became more advanced and invasive. Further, trichrome staining showed clear stroma, which was barely observed in the normal tissues. It meant that the nine week tumor mouse started to have the stromal lesion. It was also seen that TSPO had higher expression in more advanced lesions compared with early stage lesions. The histology results demonstrated that nine week tumor mouse had more advanced tumors, though few normal cells can still be observed.

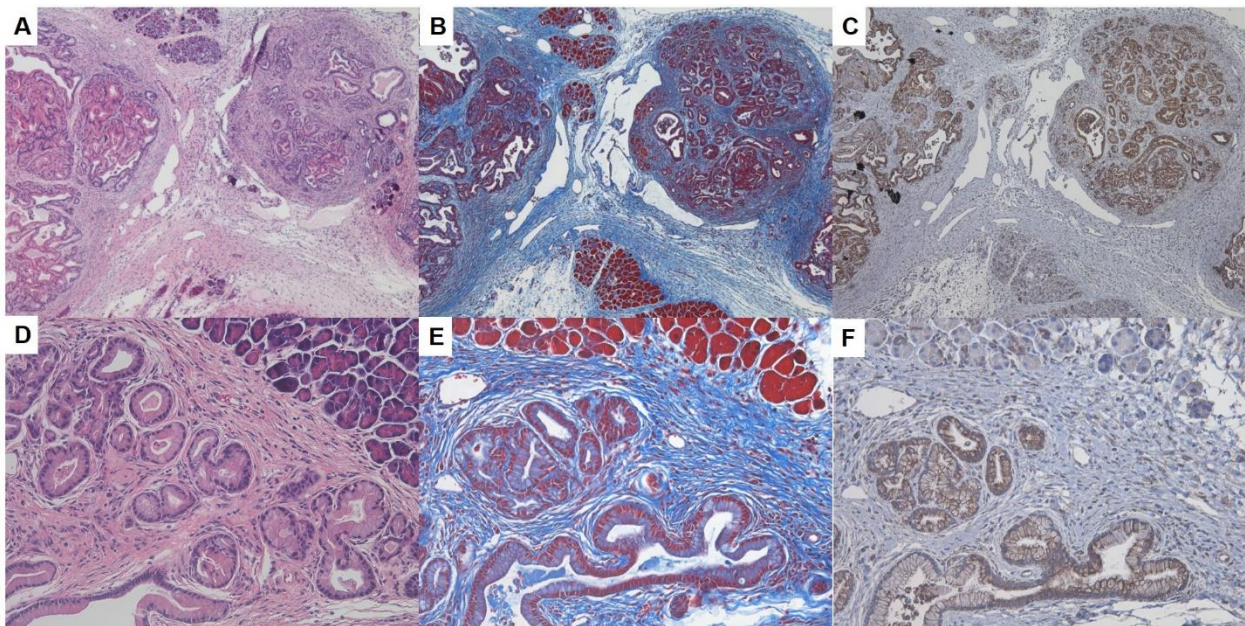


Figure 6.7.5 H&E (A and D), trichrome (B and E), and TSPO IHC (C and F) stain of pancreas from the nine week genetically engineered tumor mouse. The magnification of A, B, and C was 5x, of D, E, and F was 10x.

However, the probe had different performance in highly advanced tumor (**Figure 6.7.6**). Though the level of signal intensity of most organs did not show much difference with the younger mice, the signal in the pancreas of mice with advanced tumors was decreased. Given the strong signal intensity of pancreas in the 4-9 week old tumor mice, pancreas of fifteen week

tumor mouse had a very weak signal. More strikingly, the signal intensity was almost the same as the pancreas from the control mouse at the same age.

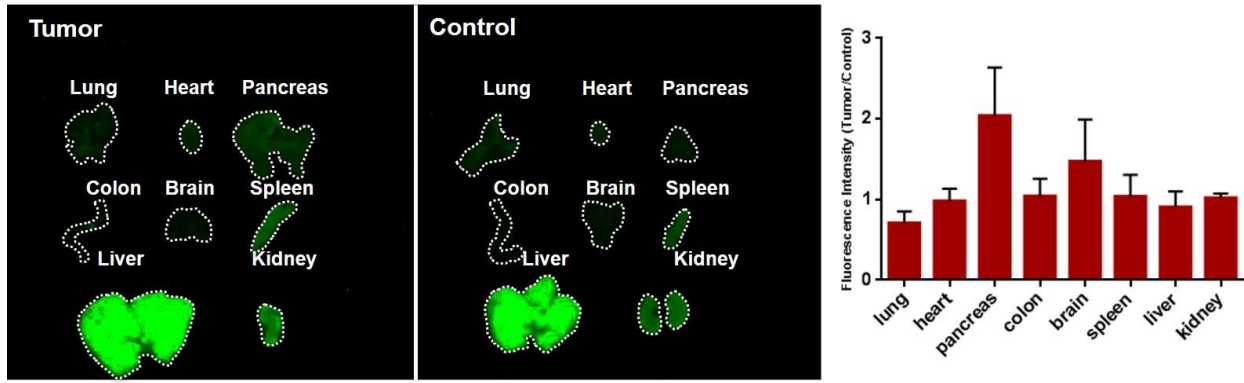


Figure 6.7.6 Excised tissue imaging by Odyssey of genetically engineered tumor mouse and control mouse aged at fifteen weeks. The ratio of signal intensity was averaged of tissue samples collected from three tumor and three control mice.

Tissue staining from fifteen week genetically engineered mouse can be seen in **Figure 6.7.7**. Apparently, the tumor had become highly advanced and invasive. The normal cells cannot be observed, advanced lesions and expanded stroma can be found throughout the slice.

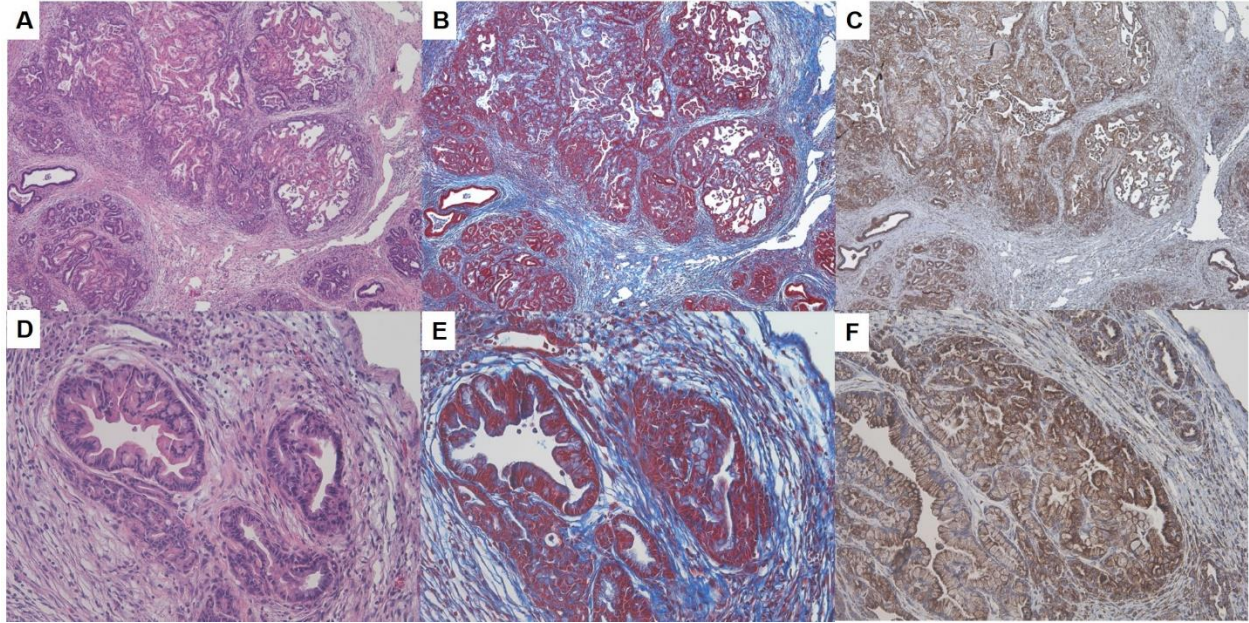


Figure 6.7.7 H&E (A and D), trichrome (B and E), and TSPO IHC (C and F) stain of pancreas from the fifteen week genetically engineered tumor mouse. The magnification of A, B, and C was 5x, of D, E, and F was 10x.

As previously reported by Komar G. *et al.*, decreased blood flow was considered as a sign of pancreatic tumor aggressiveness. It was also used to partially explain the poor effect of radiotherapy and chemotherapy in late stage pancreatic tumor treatment. Since the probe was injected through intravenous administration, the decreased blood flow made it difficult for the probe to reach the tumor, resulting in significantly reduced signal intensity.

We further examined the ratio of signal intensity between tumor and control mice in triplicate (**Figure 6.7.8**). All the other tissues except pancreas maintained a low intensity ratio ranging from young mice to old mice with advanced tumor. However, for the mice aged between four to nine weeks, the tumor mice pancreas exhibited about a 10-fold increase in signal intensity than control mice (mean ratio of 10.783 for four week mice, and 9.645 for nine week mice), but the mean ratio dropped to 2-fold for fifteen week mice with advanced tumor.

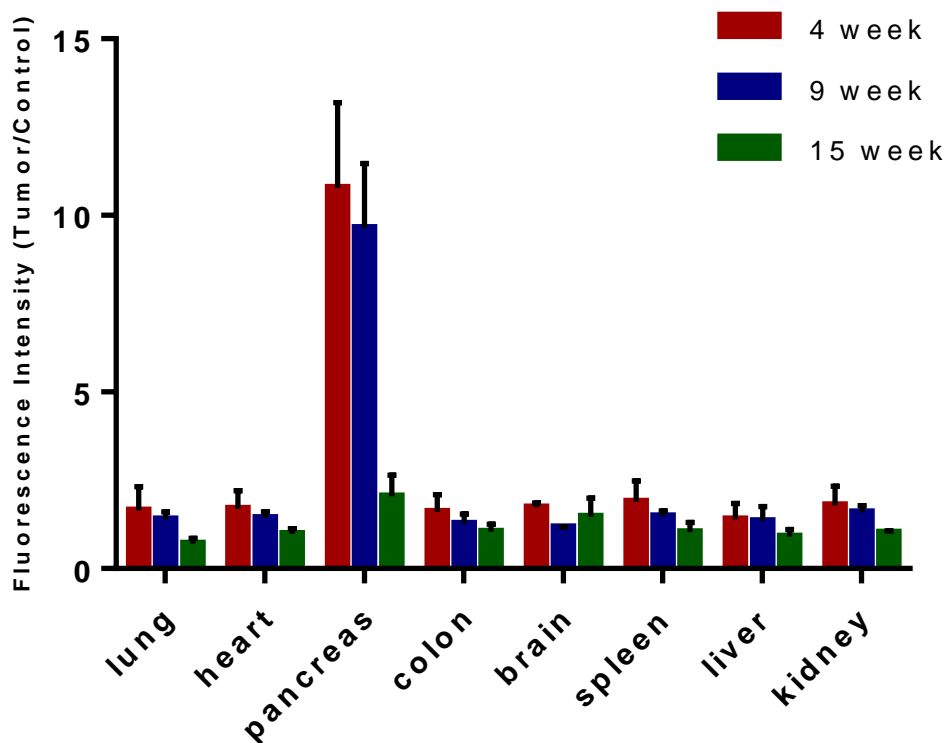


Figure 6.7.8 Ratio of signal intensity between tumor mice and control mice at different age.

Interestingly, it was also found that nine week mice generally exhibited lower signal intensity ratio than four week mice. It may be caused by decreased blood flow when the pancreatic tumor became more advanced. Another factor may come from the diminished TSPO expression. As previously shown in **Figure 6.2.2**, TSPO expression was lower in the more advanced pancreatic tumor, although the reason behind this phenomenon is still unclear.

6.8 Free Dye Imaging

To further analyze the specificity of the conjugated TSPO NIR probe VUIIS-1520, the retention of the unconjugated free dye (LI-COR IRDye 800CW) was used to compare with conjugated probe in tumor mice (**Figure 6.8.1**). After injection and circulation for the same time,

the free dye didn't accumulate in the pancreas of the tumor mice and more than 14-fold decrease in signal intensity was observed comparing with the conjugated probe. Unbound dye also cleared more rapidly through the mouse body. It was seen that in all the examined tissues, the free dye imaging exhibited decreased signal intensity.

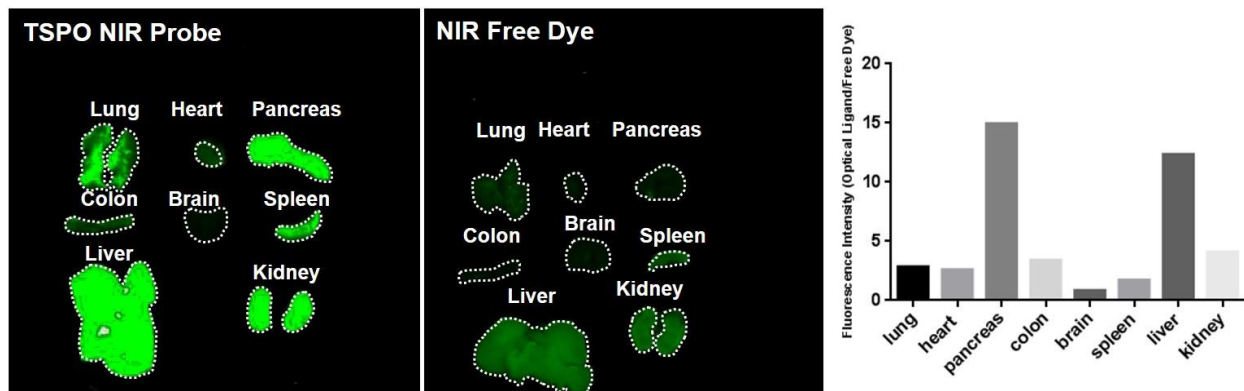


Figure 6.8.1 Specificity of conjugated TSPO NIR probe. Images of excised tissues from nine weeks tumor mice injected with VUIIS-1520 (left), unconjugated LI-COR IRDye 800CW (middle), and the ratio of signal intensity (right).

Free dye images in the tumor and control mice further illustrated that unconjugated dye was not able to bind specifically to the target (**Figure 6.8.2**), since signal intensity was comparable in both tumor and normal tissues, which can be further confirmed by comparing the ratio of intensity from injection of free dye and conjugated probe.

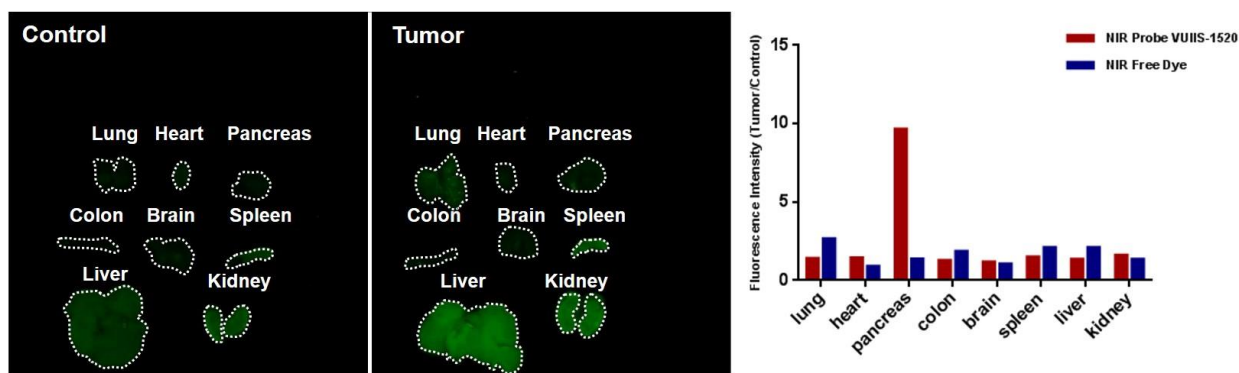


Figure 6.8.2 Images of excised tissues of free dye injection into the control mouse (left) and tumor mouse (middle). The right image compared the ratio of signal intensity from injection of VUIIS-1520 and free dye.

As shown in **Figure 6.8.1**, malignant pancreas showed dramatically elevated fluorescent signal by injecting TSPO selected ligand VUIIS-1520, which was caused by overexpressed TSPO in pancreas tumor. Interestingly, however, the TSPO NIR probe also had much stronger signal than free dye in the normal liver of tumor mice. From prior research, liver exhibited only modest expression and should not behave such differently. To further understand the probe behavior in liver, both VUIIS-1520 probe and free dye were injected into control mice (**Figure 6.8.3**). We observed that in both tumor and control mice, the ratio of signal intensity in liver between TSPO optical ligand and free dye was almost the same, which indicated that the higher signal intensity of the NIR probe in the liver of tumor mice was caused by the circulation. Since the free dye and the NIR probe VUIIS-1520 have different chemical structure, and the probe is larger than the free dye, it might take more time to be cleared from the liver. By comparing the signal intensity ratio in tumor and control mice, it can also be found that the only difference coming from TSPO overexpressed pancreas of tumor mice. Therefore, the probe accumulation in malignant pancreas was specifically associated with biomarker expression in tumor.

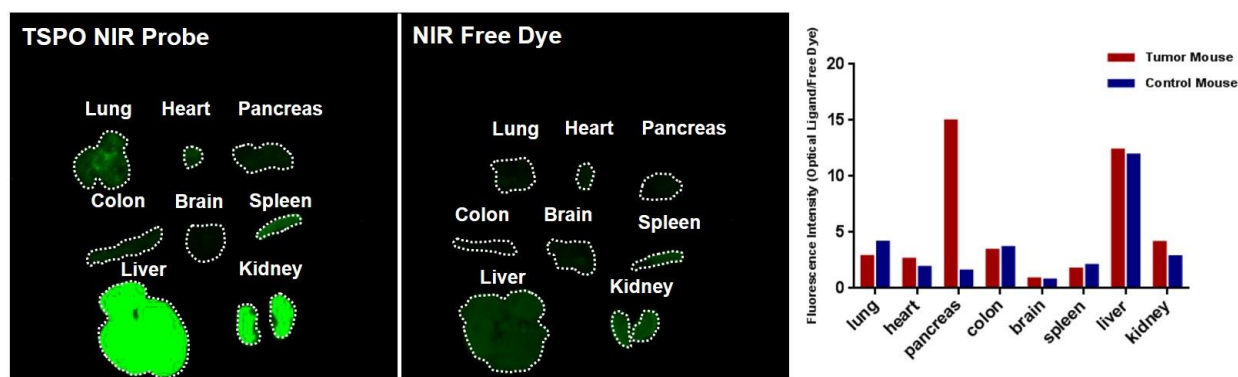


Figure 6.8.3 Images of excised tissues from control mice injected with VUIIS-1520 (left), unconjugated LI-COR IRDye 800CW (middle), and the ratio of signal intensity (right).

6.9 Displacement

Unlike the displacement in the PET imaging, where we can treat with the cold compound that is almost the same as the radioactive tracer with only minor difference on the isotope, whose influence on pharmacokinetics can be ignored; in the displacement study of optical imaging, the “cold” compound (the parent ligand) was different from the imaging probe, which makes it difficult to effectively displace or block the optical probe.

A displacement experiment was performed by treating the mice with VUIIS-1520 and its parent ligand (**Figure 6.9.1**). Though the parent ligand cannot totally displace the optical probe, a decrease in signal intensity can still be observed in the excised tissue imaging.

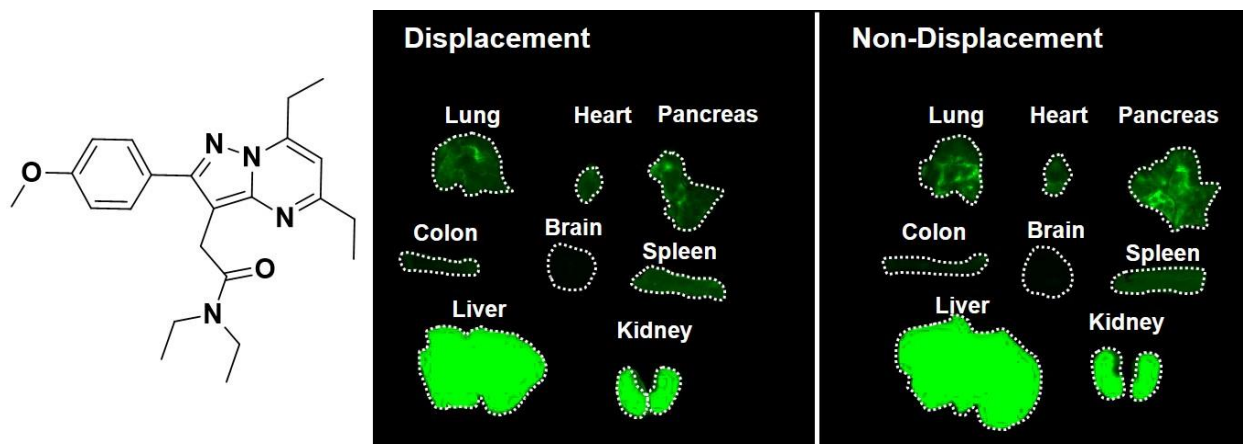


Figure 6.9.1 Displacement of VUIIS-1520 with its parent ligand (left). Images of excised tissues with (middle) or without (right) displacement.

6.10 Optical Surgical Navigation

As discussed earlier, another application of optical probe is in surgical navigation. To further study the application of our newly developed TSPO NIR probe, VUIIS-1520 was injected into control and tumor mice through intravenous and Maestro Imaging System was used to mimic the surgery.

Figure 6.10.1 showed that the probe didn't accumulate in normal pancreas, and the pancreas cannot be distinguished from the background. Liver was the only organ that can be seen in the surgery of control mouse. In the tumor mouse surgery, however, pancreas emitted strong optical signal and was well-differentiated from the background, which indicated that we can utilize the new TSPO NIR probe in surgery to help the surgeons to precisely locate and remove the pancreatic tumor.

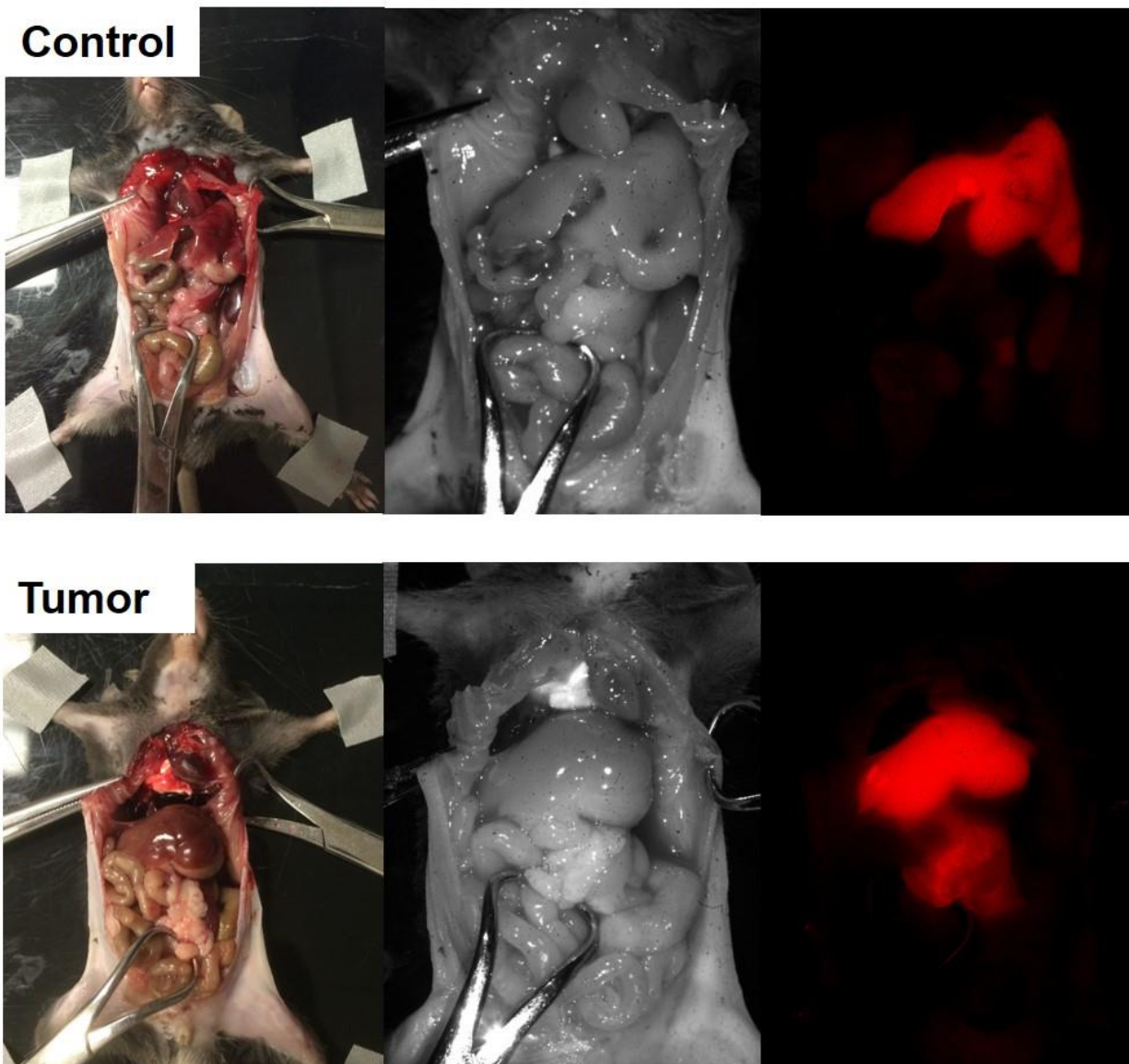


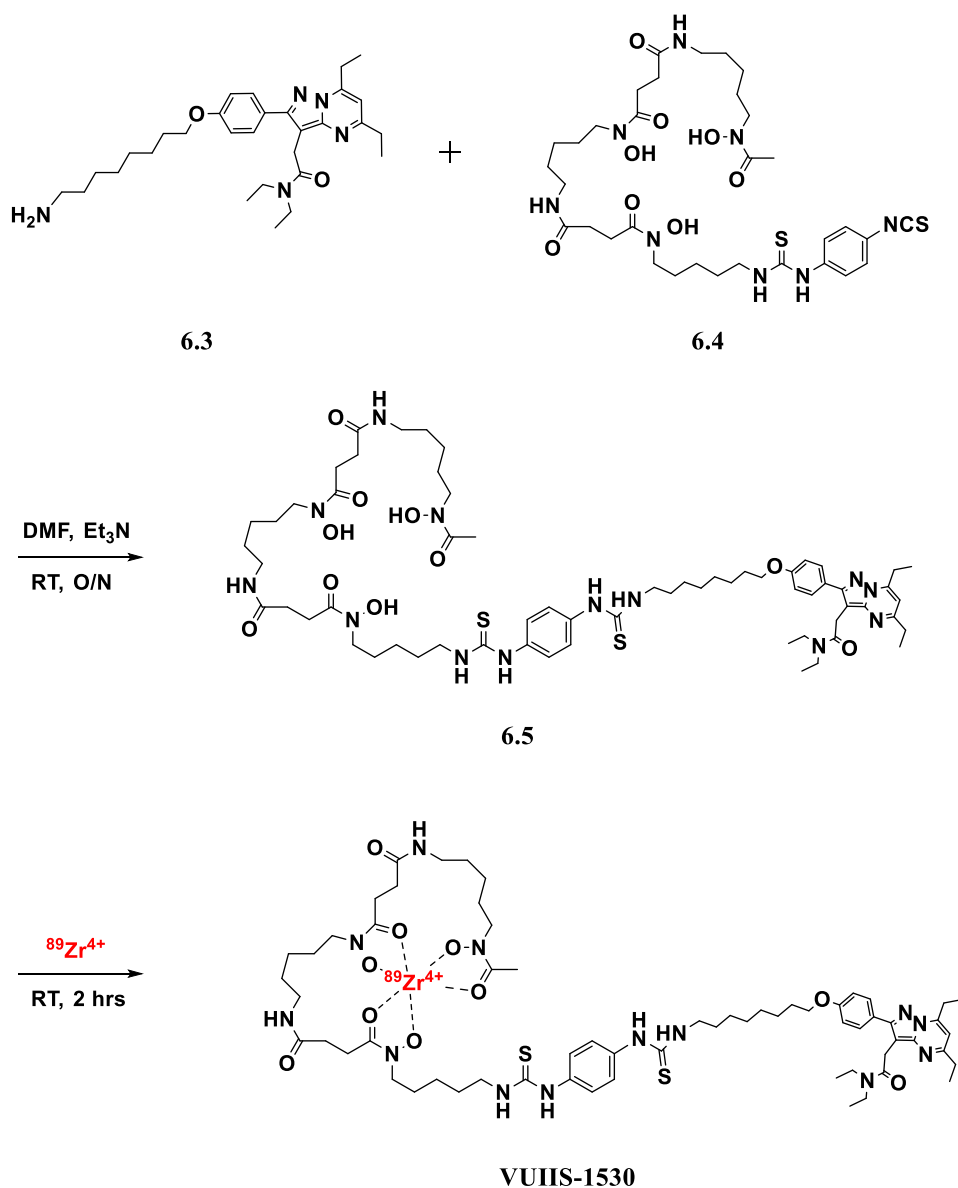
Figure 6.10.1 Optical surgical navigation of pancreatic tumor by using VUIIS-1520.

6.11 Chemistry and Radiochemistry of Zr-89 PET Tracer

The synthetic route and radiolabeling was shown in **Scheme 6.11.1**. Starting from previously synthesized TSPO ligand unit **6.3** (**Chapter 4**), precursor **6.5** for the radiolabeling was formed by reacting of **6.3** with chelator DFO (**6.4**) in DMSO overnight at room temperature,

in the presence of triethylamine to provide a basic environment. Precursor **6.5** was then purified by HPLC.

$^{89}\text{ZrCl}_4$ was purchased from PerkinElmer in oxalic acid solution. Na_2CO_3 solution was added to adjust the pH to 9. The mixture was reacted at room temperature for 2 hrs. Subsequently, the compound was purified with Sep-Pak C18 cartridge and dried with N_2 gas flow to generate the TSPO Zr-89 ligand VUIIS-1530.



Scheme 6.11.1 Radiosynthesis of TSPO probe VUIIS-1530.

6.12 Binding Affinity and Computational Modeling

The binding affinity of VUIIS-1530 was measured with C6 glioma cell lysate assay. Its K_i value was found to be 32.3 nM ($IC_{50} = 71.06$ nM). VUIIS-1530 shared the same TSPO ligand unit and linker with TSPO NIR probe VUIIS-1520, but the binding affinity exhibited over 15-fold decrease. It indicated that the DFO chelator with Zr^{+} had a more negative impact on affinity than NIR dye. However, affinity exhibited in the nanomolar range was still very promising for imaging.

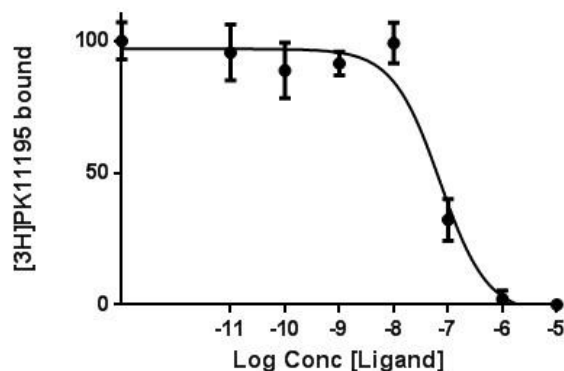


Figure 6.12.1 Binding affinity of VUIIS-1530.

Computational modeling was carried out to evaluate the interaction between the tracer and protein (**Figure 6.12.2**). The TSPO ligand unit was found to sit inside the protein pocket, while the DFO and Zr-89 were protruding outside by the 8-carbon linker. Unlike modeling of NIR probe VUIIS-1520, where the large dye unit was spread and took space close to the protein pocket, the DFO with Zr-89 of VUIIS-1530 formed a very steric bulky cyclical structure and was further away from the protein. That might result in the comparably lower affinity of the PET tracer.

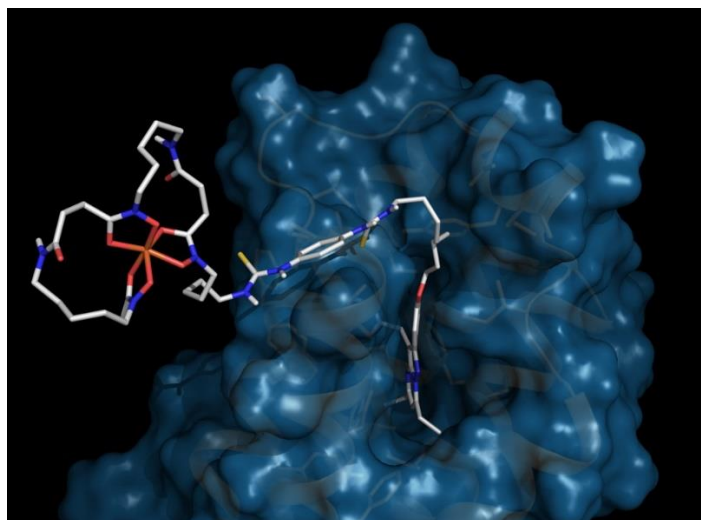


Figure 6.12.2 Computational modeling of VUIIS-1530 interaction with TSPO.

6.13 Autoradiography

Autoradiography can determine the localization and distribution of radiolabeled ligand in the tissue sections. Herein, autoradiography was performed in two ways.

Figure 6.13.1 showed the autoradiograph of the pancreas after the injection of VUIIS-1530. It was noted that the tracer accumulated in the pancreas of the six weeks tumor mouse, while the pancreas from the control mouse didn't show elevated signal intensity. Similar to what we found in the near-infrared dye imaging, the twelve weeks advanced tumor didn't exhibit high tracer uptake due to decreased blood flow inside the tumor. Instead of retro-orbital injection, the injection through peritoneum was not able to circulate the tracer into the pancreas, and the tissue cannot be distinguished from the background.

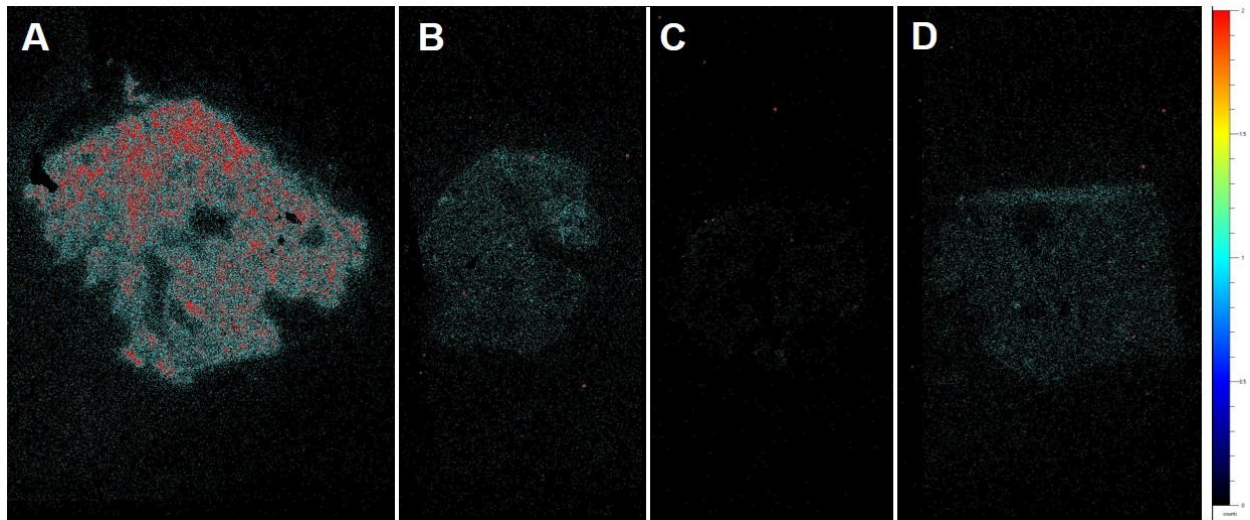


Figure 6.13.1 Autoradiograph of pancreas. Six week tumor mouse (A), twelve week tumor mouse (B), and control mouse (D) with retro orbital injection of VUIIS-1530; six week tumor mouse with intraperitoneal injection of VUIIS-1530 (C).

We further utilized the whole mouse cross sectional imaging to analyze the tracer distribution. After the mouse was sacrificed, the mouse was put into a tube filled with water and frozen in the cooling bath. The cross section of the mouse was sliced subsequently. It was found that the tracer was accumulated in pancreatic tumor, liver, and spleen tissues. It had medium signal strength in the stomach, and low in the intestine.

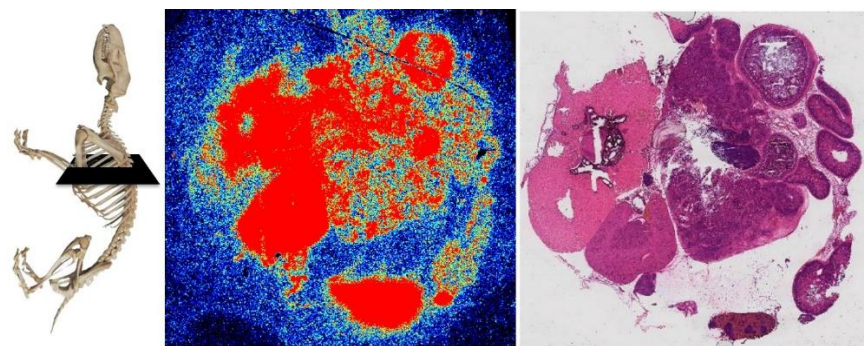


Figure 6.13.2 Autoradiography of cross section of tumor mouse.

6.14 PET Imaging

PET imaging of VUIIS-1530 was performed in the pancreatic tumor mouse. As shown in **Figure 6.14.1**, VUIIS-1530 was observed to accumulate in the tumor. Similar to the TSPO NIR probe, the PET tracer was also found to have elevated expression in the liver and kidney.

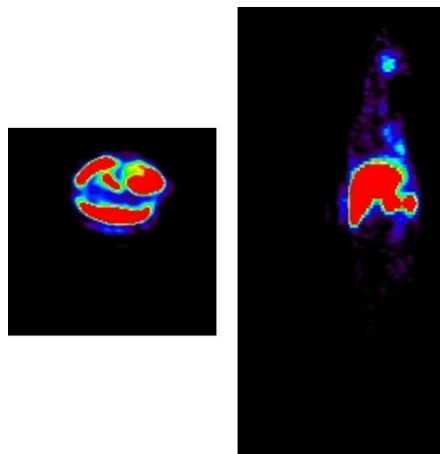


Figure 6.14.1 PET imaging of VUIIS-1530. Transverse (left) and sagittal (right) slices of a representative tumor mouse are shown.

6.15 Conclusion

In summary, we establish the connection between TSPO expression with both invasive, highly advanced pancreatic cancer and pre-malignant pancreatic lesions, and develop a novel near-infrared probe which exhibited high binding affinity to TSPO. The probe was found to be accumulated in pancreatic tumor instead of normal pancreas, and was very promising in optical surgical navigation. Further, a small molecule PET tracer functionalized with Zr-89 was developed for the first time and showed promising in the pancreatic cancer PET imaging. We envision these probes can help with pancreatic cancer diagnosis and surgery, and possibly be used in other TSPO related disease, including colon and breast cancer.

6.16 Method and Materials

TSPO Immunohistochemistry

The sample slice was incubated with primary antibody Novus NB100-41398 at 4°C overnight and then incubated with secondary antibody Biocare Medical GHP516 for 10 mins at room temperature.

Excised Tissue Imaging

TSPO NIR Probe VUIIS-1520 or free dye was dissolved in phosphate-buffered saline (PBS) to make a final concentration of 0.1 μM . 200 μL of the solution was injected into the mice through retro-orbital. After about 18 hrs, the mice were sacrificed and the tissues were washed in PBS buffer. Excised tissues were imaged using Odyssey Imaging Systems (LI-COR Biosciences) under the 800 nm filter and intensity of 5.

Displacement

Displacement experimental was carried out by injecting 200 μL VUIIS-1520 solution at the concentration of 0.1 μM and 200 μL of its parent ligand 2-(5,7-diethyl-2-(4-methoxyphenyl)pyrazolo[1,5-*a*]pyrimidin-3-yl)-*N,N*-diethylacetamide at 1 mM. The mouse was sacrificed after 18 hrs and imaged the excised tissues.

Optical Surgical Navigation

Optical surgical navigation was carried out on Maestro imaging system (CRi). 200 μL of 10 μM VUIIS-1520 was injected into the mice. After 18hrs, the surgery was performed with Maestro using 735 nm excitation filter and 800 nm emission filter.

Radiochemistry.

$^{89}\text{ZrCl}_4$ in oxalic acid solution was purchased from PerkinElmer or IBA. The precursor with DFO conjugated was dissolved in EtOH. 4-8 mCi $^{89}\text{ZrCl}_4$ solution was pipetted into

precursor solution and mixed. 2M Na₂CO₃ aqueous solution was added to the mixture until the pH was adjusted to 7.5-8. The reaction mixture was stirred at room temperature for 2 hrs.

Waters C18 Sep-pak plus cartridge was conditioned with 5 mL EtOH followed by 20 mL of water. The reaction mixture was pushed through the cartridge. Unreacted free isotope was washed out with 2 mL water, while the labeled ligand stayed in the cartridge. After that, the product was eluted with 2 mL EtOH (200 proof) directly into the collection vial. The tracer solution was dried down under a gentle N₂ gas flow and reformulated with 10% EtOH/water, and final volume was 100-200 µL. TLC was used to characterize the labeling efficiency with the product primarily stayed at the origin.

Cross Section Autoradiography

The mouse was put into a 50 mL centrifuge tube after sacrifice. The tube was then filled with water, and frozen with dry ice/isopropanol bath for about 30 mins. The central part of the mouse with the pancreas was chosen and cut with saw.

CHAPTER 7

CONCLUSION

The overall goal of this dissertation is to explore the development and utility of TSPO ligands for rapid tracer discovery and as precision imaging diagnostics of cancer. Several modalities of molecular imaging probes have been developed, including optical, PET, and SPECT probes.

Starting from our previously optimized structure on the 5, 6, and 7 positions of a pyrazolopyrimidine, DPA713, we further elaborate on the pyrazolopyrimidine structure activity relationships related to *N,N*-disubstitutions of the terminal acetamide. In doing so, a novel synthetic route was developed for a rapid library expansion approach. A variety of novel pyrazolopyrimidine TSPO candidate ligands were further synthesized, bearing alkyl, alicyclic, aryl, and heterocyclic pendant acetamides. Several new chemical probes were discovered with good binding properties, suitable lipophilicity and protein binding to potentially serve as TSPO imaging tracers. For example, the heterozygous phenyl-ethyl substitution pattern resulted in a novel ligand with pico-molar activity. It was also observed that acetamide substitution with ethyl group was generally well-tolerated in combination with many other *N*-substitutions on the acetamide.

Our next approach was to develop a novel fluorescent ligand that is able to accelerate tracer discovery. Based upon our optimized TSPO ligand structure, a series of TSPO fluorescent probes were developed through connecting of ligand unit with a fluorescent dye FITC. By changing the linker length from two to eight carbons, a new TSPO probe with the highest binding affinity amongst TSPO fluorescent probes reported to date was discovered. The probe

also demonstrated specific binding to mitochondria and imaged tumor cells very well. More importantly, the fluorescent probe can be a good candidate to replace ^3H -PK 11195 in the competitive binding assay. The long half-life radioactive material ^3H -PK 11195 was routinely used in the screening of binding affinity of new ligands, which is expensive and poses a radiation hazard. The new assay using the fluorescent probe was fast and inexpensive, and was comparable to the current method. We further used the new assay to screen a library of compounds that were selected from the initial virtual screen of the ZINC library using our pharmacophore model. Several probes with novel chemical scaffold were found to be very promising with structural optimization.

By translating what was learned in the structure activity relationships of *N*-acetamide substituted pyrazolopyrimidines ligands and fluorescent probes, we showed the potential of using the TSPO near-infrared probe and Zr-89 PET tracer for pancreatic cancer diagnosis and surgical navigation. We firstly established the connection between TSPO expression and pancreatic cancer from analyzing the TMAs collected from 155 patients at VUMC. TSPO elevation was observed in both highly advanced pancreatic cancer and pre-malignant lesions. A near-infrared TSPO probe was developed by conjugating TSPO ligand with Li-Cor NIR dye 800CW. The probe exhibited high binding affinity to TSPO and accumulated in the pancreas of genetically engineered tumor mouse. The probe was also able to aid in optical surgical navigation. We anticipate that it can help surgeons to precisely locate and remove the tumor in the surgery of pancreatic cancer or other TSPO-related cancer. Based upon similar ligand unit and linker structure, a small molecule PET tracer using Zr-89 was successfully developed and imaged the pancreatic cancer for the first time.

In conclusion, this dissertation illustrates that TSPO molecular imaging probes represent an opportunity to promote rapid tracer discovery, diagnose pancreatic cancer, and aid in surgical navigation. We anticipate that these results will expand opportunities to deploy TSPO ligands to image and treat diseases especially relevant to peripheral tissues.

APPENDIX

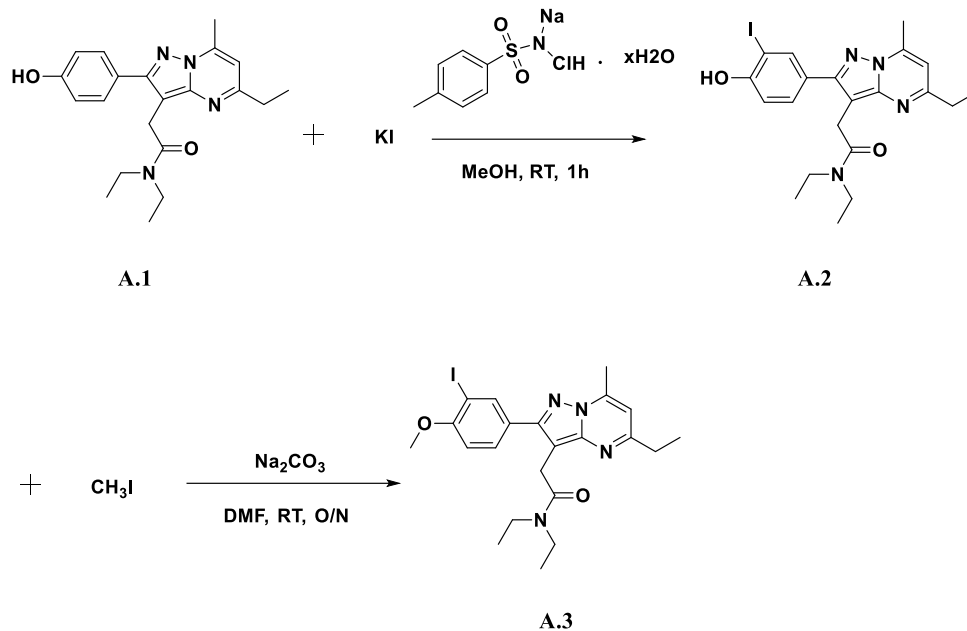
Single-photon emission computed tomography (SPECT) is another molecular imaging technique. Similar to PET, SPECT also uses radioactive tracers for imaging. However, PET tracers emit positron that will generate two gamma photons after annihilation with electrons, while SPECT tracers emit gamma photons directly. Since PET will produce more radiation information, it has higher resolution than SPECT. However, SPECT uses long half-life isotopes and is less expensive than PET.

Table A.1.1 Isotopes used in SPECT

Isotope	Half-life
I-123	13.2 hours
Ga-67	3.3 days
Sn-117	14 days
I-125	59 days
Tl-201	12.23 days
In-111	2.8 days

In addition to the PET and optical imaging probes developed in previous chapters, we also developed a novel synthetic pathway for the synthesis of TSPO SPECT tracer.

Scheme A.1.1 showed the synthesis of cold SPECT probe appended iodine. Starting from previously reported compound **A.1**, iodination was accomplished by reacting of **A.1** with KI and chloramine-T hydrate which can form iodine monochloride (ICl). In the second step, **A.2** was reacted with methyl iodide in DMF, in the presence of Na₂CO₃ overnight.



Scheme A.1.1 Synthetic route to TSPO SPECT probe.

To introduce radioactive isotope of iodine, it required a two-step reaction. Since the second step is an over-night reaction, a long half-life isotope is needed, such as ^{125}I . However, long half-life isotope can bring in many troubles and increase the risk when the contamination happens. If we want to use shorter half-life isotope ^{123}I , we need to further optimize the second step of the reaction.

It was observed that when we used a stronger base NaH to replace Na_2CO_3 in the second step, the reaction time can be significantly decreased. One hour reaction yield was 30%, and two hour yield can reach to 50%, which was ideal for the radiosynthesis.

REFERENCES

1. Papadopoulos, V., et al., *Translocator protein (18kDa): new nomenclature for the peripheral-type benzodiazepine receptor based on its structure and molecular function*. Trends in pharmacological sciences, 2006. 27(8): p. 402-409.
2. Papadopoulos, V. and L. Lecanu, *Translocator protein (18 kDa) TSPO: an emerging therapeutic target in neurotrauma*. Experimental neurology, 2009. 219(1): p. 53-57.
3. Maaser, K., et al., *Specific ligands of the peripheral benzodiazepine receptor induce apoptosis and cell cycle arrest in human colorectal cancer cells*. British journal of cancer, 2001. 85(11): p. 1771.
4. Deane, N.G., et al., *Targeted imaging of colonic tumors in smad3^{-/-} mice discriminates cancer and inflammation*. Molecular cancer research, 2007. 5(4): p. 341-349.
5. Han, Z., et al., *Expression of peripheral benzodiazepine receptor (PBR) in human tumors: relationship to breast, colorectal, and prostate tumor progression*. Journal of Receptors and Signal Transduction, 2003. 23(2-3): p. 225-238.
6. Nagler, R., et al., *Oral cancer, cigarette smoke and mitochondrial 18kDa translocator protein (TSPO)—In vitro, in vivo, salivary analysis*. Biochimica et Biophysica Acta (BBA)-Molecular Basis of Disease, 2010. 1802(5): p. 454-461.
7. Venturini, I., et al., *Up-regulation of peripheral benzodiazepine receptor system in hepatocellular carcinoma*. Life sciences, 1998. 63(14): p. 1269-1280.
8. Carmel, I., et al., *Peripheral-type benzodiazepine receptors in the regulation of proliferation of MCF-7 human breast carcinoma cell line*. Biochemical pharmacology, 1999. 58(2): p. 273-278.

9. Decaudin, D., et al., *Peripheral benzodiazepine receptor ligands reverse apoptosis resistance of cancer cells in vitro and in vivo*. *Cancer research*, 2002. 62(5): p. 1388-1393.
10. Starosta-Rubinstein, S., et al., *Imaging of a glioma using peripheral benzodiazepine receptor ligands*. *Proceedings of the National Academy of Sciences*, 1987. 84(3): p. 891-895.
11. Maaser, K., et al., *Overexpression of the peripheral benzodiazepine receptor is a relevant prognostic factor in stage III colorectal cancer*. *Clinical cancer research*, 2002. 8(10): p. 3205-3209.
12. Wyatt, S.K., et al., *Molecular imaging of the translocator protein (TSPO) in a pre-clinical model of breast cancer*. *Molecular Imaging and Biology*, 2010. 12(3): p. 349-358.
13. Manning, H.C., et al., *Targeted molecular imaging agents for cellular-scale bimodal imaging*. *Bioconjugate chemistry*, 2004. 15(6): p. 1488-1495.
14. Tang, D., et al., *Synthesis and Structure–Activity Relationships of 5, 6, 7-Substituted Pyrazolopyrimidines: Discovery of a Novel TSPO PET Ligand for Cancer Imaging*. *Journal of medicinal chemistry*, 2013. 56(8): p. 3429-3433.
15. Bailey, D.L., et al., *Positron emission tomography*. 2005: Springer.
16. Suetens, P., *Fundamentals of medical imaging*. 2009: Cambridge university press.
17. Trapani, A., et al., *Targeting of the translocator protein 18 kDa (TSPO): a valuable approach for nuclear and optical imaging of activated microglia*. *Bioconjugate chemistry*, 2013. 24(9): p. 1415-1428.

18. Kobayashi, H., et al., *New Strategies for Fluorescent Probe Design in Medical Diagnostic Imaging*. Chemical Reviews, 2010. 110(5): p. 2620-2640.
19. Pacák, J., Z. Točík, and M. Černý, *Synthesis of 2-deoxy-2-fluoro-D-glucose*. Journal of the Chemical Society D: Chemical Communications, 1969(2): p. 77-77.
20. Ido, T., et al., *Labeled 2-deoxy-D-glucose analogs. 18F-labeled 2-deoxy-2-fluoro-D-glucose, 2-deoxy-2-fluoro-D-mannose and 14C-2-deoxy-2-fluoro-D-glucose*. Journal of Labelled Compounds and Radiopharmaceuticals, 1978. 14(2): p. 175-183.
21. Vaughan, D., *A vital legacy: Biological and environmental research in the atomic age*. 1997, Lawrence Berkeley National Lab., CA (United States).
22. Som, P., et al., *A fluorinated glucose analog, 2-fluoro-2-deoxy-D-glucose (F-18): nontoxic tracer for rapid tumor detection*. J Nucl Med, 1980. 21(7): p. 670-675.
23. Chang, J.M., et al., *False positive and false negative FDG-PET scans in various thoracic diseases*. Korean Journal of Radiology, 2006. 7(1): p. 57-69.
24. Anzini, M., et al., *Molecular Basis of Peripheral vs Central Benzodiazepine Receptor Selectivity in a New Class of Peripheral Benzodiazepine Receptor Ligands Related to Alpidem*. Journal of Medicinal Chemistry, 1996. 39(21): p. 4275-4284.
25. Kozikowski, A.P., et al., *Synthesis and biology of a 7-nitro-2, 1, 3-benzoxadiazol-4-yl derivative of 2-phenylindole-3-acetamide: a fluorescent probe for the peripheral-type benzodiazepine receptor*. Journal of medicinal chemistry, 1997. 40(16): p. 2435-2439.
26. Galiegue, S., N. Tinel, and P. Casellas, *The peripheral benzodiazepine receptor: a promising therapeutic drug target*. Current medicinal chemistry, 2003. 10(16): p. 1563-1572.

27. Veenman, L., Y. Shandalov, and M. Gavish, *VDAC activation by the 18 kDa translocator protein (TSPO), implications for apoptosis*. Journal of bioenergetics and biomembranes, 2008. 40(3): p. 199-205.
28. Chen, M.-K. and T.R. Guilarte, *Translocator protein 18 kDa (TSPO): molecular sensor of brain injury and repair*. Pharmacology & therapeutics, 2008. 118(1): p. 1-17.
29. Maaser, K., et al., *Up-regulation of the peripheral benzodiazepine receptor during human colorectal carcinogenesis and tumor spread*. Clinical cancer research, 2005. 11(5): p. 1751-1756.
30. Fafalios, A., et al., *Translocator protein blockade reduces prostate tumor growth*. Clinical Cancer Research, 2009. 15(19): p. 6177-6184.
31. Black, K.L., K. Ikezaki, and A.W. Toga, *Imaging of brain tumors using peripheral benzodiazepine receptor ligands*. Journal of neurosurgery, 1989. 71(1): p. 113-118.
32. Miettinen, H., et al., *Expression of peripheral-type benzodiazepine receptor and diazepam binding inhibitor in human astrocytomas: relationship to cell proliferation*. Cancer research, 1995. 55(12): p. 2691-2695.
33. Hardwick, M., et al., *Peripheral-type benzodiazepine receptor levels correlate with the ability of human breast cancer MDA-MB-231 cell line to grow in scid mice*. International journal of cancer, 2001. 94(3): p. 322-327.
34. Le Fur, G., et al., *Peripheral benzodiazepine binding sites: effect of PK 11195, 1-(2-chlorophenyl)-N-methyl-N-(1-methylpropyl)-3-isoquinolinecarboxamide: I. In vitro studies*. Life sciences, 1983. 32(16): p. 1839-1847.
35. Marangos, P.J., et al., *Characterization of peripheral-type benzodiazepine binding sites in brain using [3H] Ro 5-4864*. Molecular pharmacology, 1982. 22(1): p. 26-32.

36. James, M.L., et al., *Synthesis and in vivo evaluation of a novel peripheral benzodiazepine receptor PET radioligand*. *Bioorganic & medicinal chemistry*, 2005. 13(22): p. 6188-6194.
37. Denora, N., et al., *2-Phenyl-imidazo [1, 2-a] pyridine compounds containing hydrophilic groups as potent and selective ligands for peripheral benzodiazepine receptors: synthesis, binding affinity and electrophysiological studies*. *Journal of medicinal chemistry*, 2008. 51(21): p. 6876-6888.
38. Müller, N., et al., *Anti-inflammatory treatment in schizophrenia*. *Progress in Neuro-Psychopharmacology and Biological Psychiatry*, 2013. 42: p. 146-153.
39. Taliani, S., et al., *Translocator protein ligands as promising therapeutic tools for anxiety disorders*. *Current medicinal chemistry*, 2009. 16(26): p. 3359-3380.
40. Chaki, S., et al., *Binding characteristics of [3H] DAA1106, a novel and selective ligand for peripheral benzodiazepine receptors*. *European journal of pharmacology*, 1999. 371(2): p. 197-204.
41. Briard, E., et al., *Single-step high-yield radiosynthesis and evaluation of a sensitive 18F-labeled ligand for imaging brain peripheral benzodiazepine receptors with PET*. *Journal of medicinal chemistry*, 2009. 52(3): p. 688-699.
42. Delavoie, F., et al., *In Vivo and in Vitro Peripheral-Type Benzodiazepine Receptor Polymerization: Functional Significance in Drug Ligand and Cholesterol Binding†*. *Biochemistry*, 2003. 42(15): p. 4506-4519.
43. Gaillard, Y., J.-P. Gay-Montchamp, and M. Ollagnier, *Simultaneous screening and quantitation of alpidem, zolpidem, buspirone and benzodiazepines by dual-channel gas chromatography using electron-capture and nitrogen—phosphorus detection after solid-*

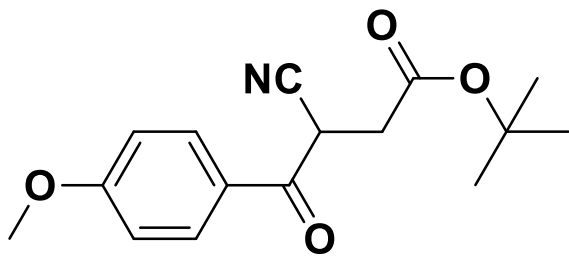
- phase extraction*. Journal of Chromatography B: Biomedical Sciences and Applications, 1993. 622(2): p. 197-208.
44. Byrnes, J.J., D.J. Greenblatt, and L.G. Miller, *Benzodiazepine receptor binding of nonbenzodiazepines in vivo: alpidem, zolpidem and zopiclone*. Brain research bulletin, 1992. 29(6): p. 905-908.
45. Selleri, S., et al., *2-Arylpyrazolo [1, 5-a] pyrimidin-3-yl acetamides. New potent and selective peripheral benzodiazepine receptor ligands*. Bioorganic & medicinal chemistry, 2001. 9(10): p. 2661-2671.
46. Selleri, S., et al., *Insight into 2-phenylpyrazolo [1, 5-a] pyrimidin-3-yl acetamides as peripheral benzodiazepine receptor ligands: synthesis, biological evaluation and 3D-QSAR investigation*. Bioorganic & medicinal chemistry, 2005. 13(16): p. 4821-4834.
47. Tang, D., et al., *Preclinical Imaging Evaluation of Novel TSPO-PET Ligand 2-(5, 7-Diethyl-2-(4-(2-[18F] fluoroethoxy) phenyl) pyrazolo [1, 5-a] pyrimidin-3-yl)-N, N-diethylacetamide ([18F] VUIIS1008) in Glioma*. Molecular Imaging and Biology, 2014. 16(6): p. 813-820.
48. Manning, H.C., et al., *A peripheral benzodiazepine receptor targeted agent for in vitro imaging and screening*. Bioconjugate chemistry, 2006. 17(3): p. 735-740.
49. Bai, M., et al., *A novel conjugable translocator protein ligand labeled with a fluorescence dye for in vitro imaging*. Bioconjugate chemistry, 2007. 18(4): p. 1118-1122.
50. Bai, M., et al., *A Novel Functional Translocator Protein Ligand for Cancer Imaging*. Bioconjugate chemistry, 2007. 18(6): p. 2018-2023.

51. Chen, M.K., et al., *Peripheral benzodiazepine receptor imaging in CNS demyelination: functional implications of anatomical and cellular localization*. *Brain*, 2004. 127(6): p. 1379-1392.
52. Tang, D., et al., *Microwave-assisted organic synthesis of a high-affinity pyrazolo-pyrimidinyl TSPO ligand*. *Tetrahedron letters*, 2010. 51(35): p. 4595-4598.
53. Tang, D., et al., *Quantitative preclinical imaging of TSPO expression in glioma using N, N-diethyl-2-(2-(4-(2-¹⁸F-fluoroethoxy) phenyl)-5, 7-dimethylpyrazolo [1, 5-a] pyrimidin-3-yl) acetamide*. *Journal of Nuclear Medicine*, 2012. 53(2): p. 287-294.
54. Cheung, Y.-Y., et al., *Facile synthesis of SSR180575 and discovery of 7-chloro-N, N, 5-trimethyl-4-oxo-3 (6-[¹⁸F] fluoropyridin-2-yl)-3, 5-dihydro-4H-pyridazino [4, 5-b] indole-1-acetamide, a potent pyridazinoindole ligand for PET imaging of TSPO in cancer*. *Bioorganic & medicinal chemistry letters*, 2014. 24(18): p. 4466-4471.
55. Buck, J.R., et al., *Quantitative, preclinical PET of translocator protein expression in glioma using ¹⁸F-N-fluoroacetyl-N-(2, 5-dimethoxybenzyl)-2-phenoxyaniline*. *Journal of Nuclear Medicine*, 2011. 52(1): p. 107-114.
56. Buck, J.R., et al., *Rapid, microwave-assisted organic synthesis of selective V600E BRAF inhibitors for preclinical cancer research*. *Tetrahedron letters*, 2012. 53(32): p. 4161-4165.
57. Doorduyn, J., et al., *[¹¹C]-DPA-713 and [¹⁸F]-DPA-714 as new PET tracers for TSPO: a comparison with [¹¹C]-(R)-PK11195 in a rat model of herpes encephalitis*. *Molecular Imaging and Biology*, 2009. 11(6): p. 386-398.
58. Kappe, C.O., *Controlled microwave heating in modern organic synthesis*. *Angewandte Chemie International Edition*, 2004. 43(46): p. 6250-6284.

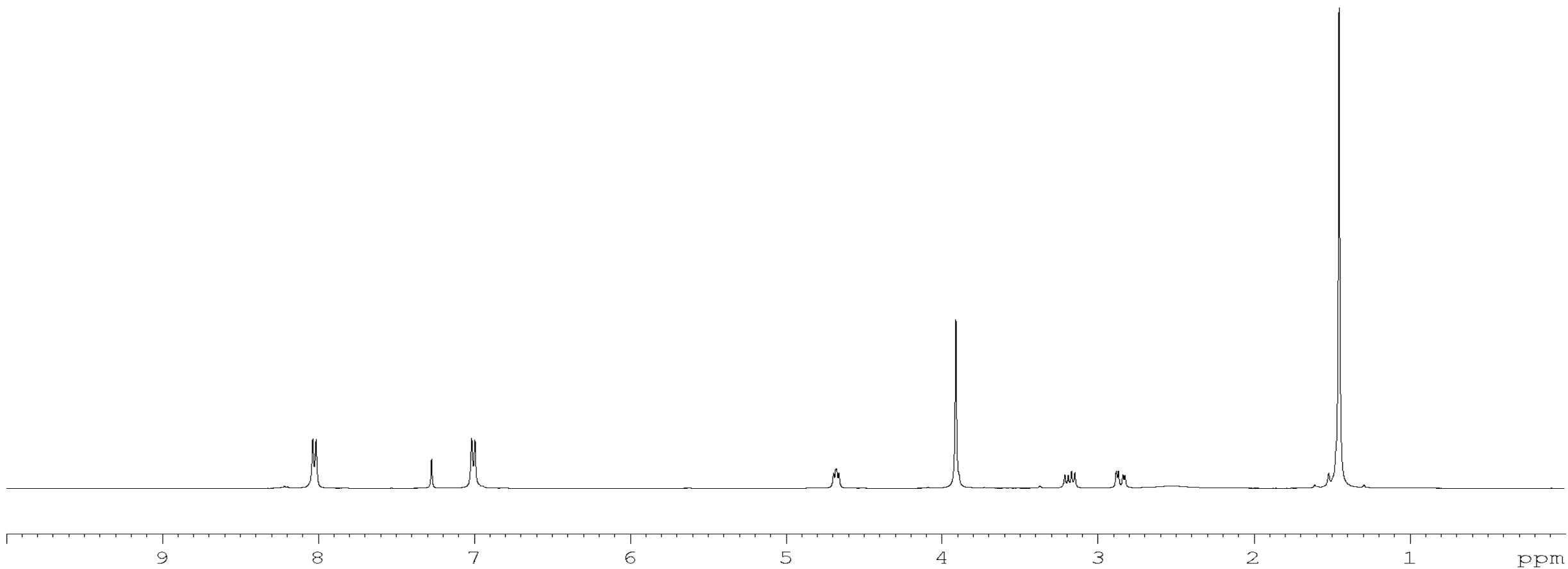
59. Stass, D., et al., *Radiofrequency magnetic field effects on chemical reaction yields*. Chemical Physics Letters, 2000. 329(1): p. 15-22.
60. Timmel, C. and P. Hore, *Oscillating magnetic field effects on the yields of radical pair reactions*. Chemical Physics Letters, 1996. 257(3): p. 401-408.
61. Westaway, K. and R. Gedye, *The question of specific activation of organic reactions by microwaves*. Journal of microwave power and electromagnetic energy, 1995. 30(4): p. 219-230.
62. Langa, F., et al., *Microwave irradiation: more than just a method for accelerating reactions*. Contemporary organic synthesis, 1997. 4(5): p. 373-386.
63. Waterhouse, R.N., K. Mardon, and J.C. O'Brien, *Synthesis and preliminary evaluation of [123I]1-(4-cyanobenzyl)-4-[[trans-iodopropen-2-yl]oxy]-methyl]piperidine: A novel high affinity sigma receptor radioligand for SPECT*. Nuclear Medicine and Biology, 1997. 24(1): p. 45-51.
64. Webster, G.R.B., et al., *Environmental fate modelling of chlorodioxins: Determination of physical constants*. Chemosphere, 1985. 14(6-7): p. 609-622.
65. van Liempd, S., et al., *Development and validation of a higher-throughput equilibrium dialysis assay for plasma protein binding*. Journal of the Association for Laboratory Automation, 2011. 16(1): p. 56-67.
66. Abreu, A.R., M.M. Pereira, and J.C. Bayón, *Synthesis of new bis-BINOL-2, 2'-ethers and bis-H₈ BINOL-2, 2'-ethers evaluation of their Titanium complexes in the asymmetric ethylation of benzaldehyde*. Tetrahedron, 2010. 66(3): p. 743-749.
67. Li, F., et al., *Crystal structures of translocator protein (TSPO) and mutant mimic of a human polymorphism*. Science, 2015. 347(6221): p. 555-558.

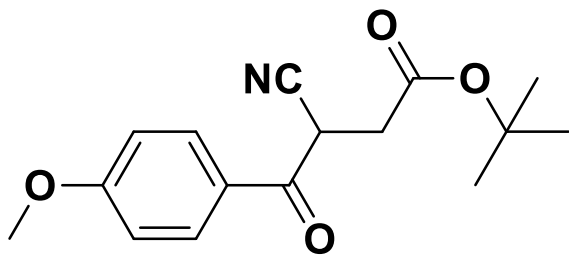
68. Jaremko, L., et al., *Structure of the Mitochondrial Translocator Protein in Complex with a Diagnostic Ligand*. Science, 2014. 343(6177): p. 1363-1366.
69. Laquintana, V., et al., *N-Benzyl-2-(6, 8-dichloro-2-(4-chlorophenyl) imidazo [1, 2-a] pyridin-3-yl)-N-(6-(7-nitrobenzo [c][1, 2, 5] oxadiazol-4-ylamino) hexyl) acetamide as a new fluorescent probe for peripheral benzodiazepine receptor and microglial cell visualization*. Bioconjugate chemistry, 2007. 18(5): p. 1397-1407.
70. Denora, N., et al., *New fluorescent probes targeting the mitochondrial-located translocator protein 18 kDa (TSPO) as activated microglia imaging agents*. Pharmaceutical research, 2011. 28(11): p. 2820-2832.
71. Yamaguchi, T., et al., *Turn-ON fluorescent affinity labeling using a small bifunctional O-nitrobenzoxadiazole unit*. Chemical Science, 2014.
72. Minamide, L. and J. Bamberg, *A filter paper dye-binding assay for quantitative determination of protein without interference from reducing agents or detergents*. Analytical biochemistry, 1990. 190(1): p. 66-70.
73. Yung-Chi, C. and W.H. Prusoff, *Relationship between the inhibition constant (K_i) and the concentration of inhibitor which causes 50 per cent inhibition (I_{50}) of an enzymatic reaction*. Biochemical pharmacology, 1973. 22(23): p. 3099-3108.
74. Rahib, L., et al., *Projecting cancer incidence and deaths to 2030: the unexpected burden of thyroid, liver, and pancreas cancers in the United States*. Cancer research, 2014. 74(11): p. 2913-2921.
75. Tanaka, Y., et al., *The impact of near-infrared in plastic surgery*. Plastic Surgery: An International Journal, 2013.

76. Houghton, J.L., et al., *Site-specifically labeled CA19. 9-targeted immunoconjugates for the PET, NIRF, and multimodal PET/NIRF imaging of pancreatic cancer*. Proceedings of the National Academy of Sciences, 2015. 112(52): p. 15850-15855.
77. Vosjan, M.J., et al., *Conjugation and radiolabeling of monoclonal antibodies with zirconium-89 for PET imaging using the bifunctional chelate p-isothiocyanatobenzyl-desferrioxamine*. Nature protocols, 2010. 5(4): p. 739-743.
78. Westphalen, C.B. and K.P. Olive, *Genetically engineered mouse models of pancreatic cancer*. Cancer journal (Sudbury, Mass.), 2012. 18(6): p. 502.
79. Herreros-Villanueva, M., et al., *Mouse models of pancreatic cancer*. World J Gastroenterol, 2012. 18(12): p. 1286-1294.
80. Ijichi, H., et al., *Aggressive pancreatic ductal adenocarcinoma in mice caused by pancreas-specific blockade of transforming growth factor- β signaling in cooperation with active Kras expression*. Genes & development, 2006. 20(22): p. 3147-3160.

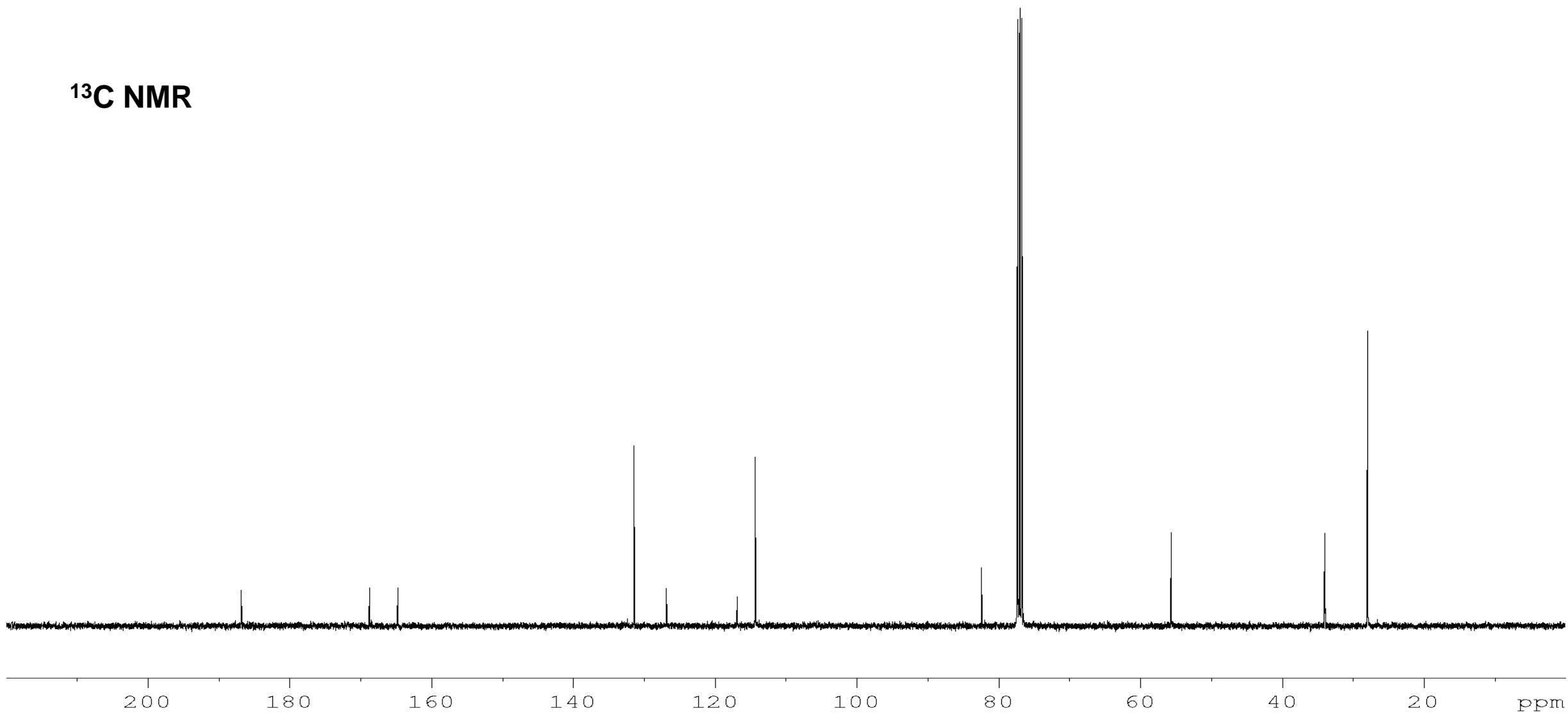


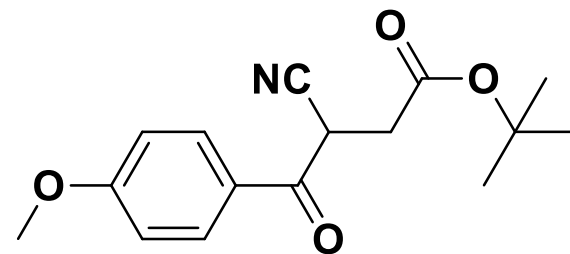
¹H NMR



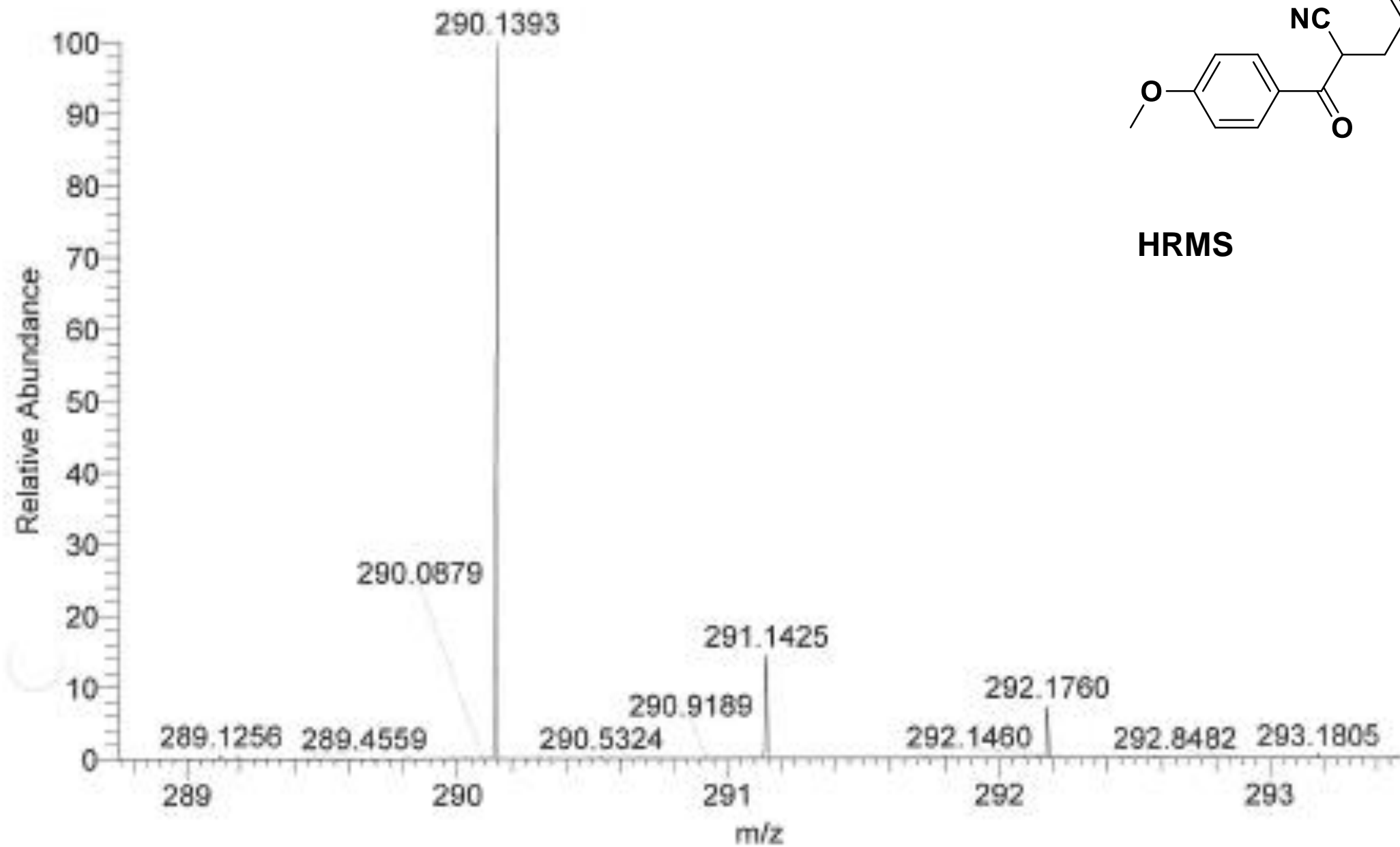


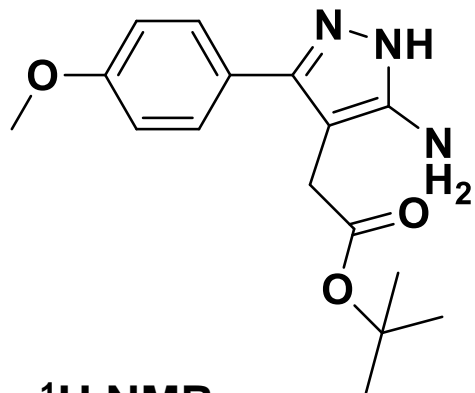
^{13}C NMR



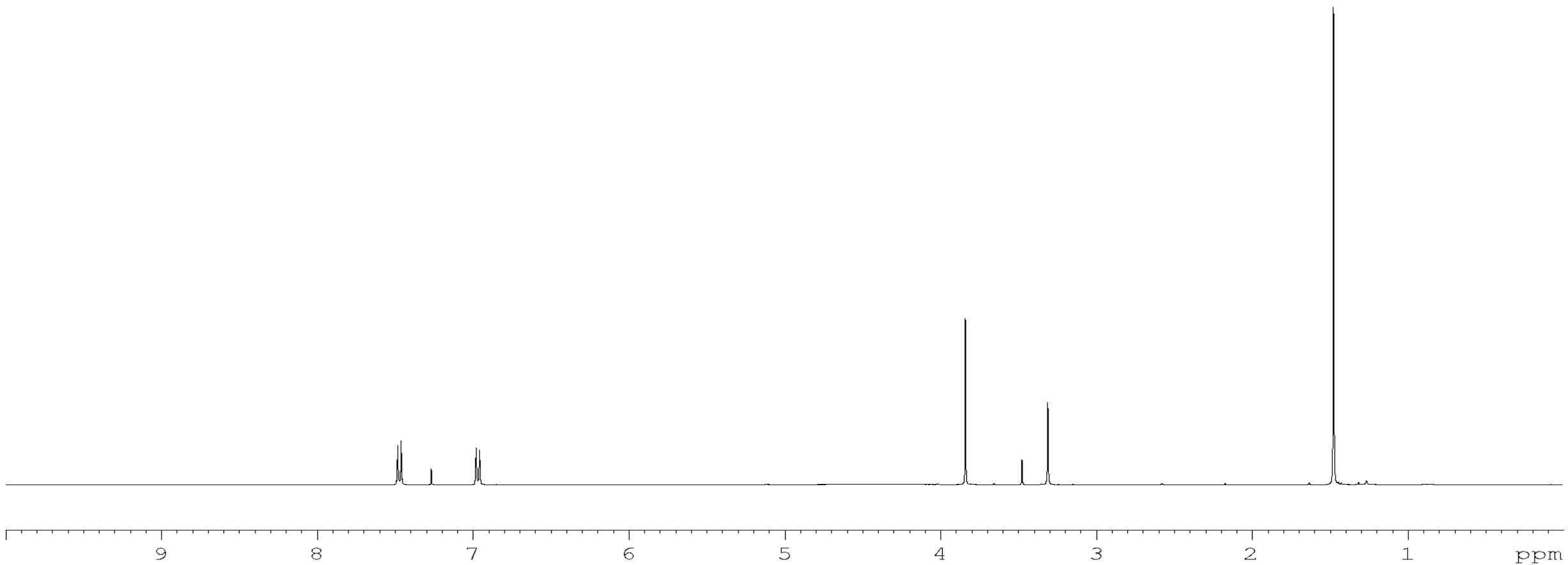


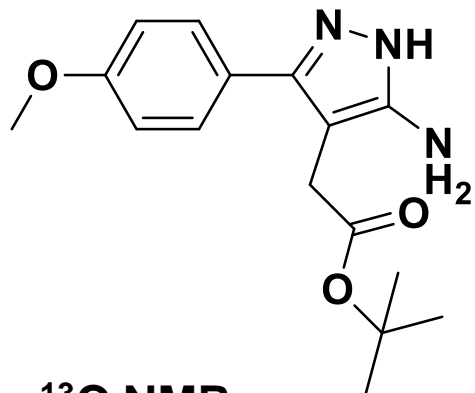
HRMS



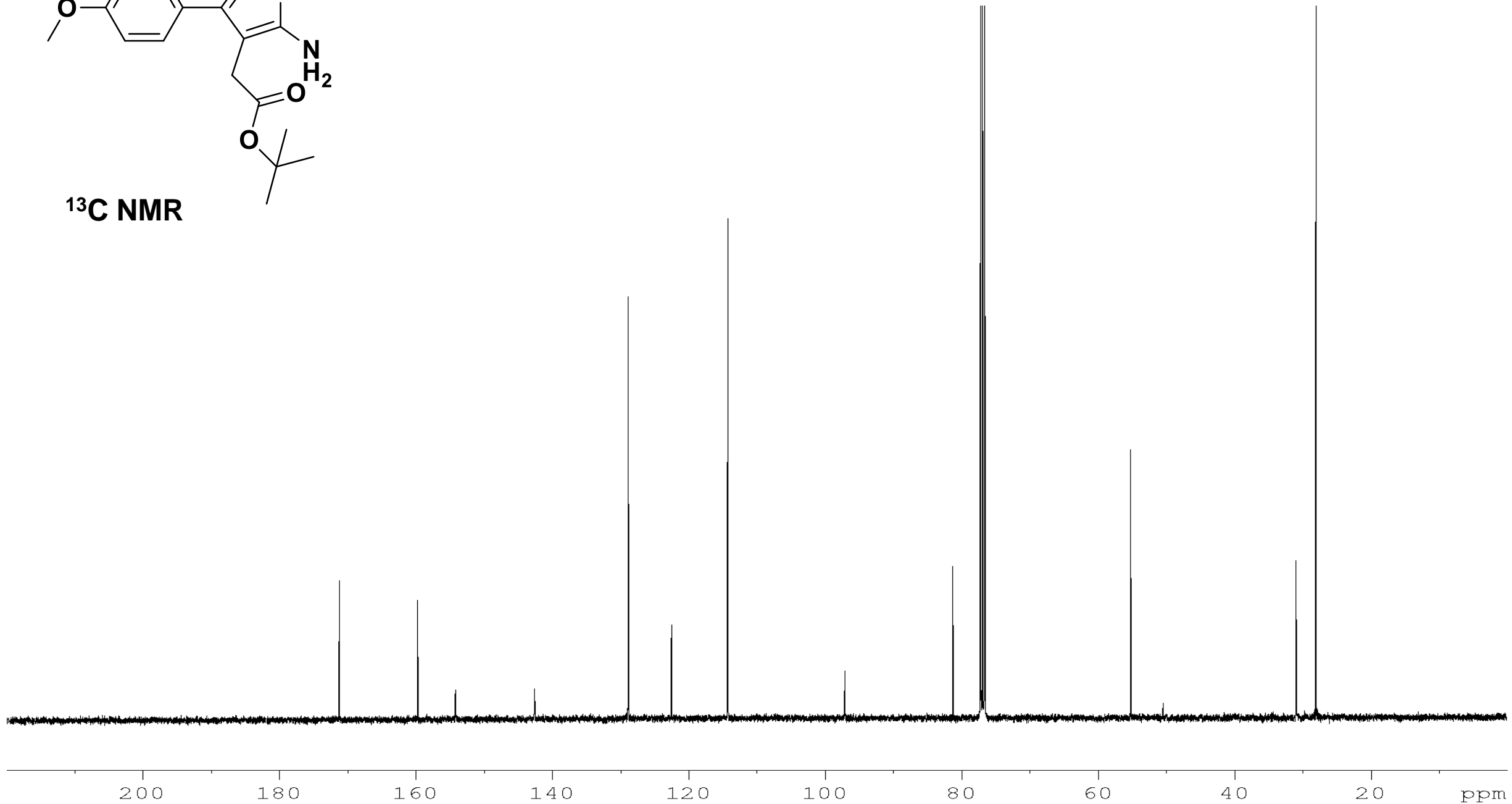


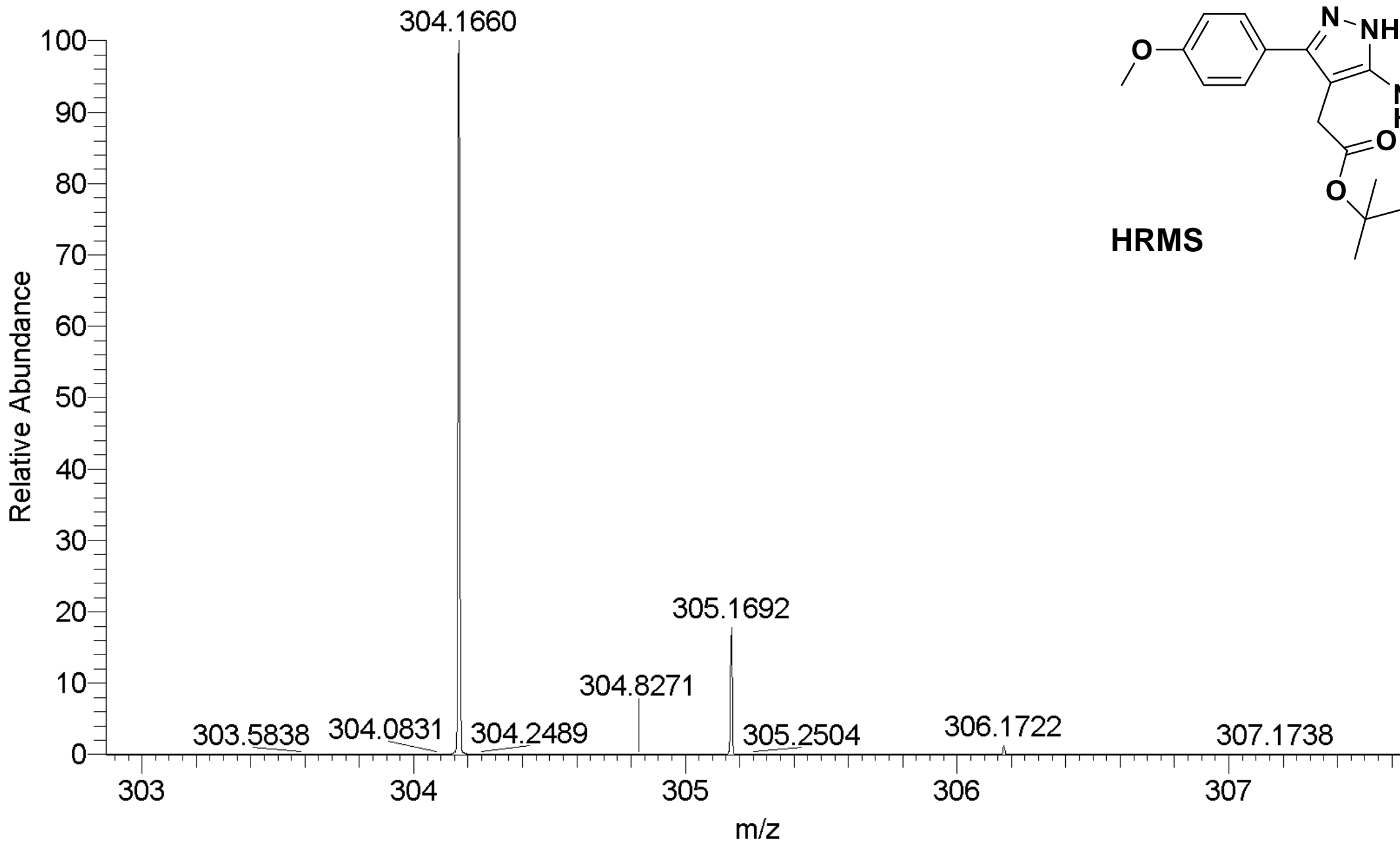
¹H NMR

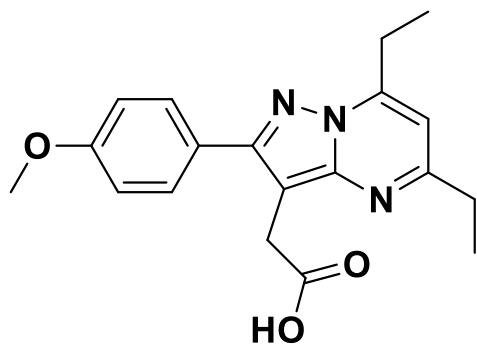




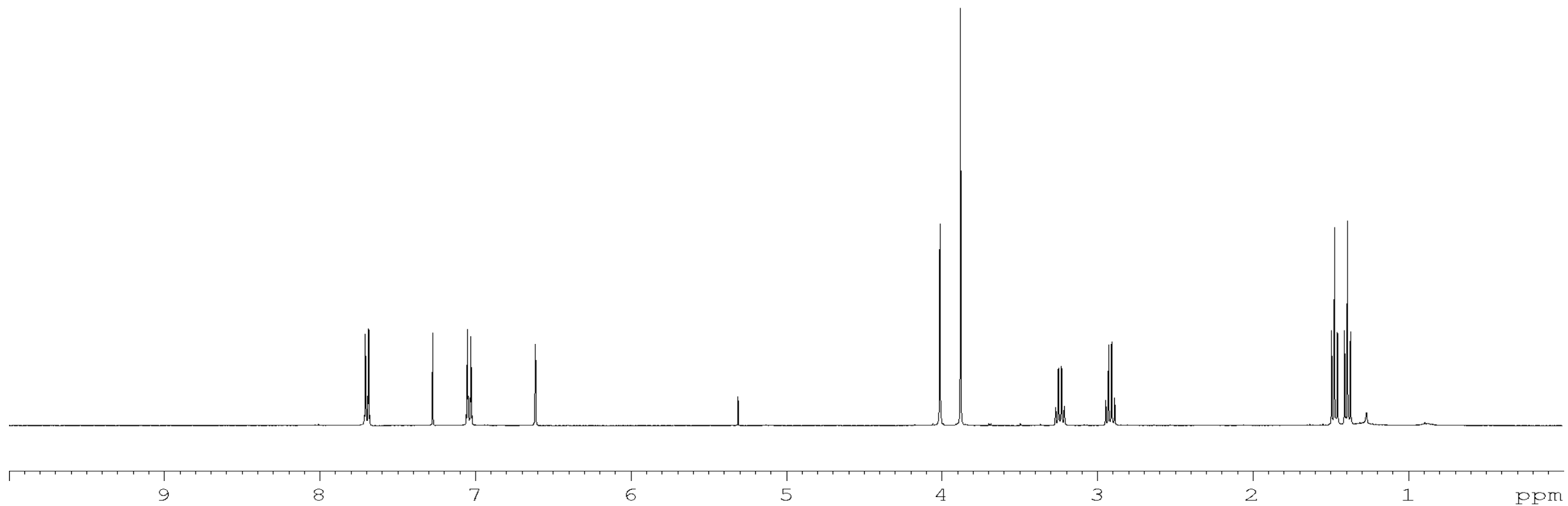
¹³C NMR

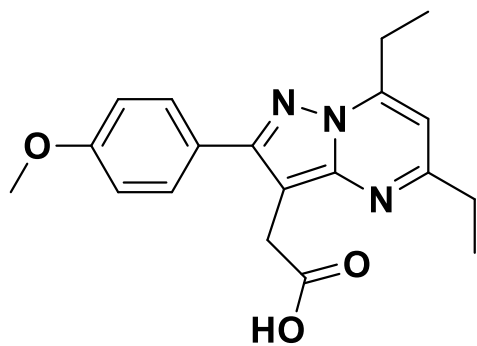




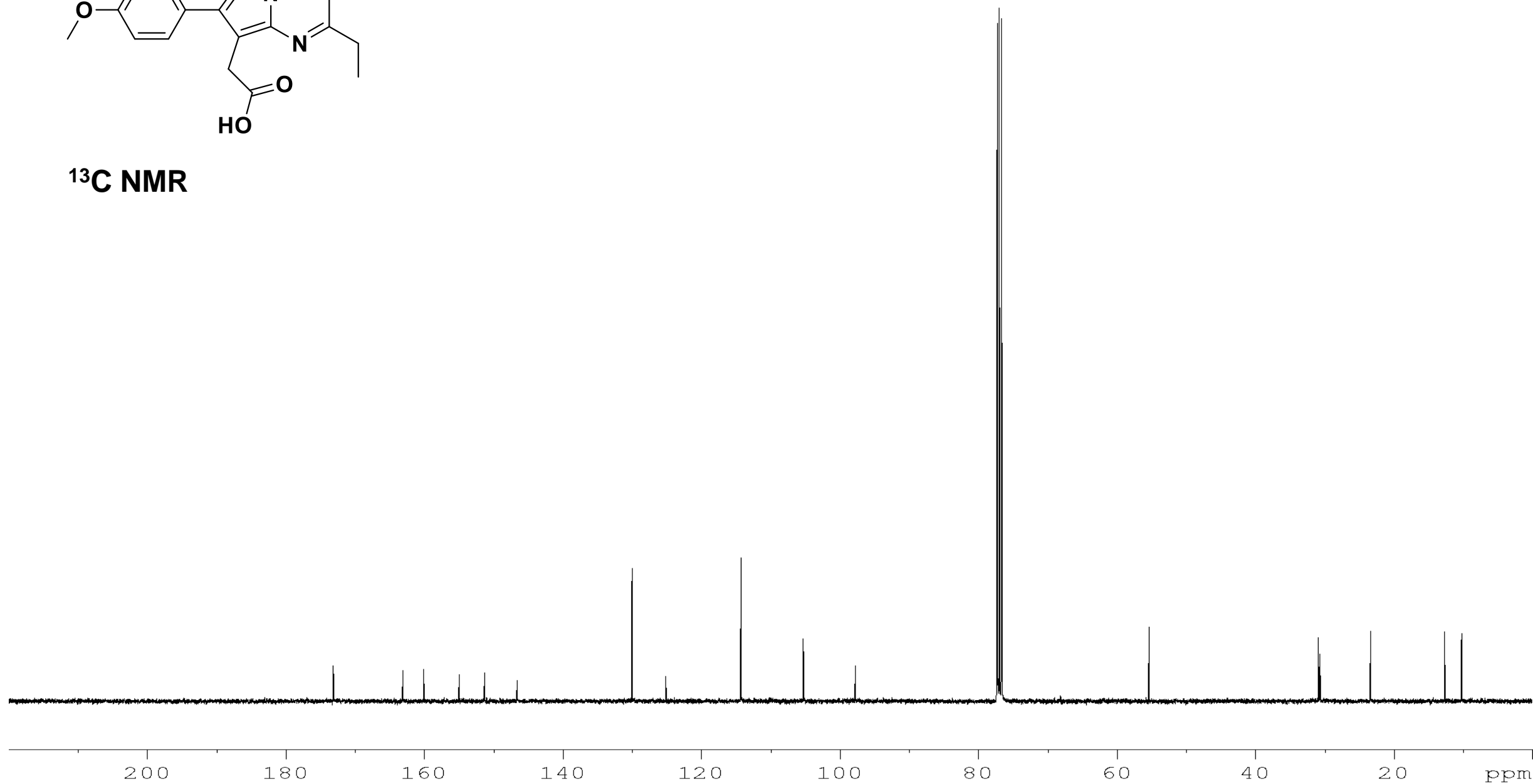


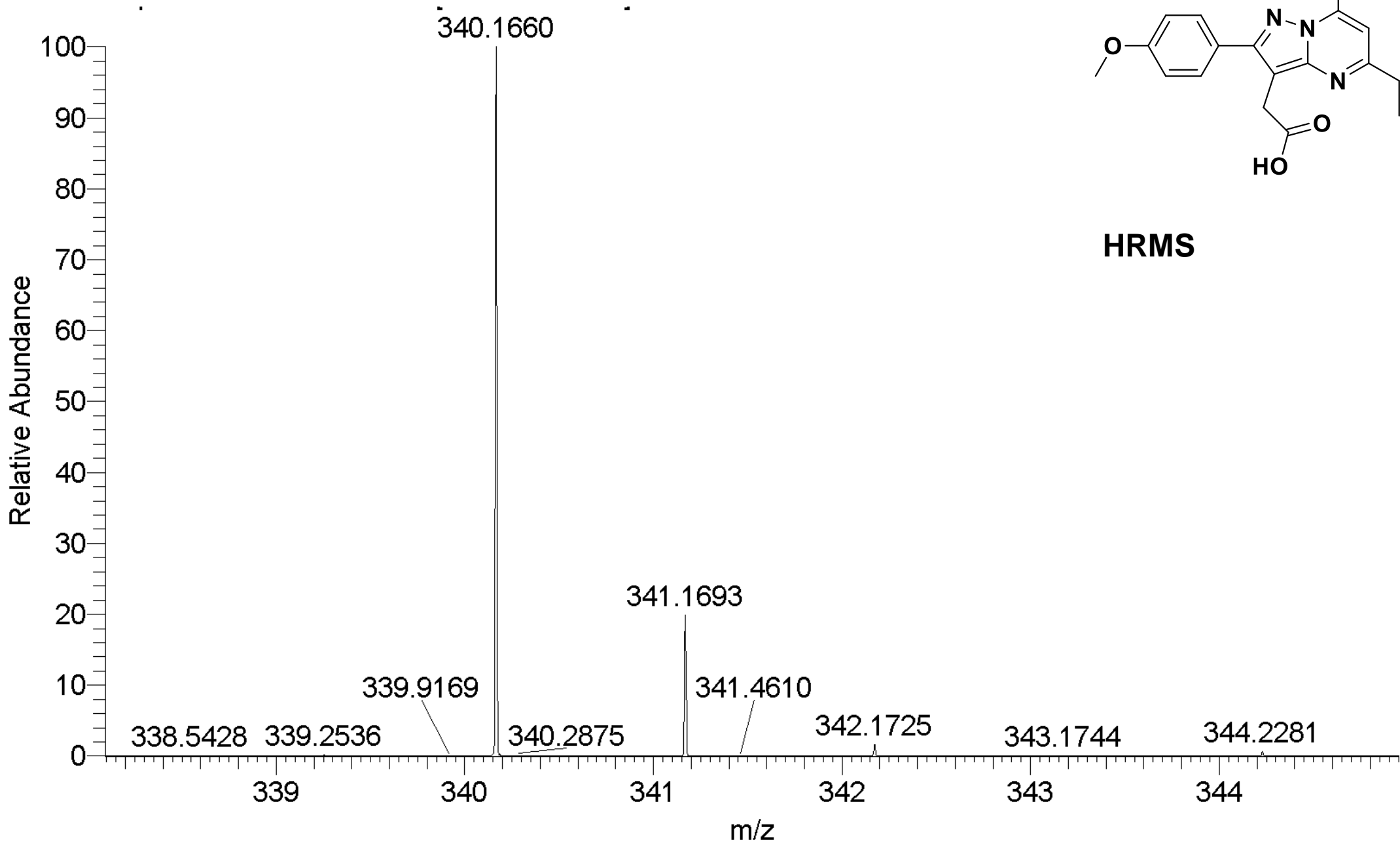
¹H NMR

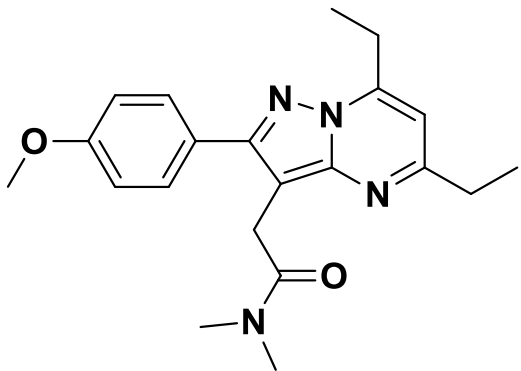




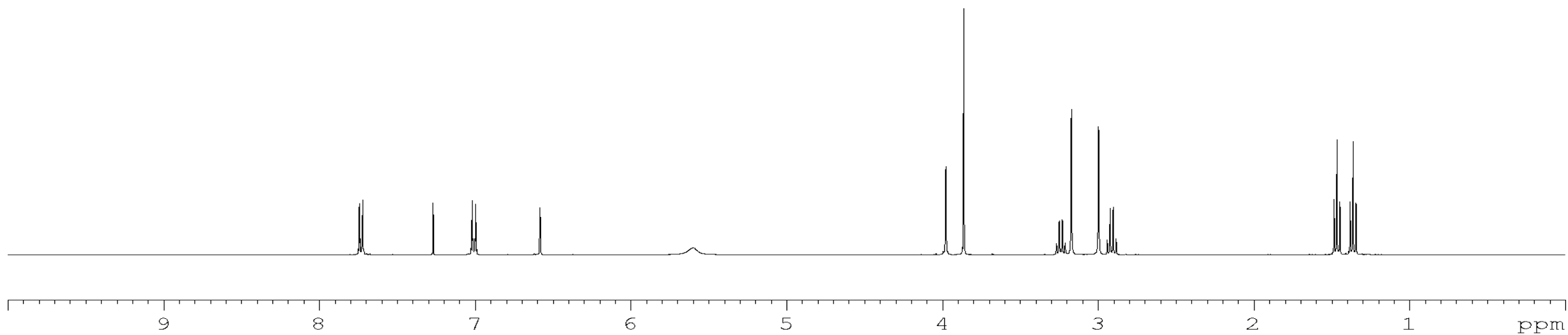
¹³C NMR

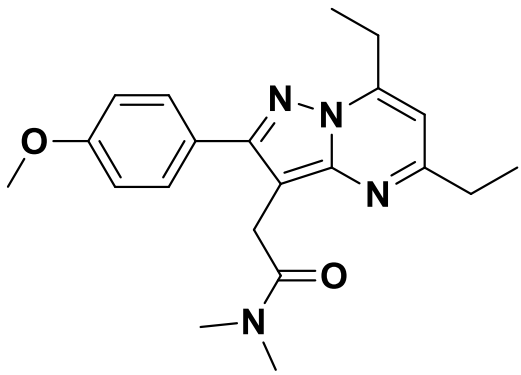




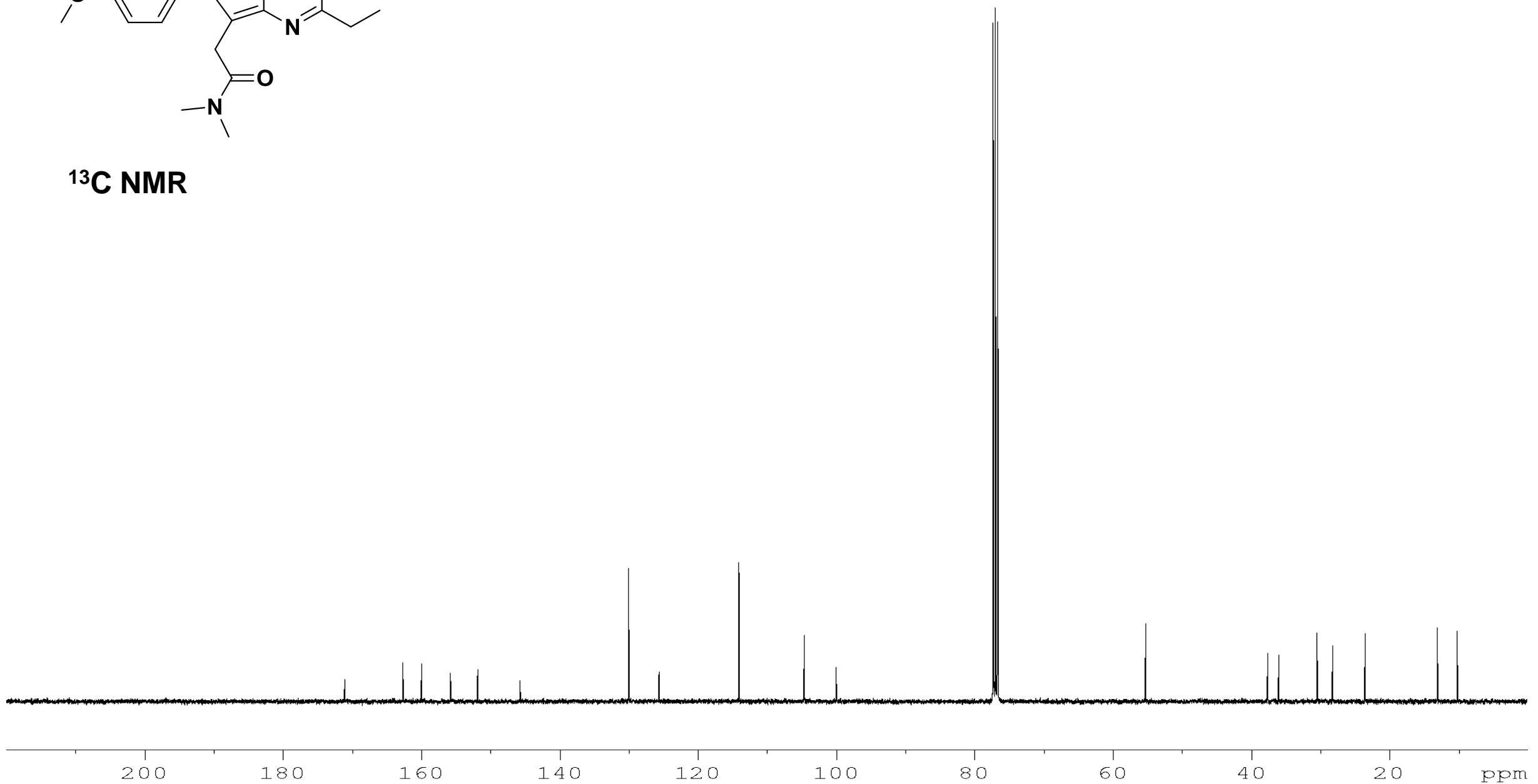


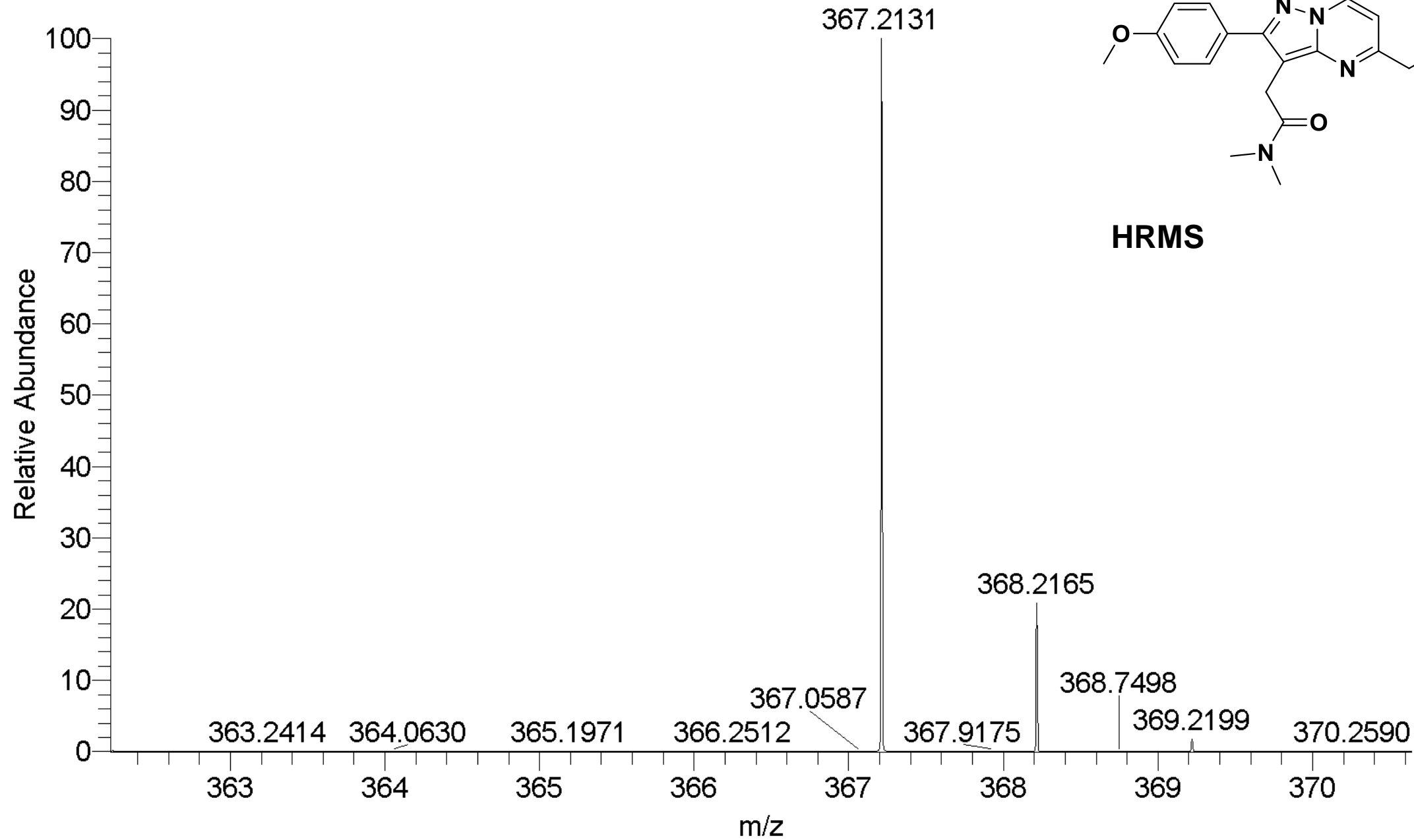
¹H NMR

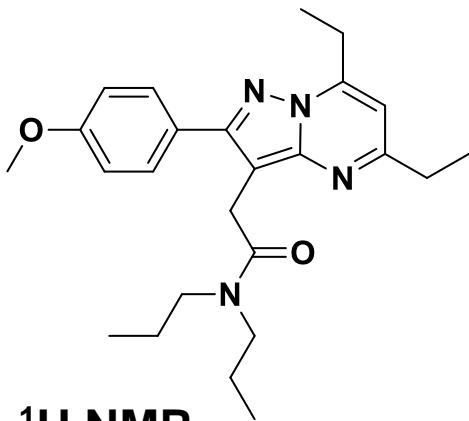




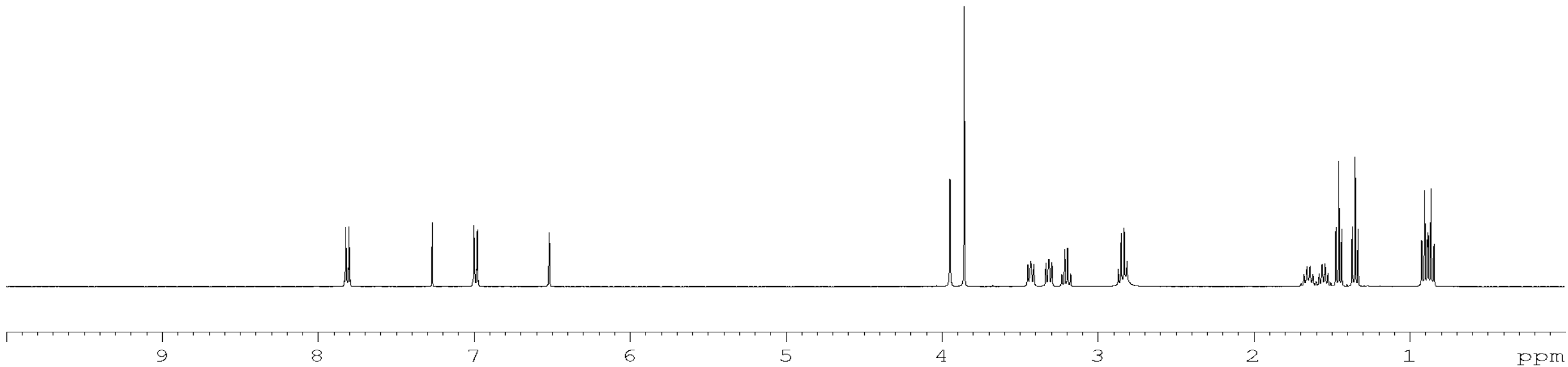
^{13}C NMR

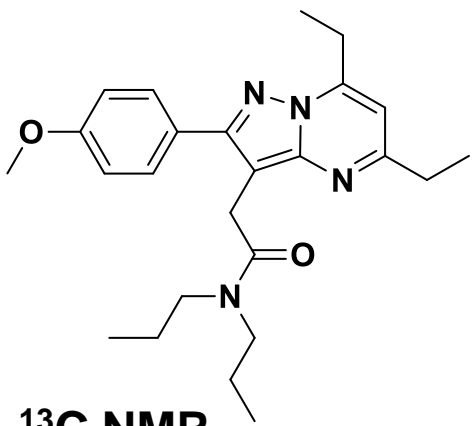




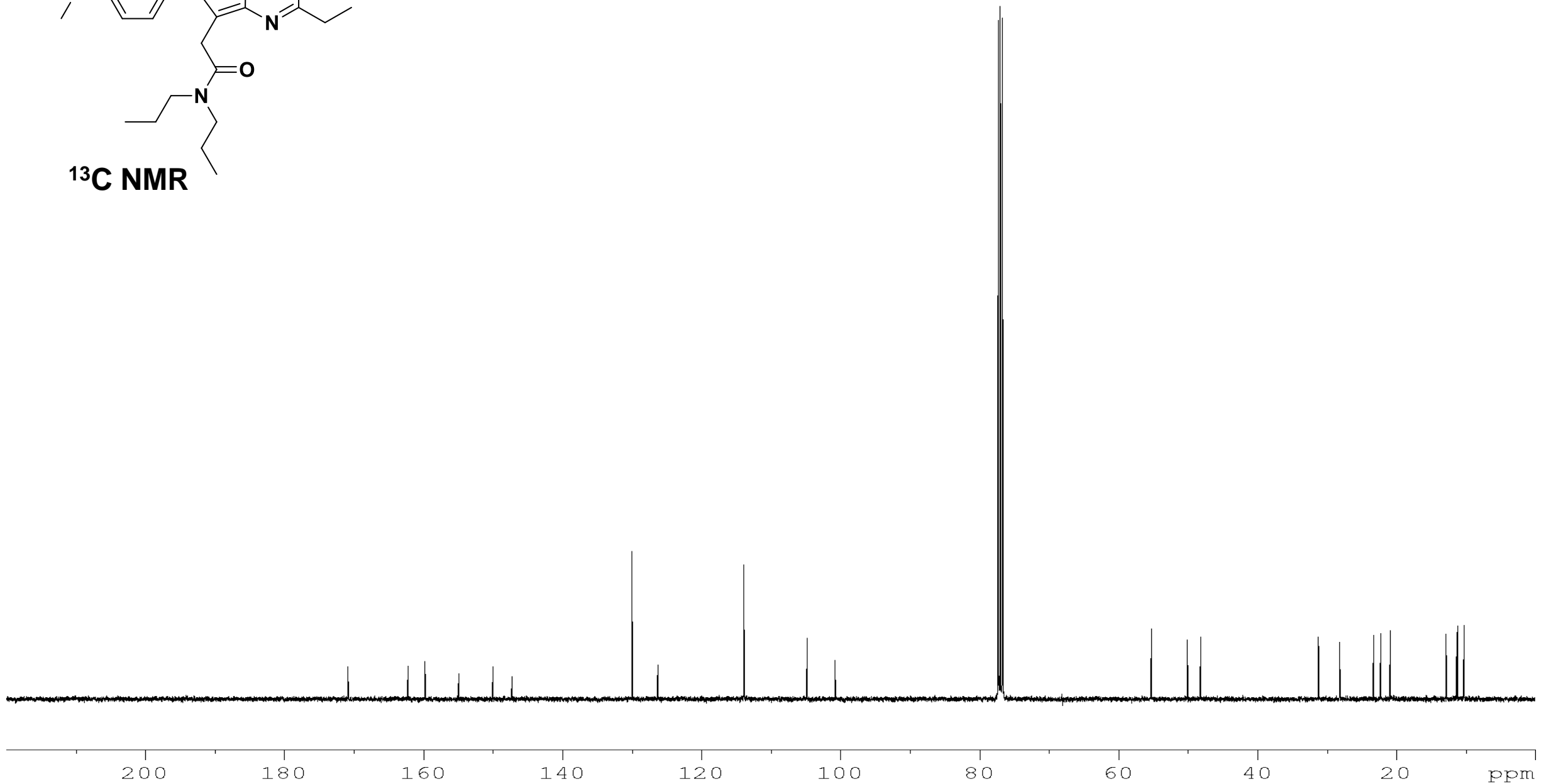


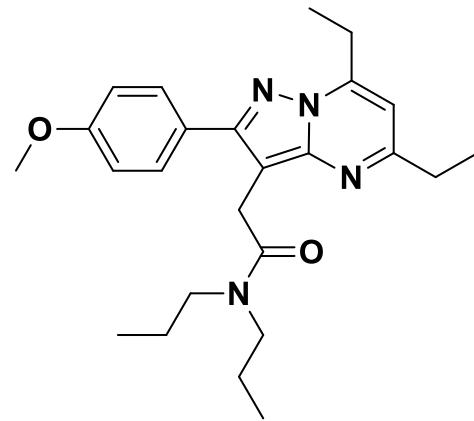
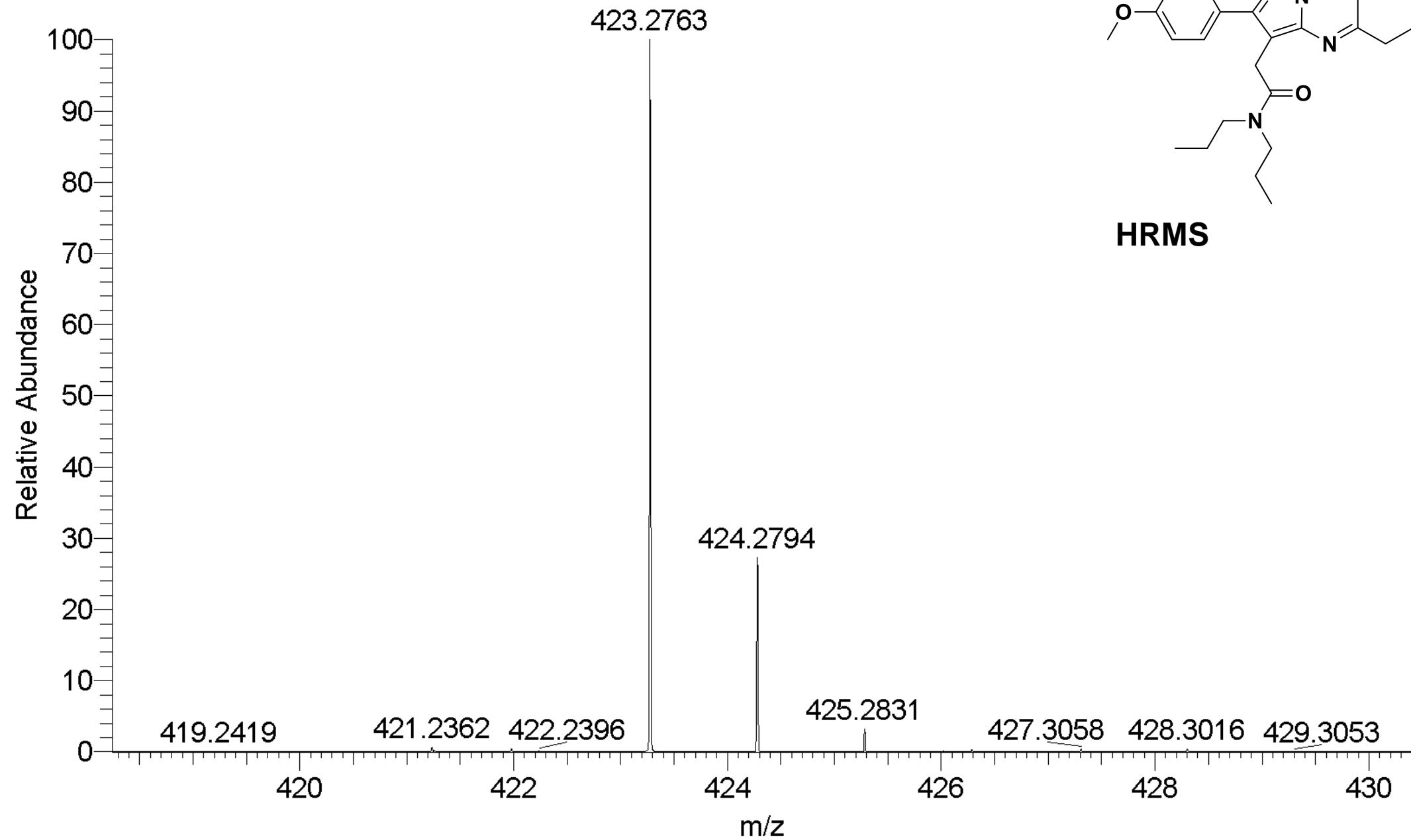
¹H NMR

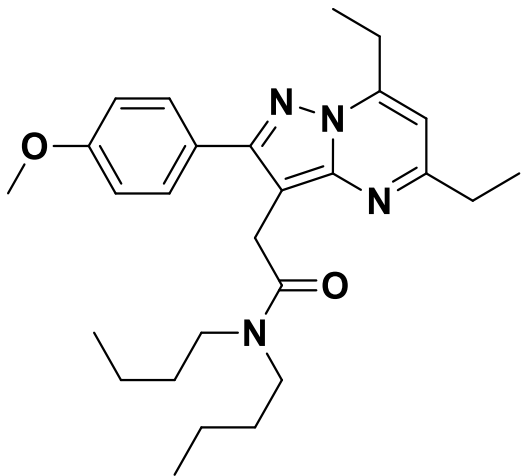




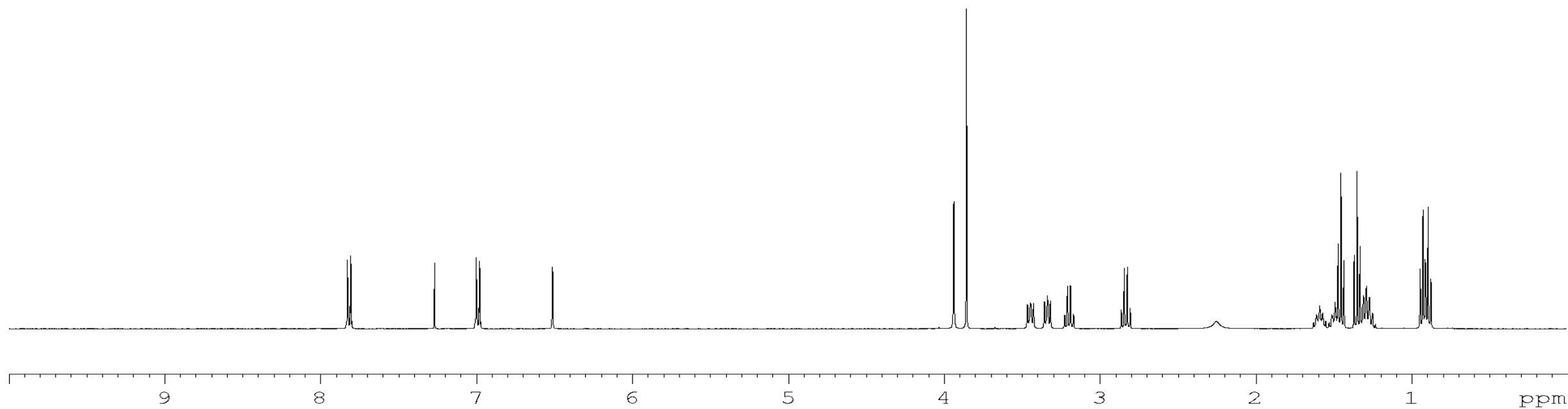
^{13}C NMR

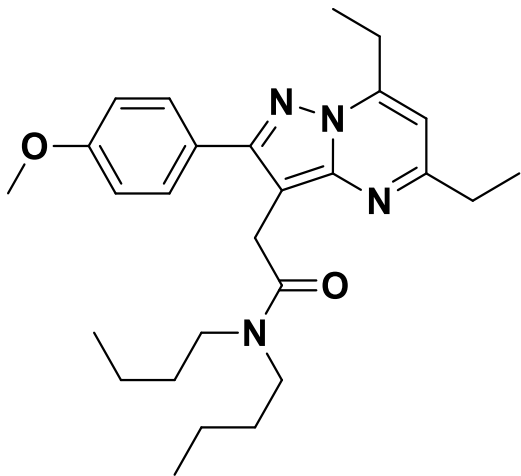




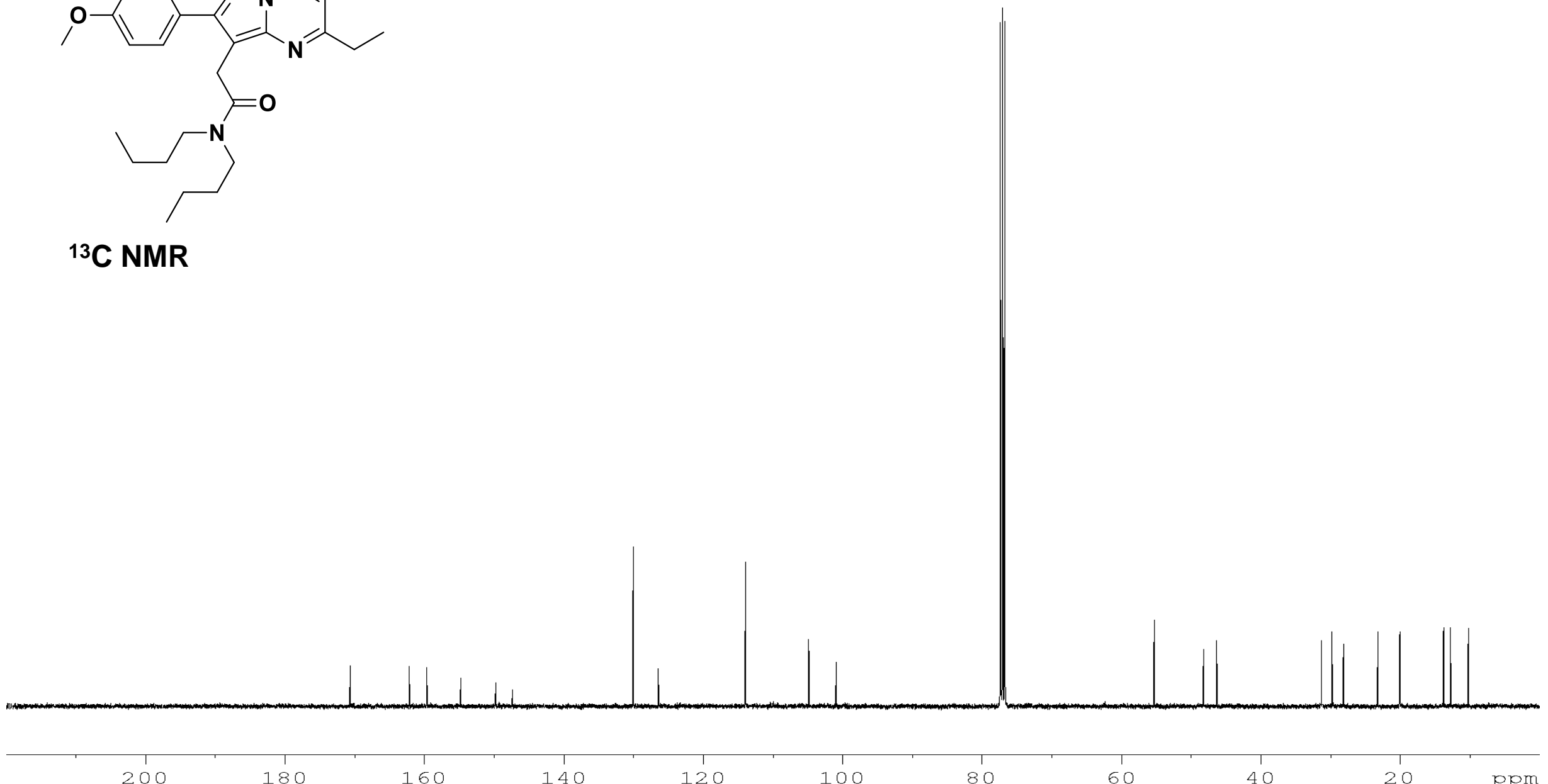


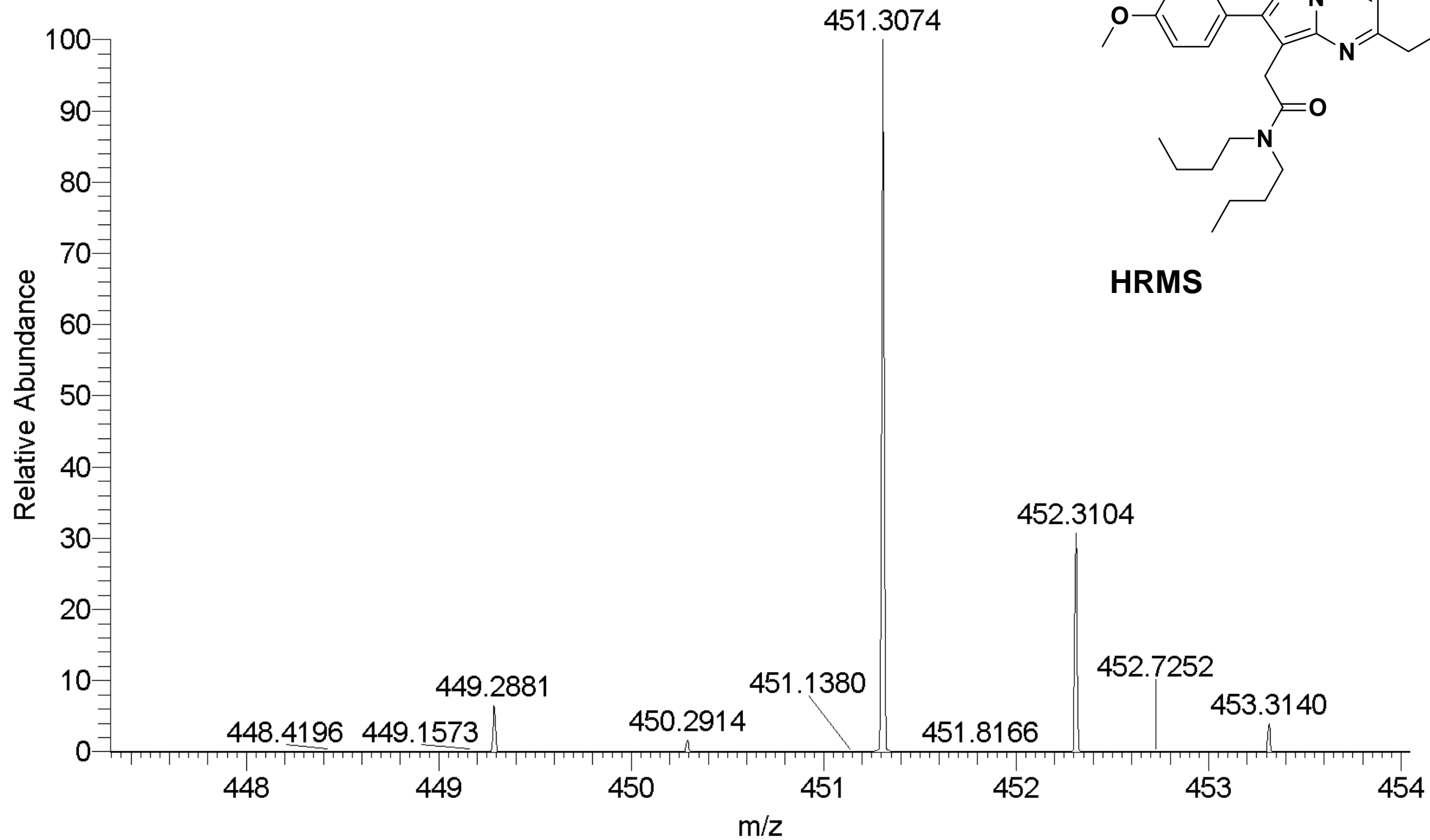
¹H NMR

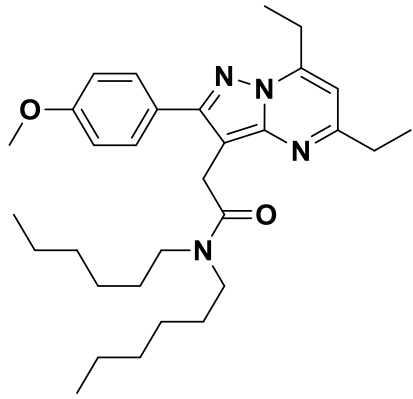




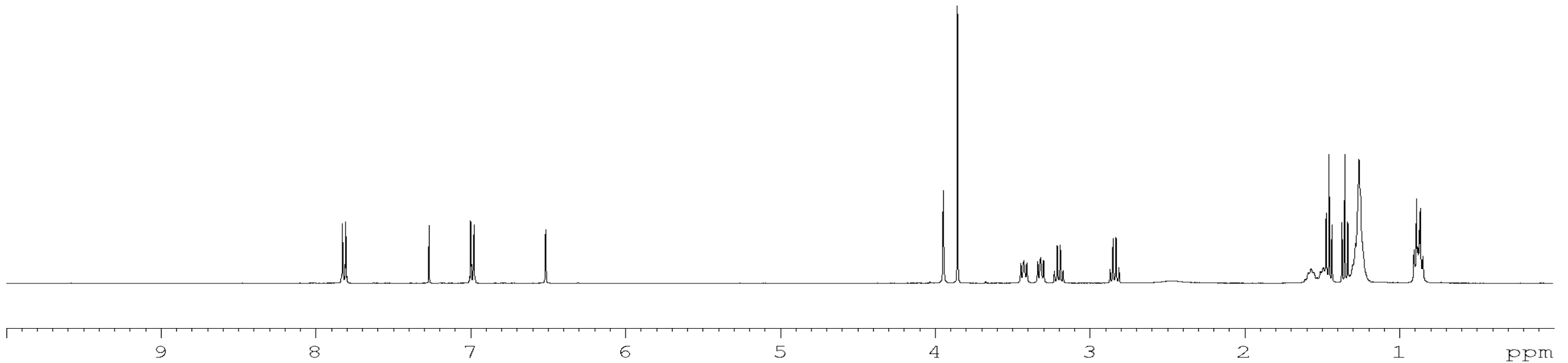
¹³C NMR

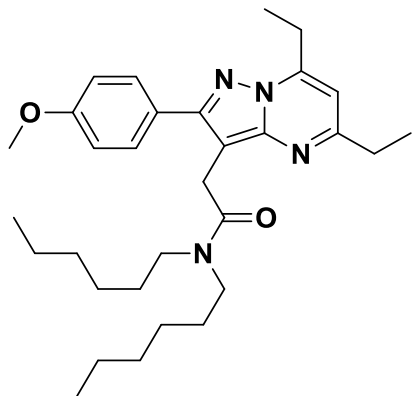




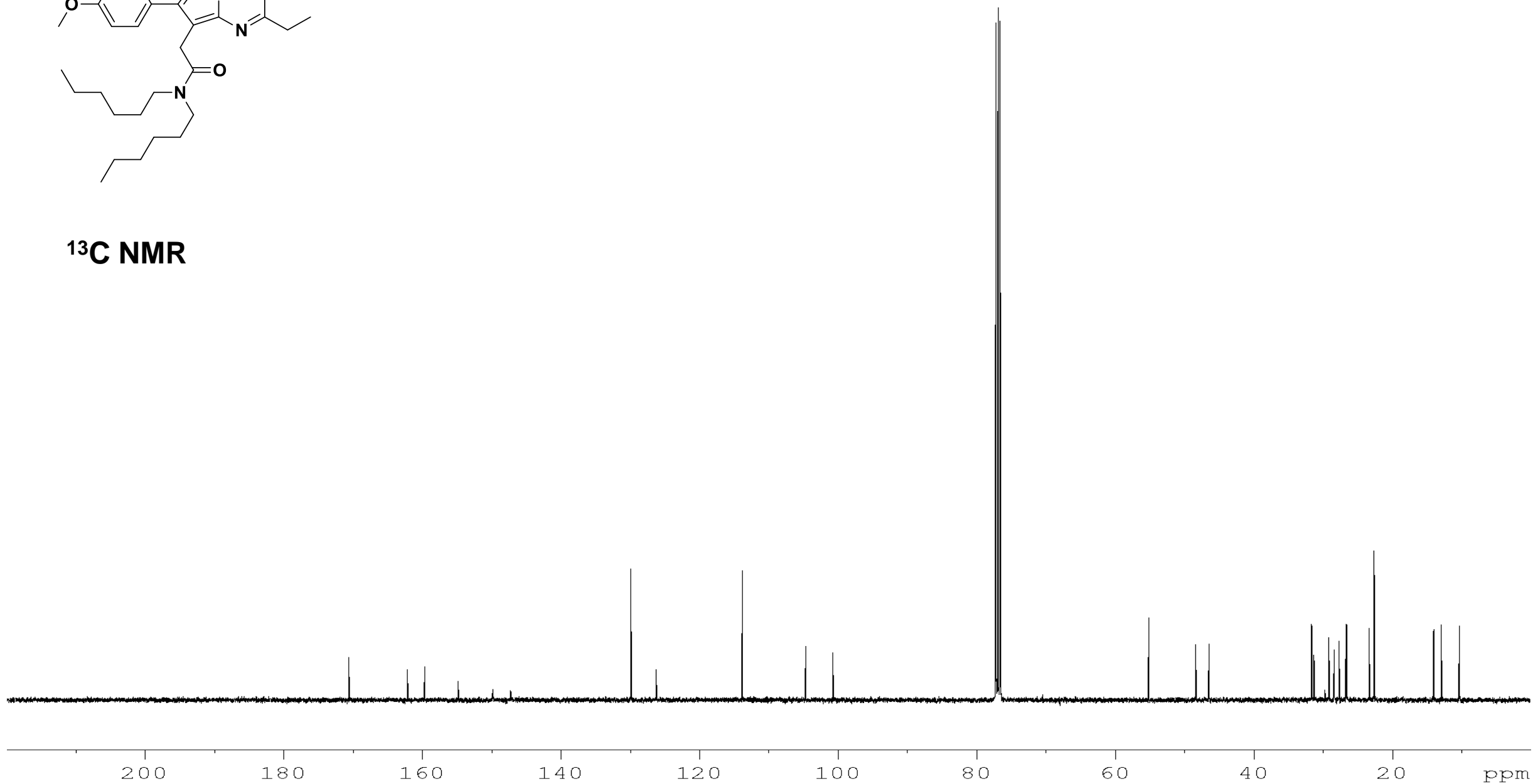


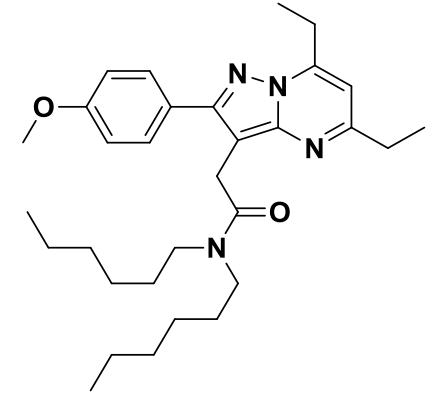
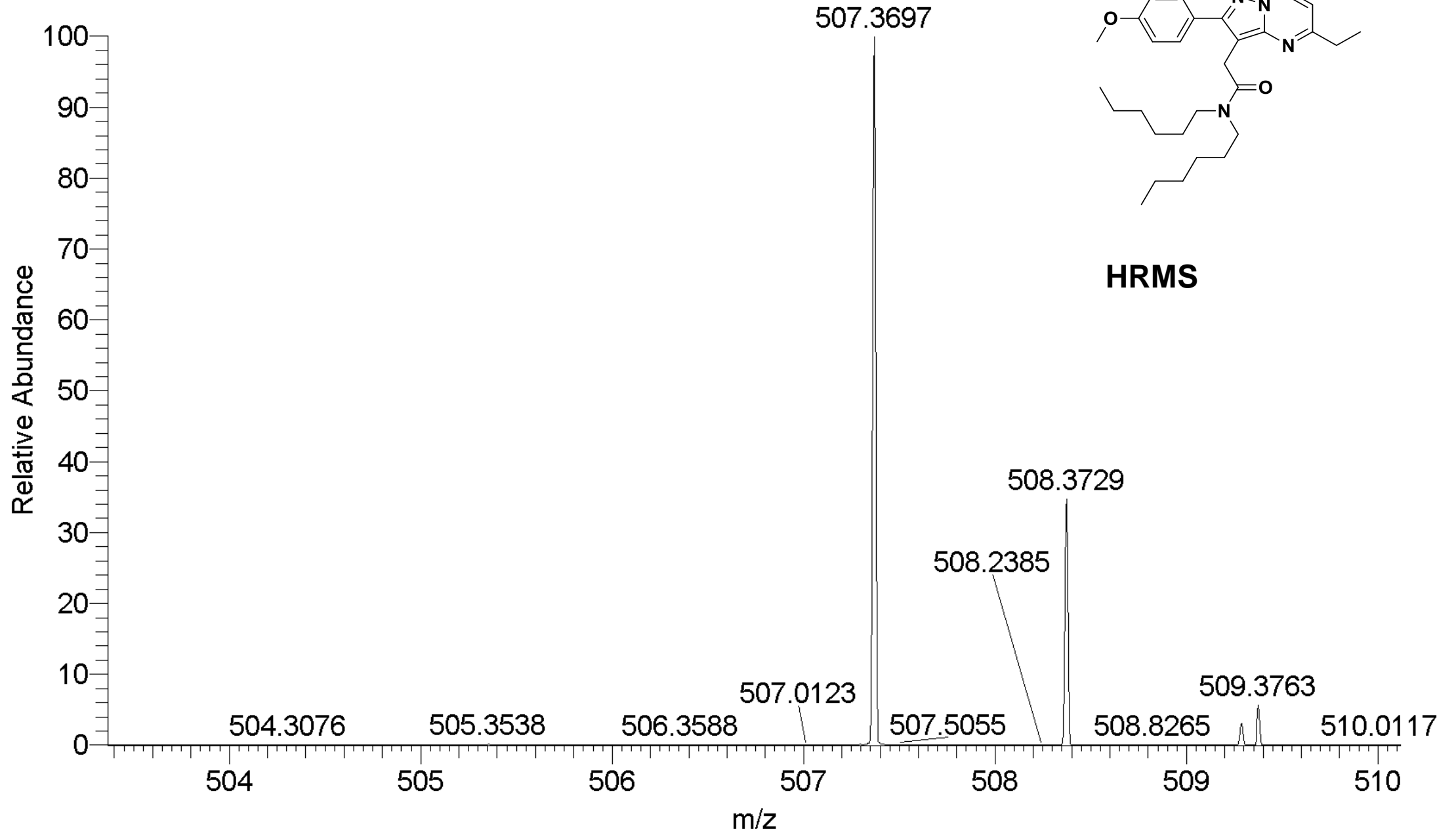
^1H NMR

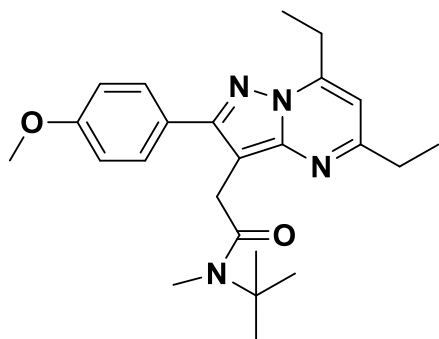




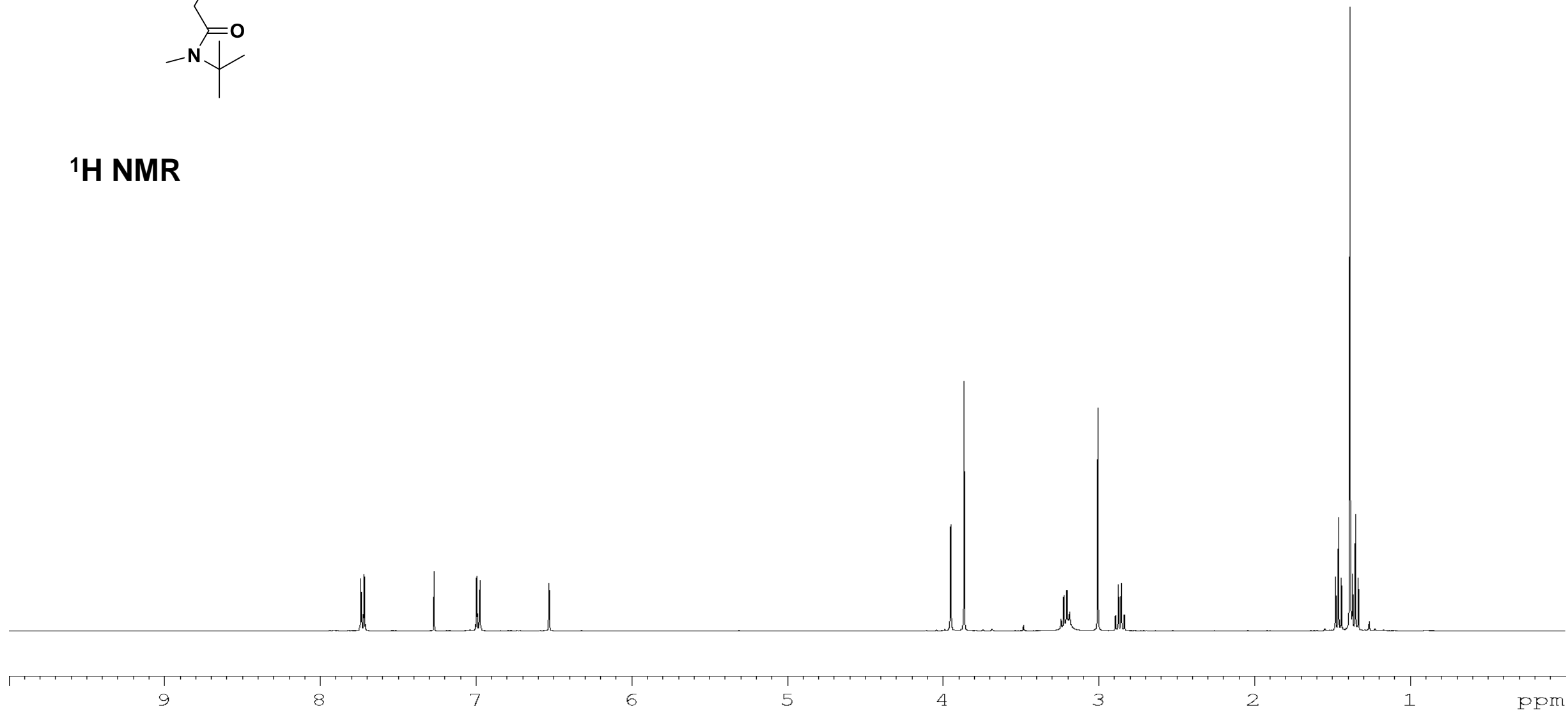
^{13}C NMR

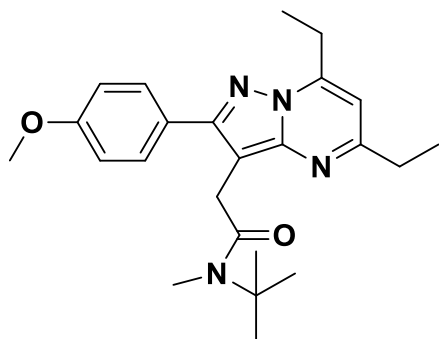




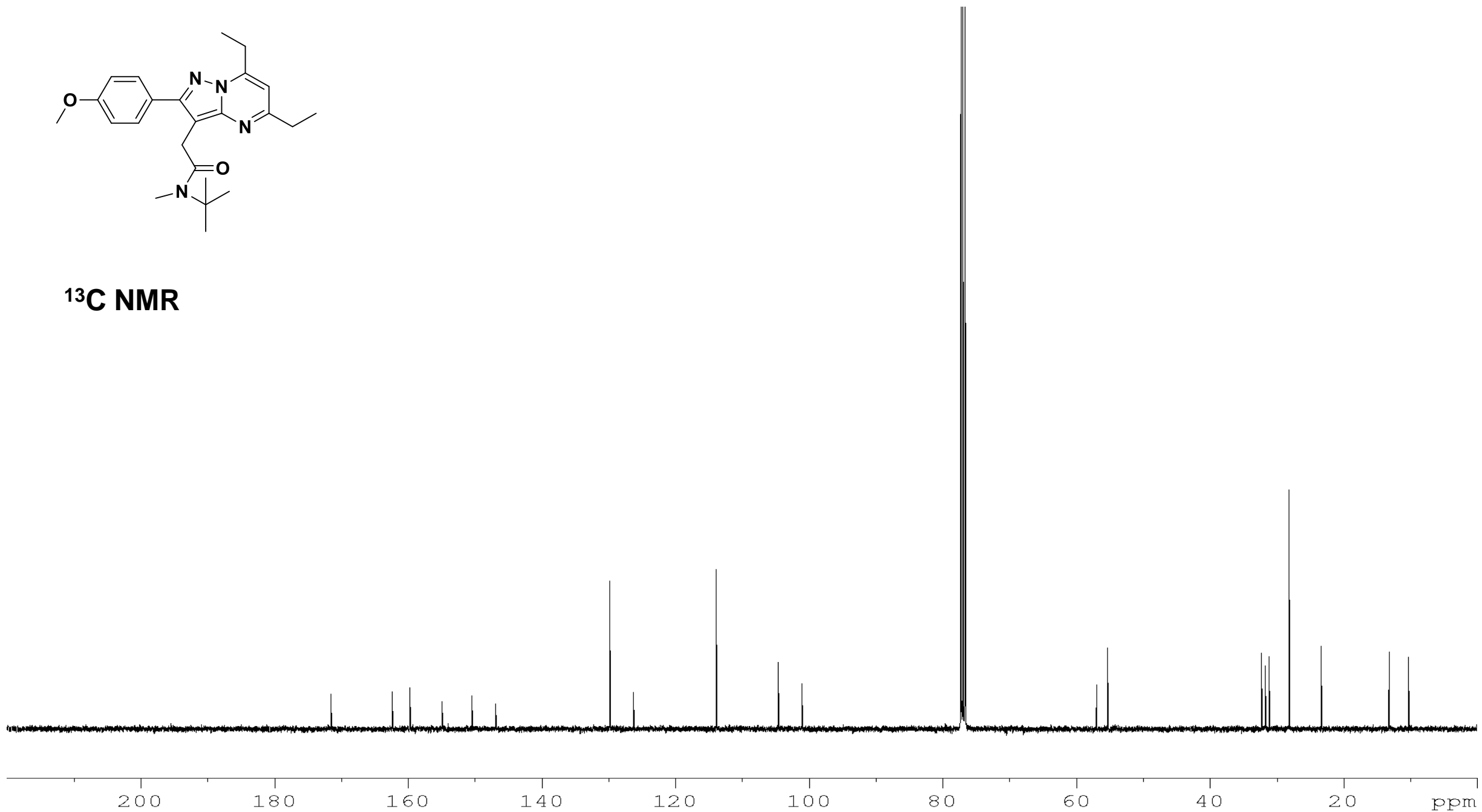


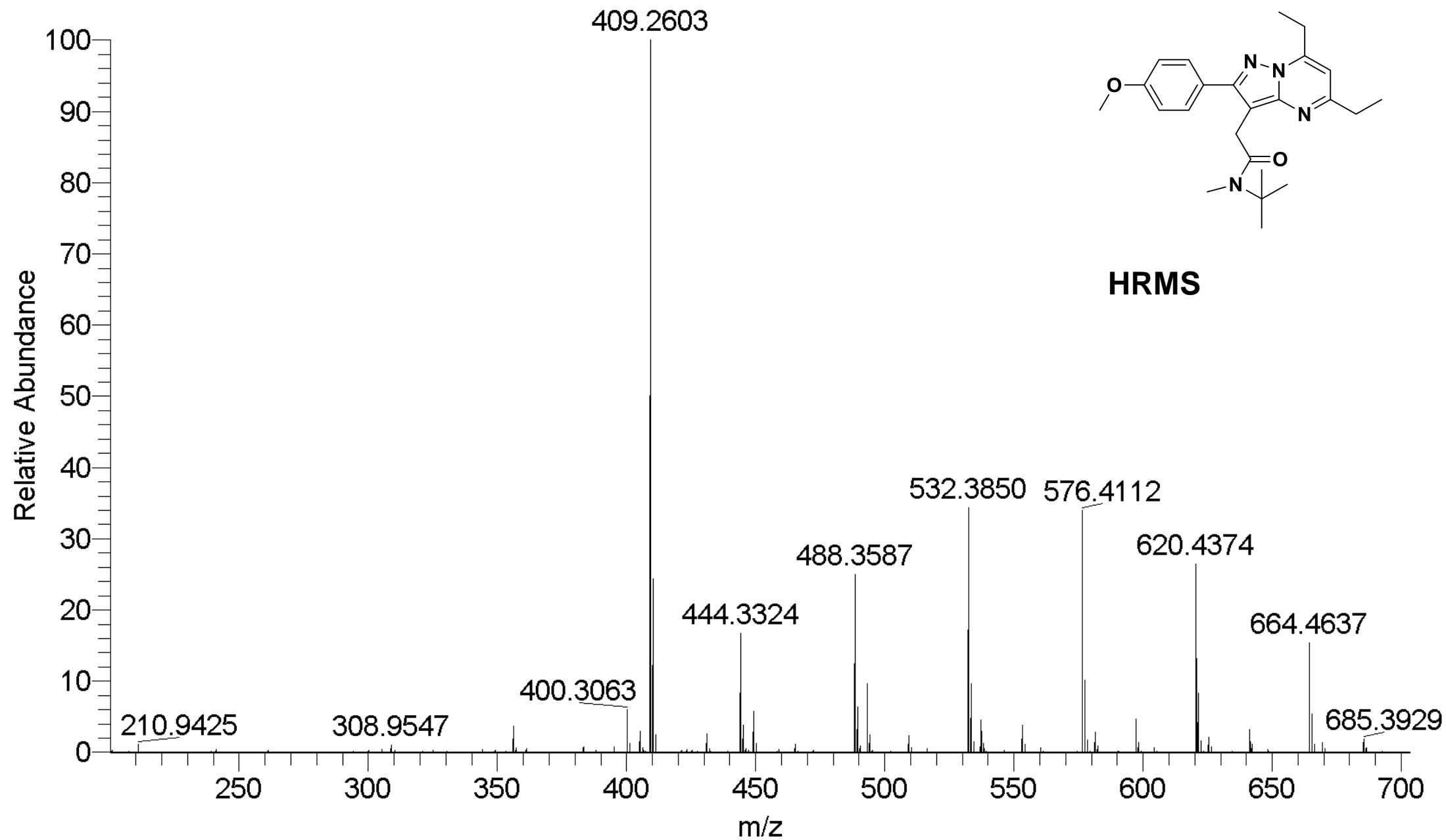
¹H NMR

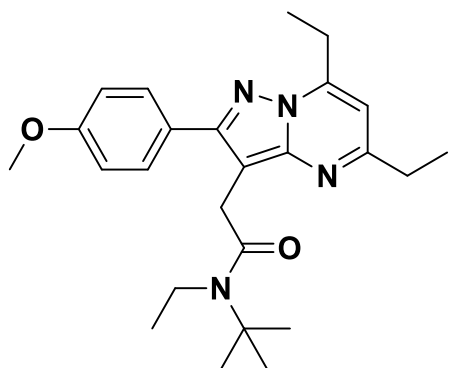




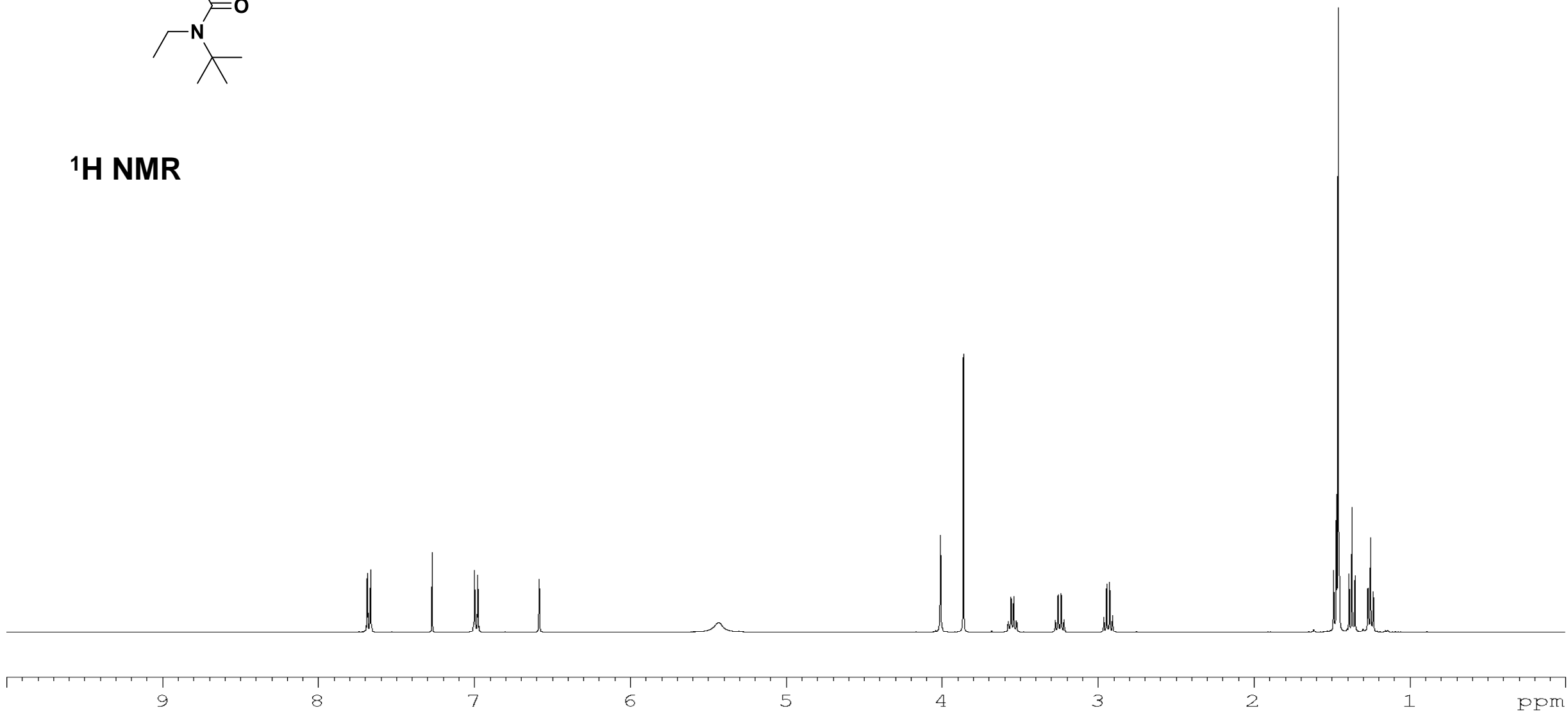
^{13}C NMR

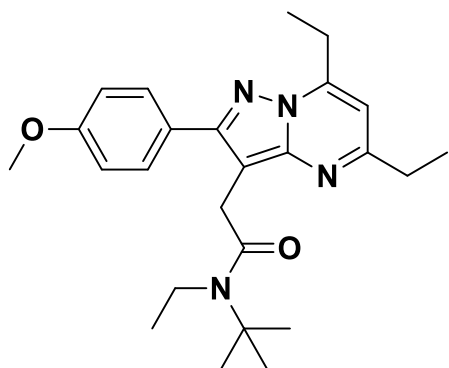




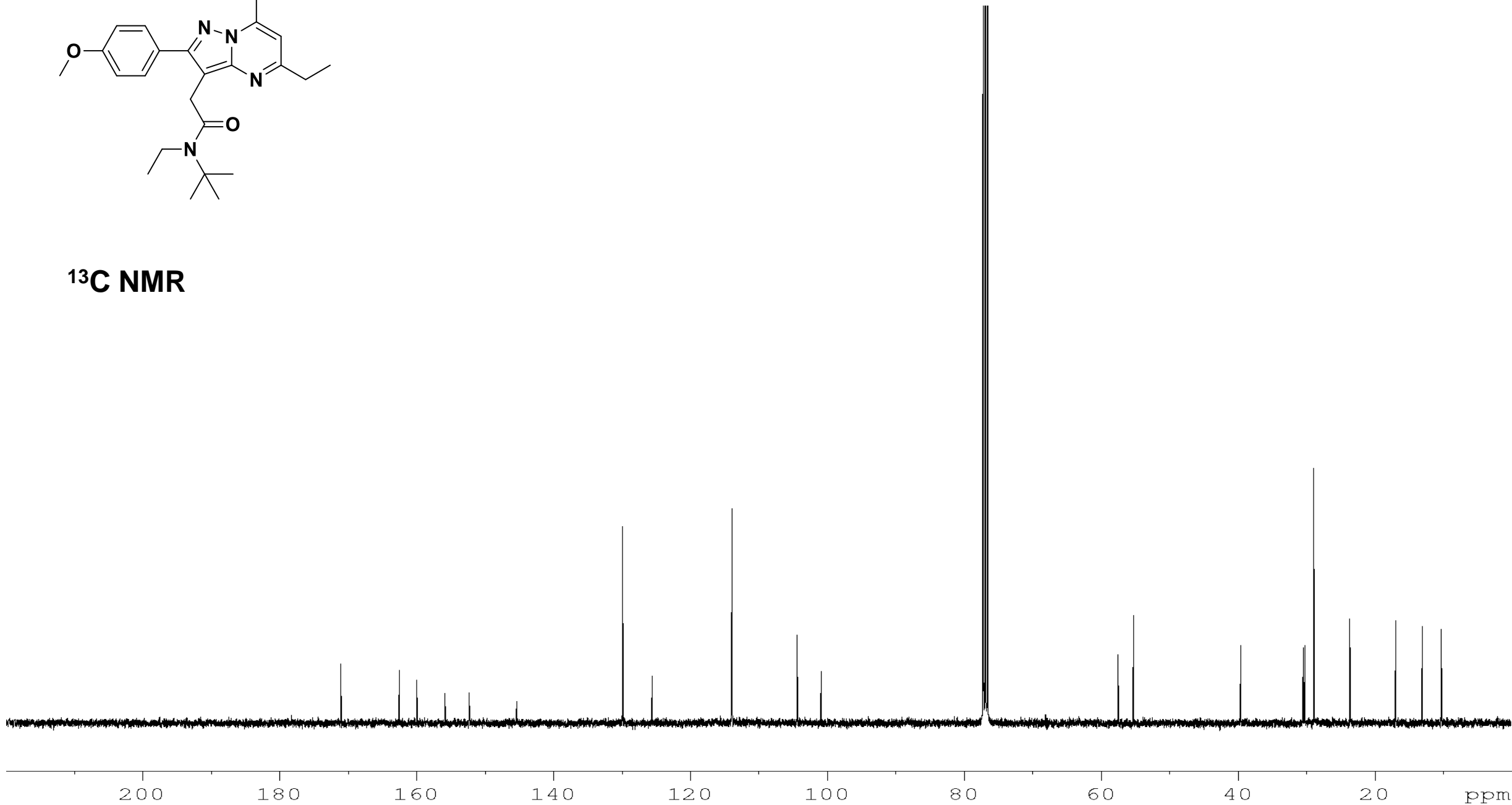


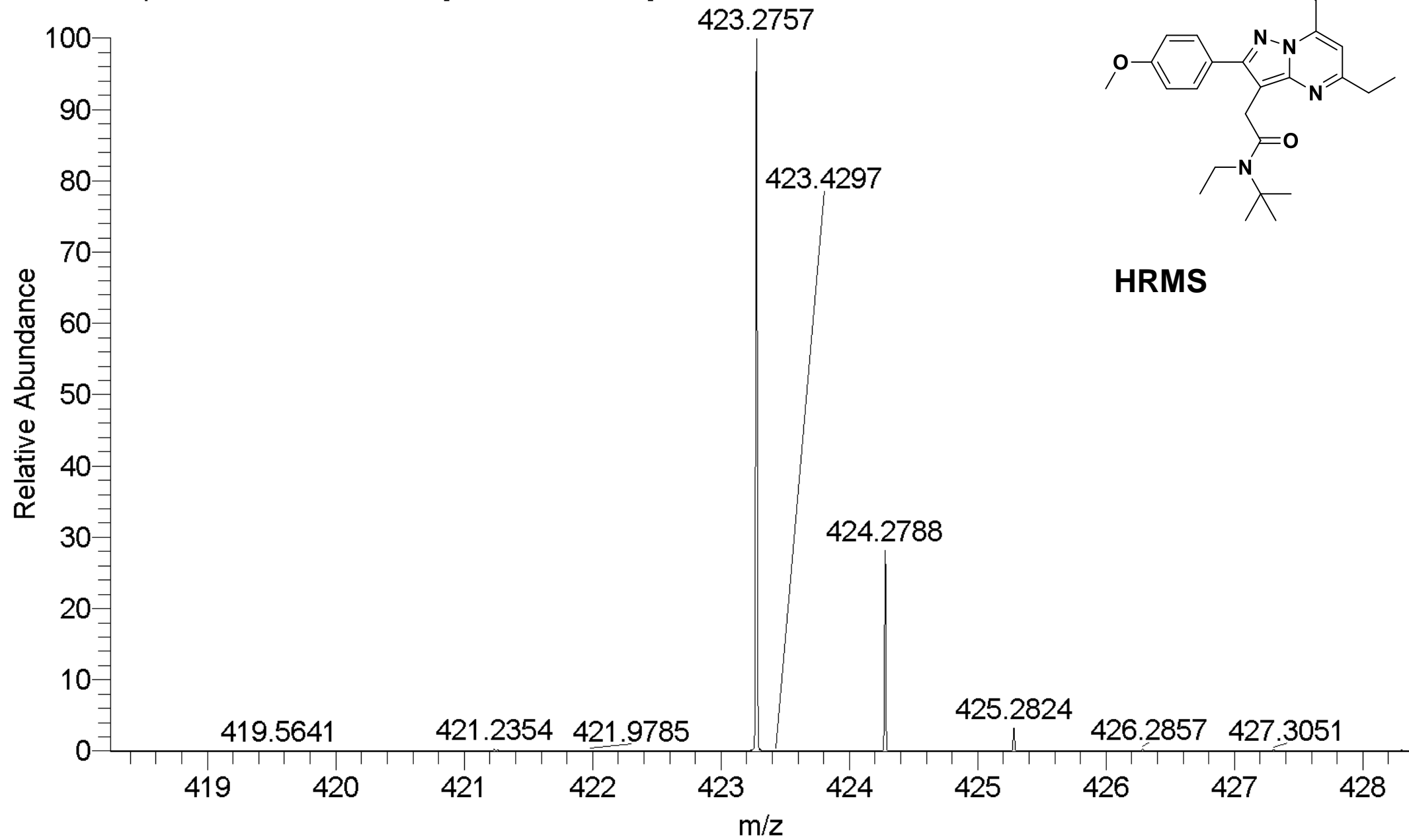
^1H NMR

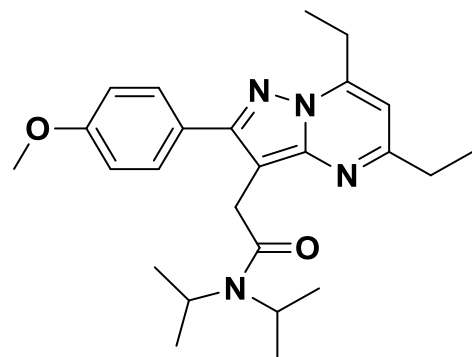




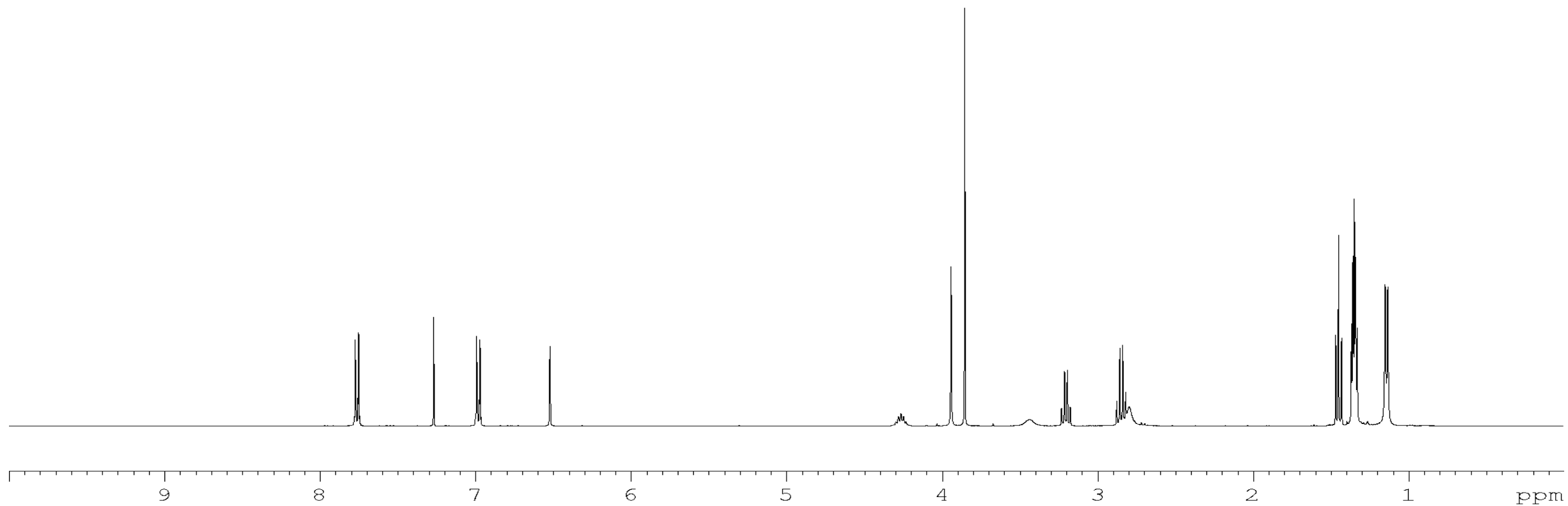
^{13}C NMR

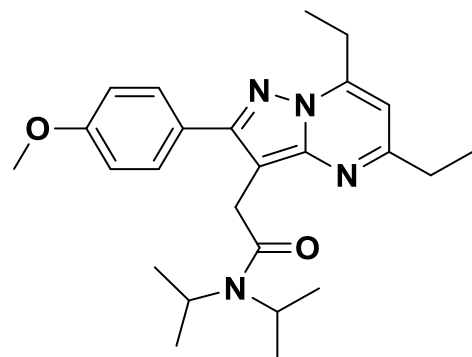




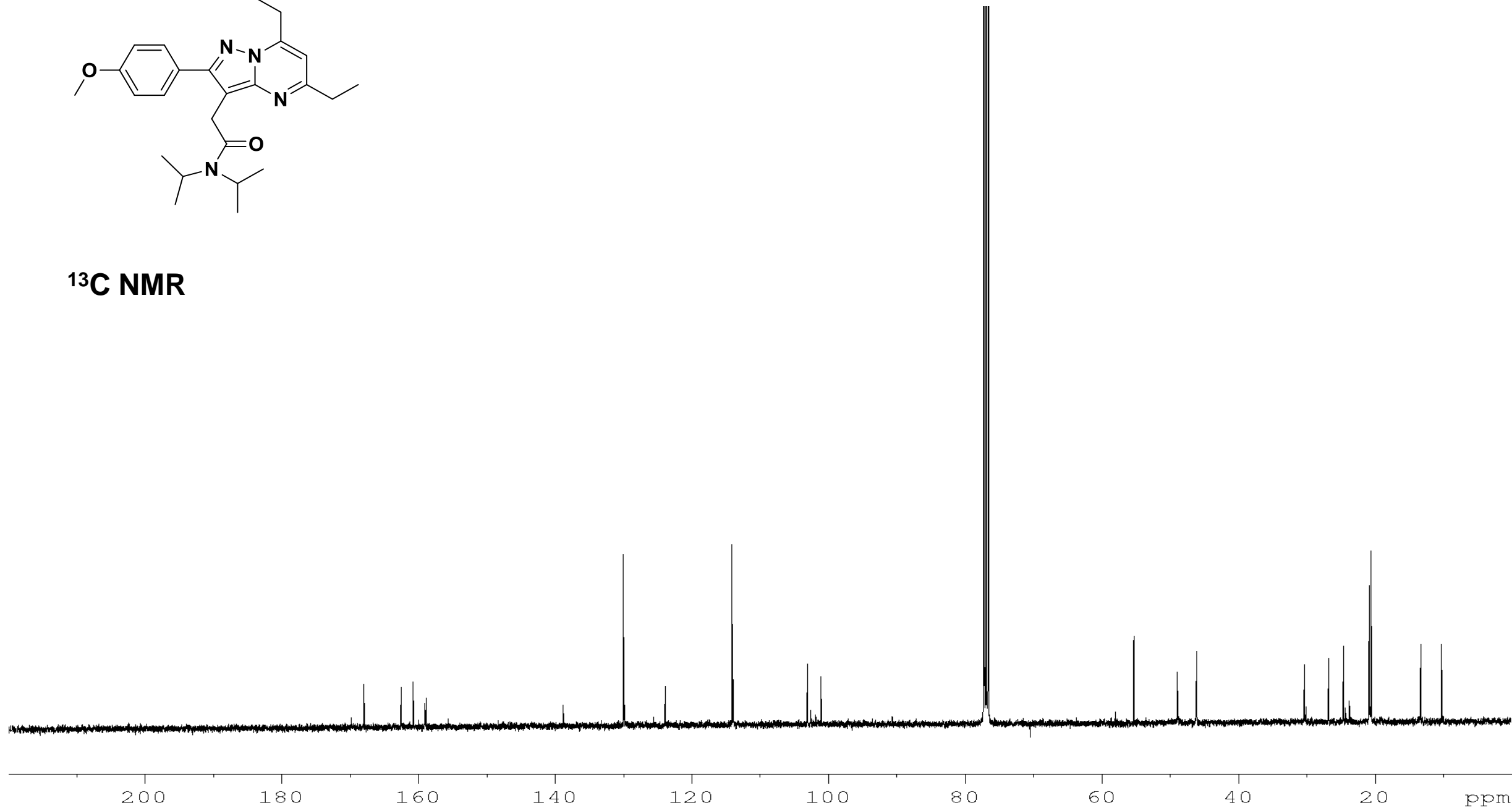


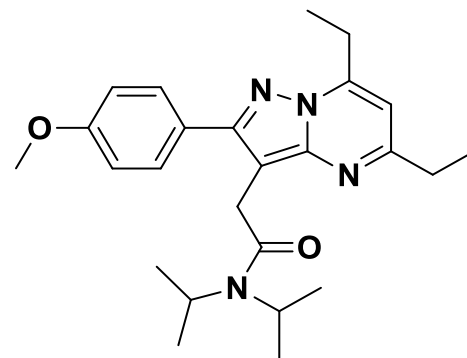
^1H NMR



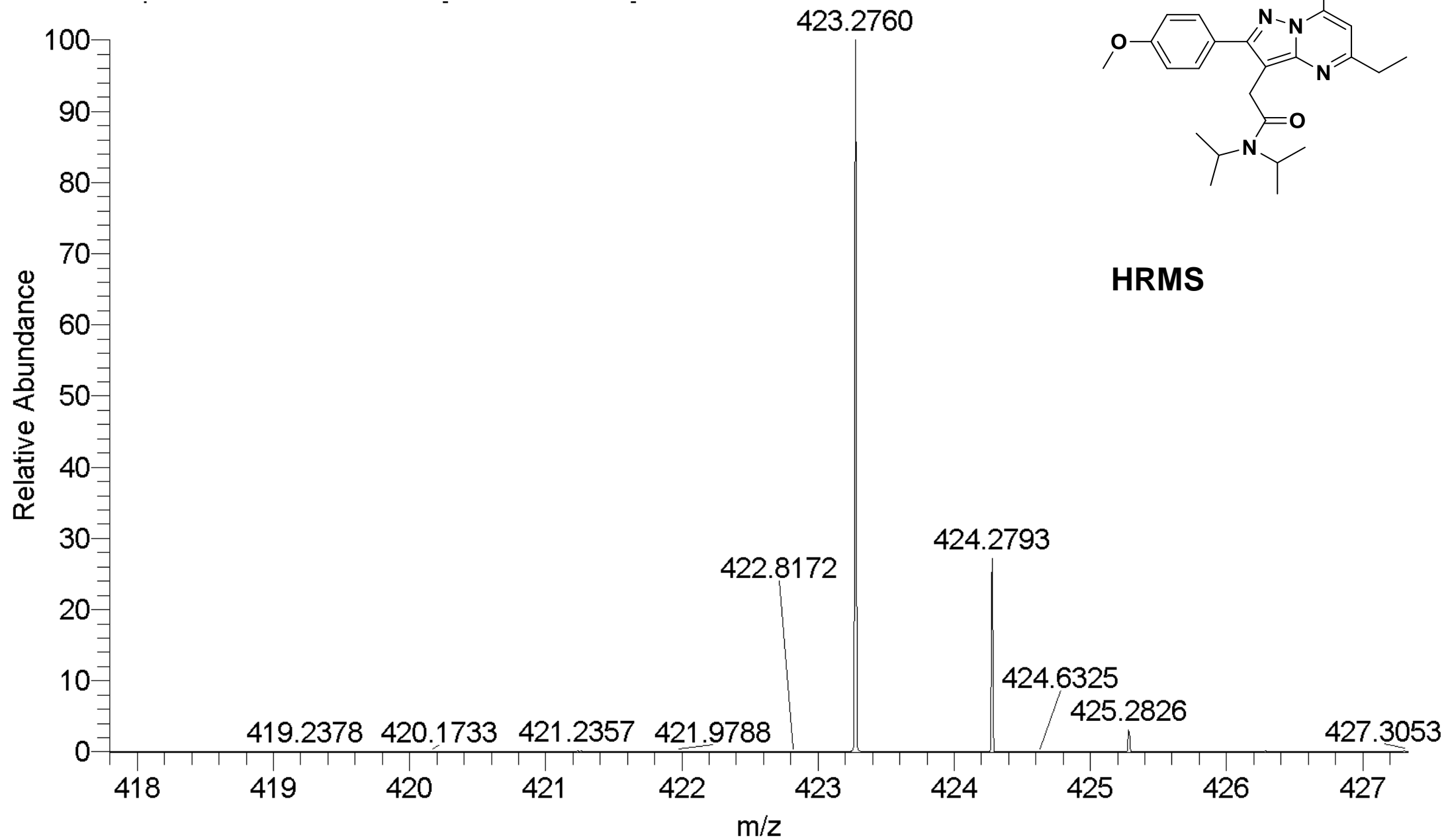


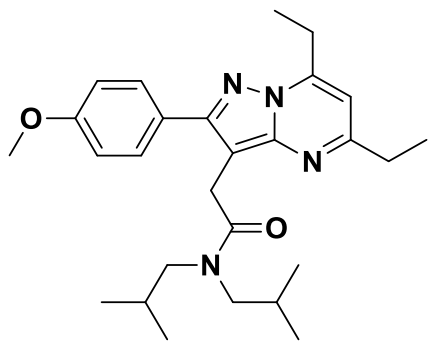
^{13}C NMR



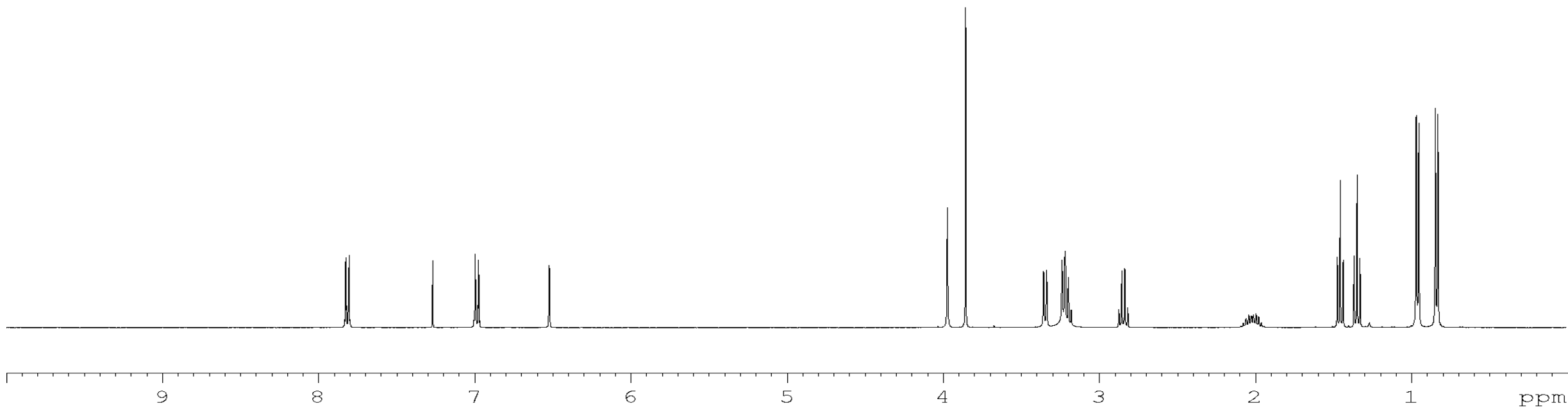


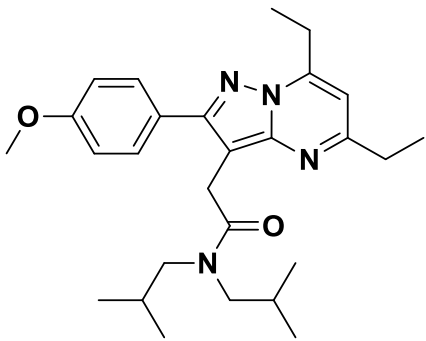
HRMS



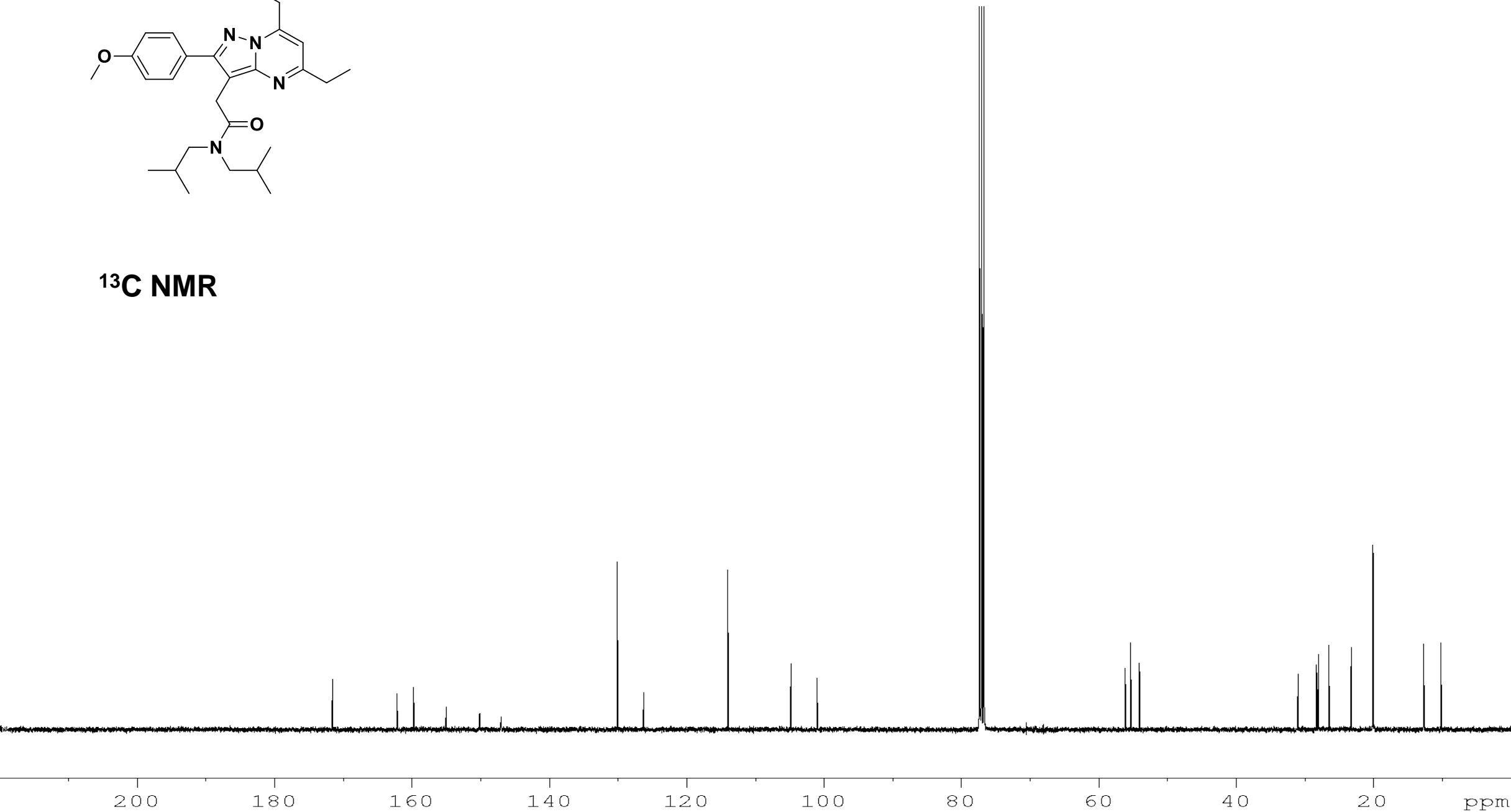


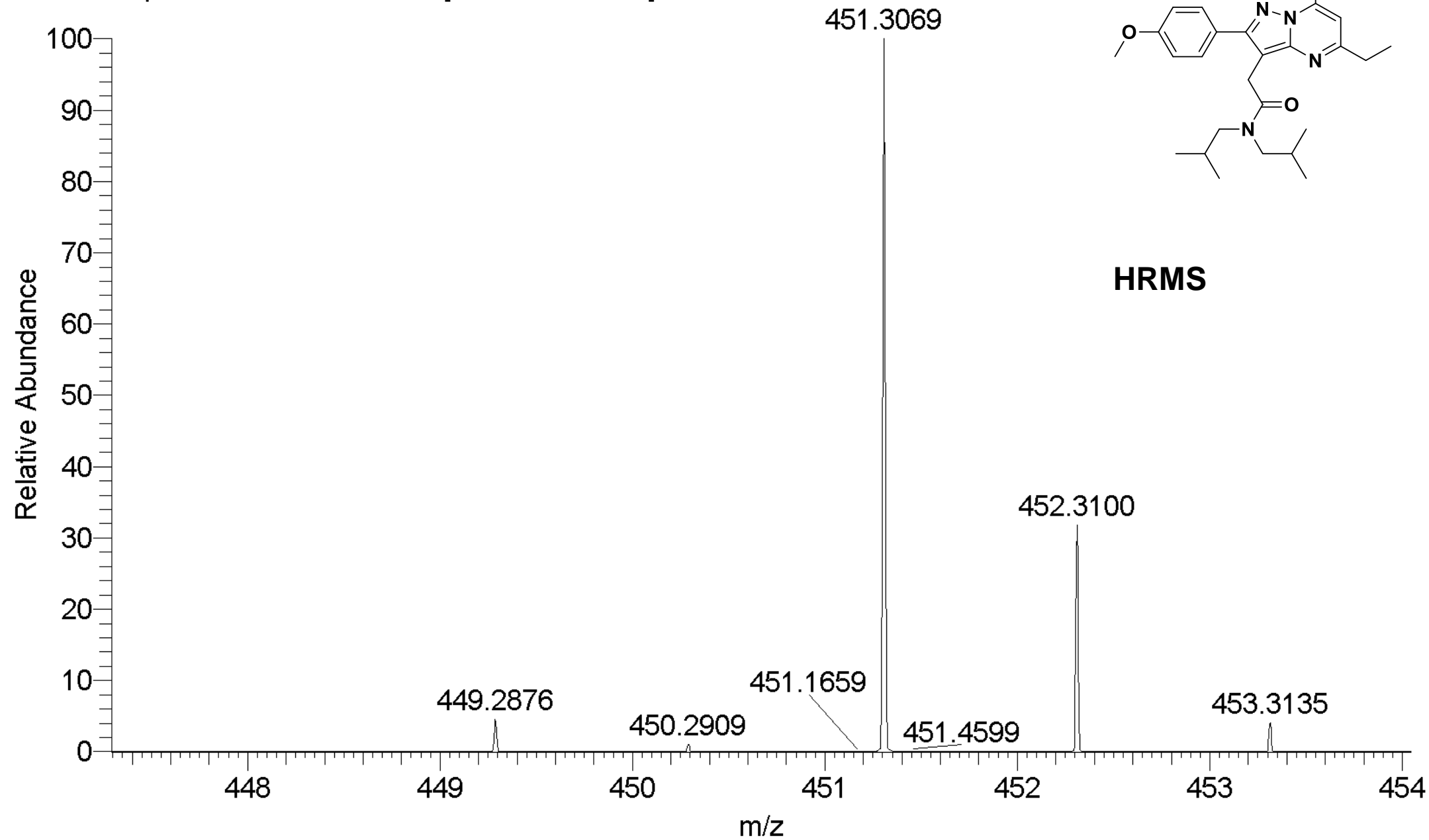
¹H NMR

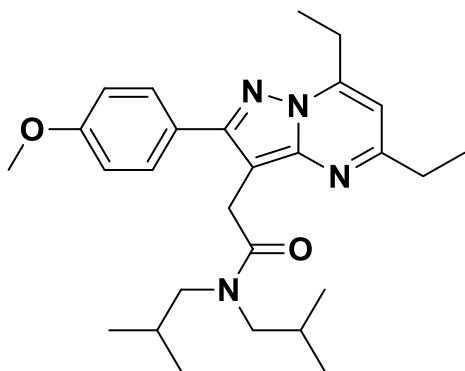




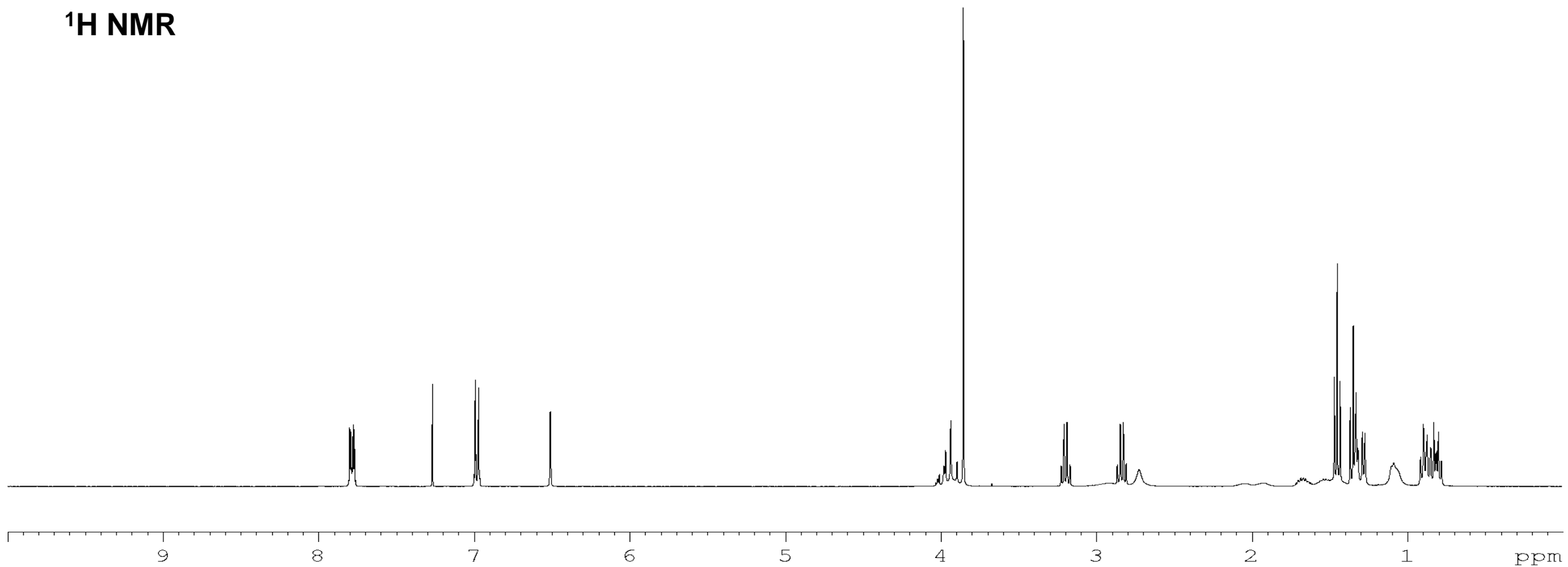
^{13}C NMR

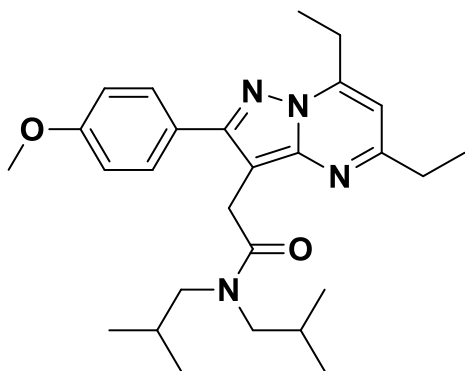




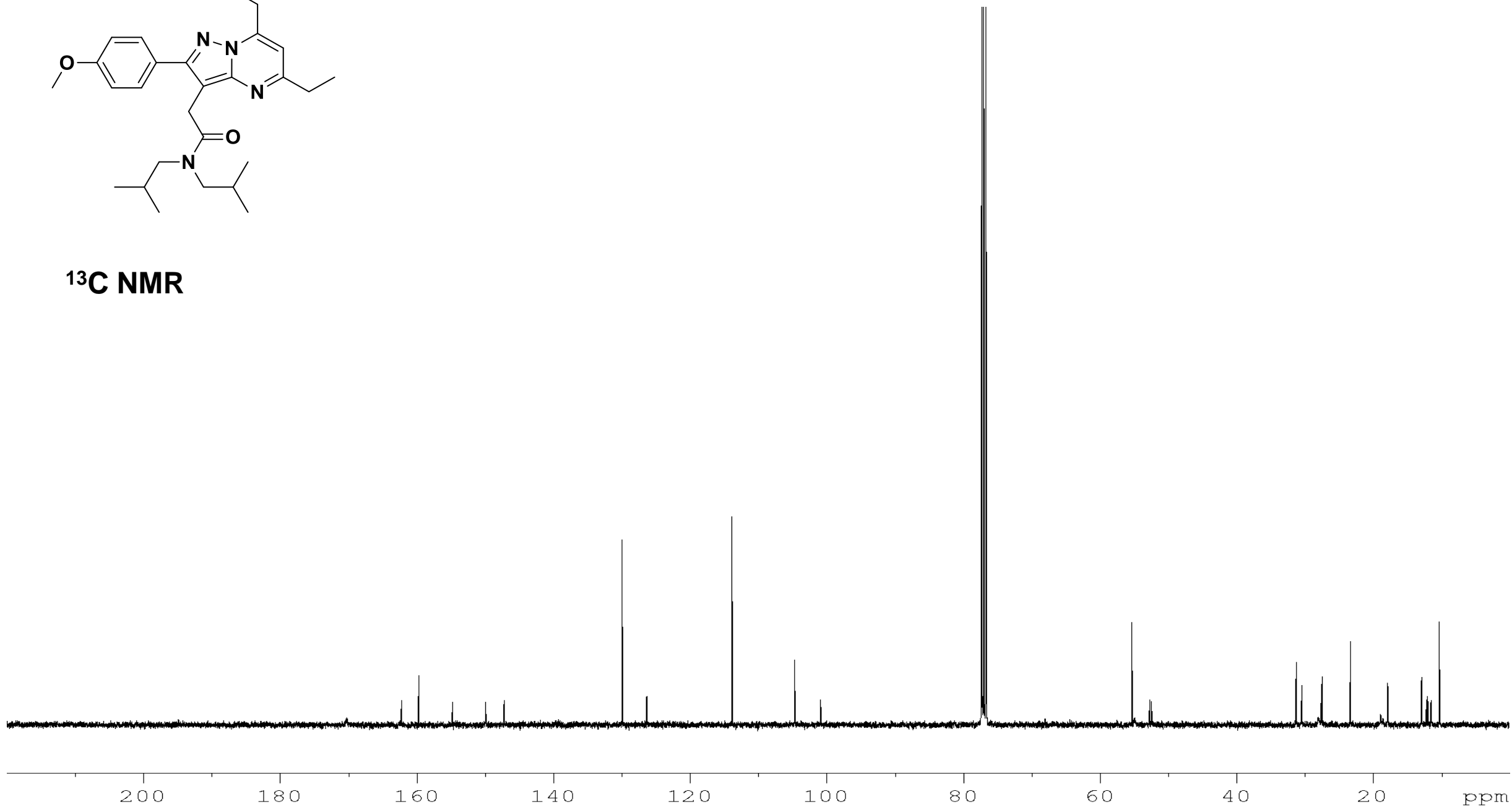


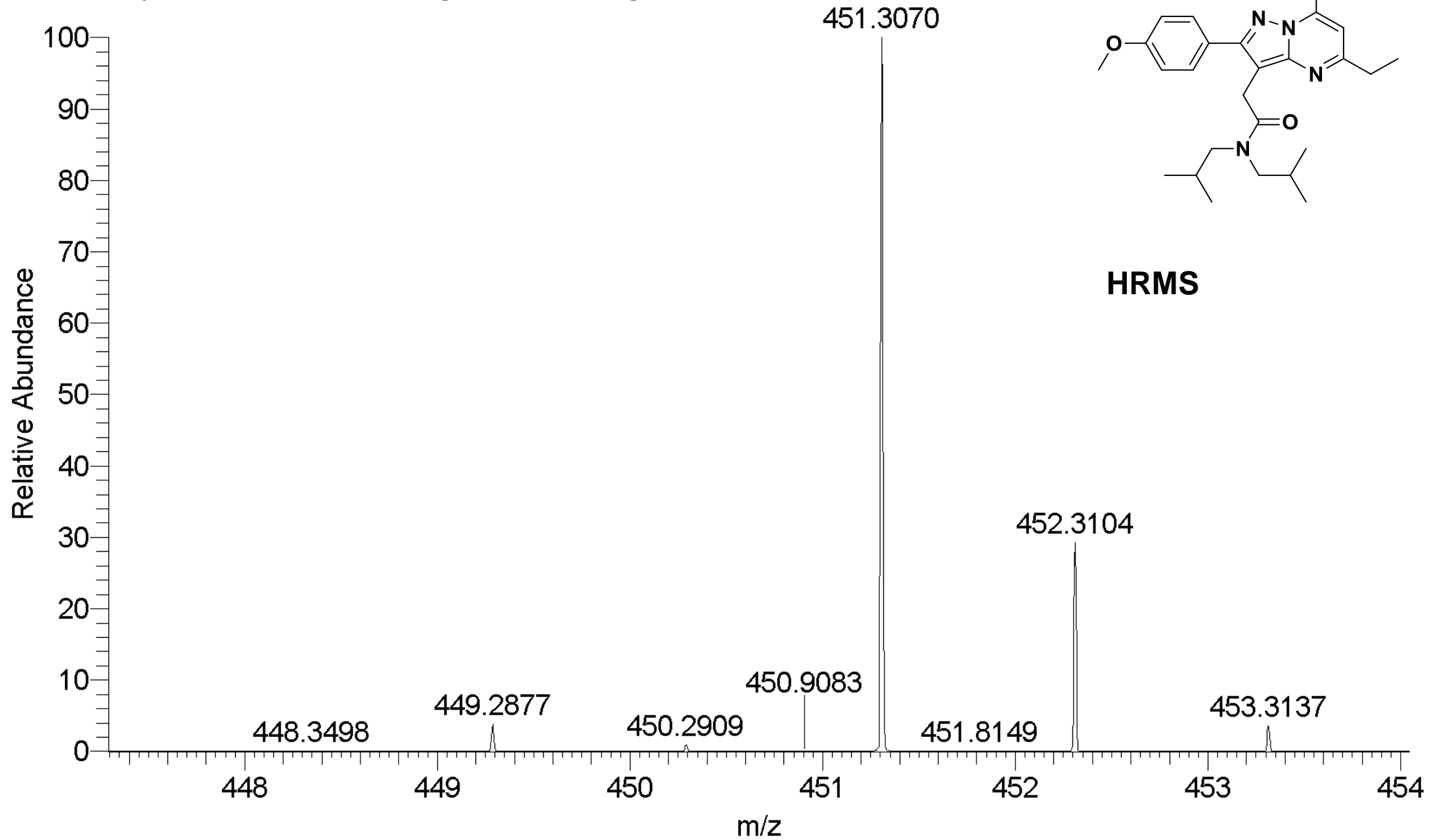
¹H NMR

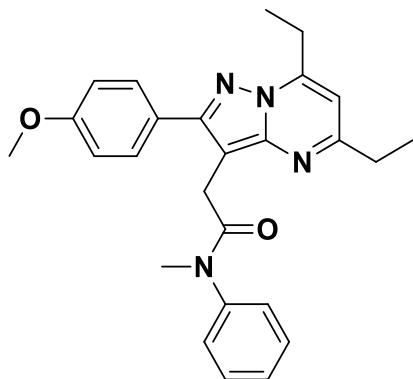




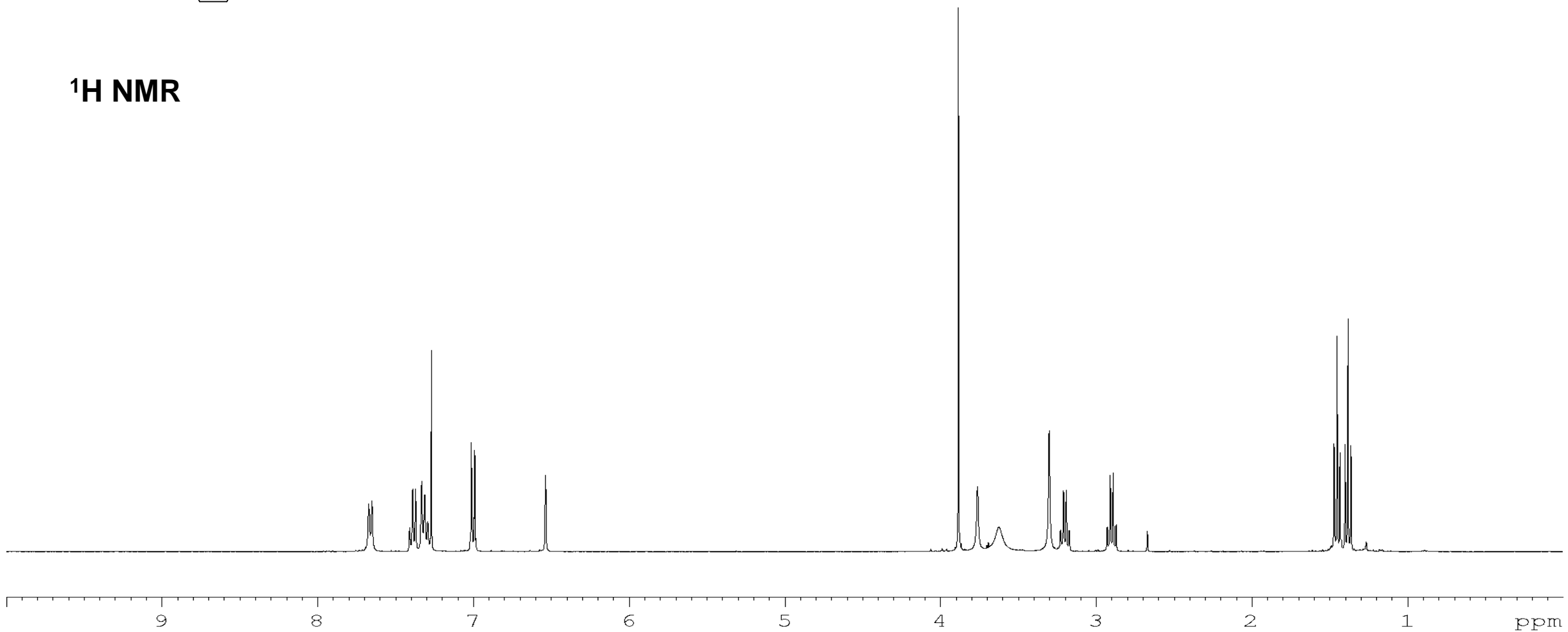
^{13}C NMR

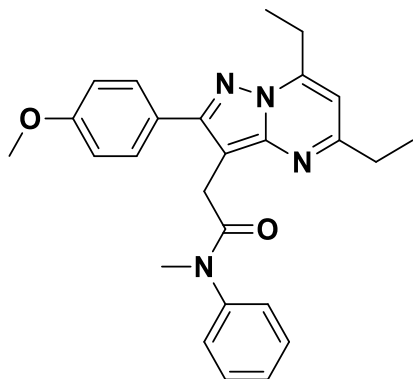




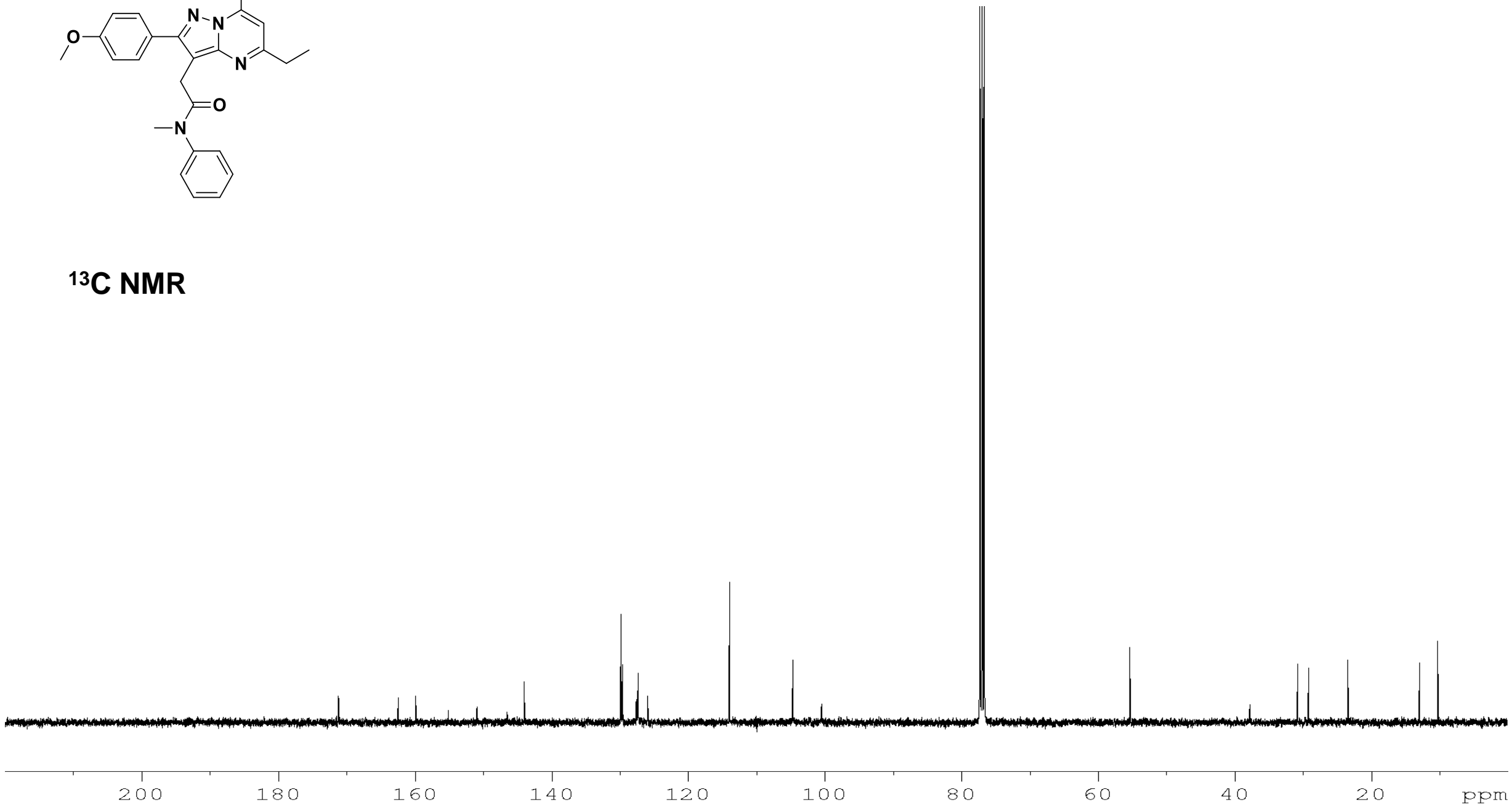


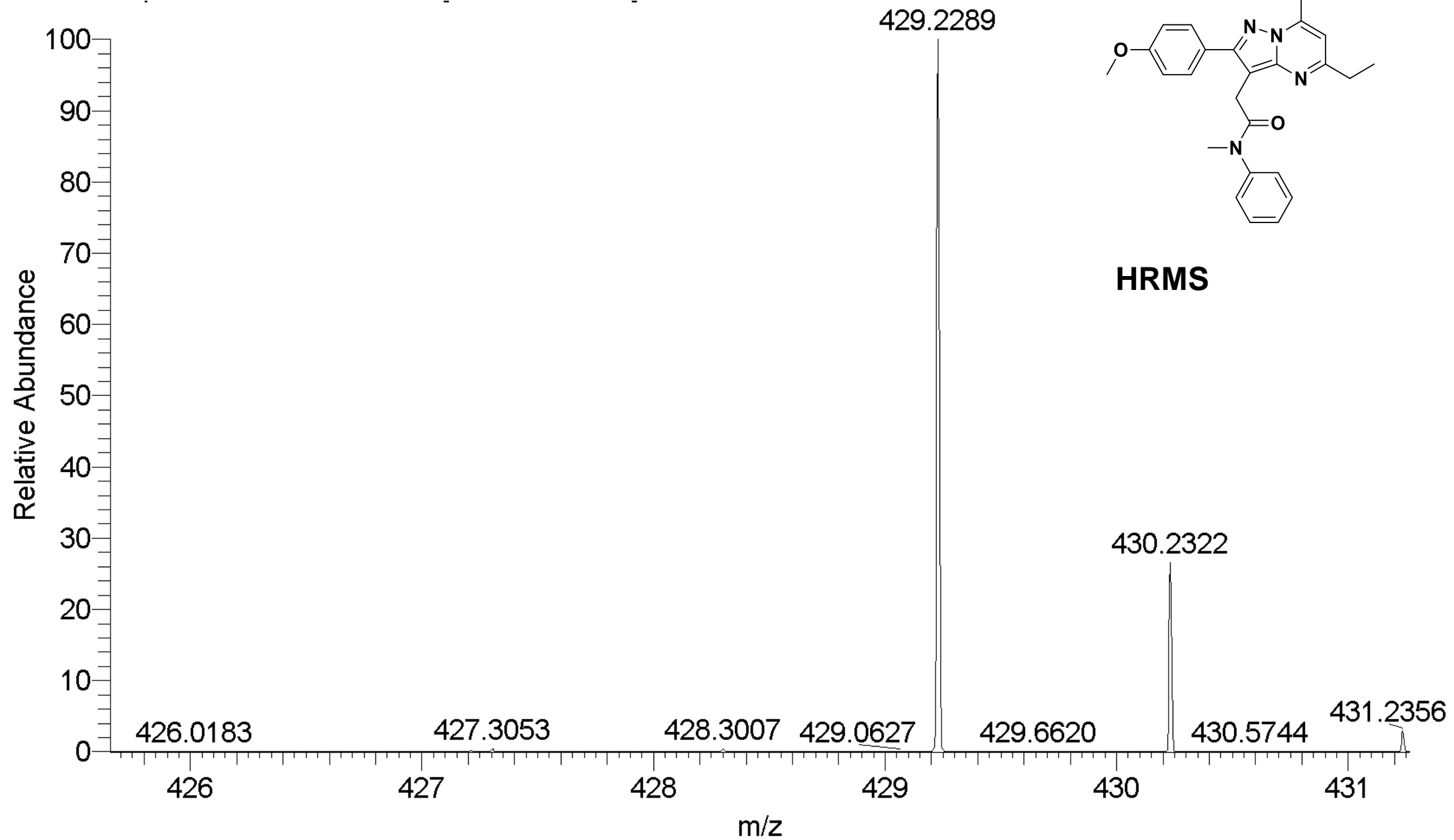
¹H NMR

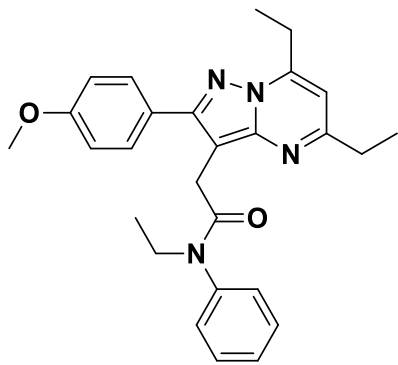




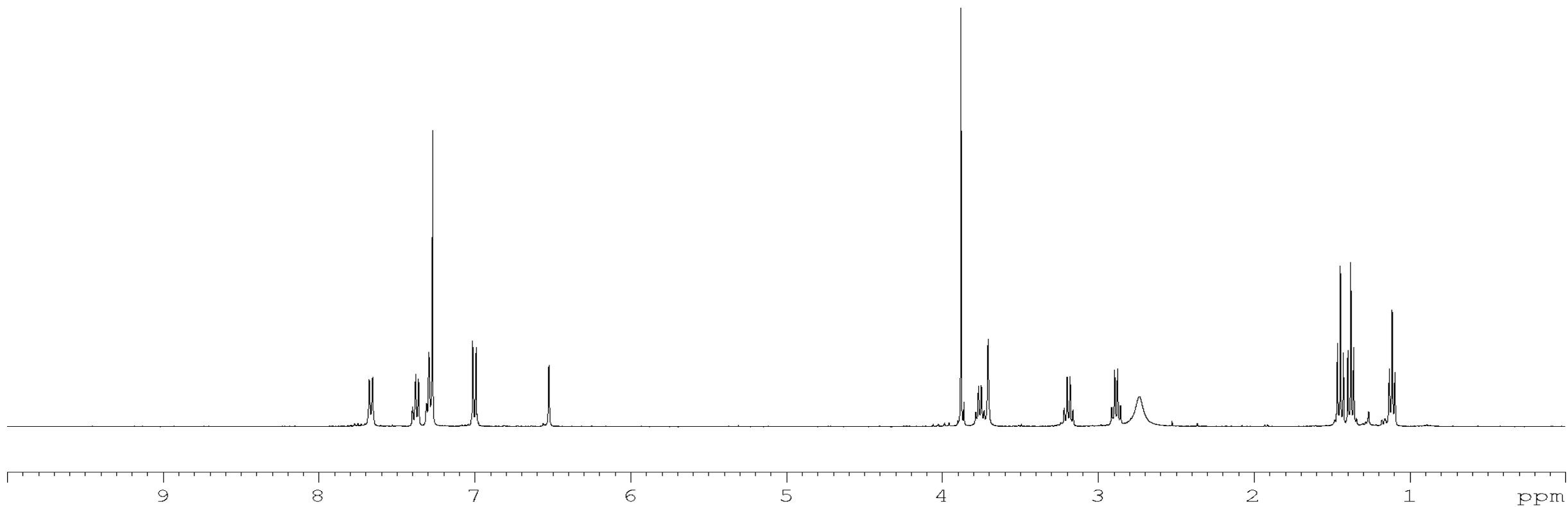
^{13}C NMR

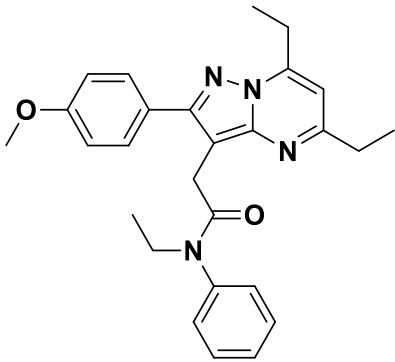




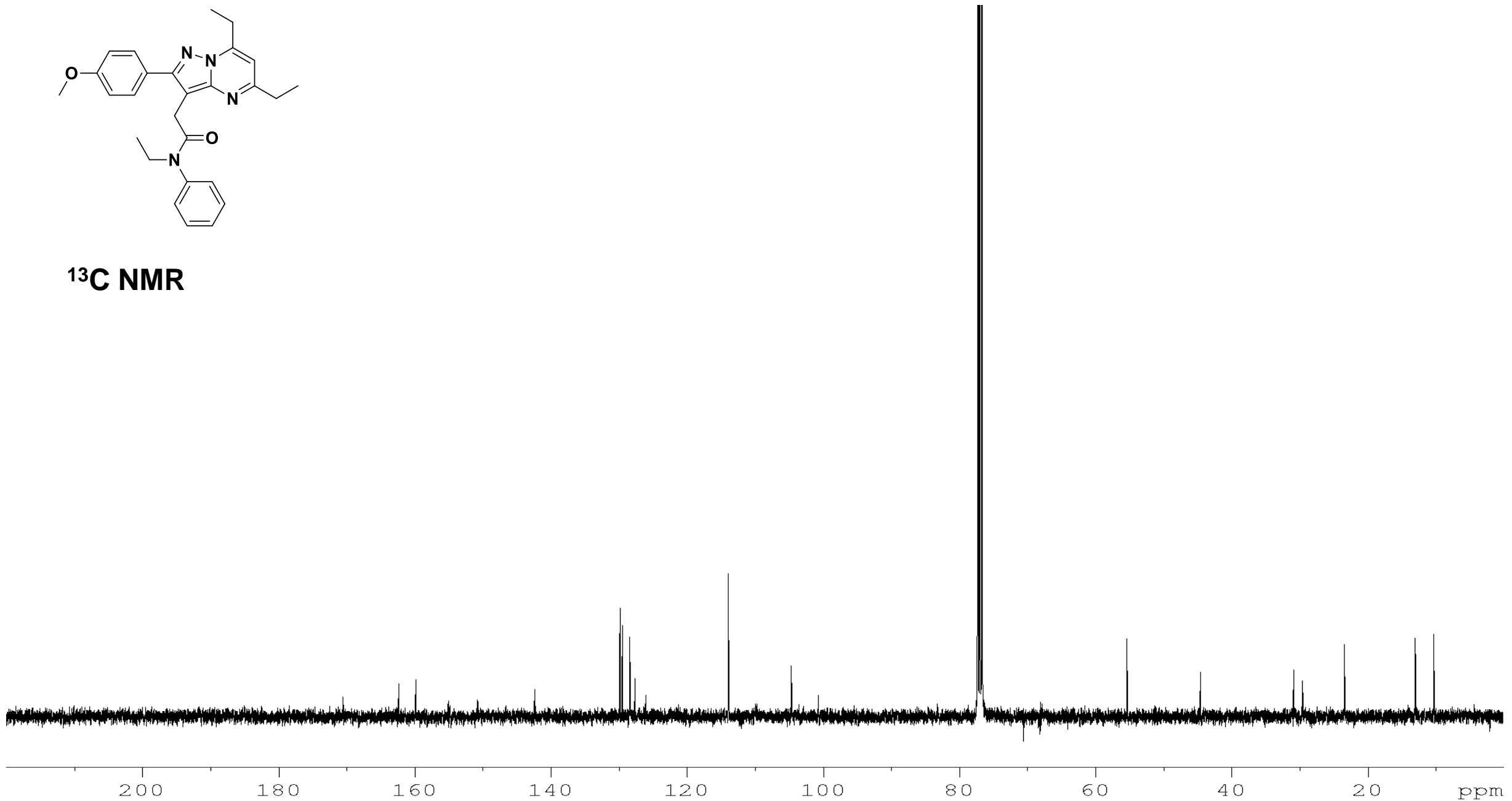


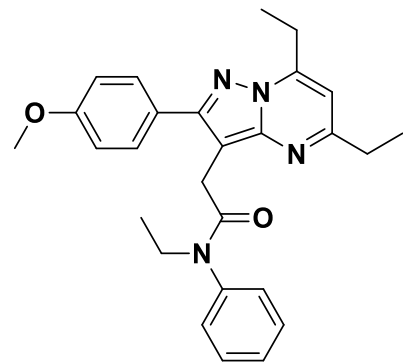
¹H NMR



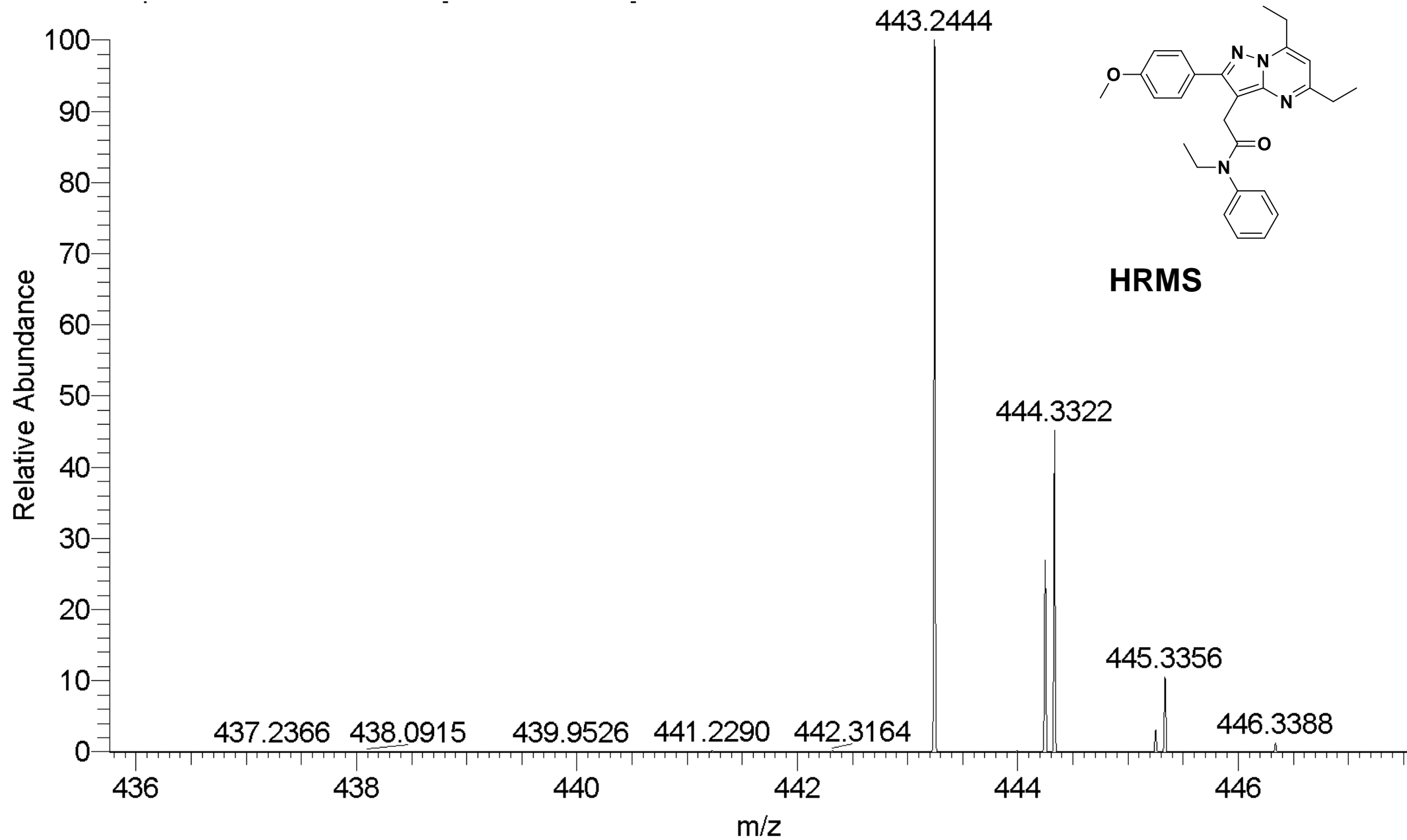


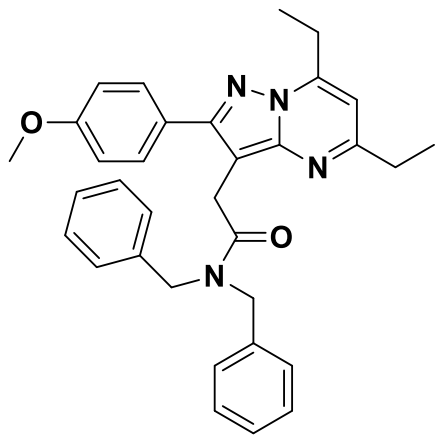
^{13}C NMR



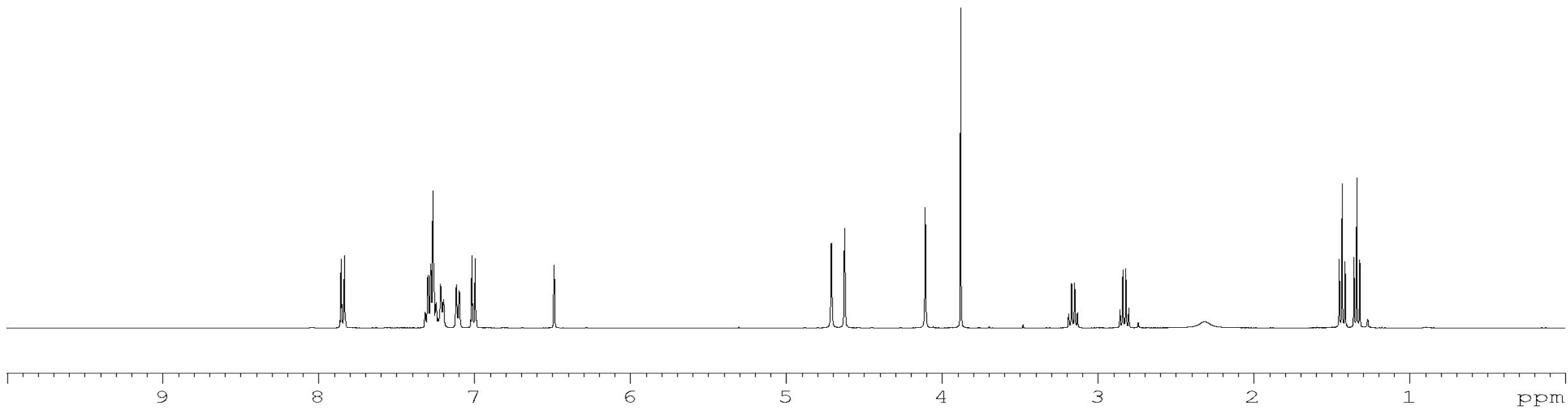


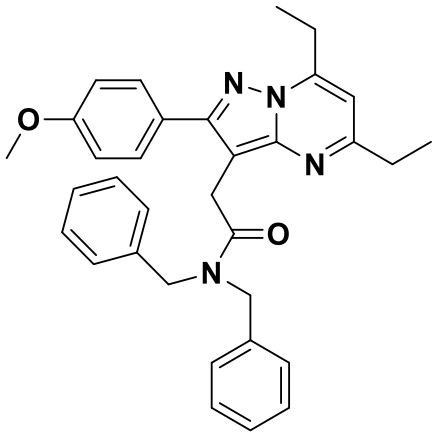
HRMS



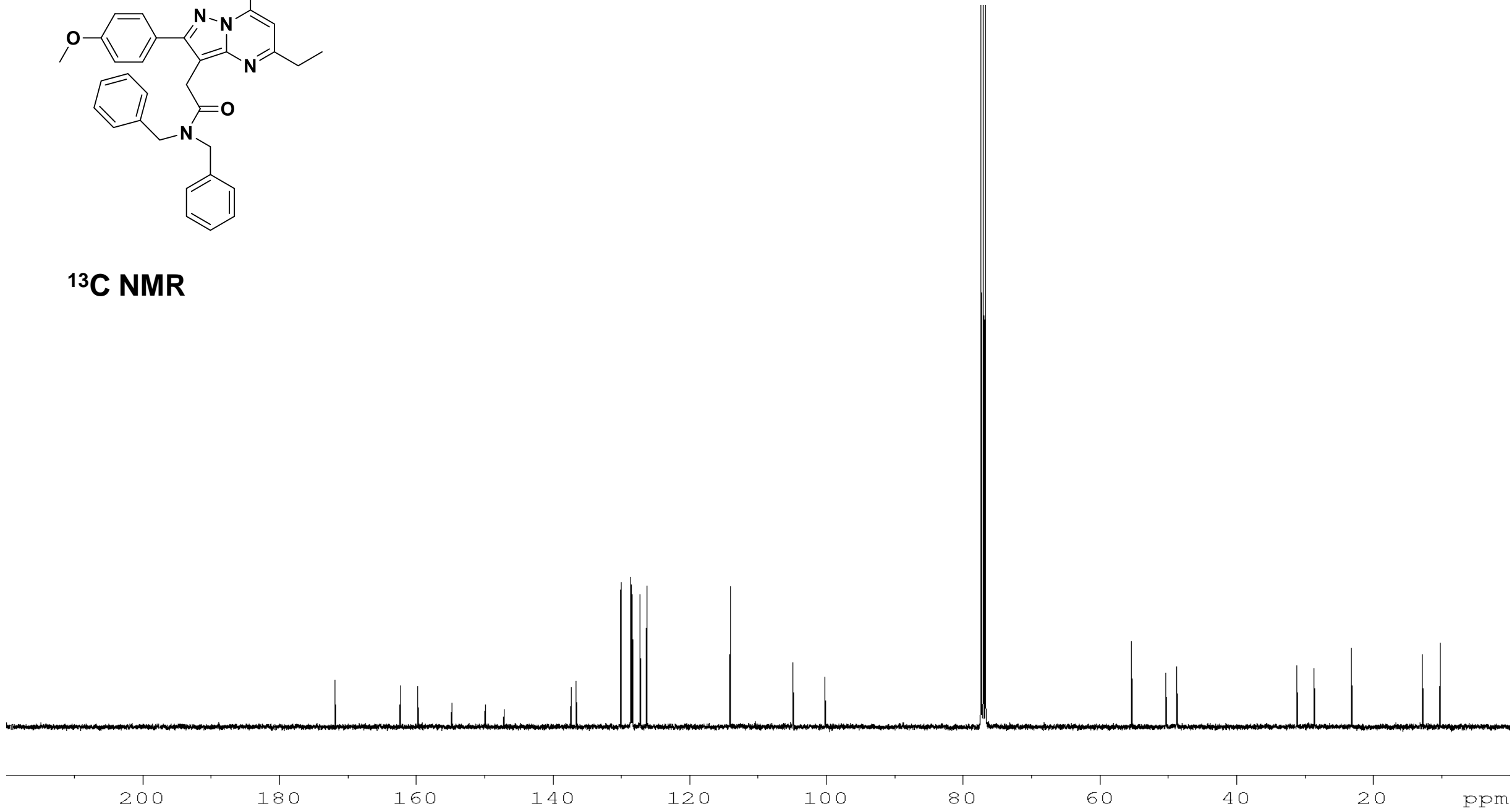


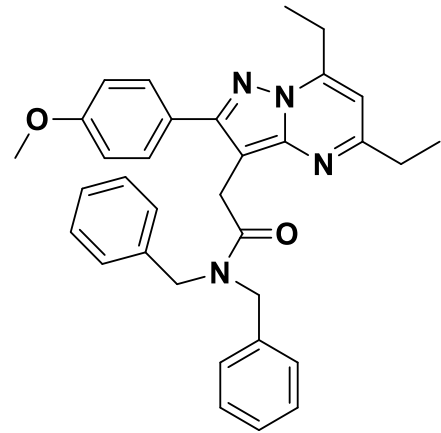
^1H NMR



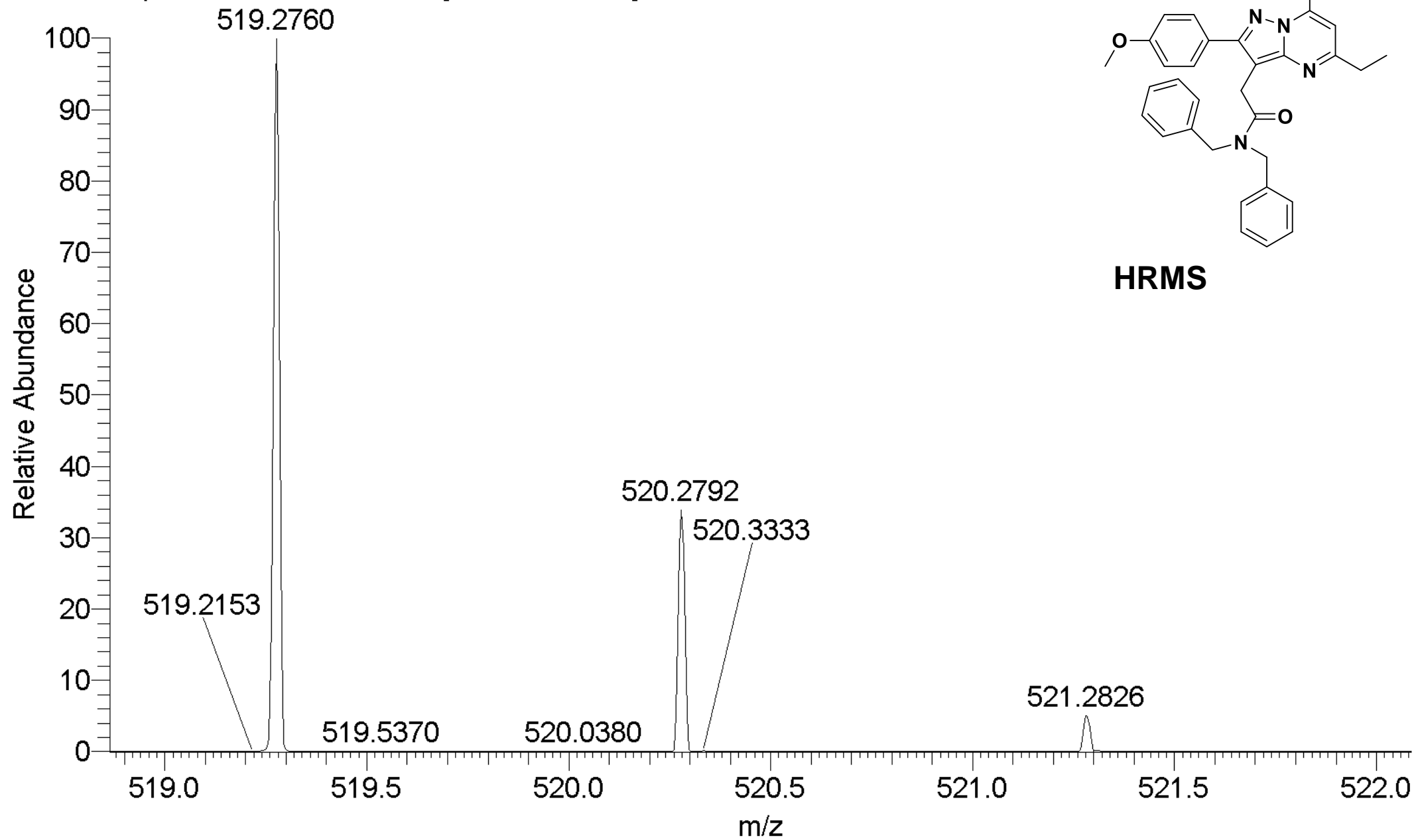


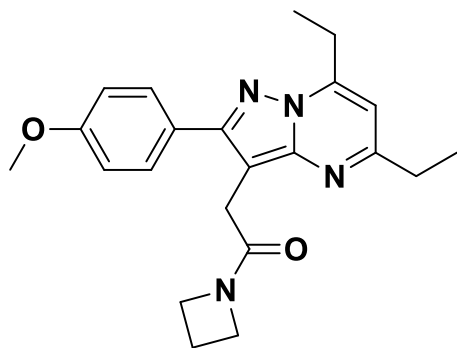
^{13}C NMR



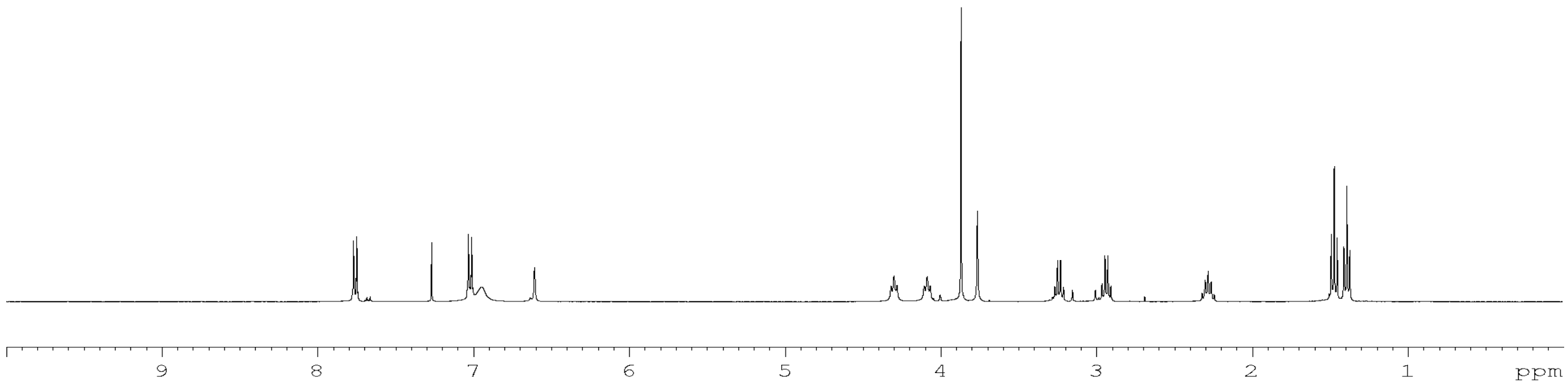


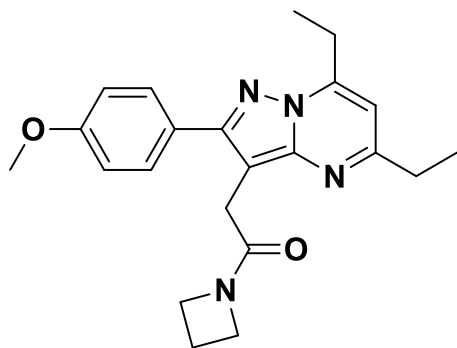
HRMS



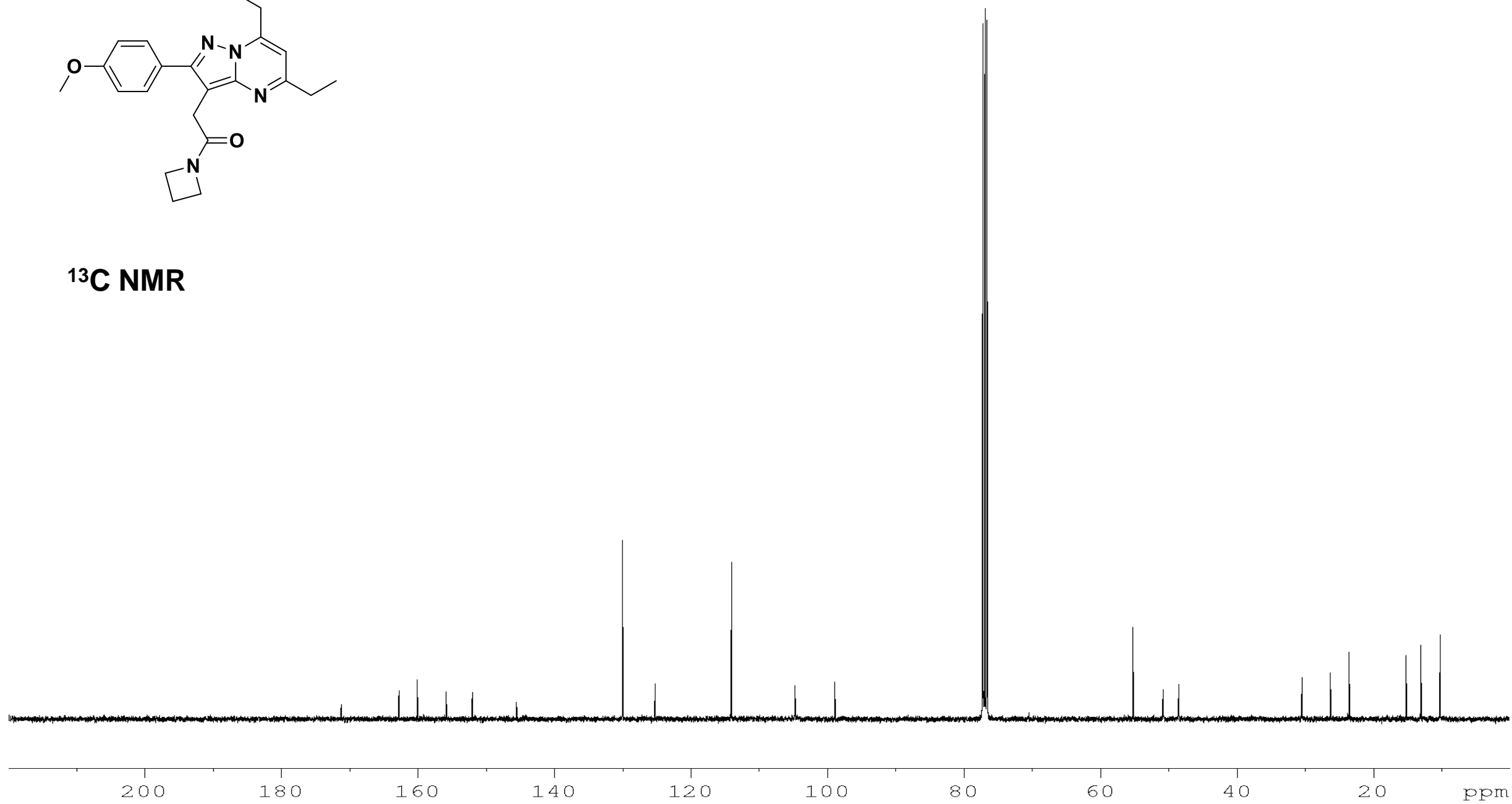


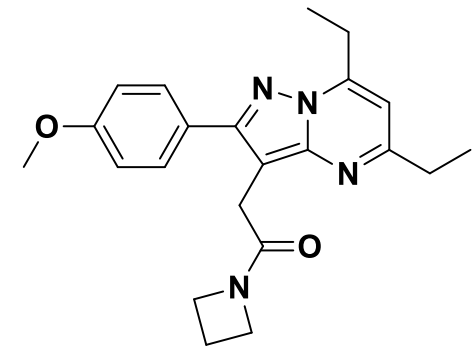
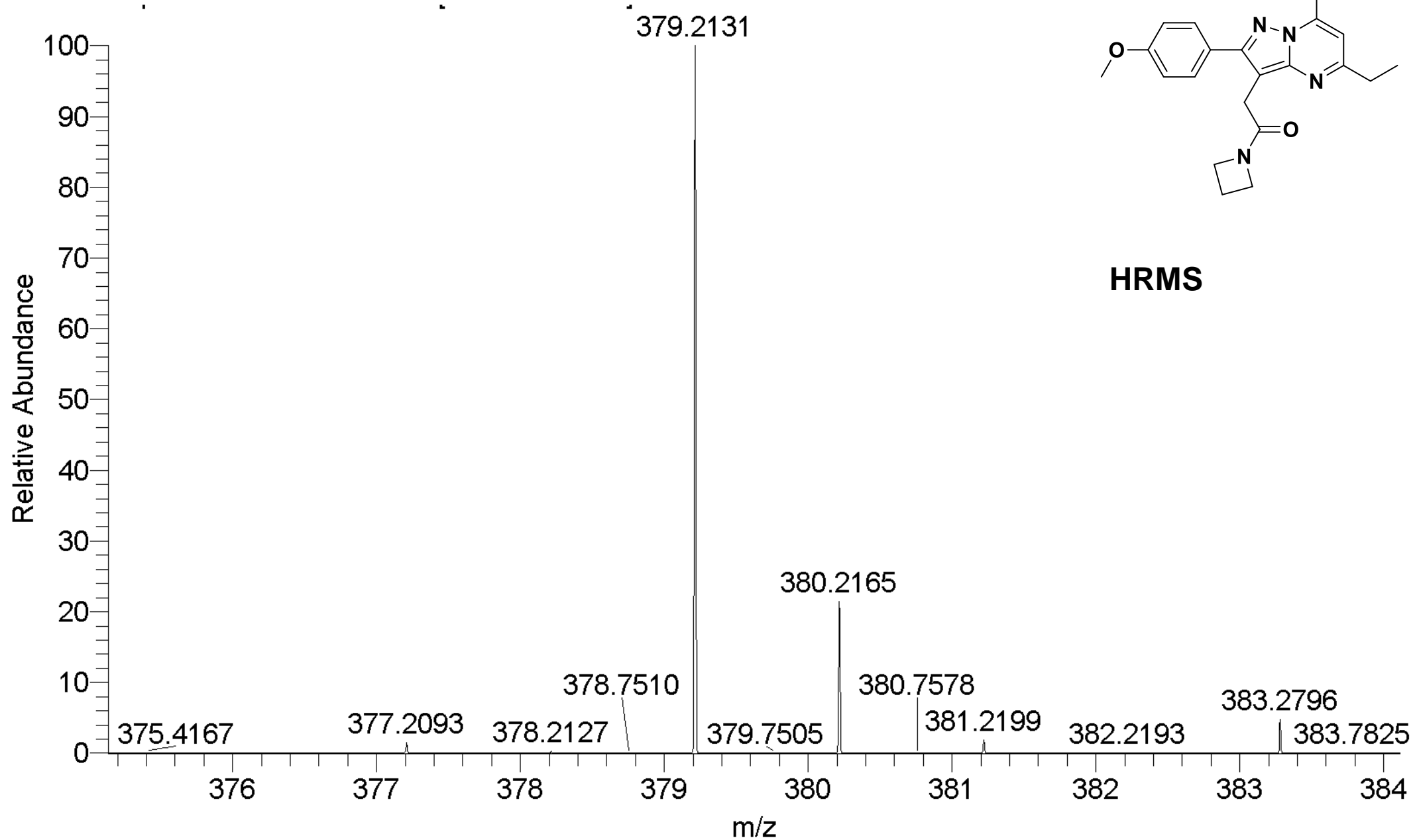
¹H NMR

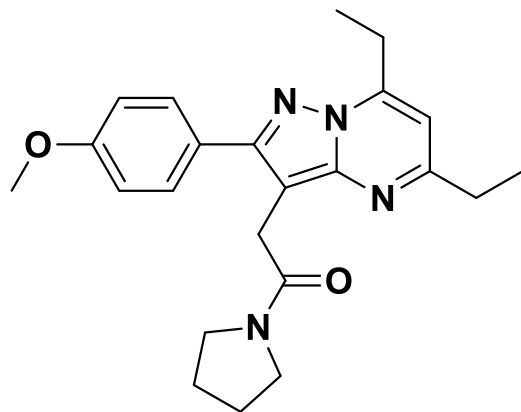




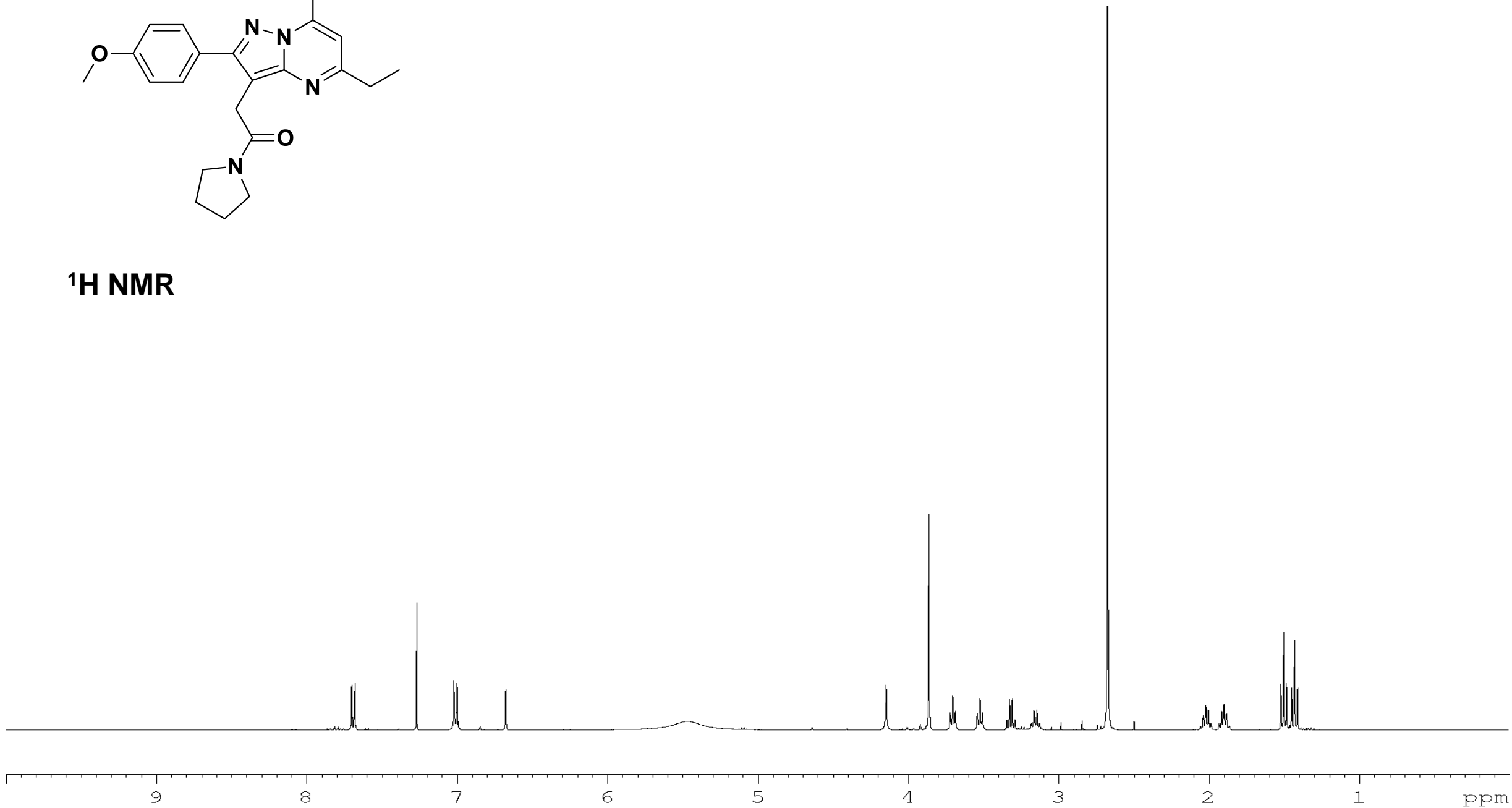
^{13}C NMR

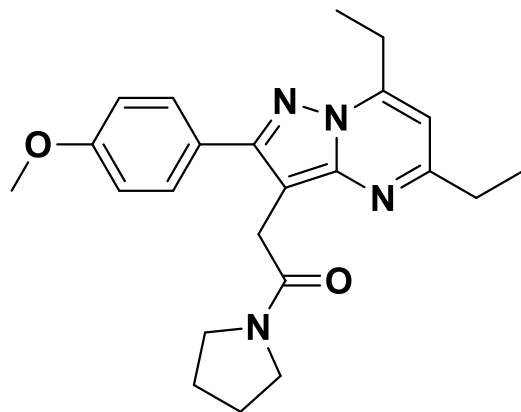




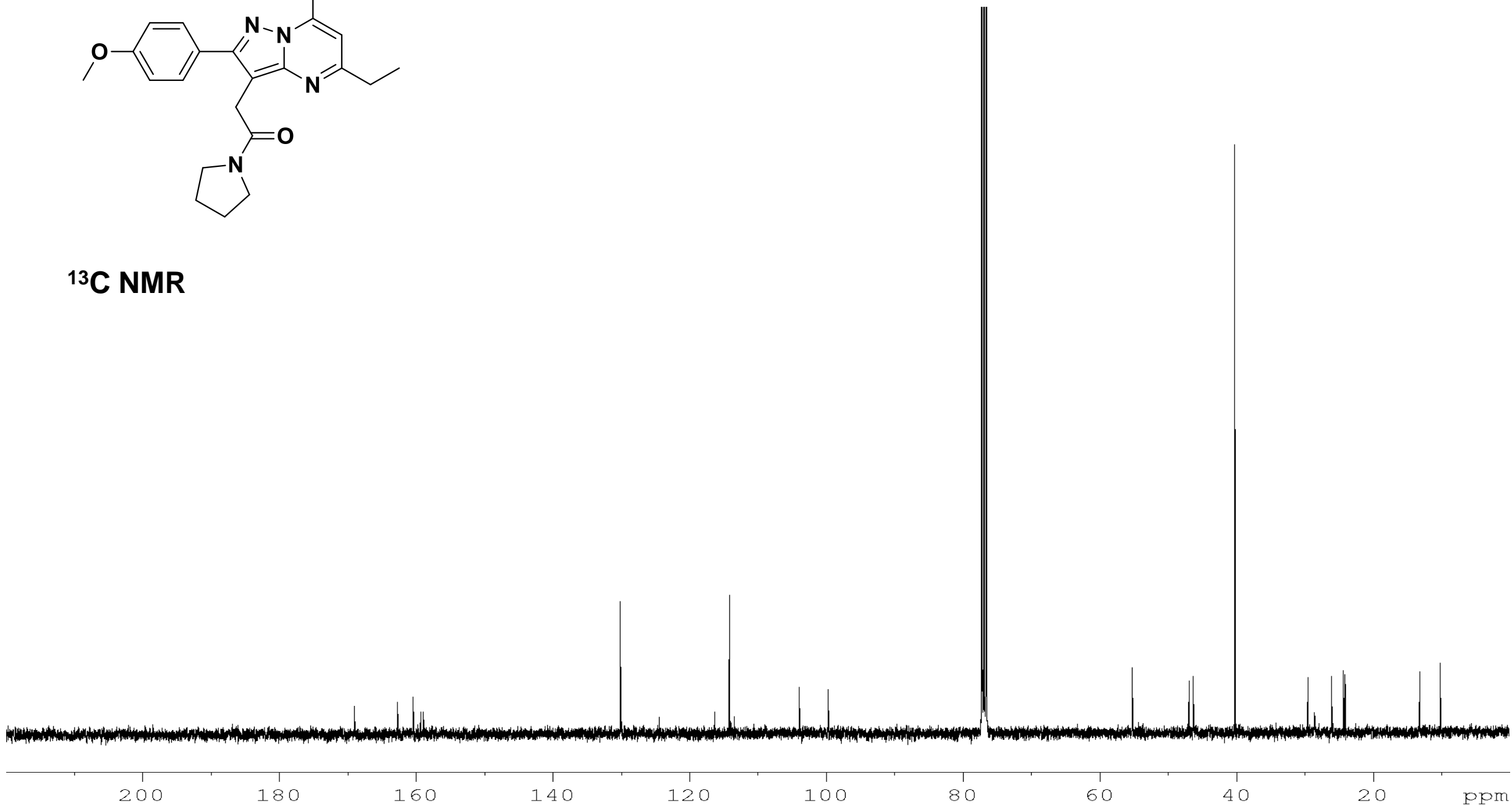


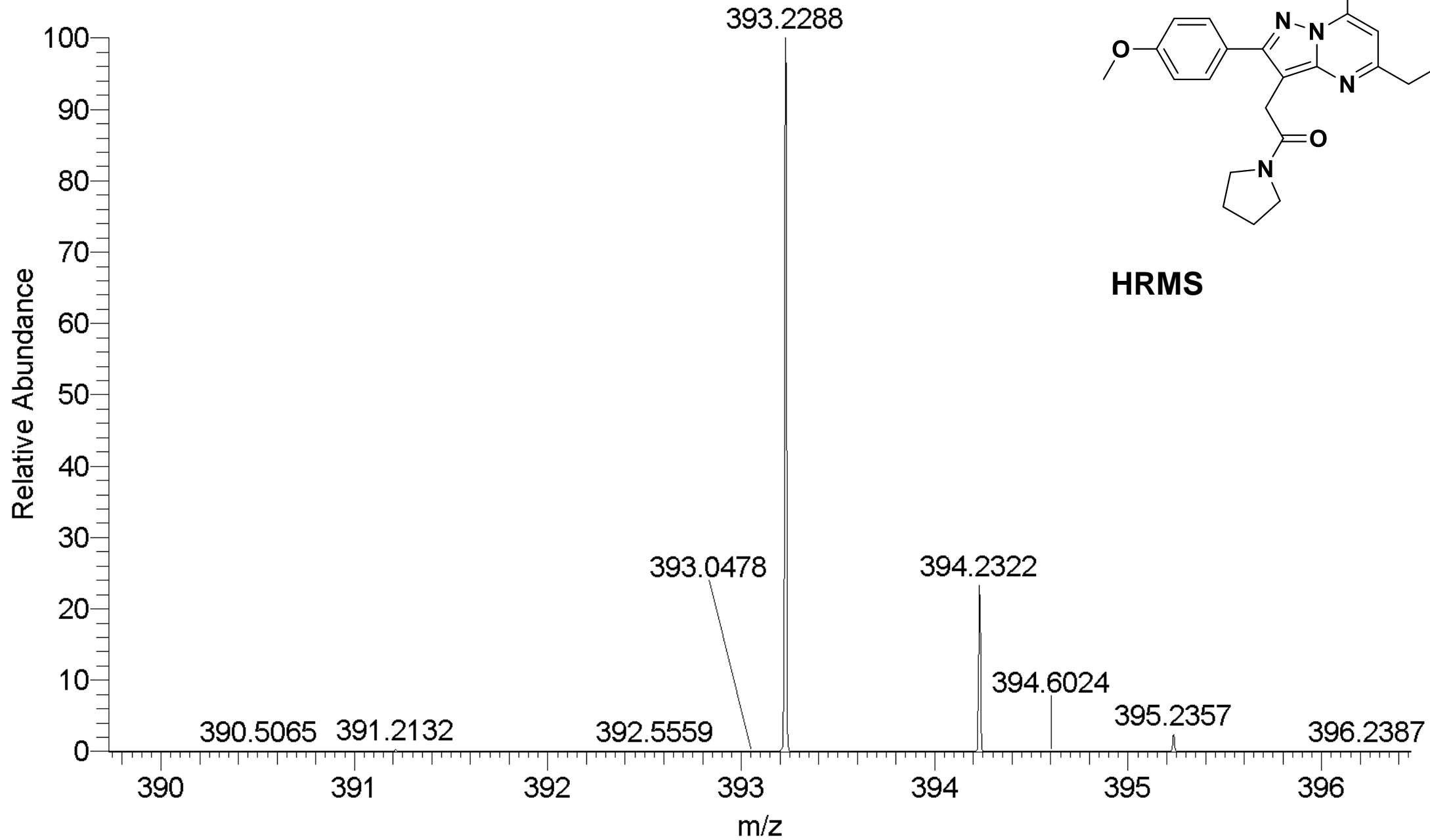
¹H NMR

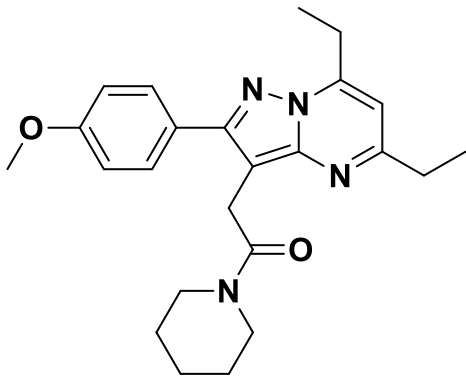




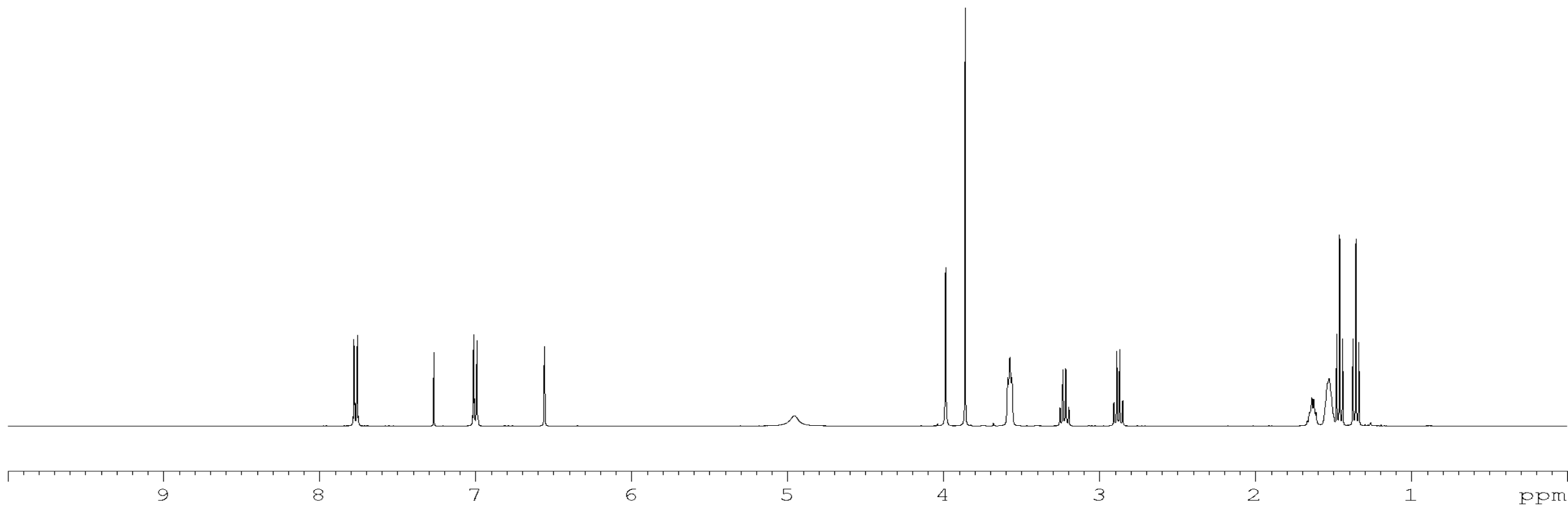
¹³C NMR

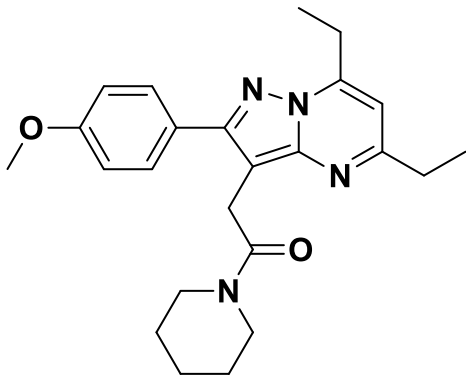




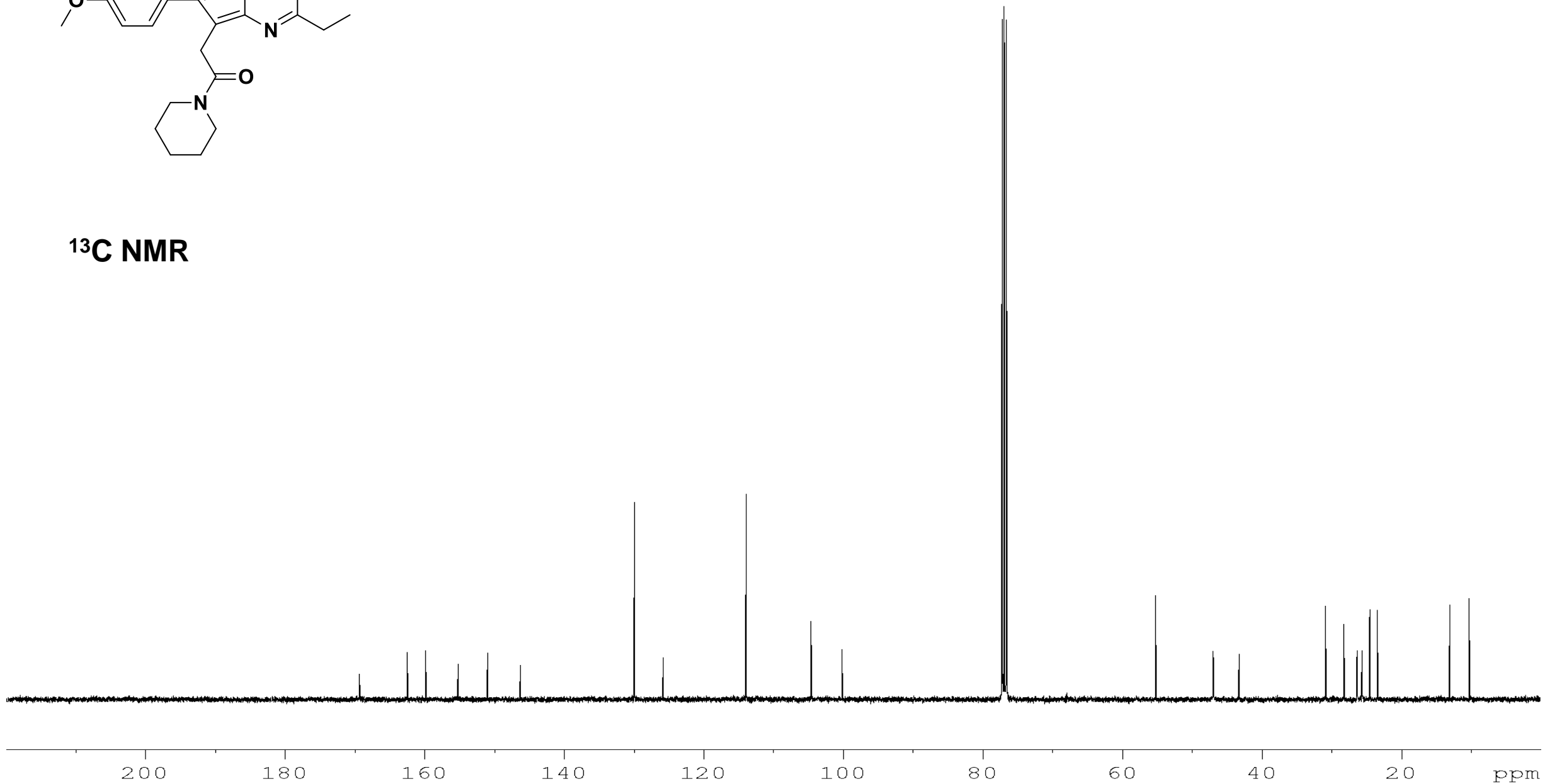


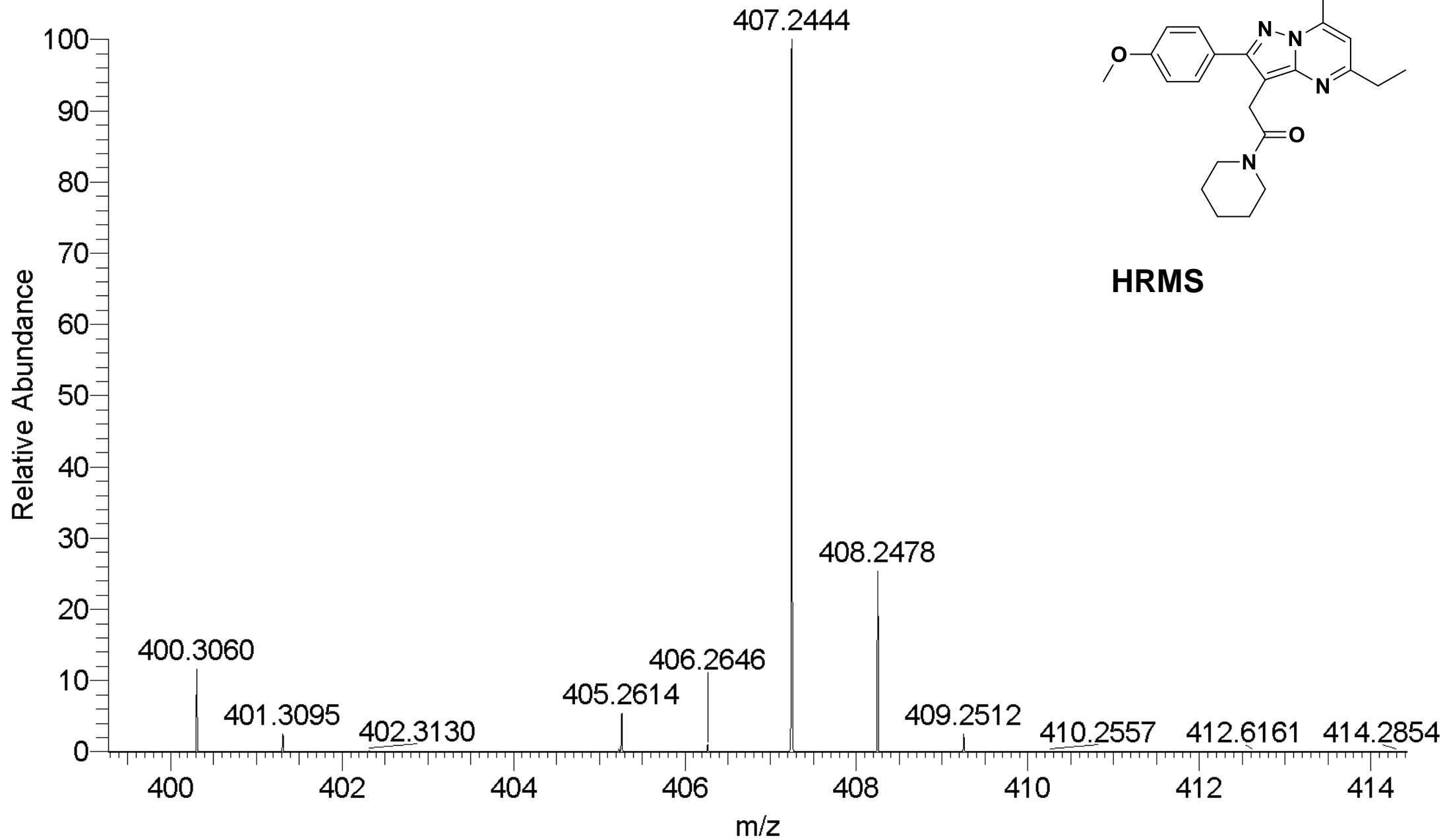
^1H NMR

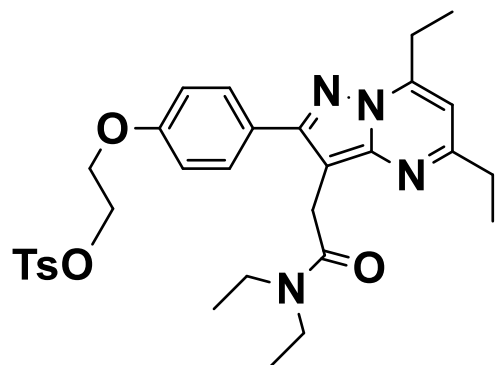




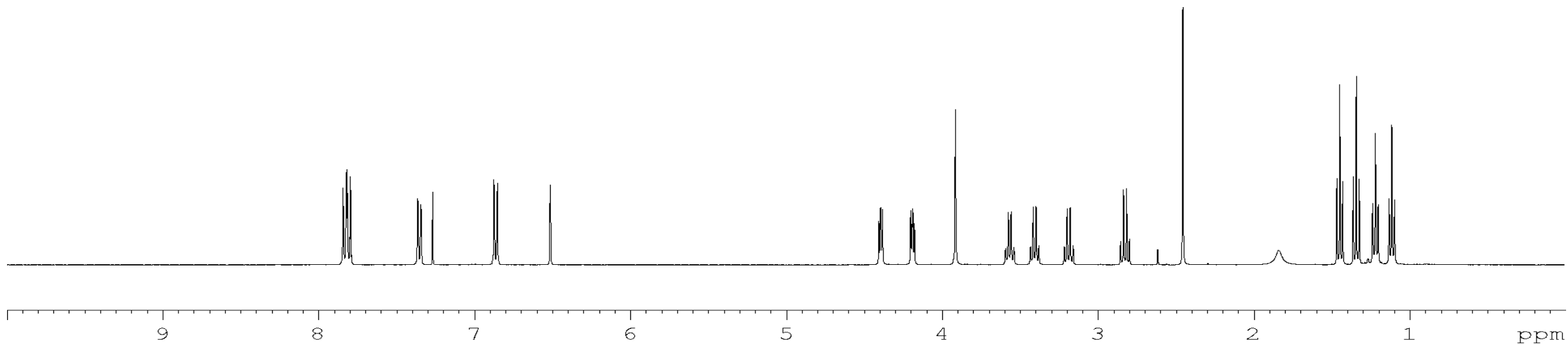
^{13}C NMR

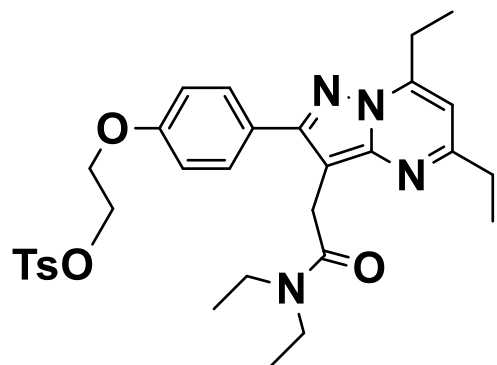




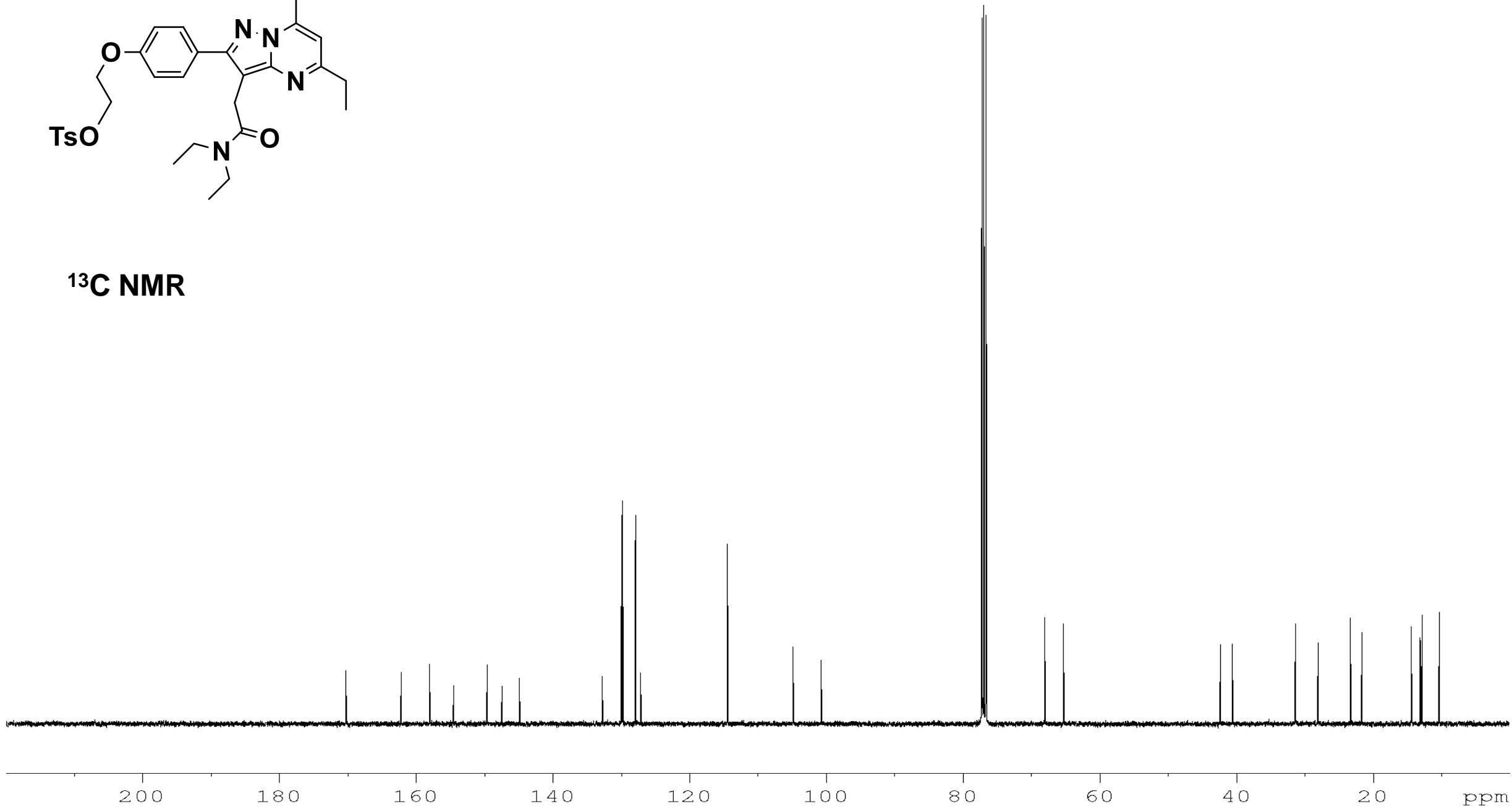


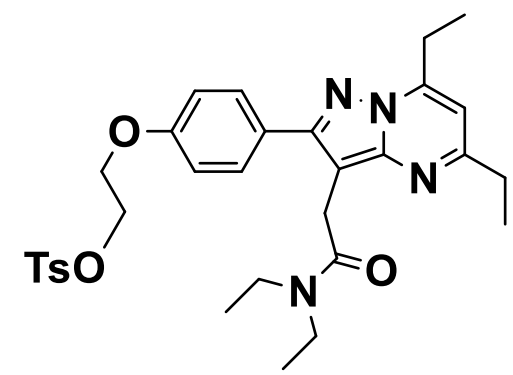
¹H NMR



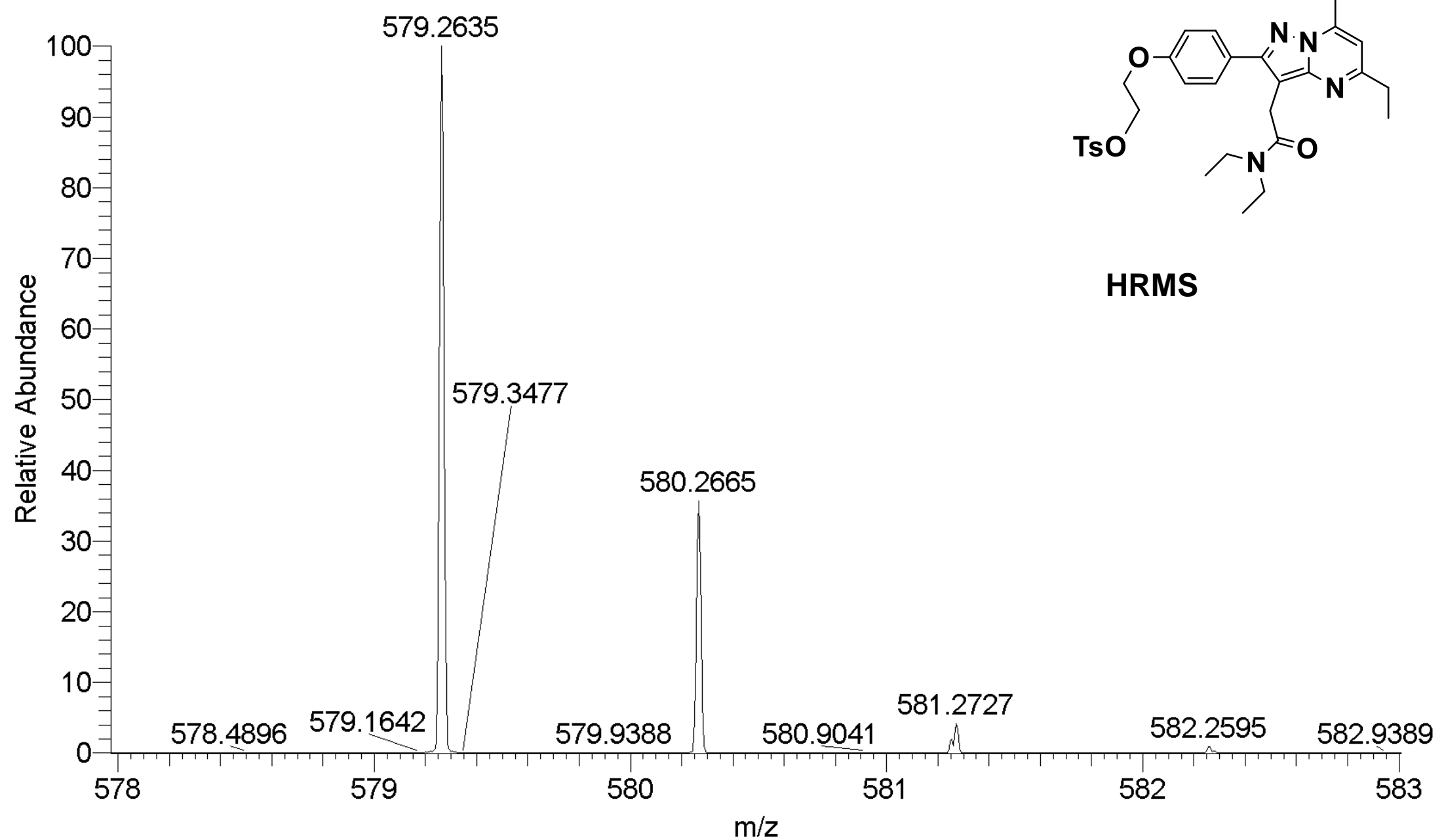


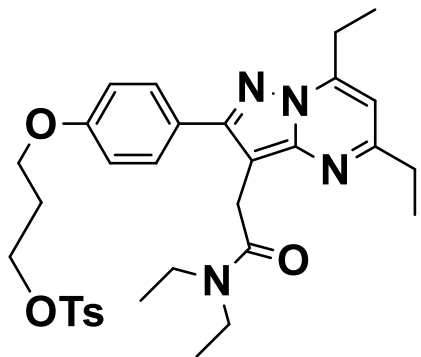
^{13}C NMR



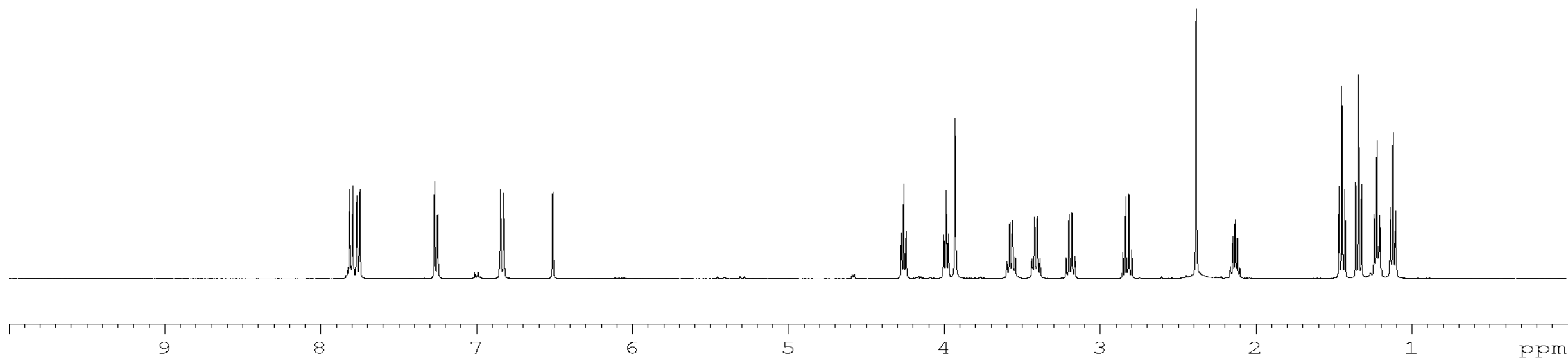


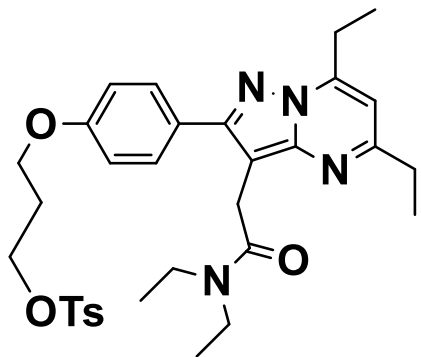
HRMS



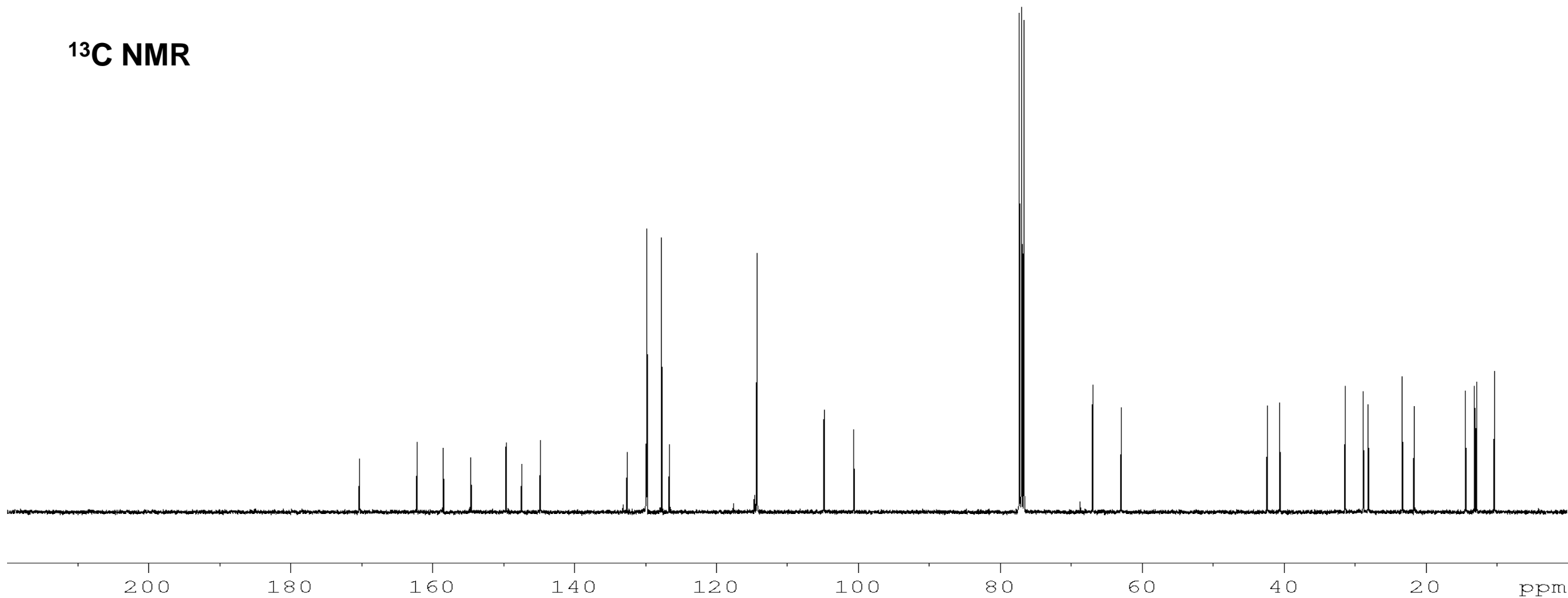


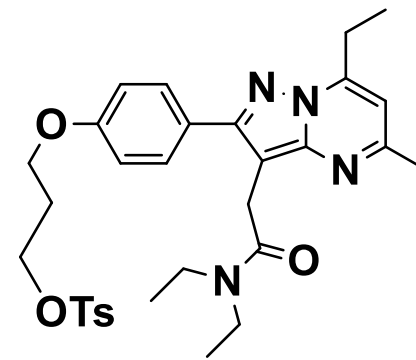
¹H NMR



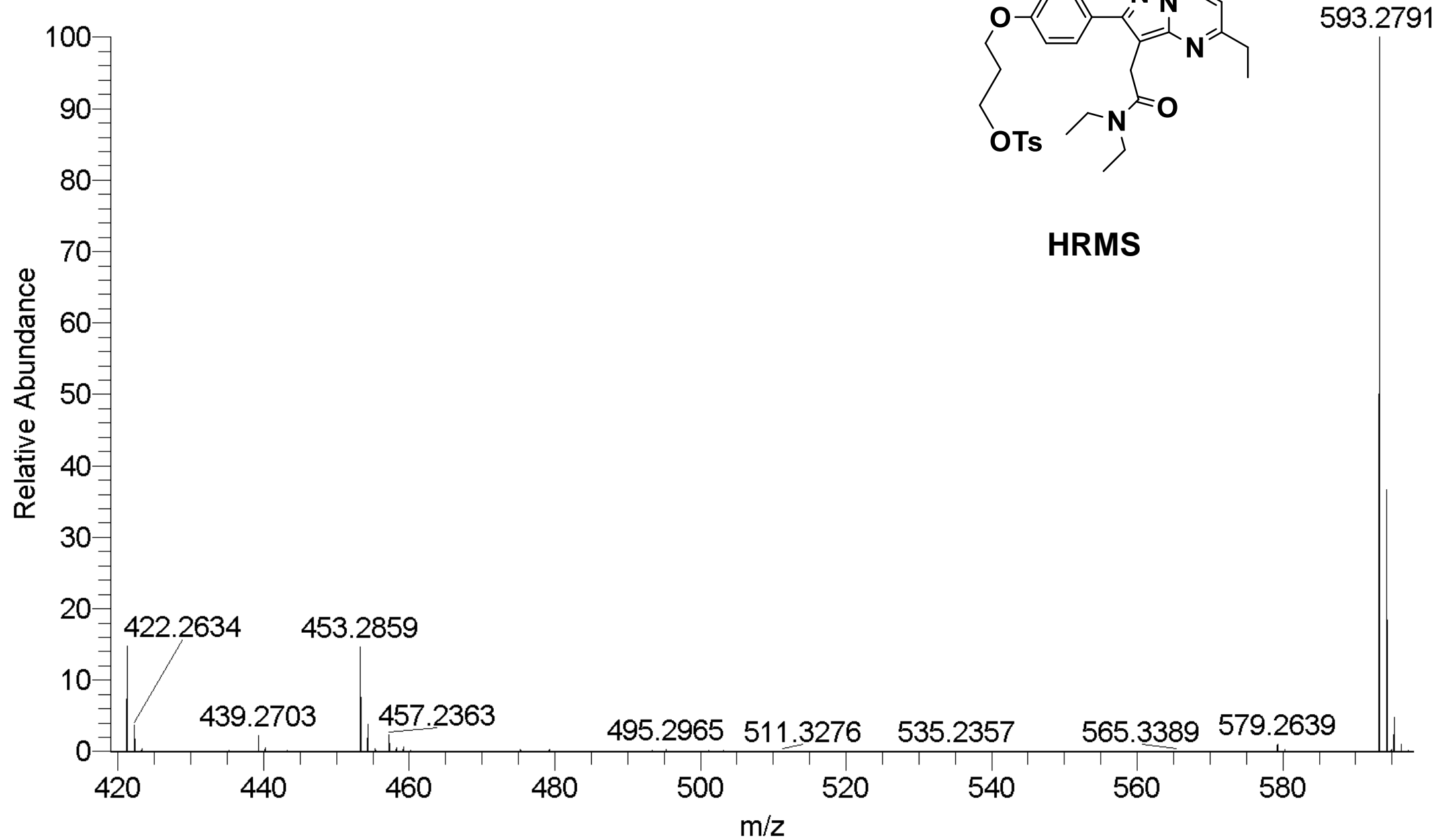


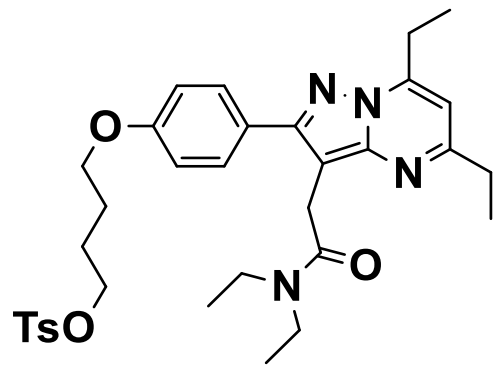
^{13}C NMR



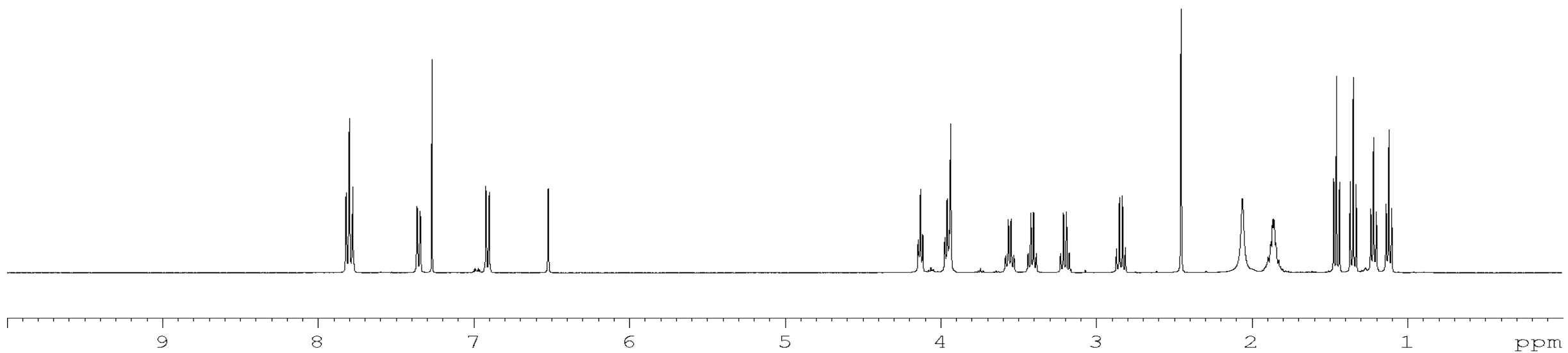


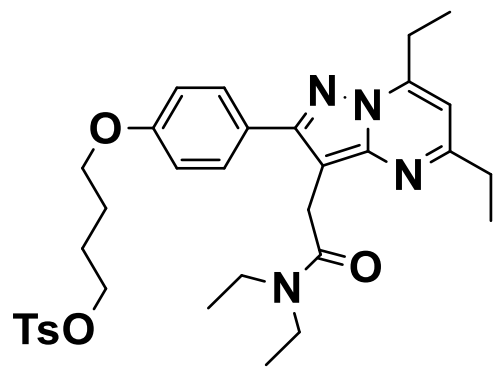
HRMS



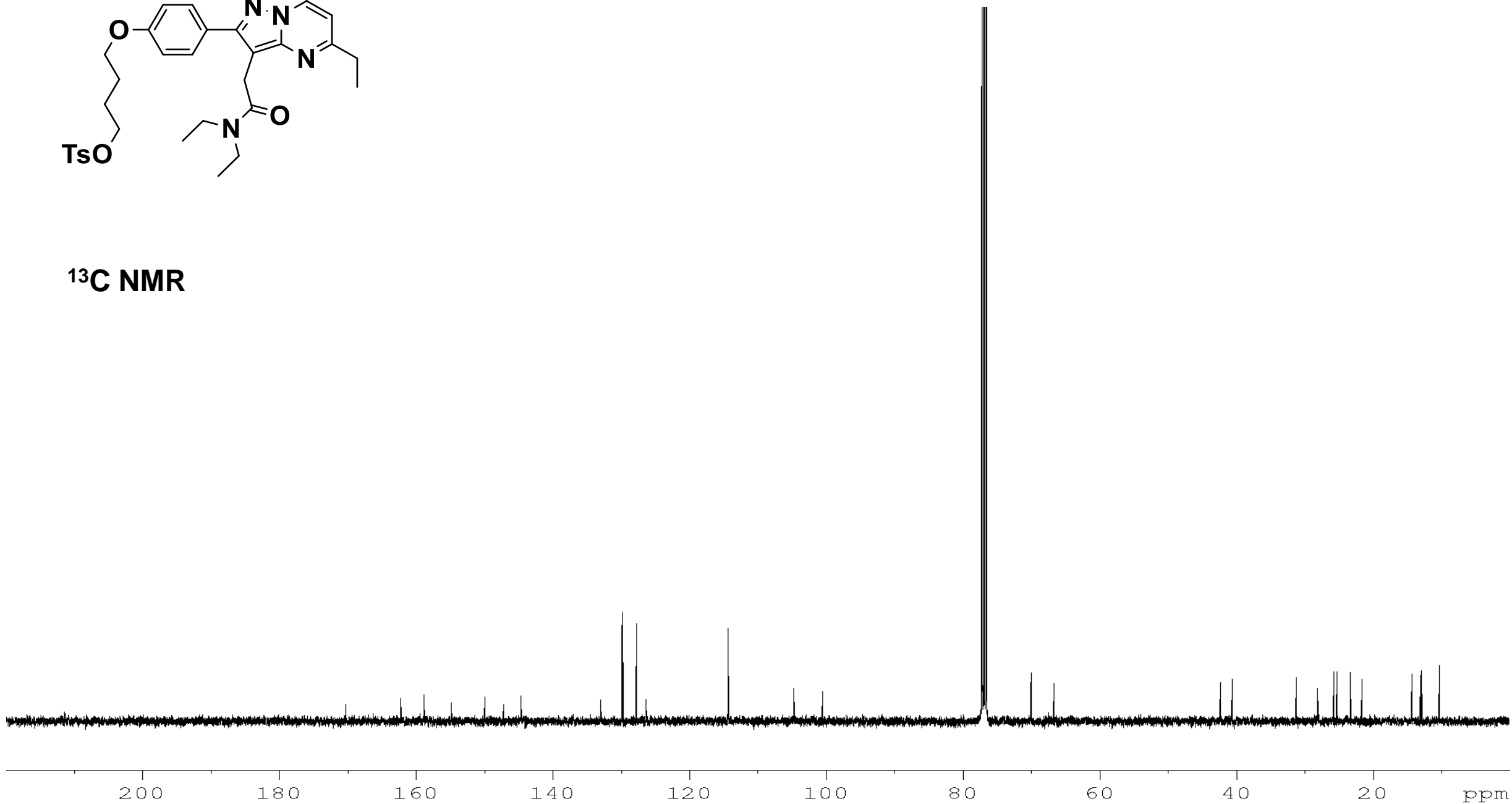


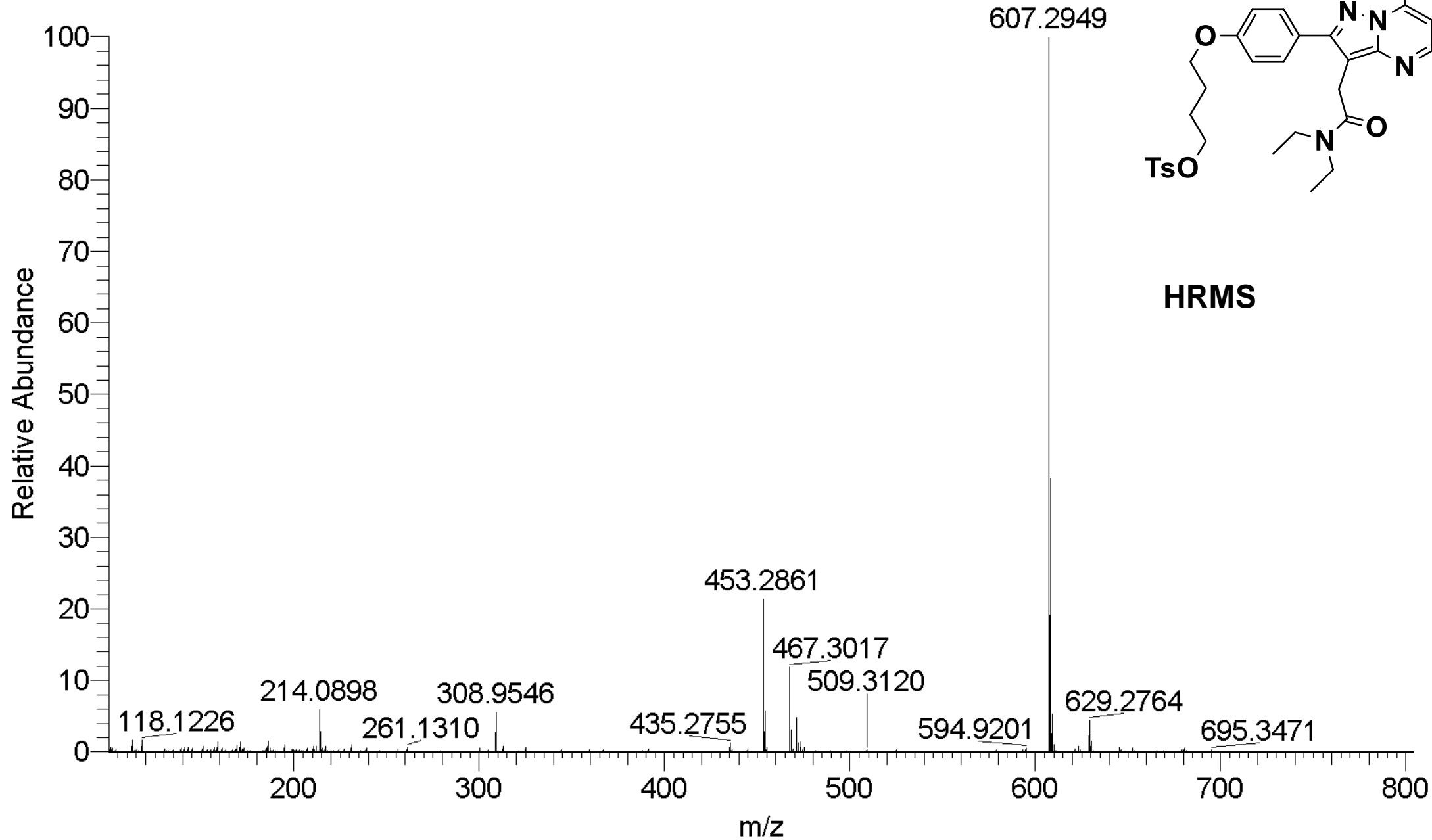
^1H NMR

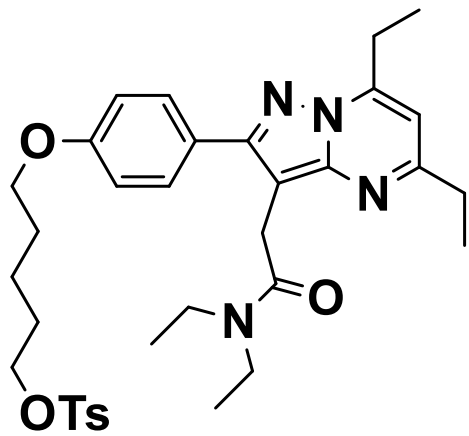




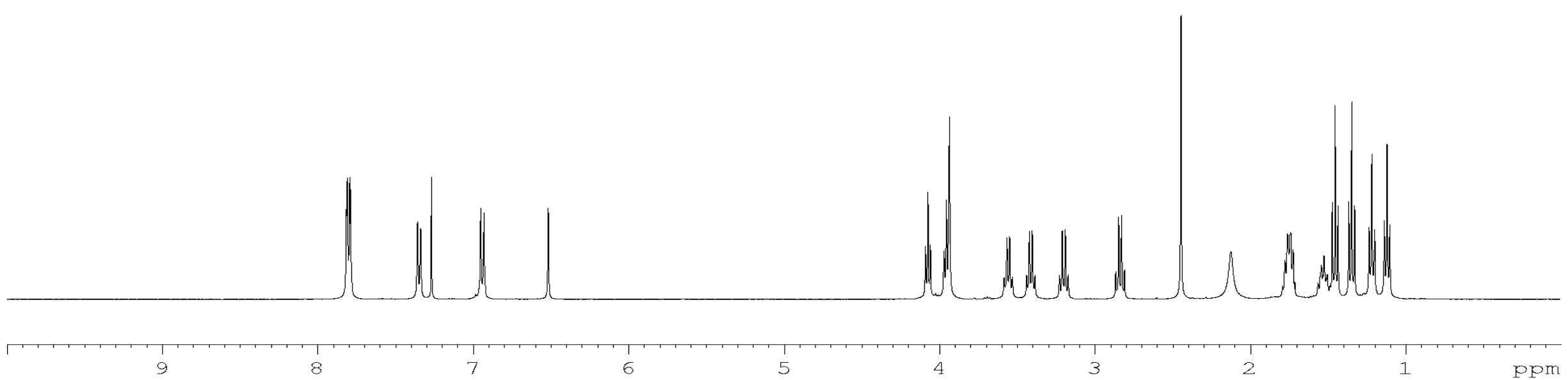
^{13}C NMR

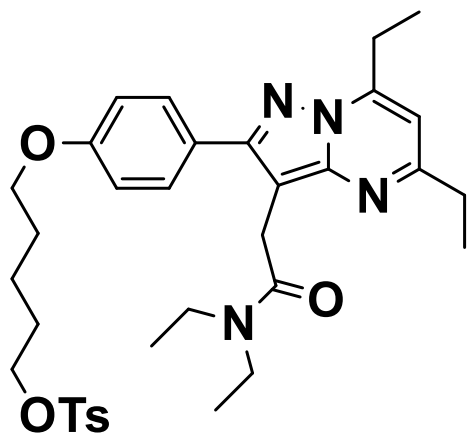




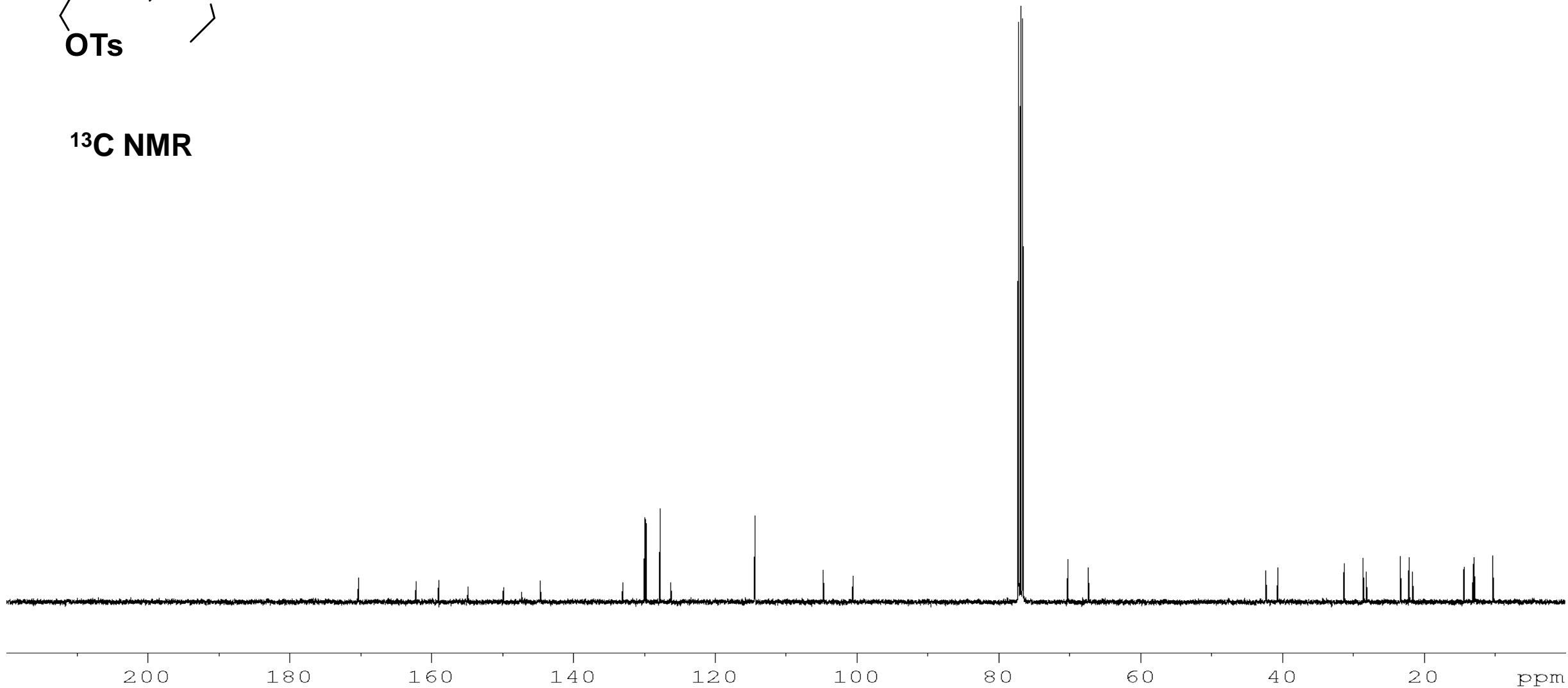


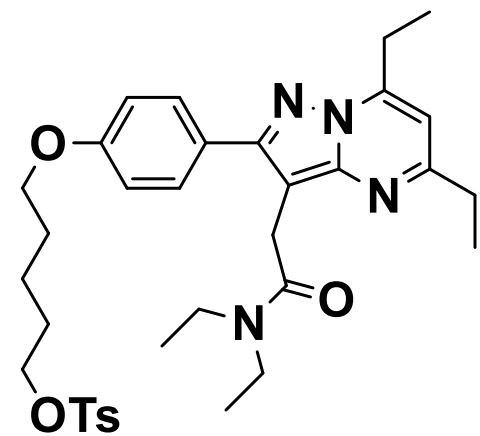
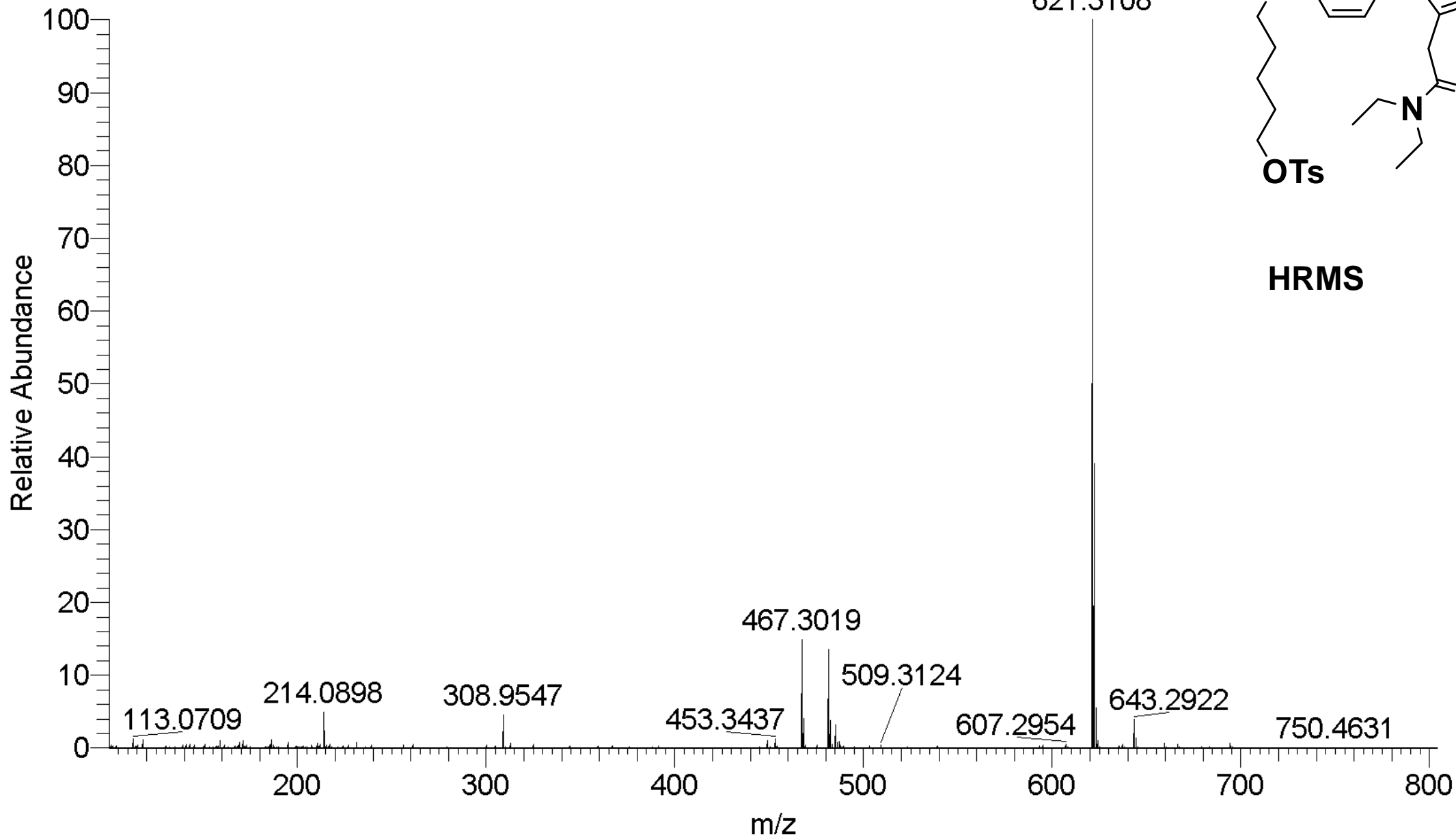
¹H NMR

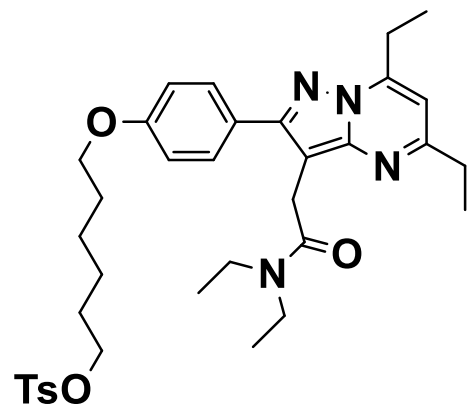




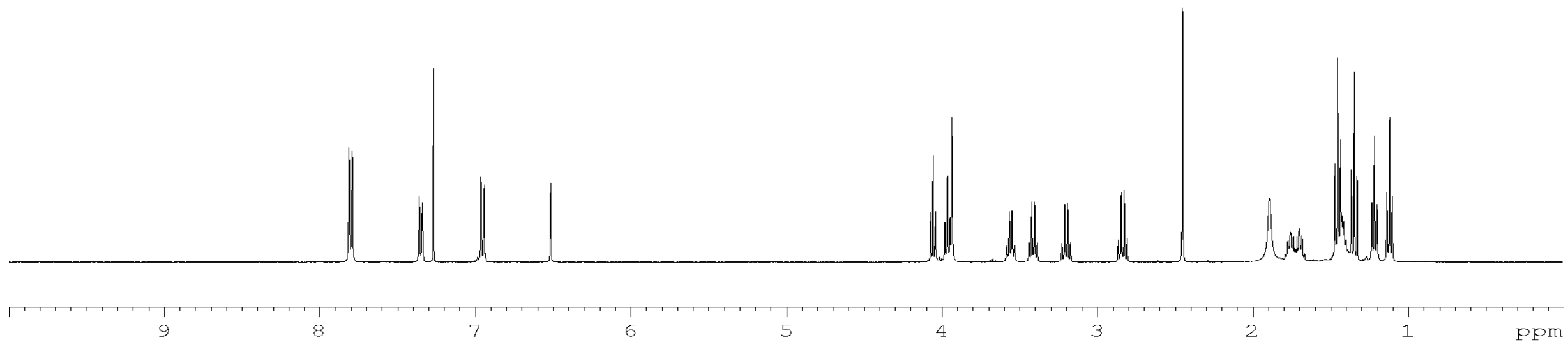
^{13}C NMR

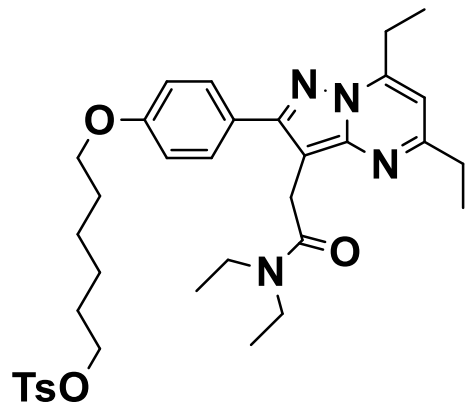




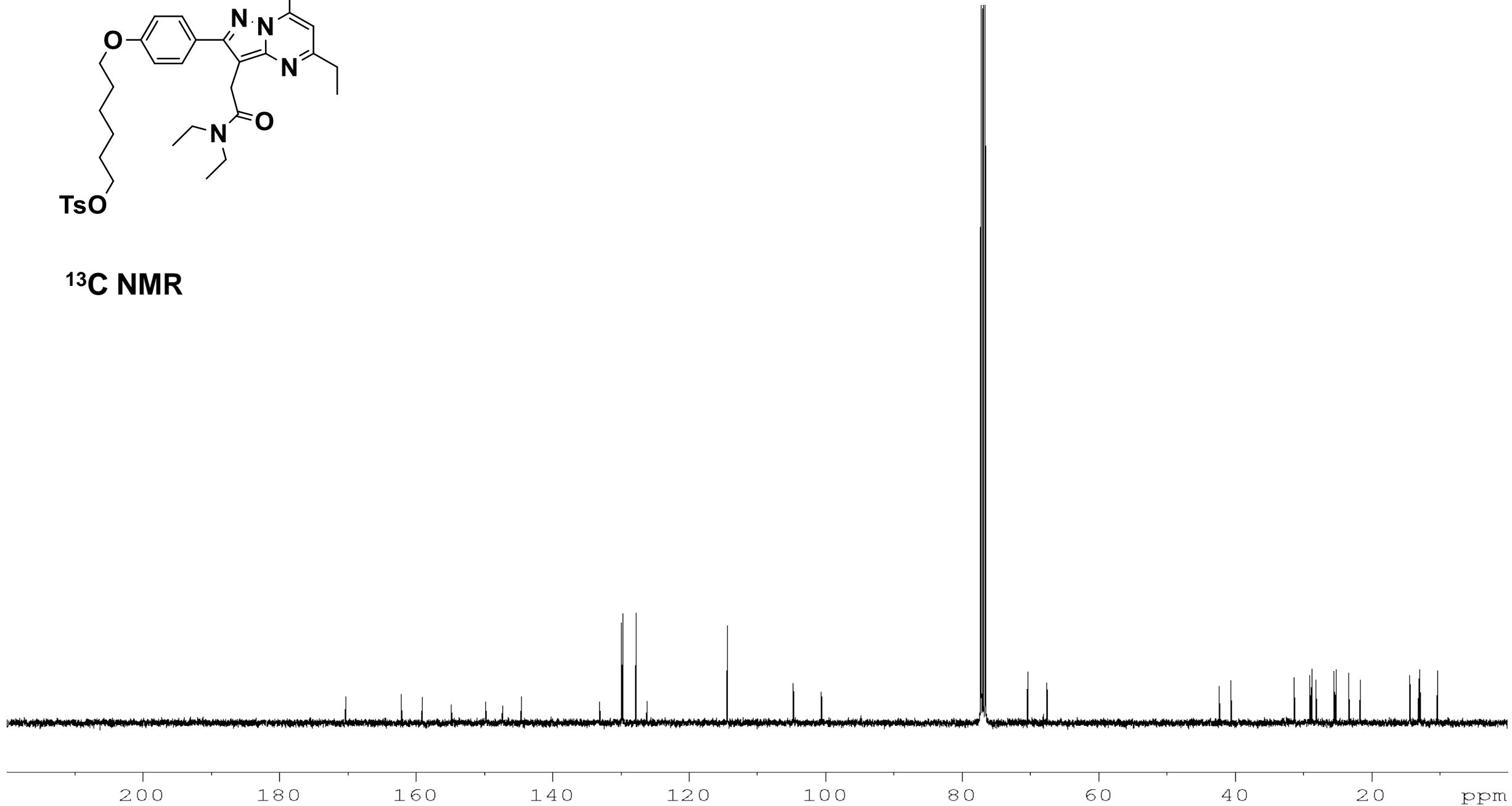


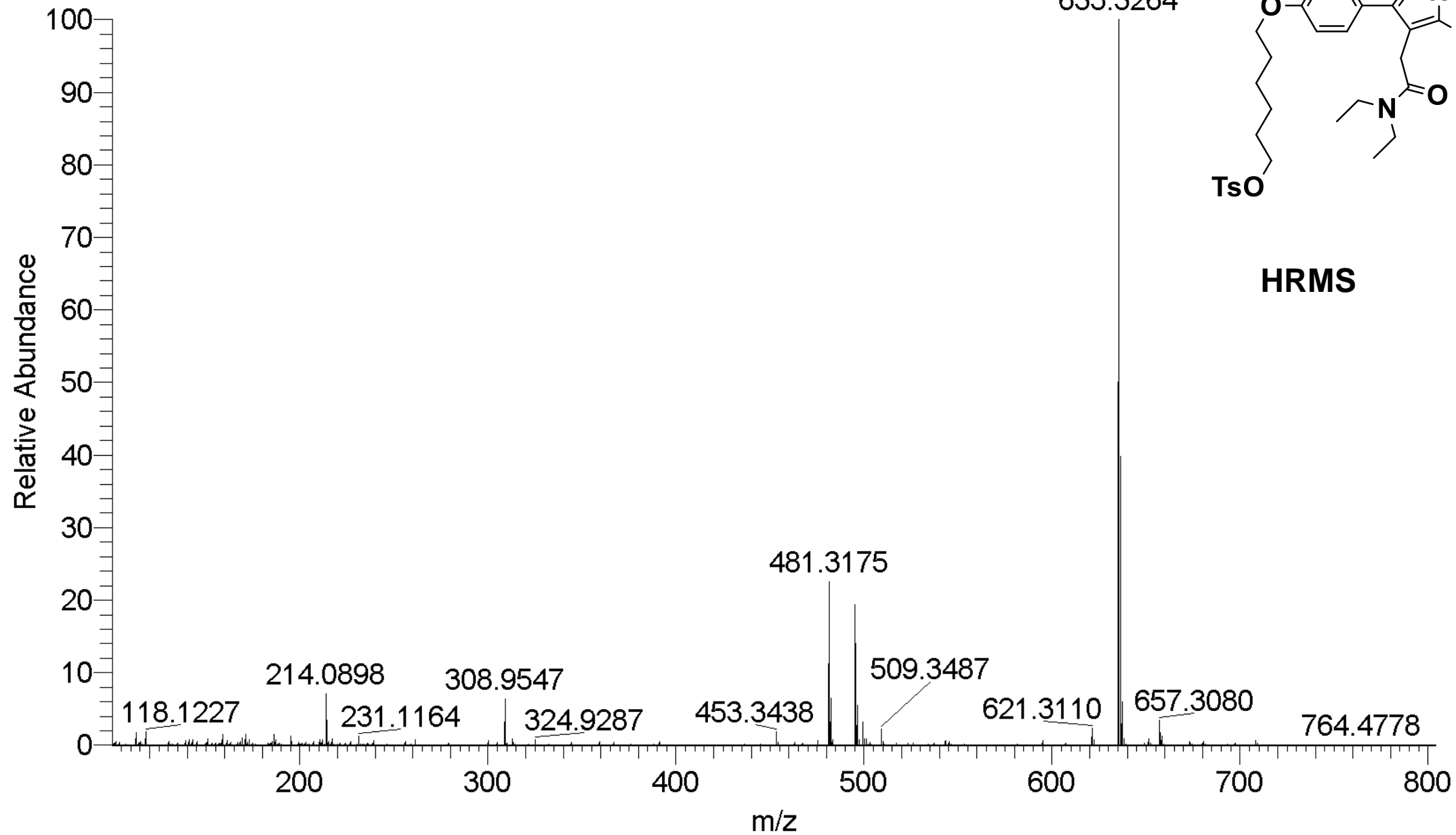
¹H NMR

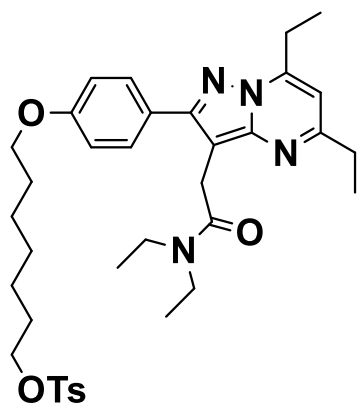




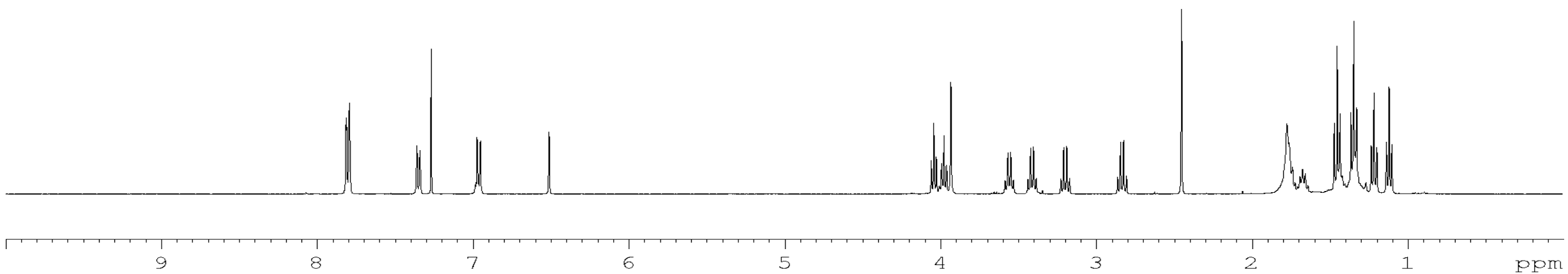
^{13}C NMR

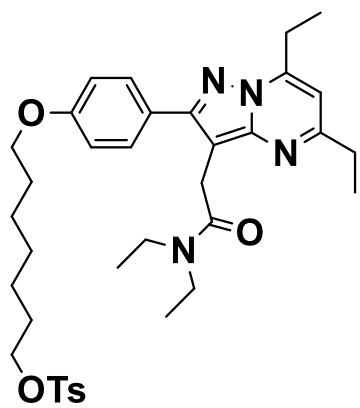




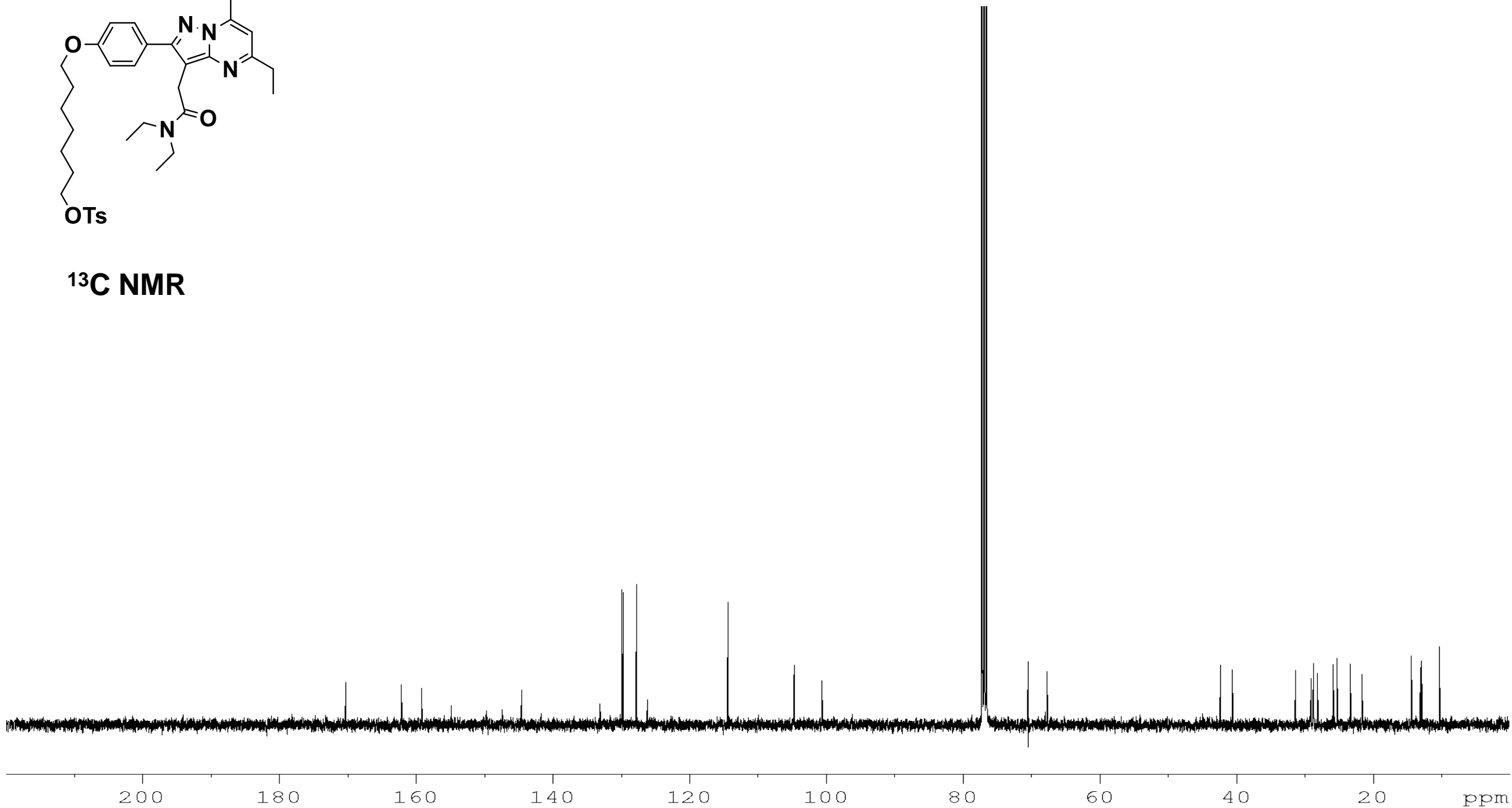


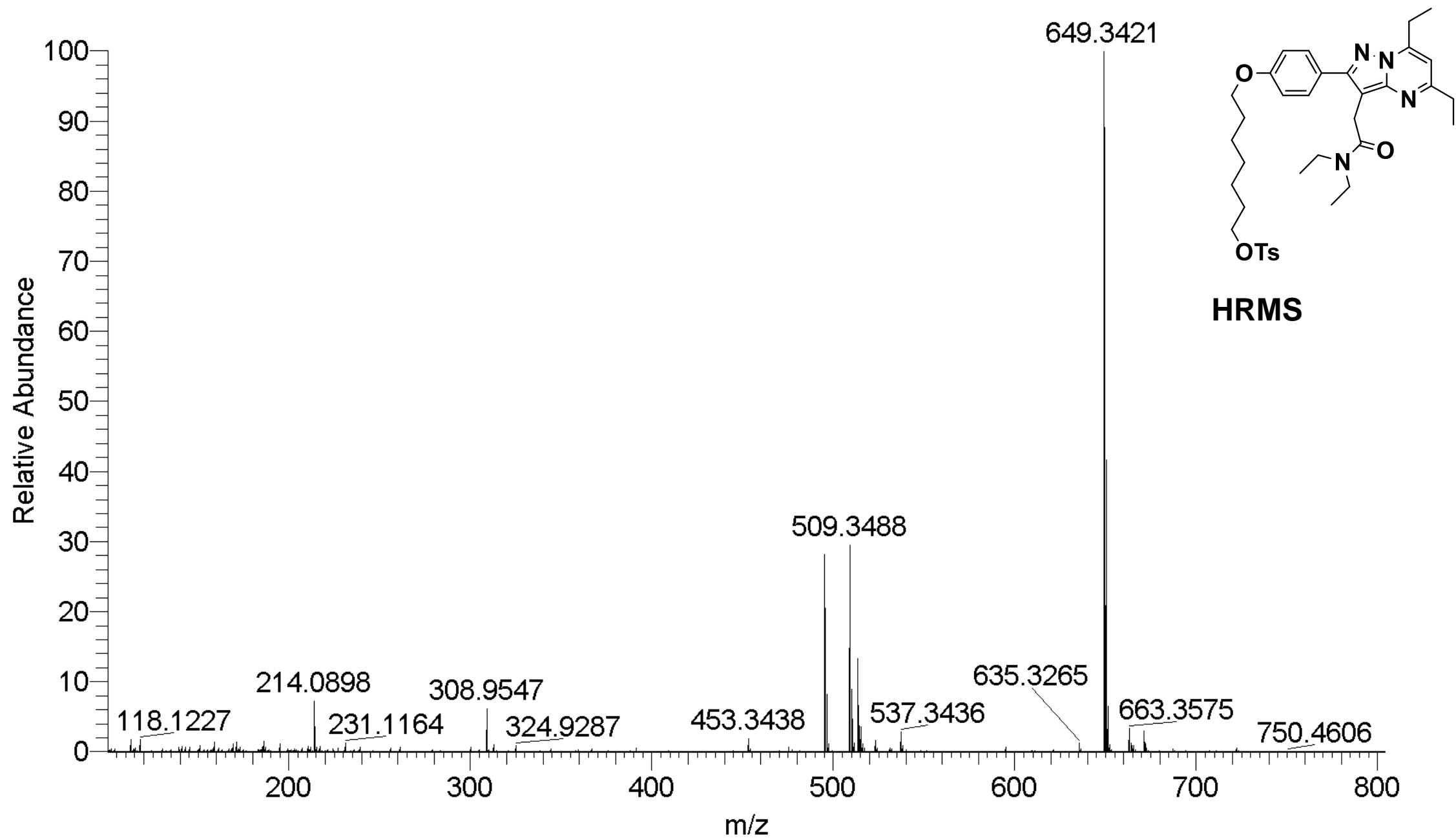
¹H NMR

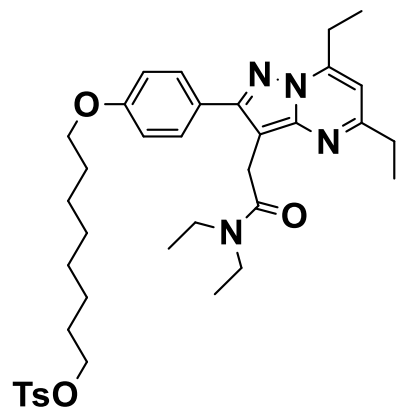




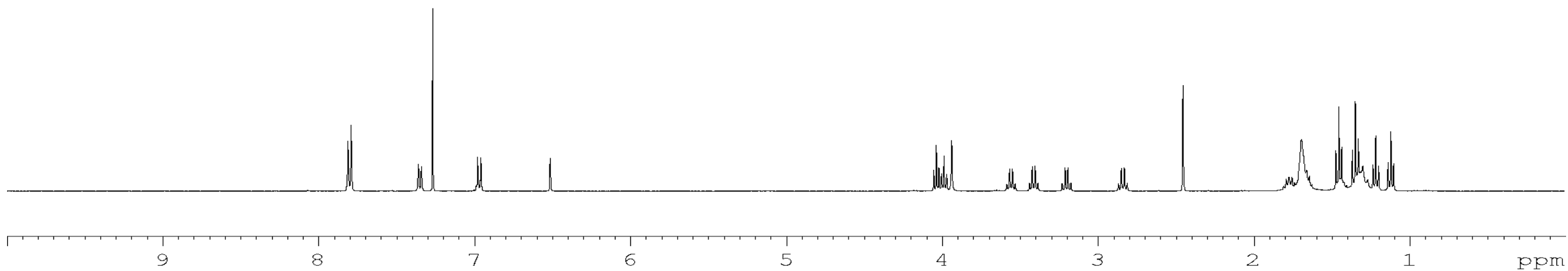
^{13}C NMR

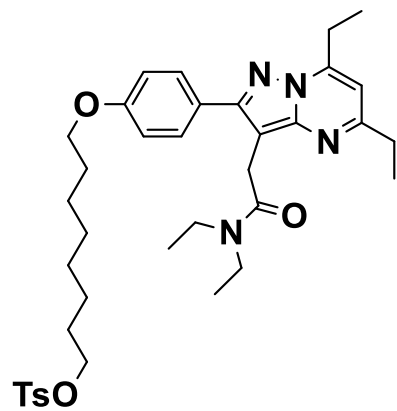




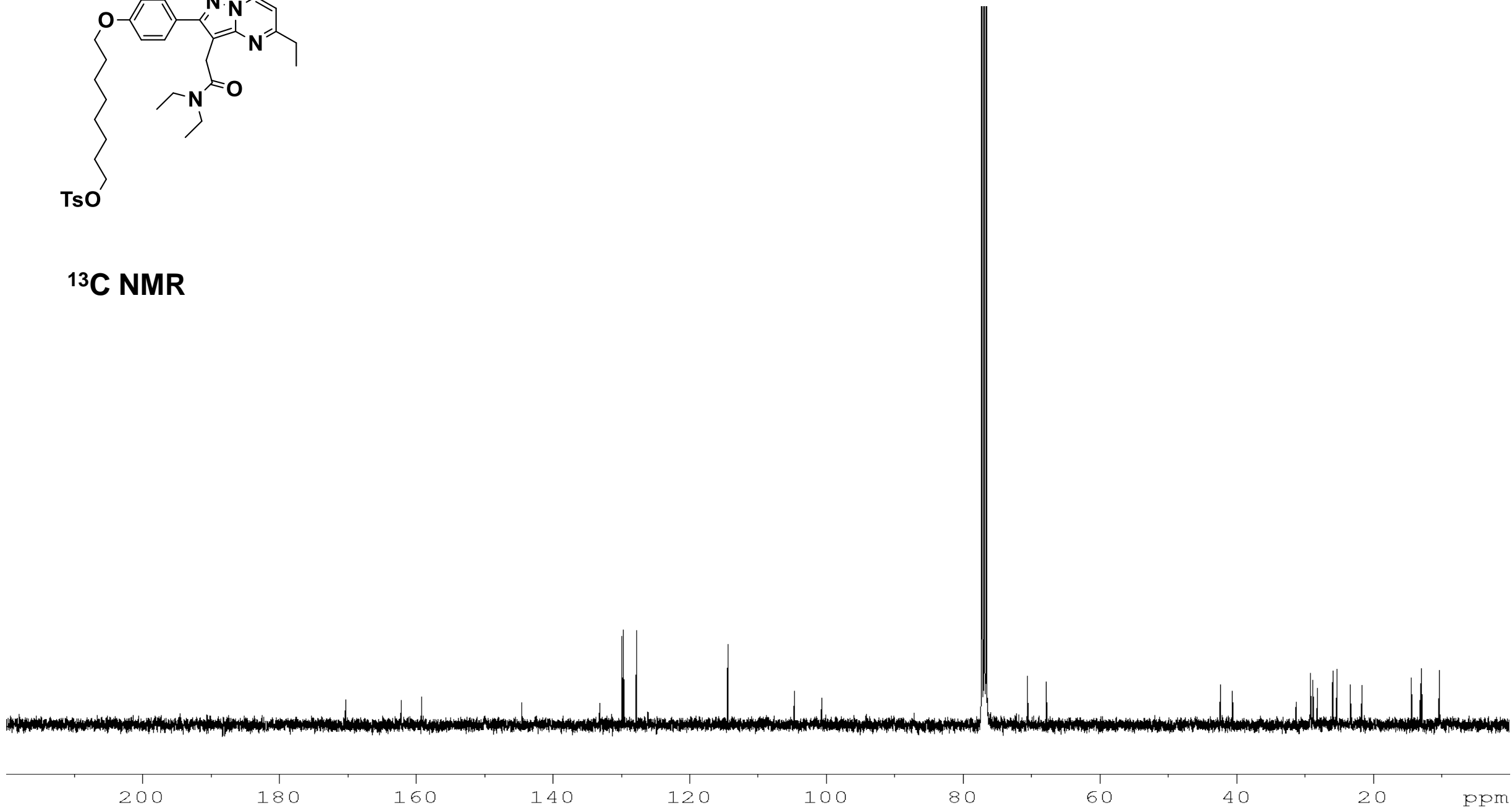


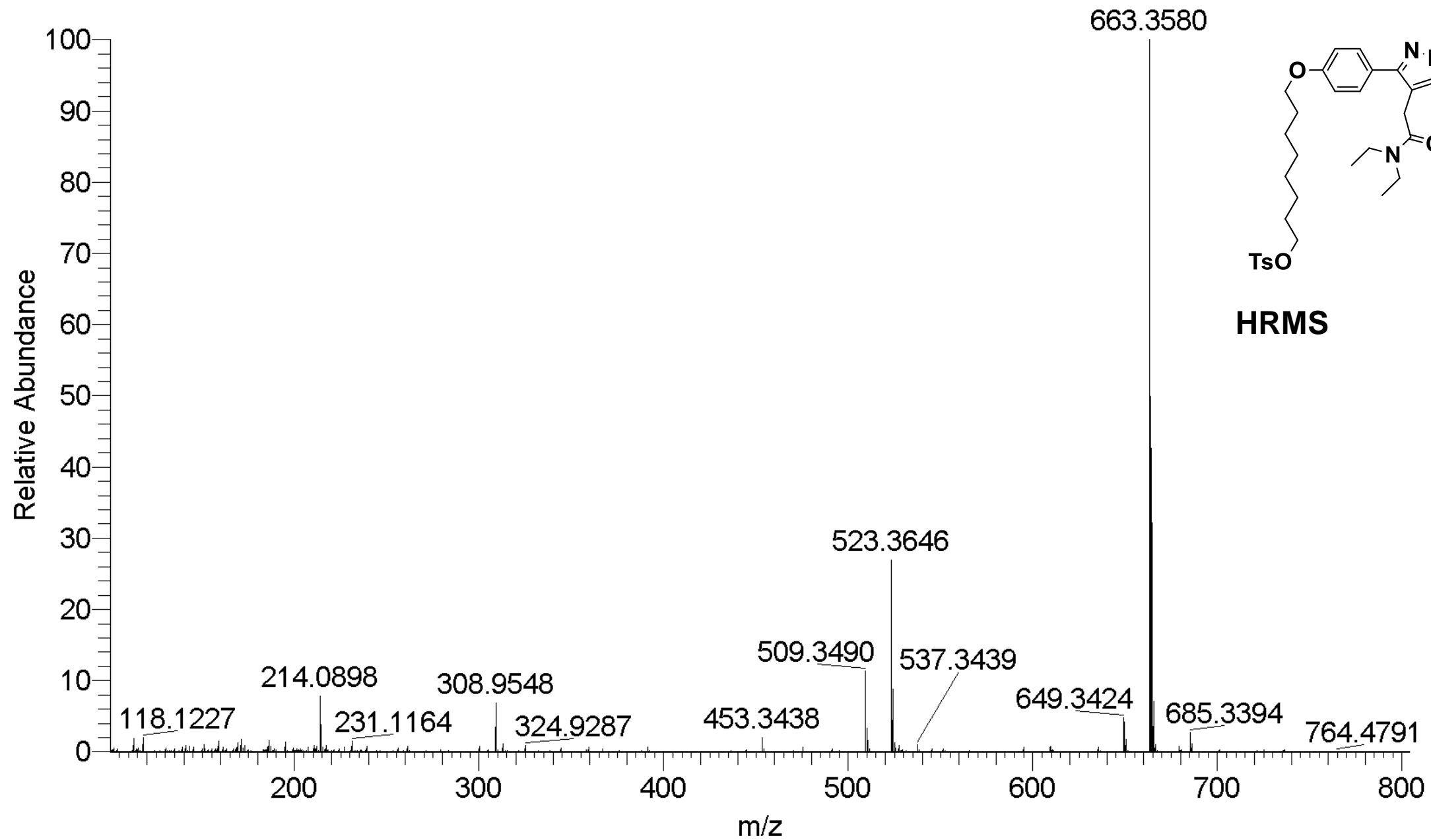
¹H NMR

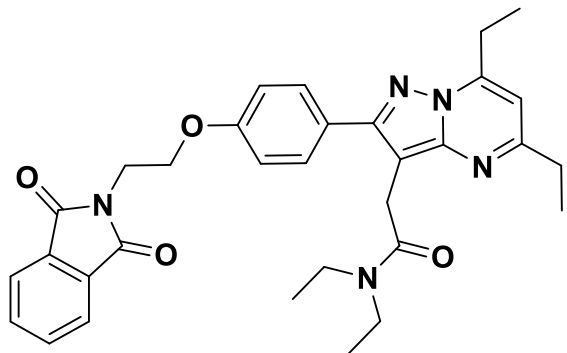




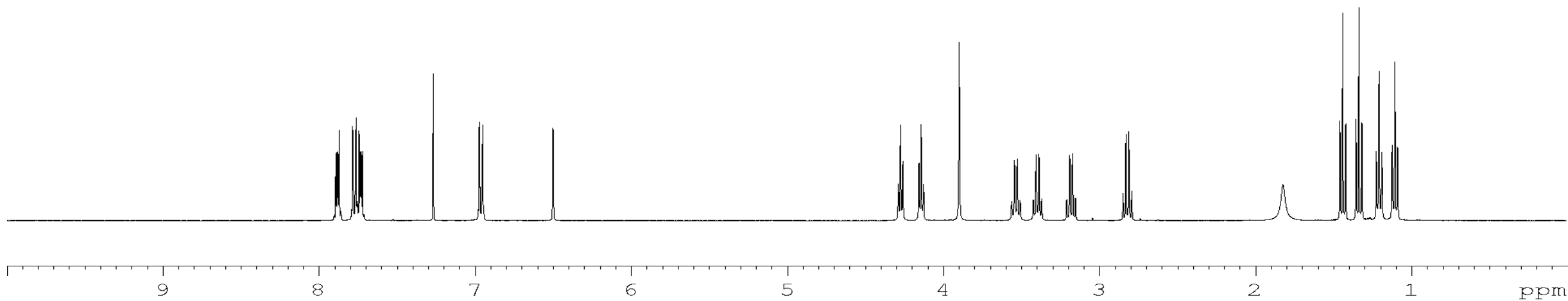
^{13}C NMR

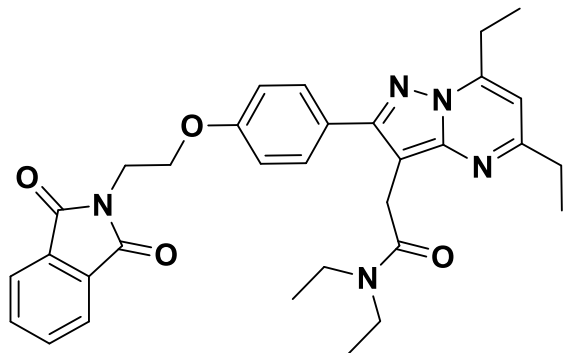




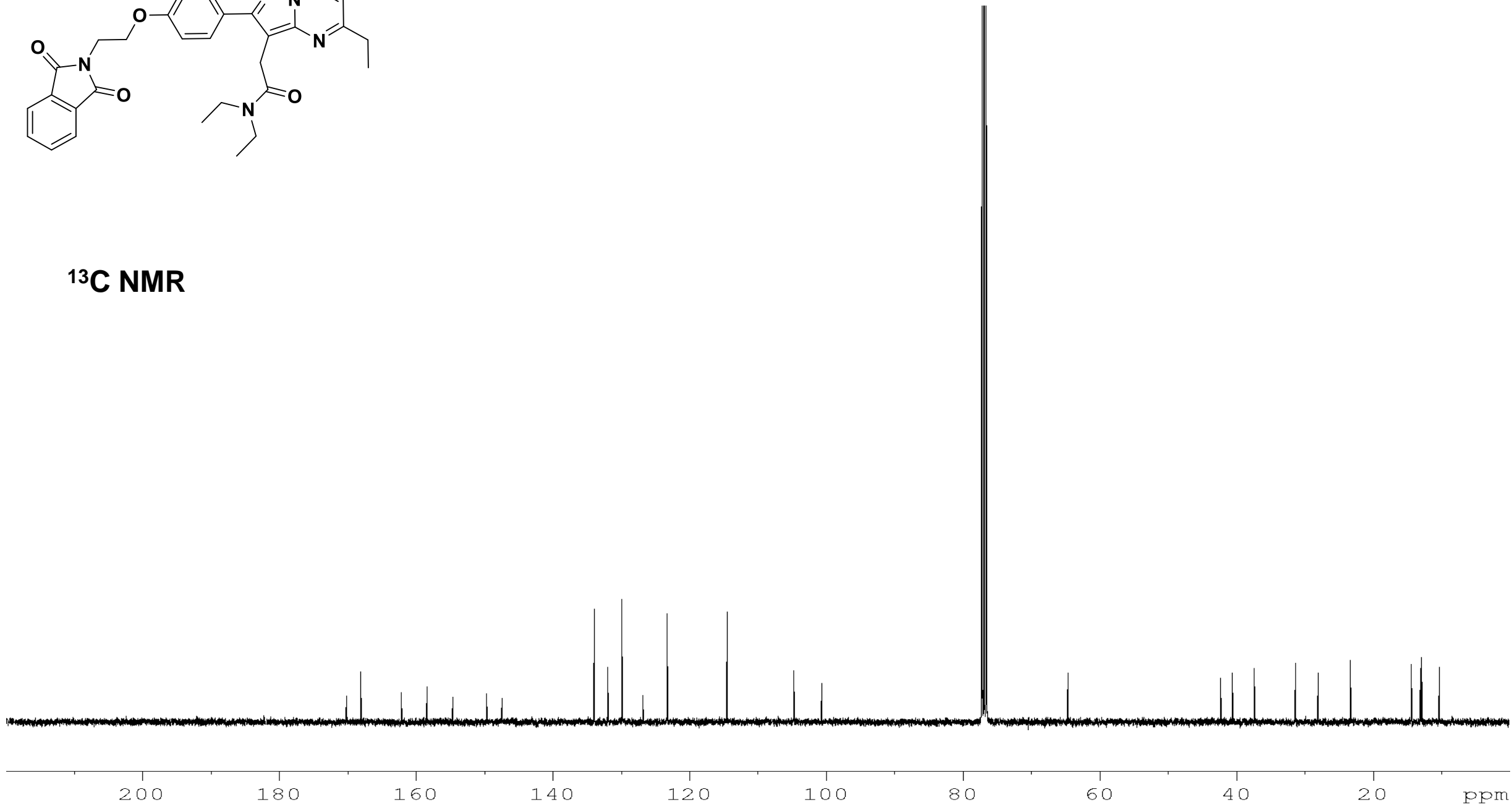


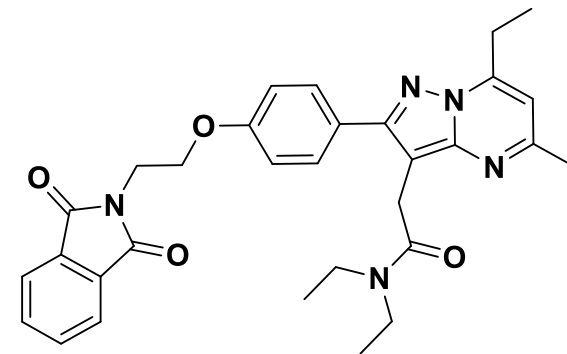
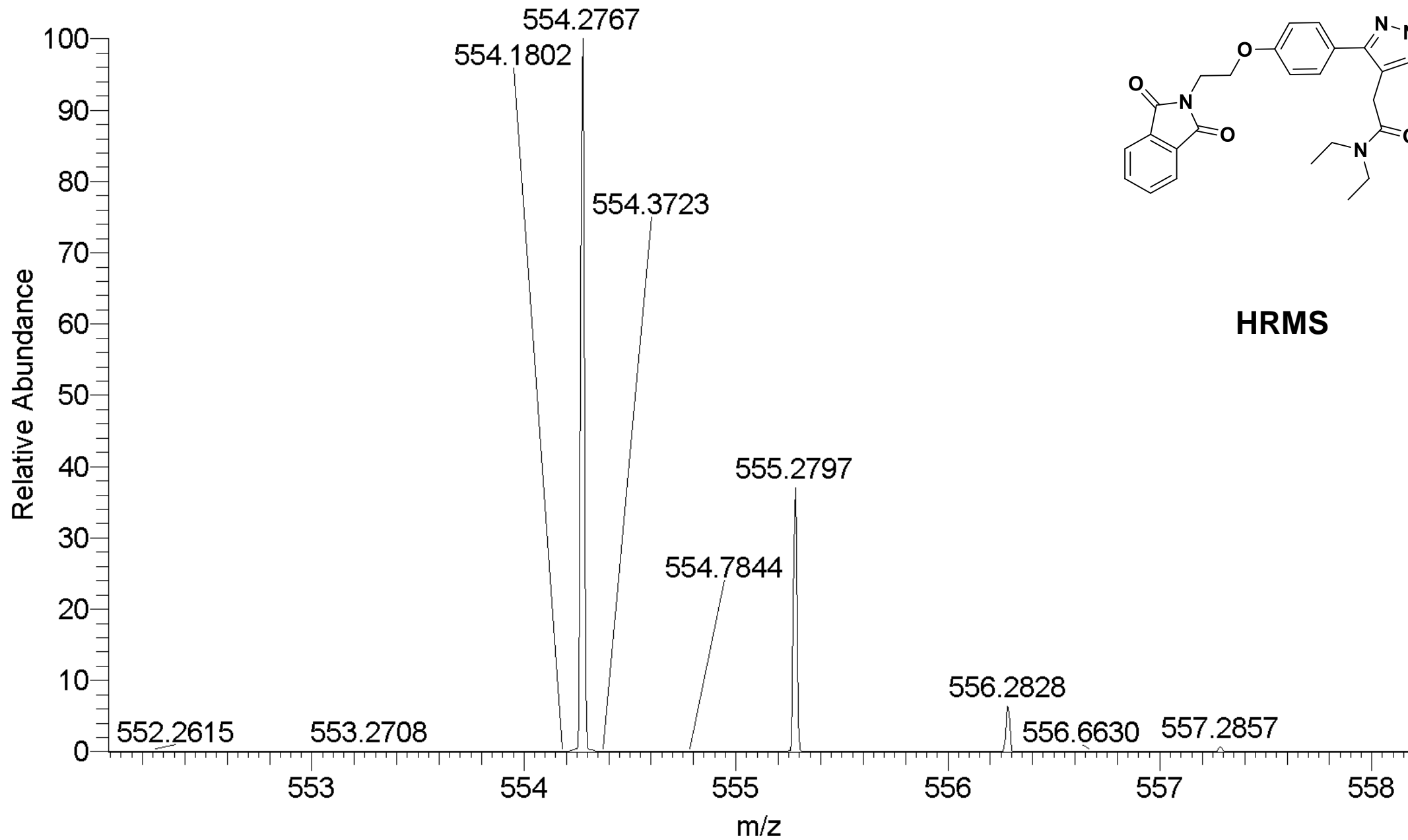
¹H NMR

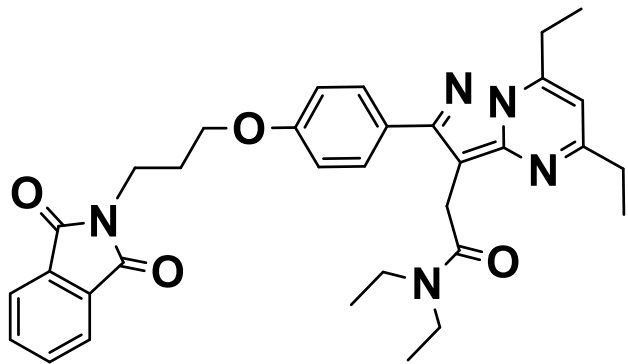




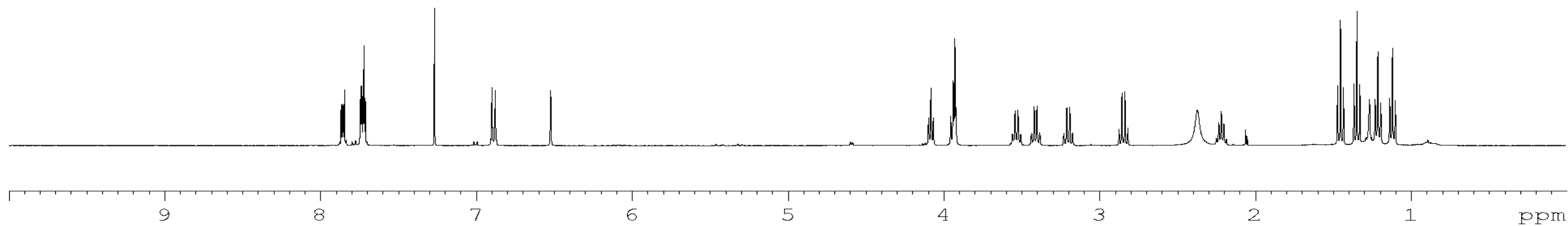
^{13}C NMR

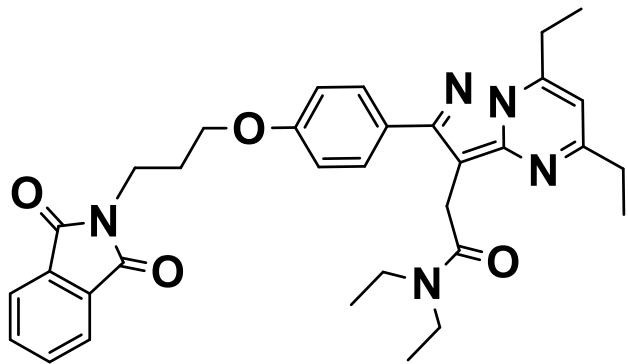




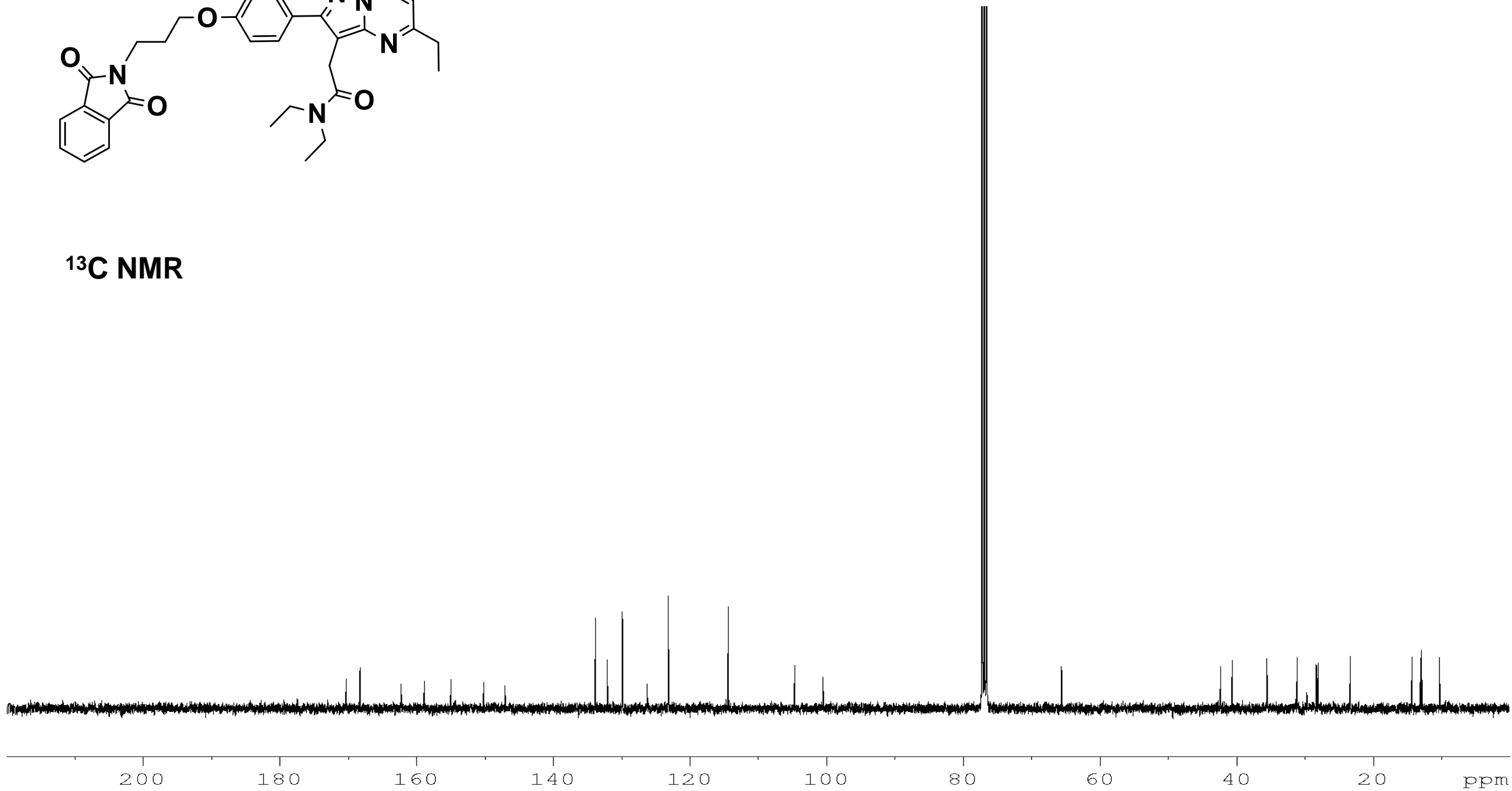


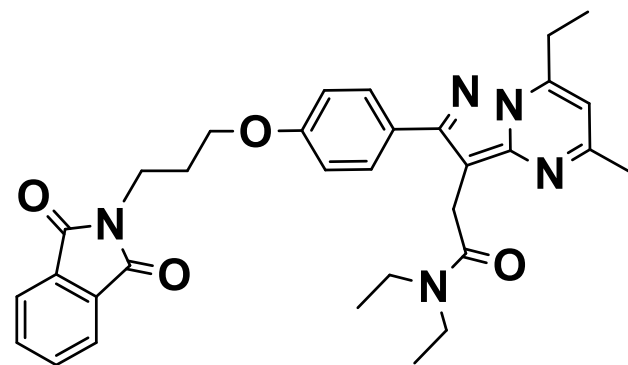
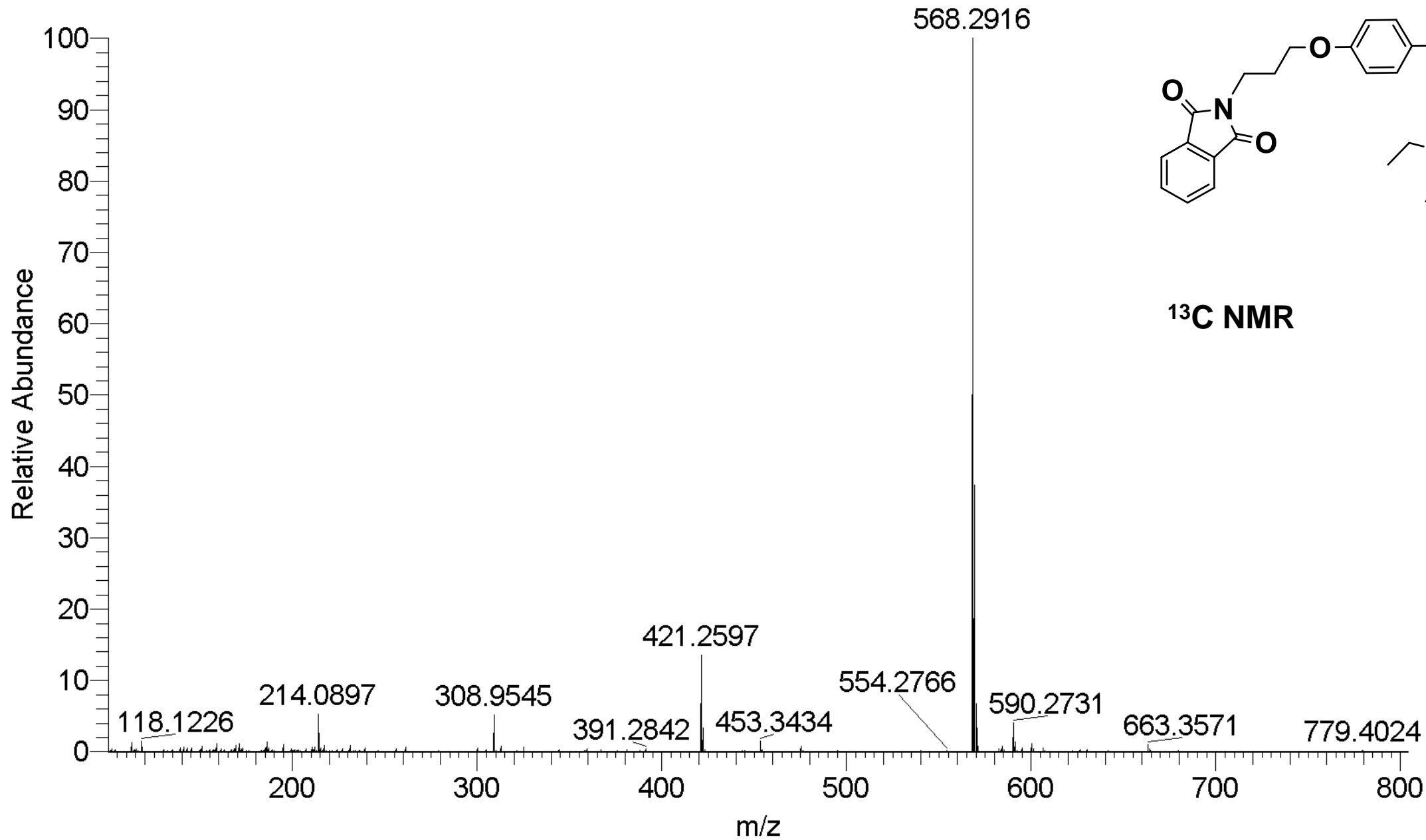
¹H NMR



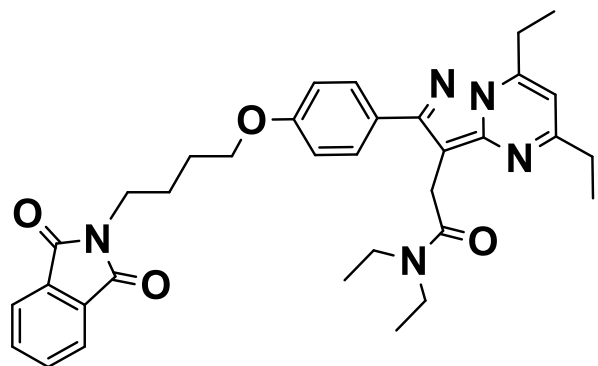


^{13}C NMR

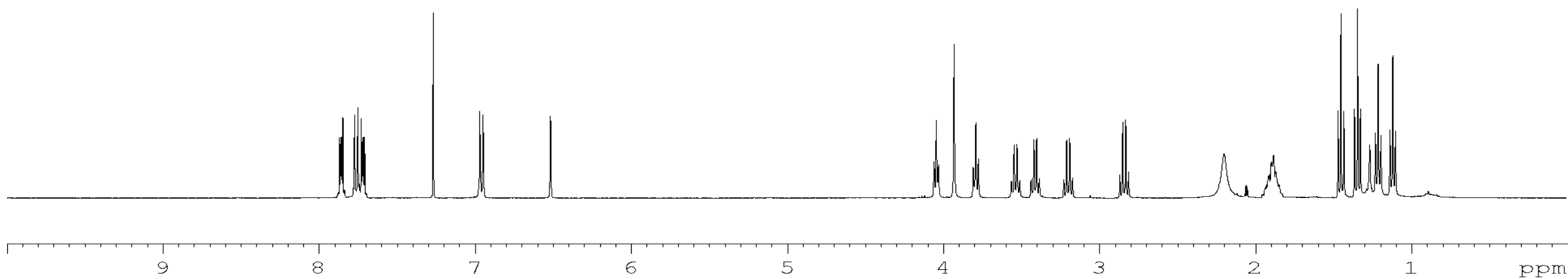


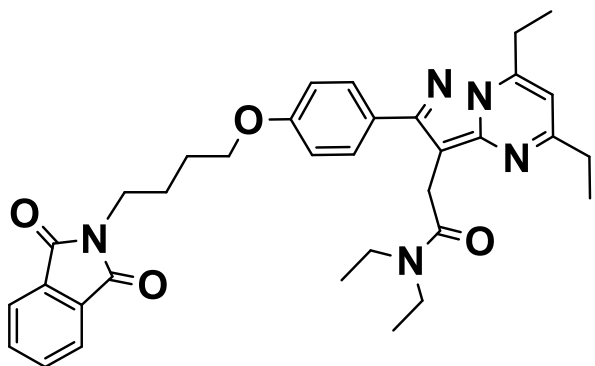


¹³C NMR

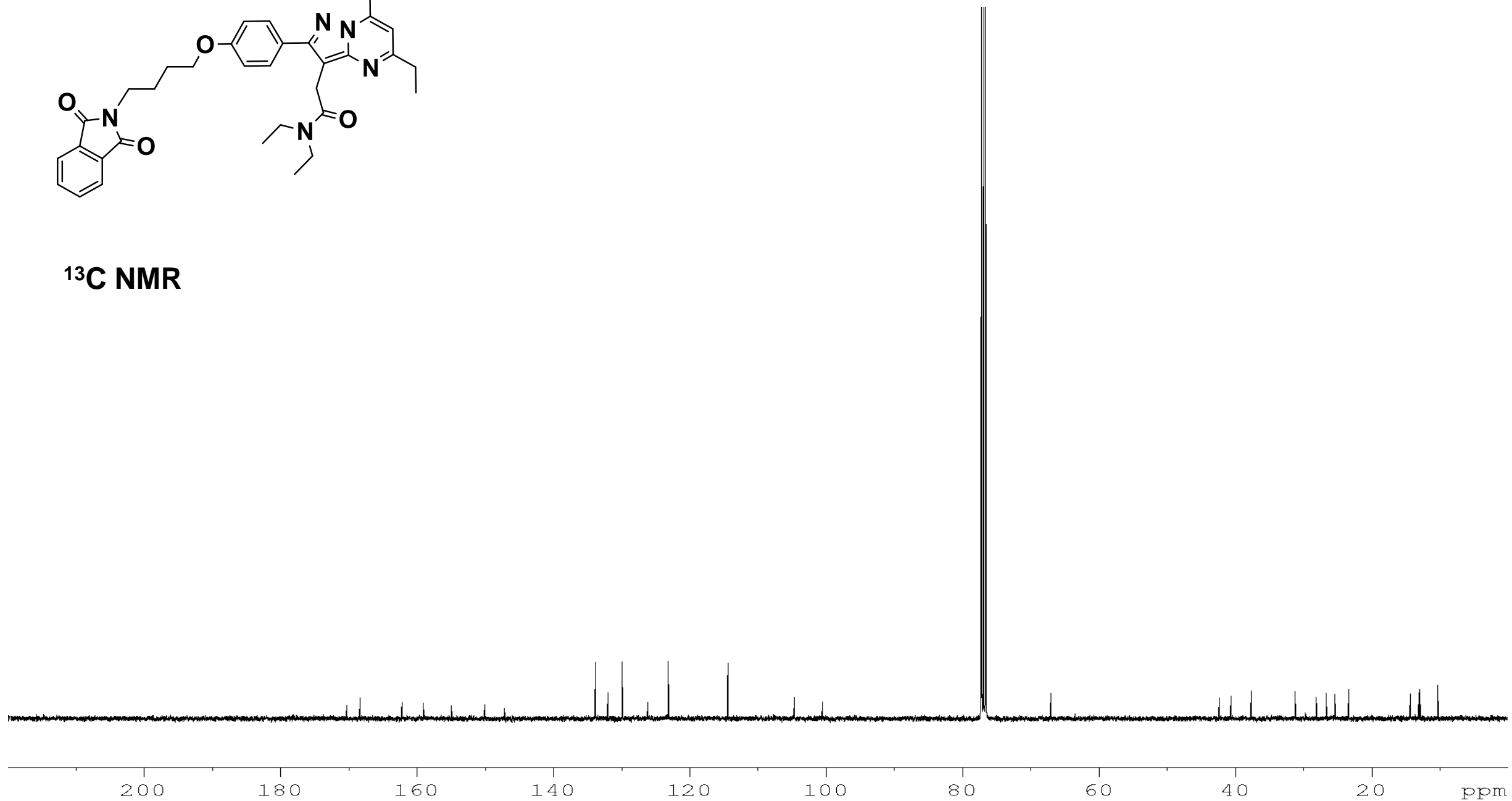


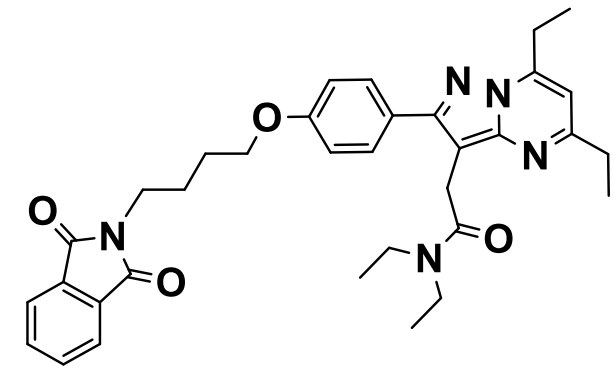
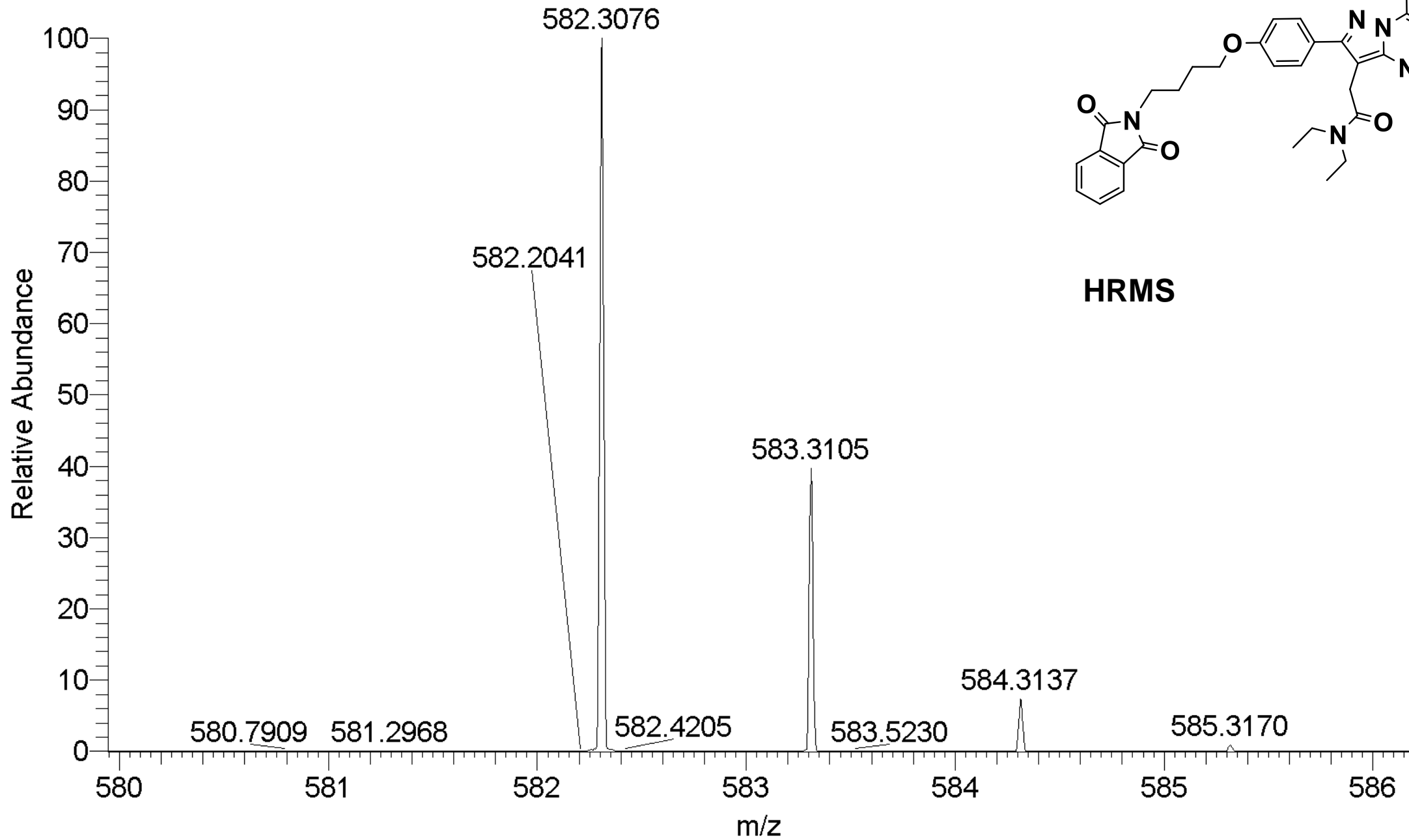
¹H NMR

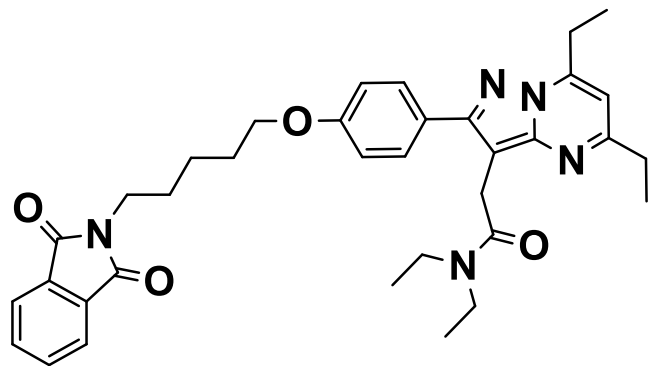




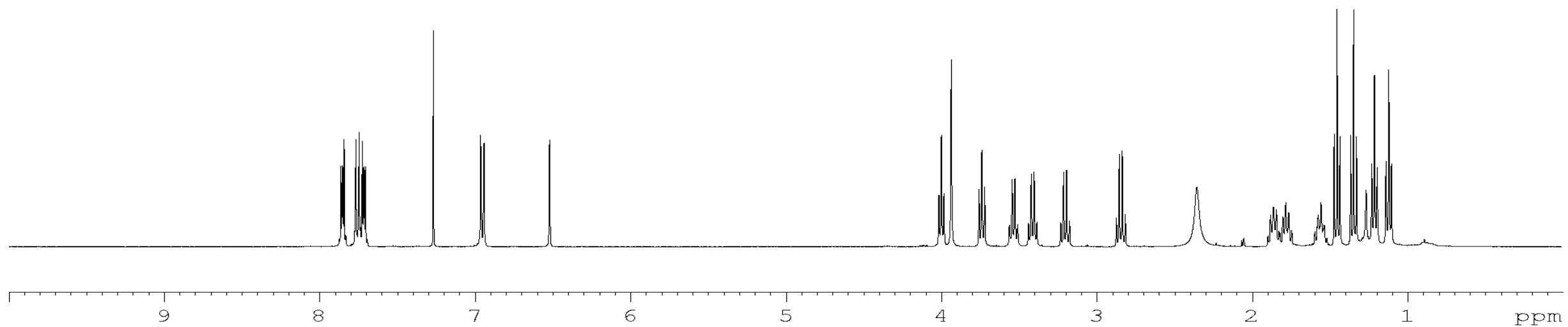
^{13}C NMR

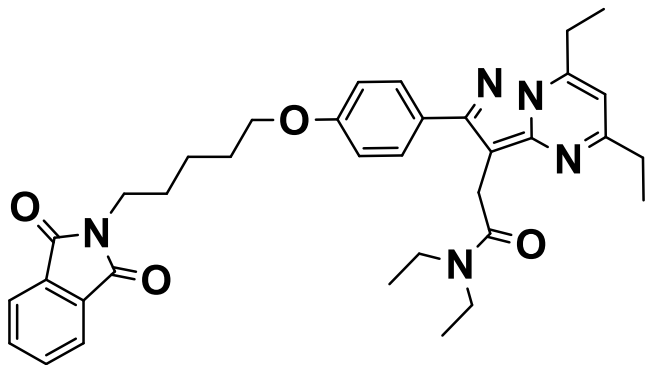




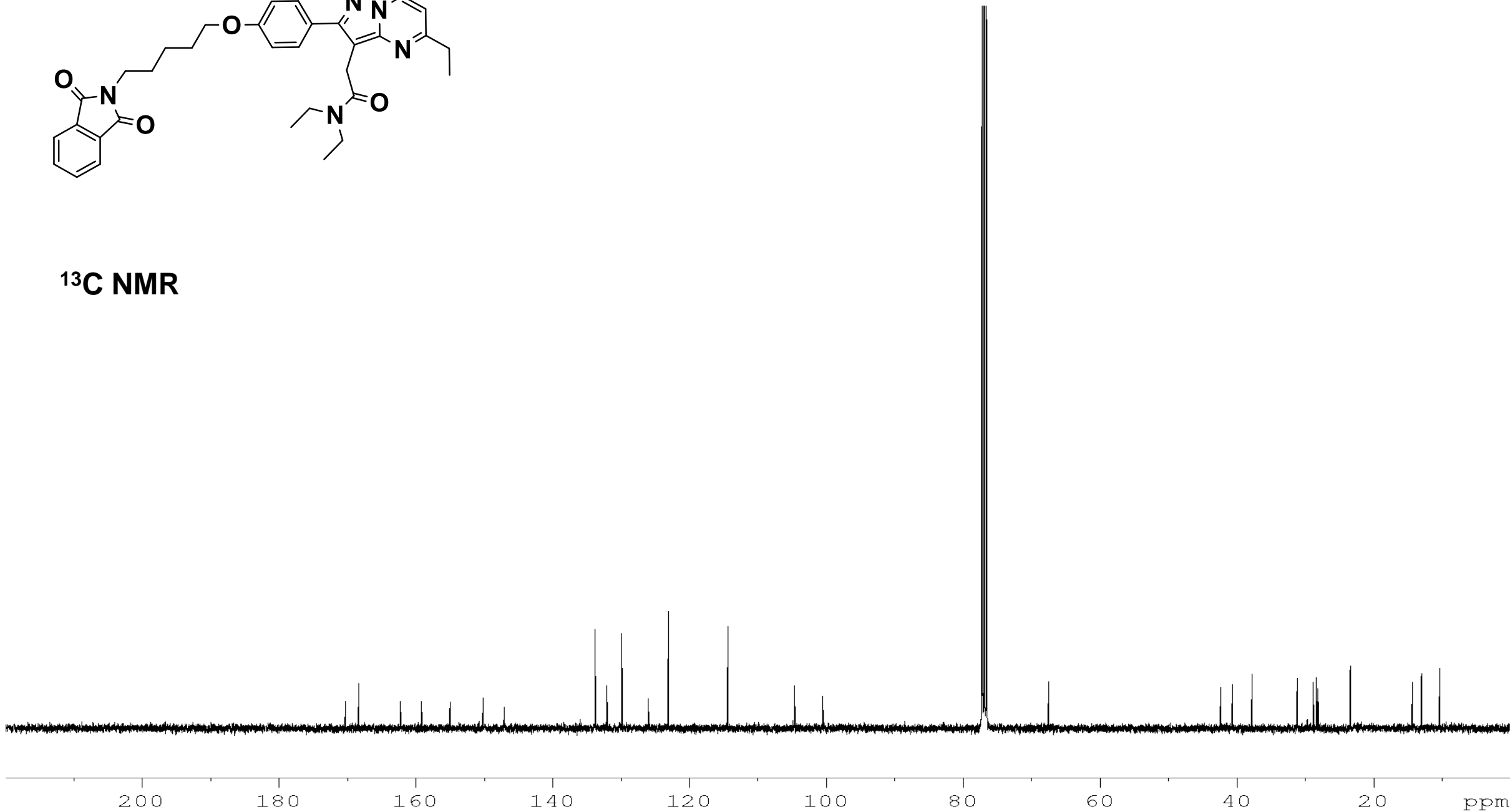


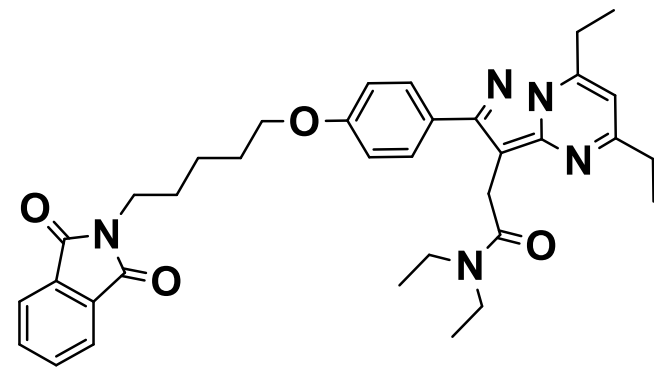
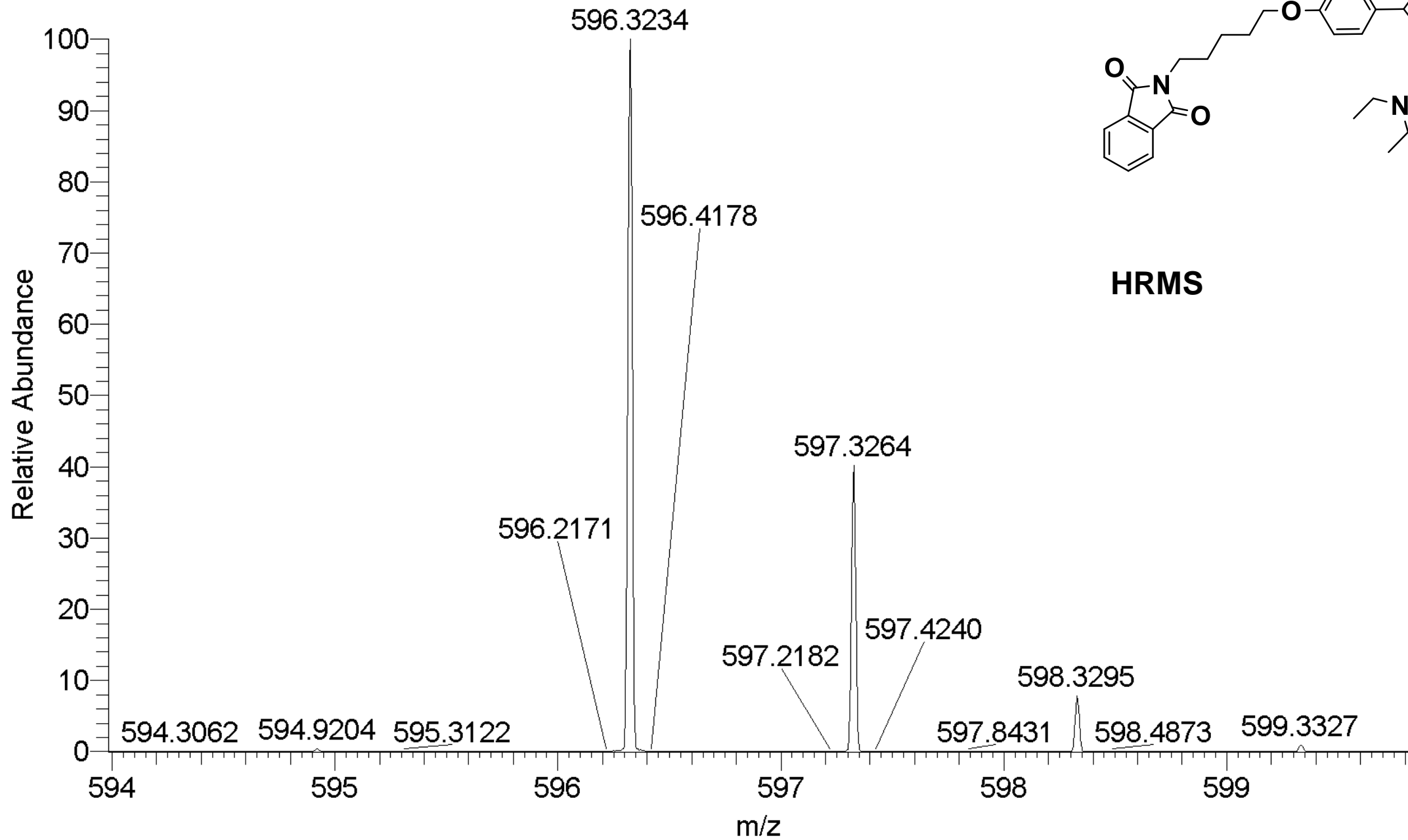
¹H NMR

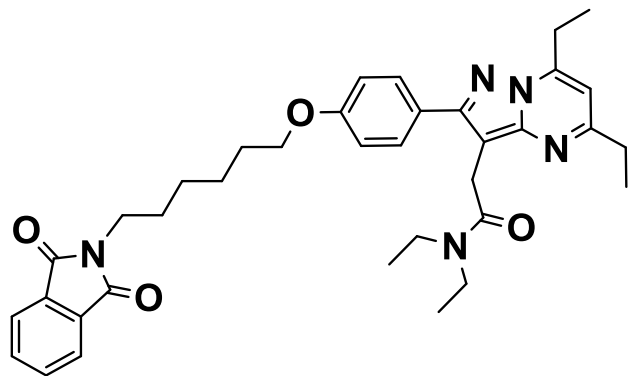




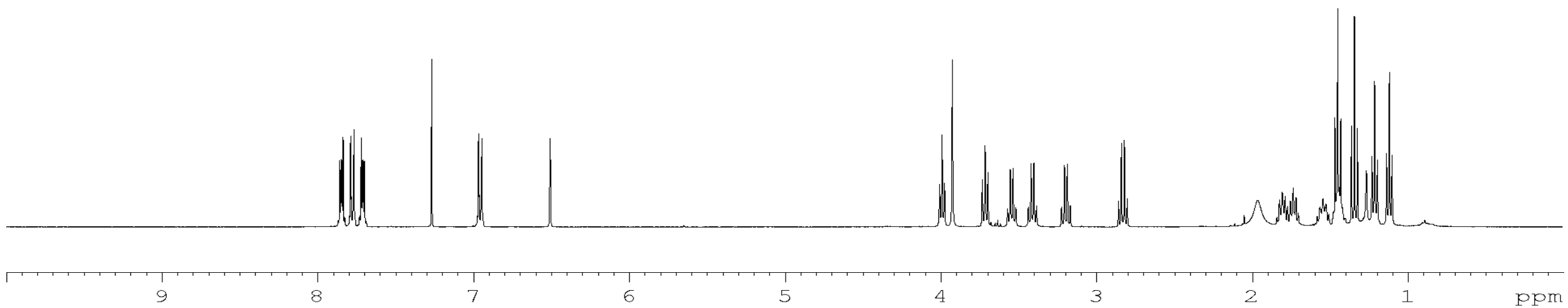
^{13}C NMR

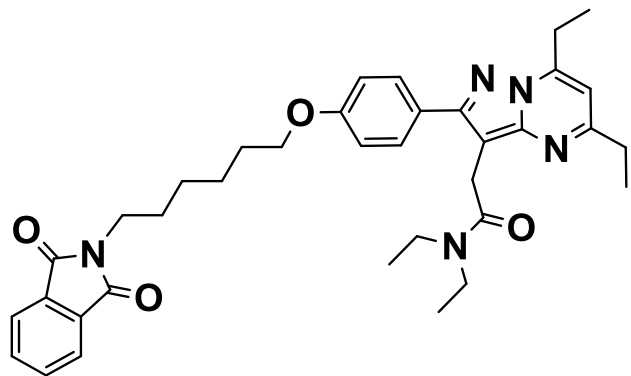




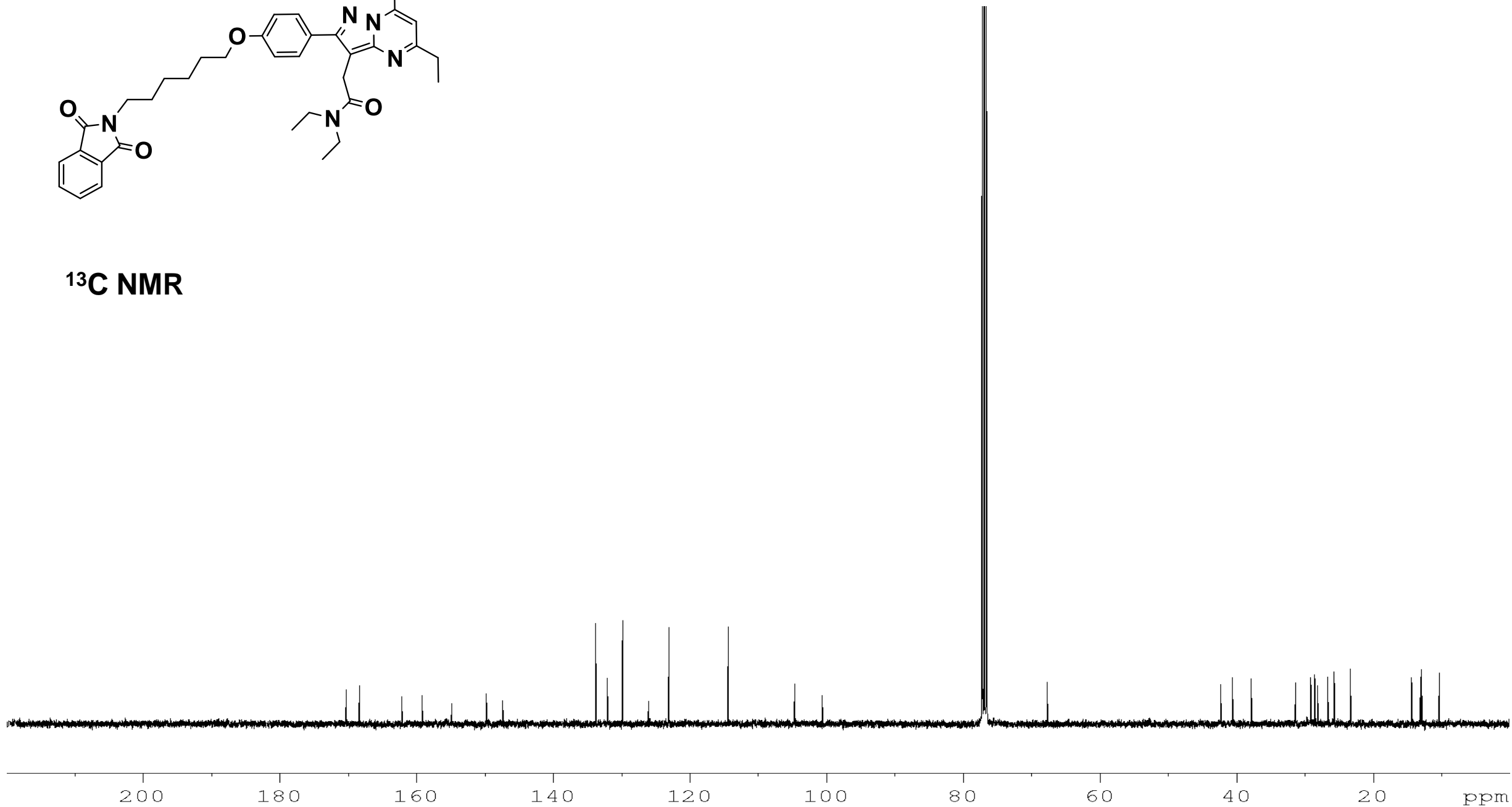


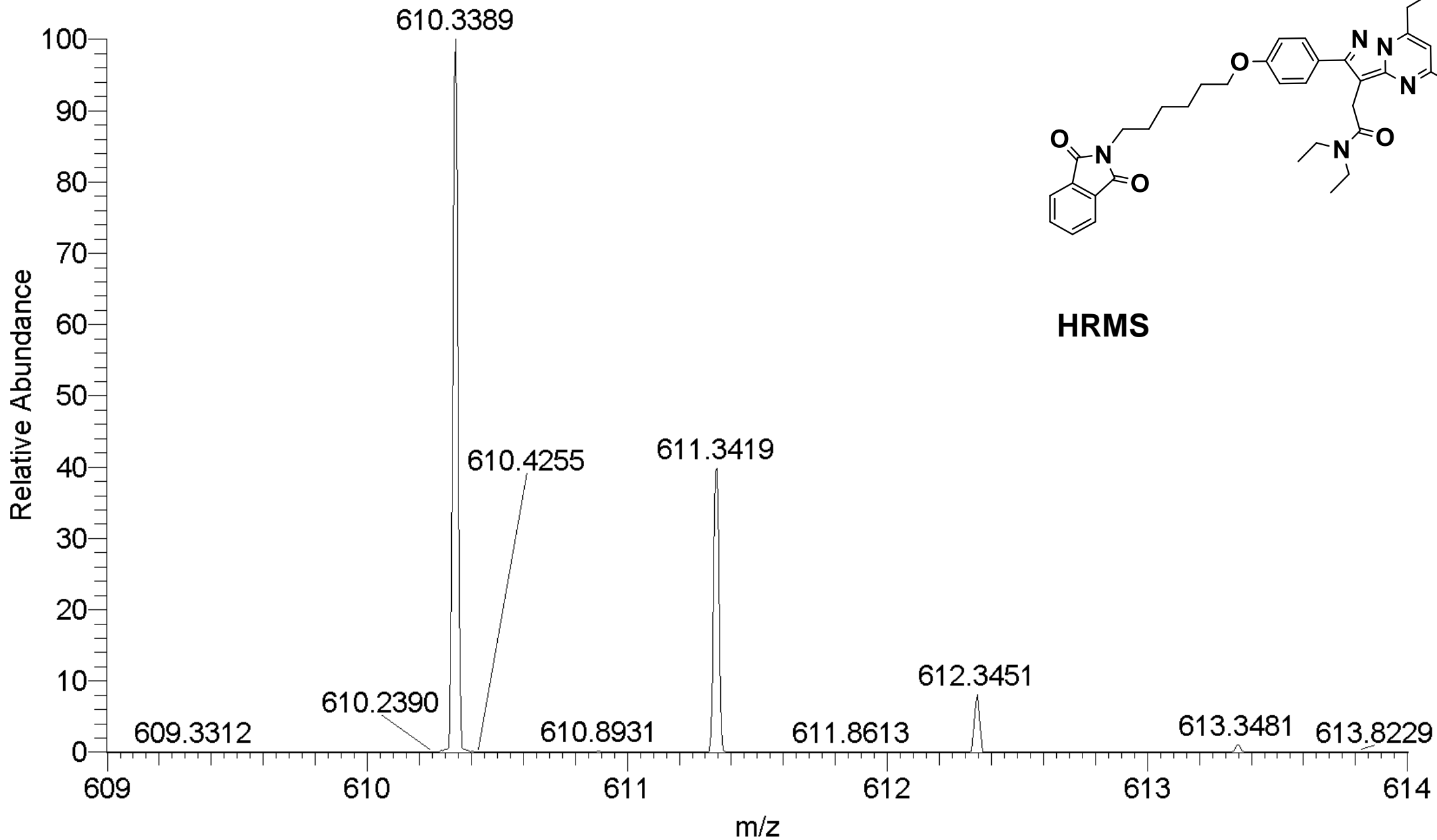
¹H NMR

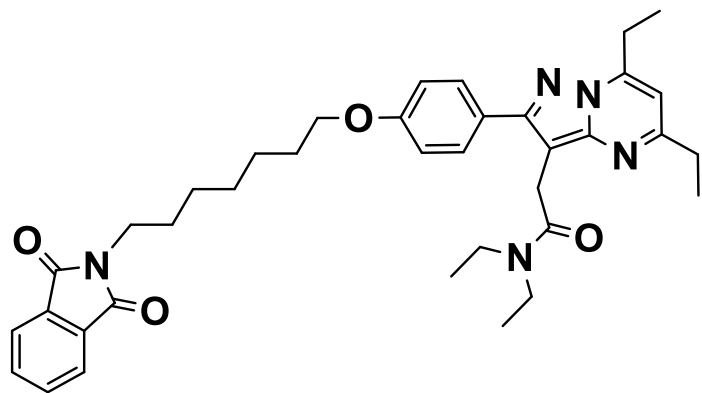




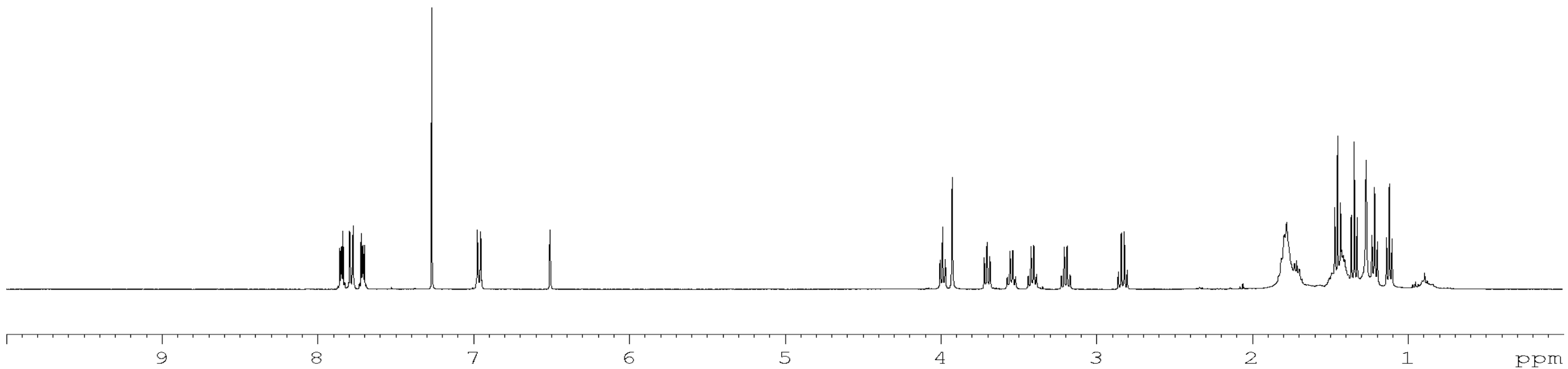
^{13}C NMR

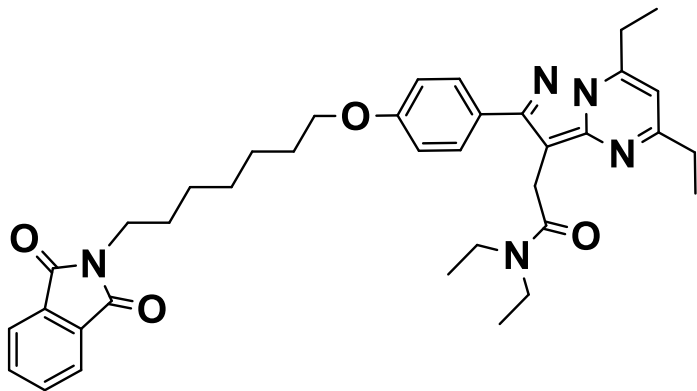




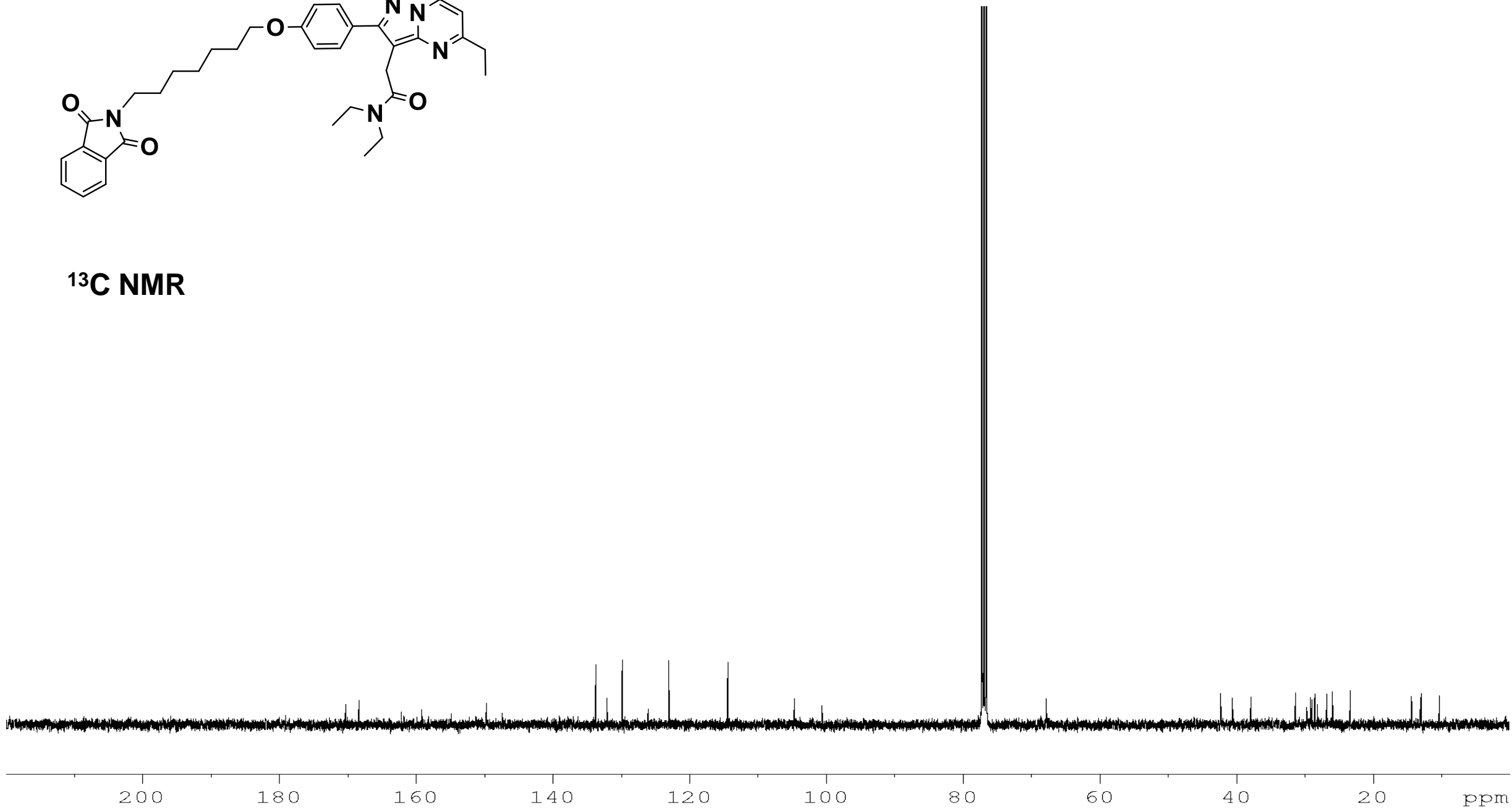


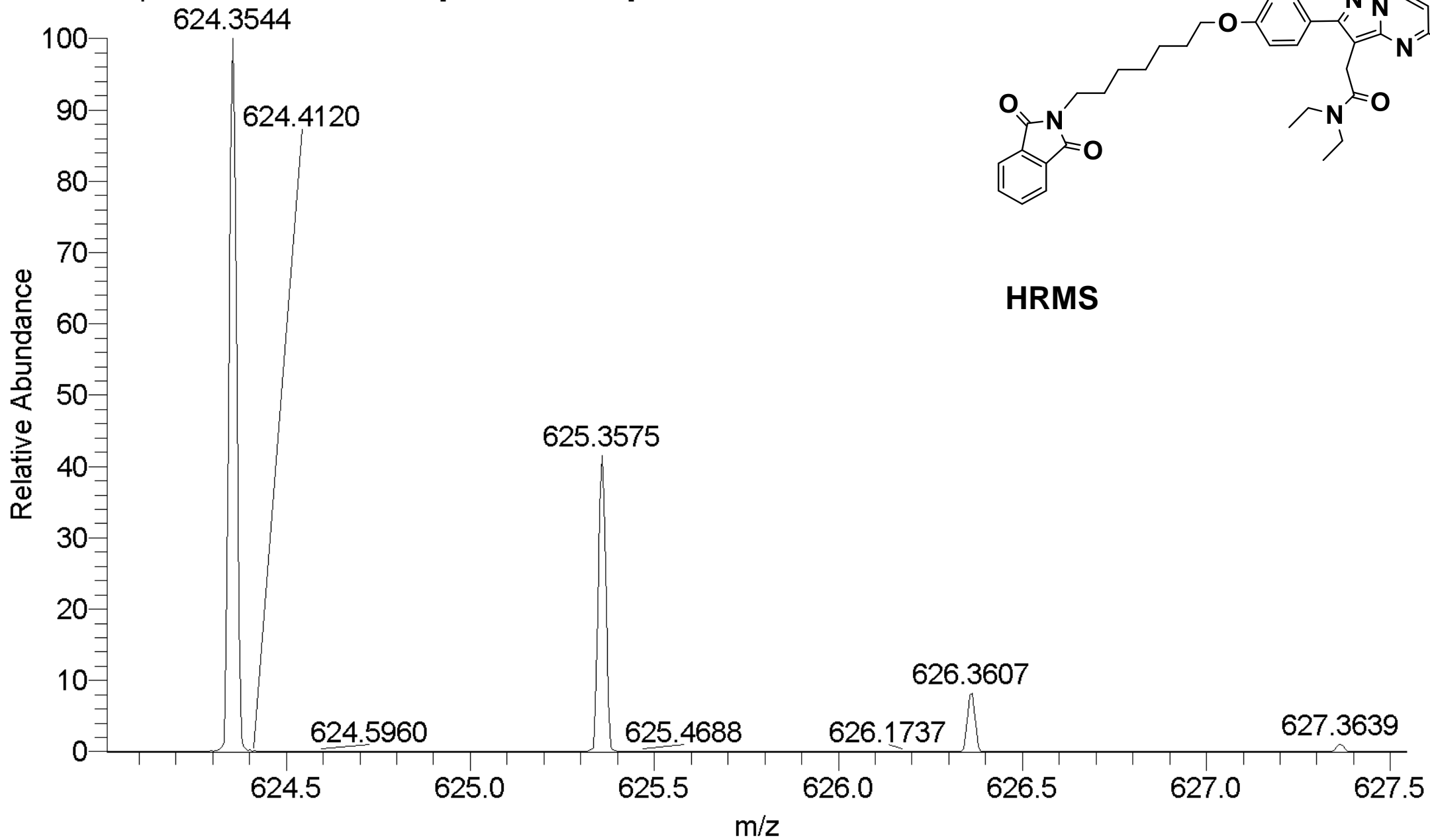
¹H NMR

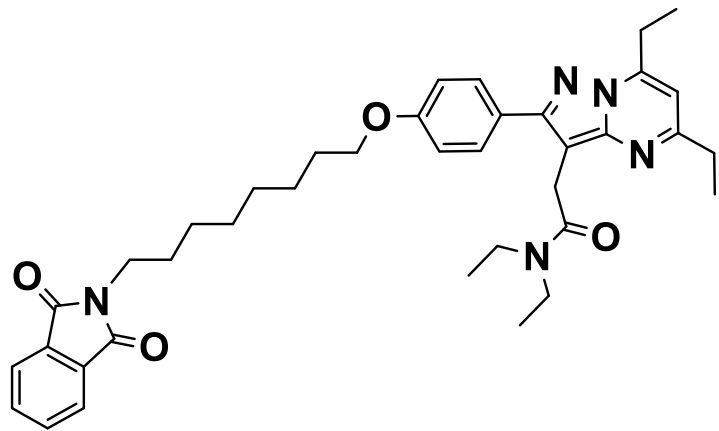




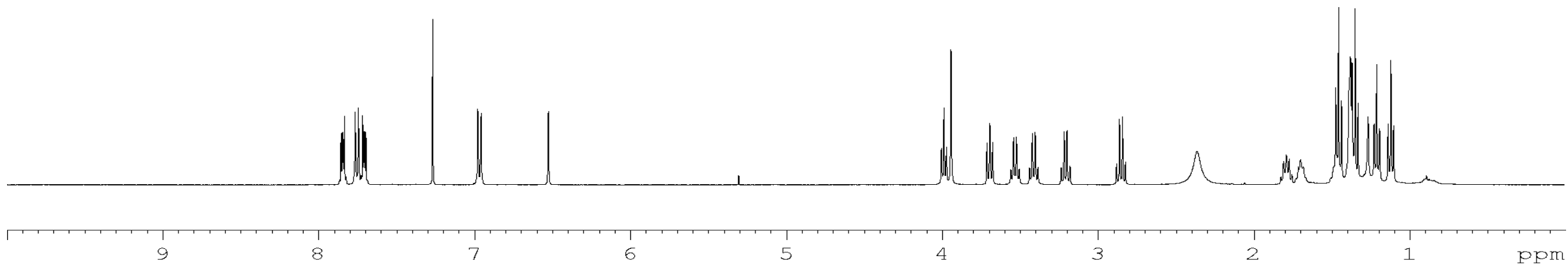
^{13}C NMR

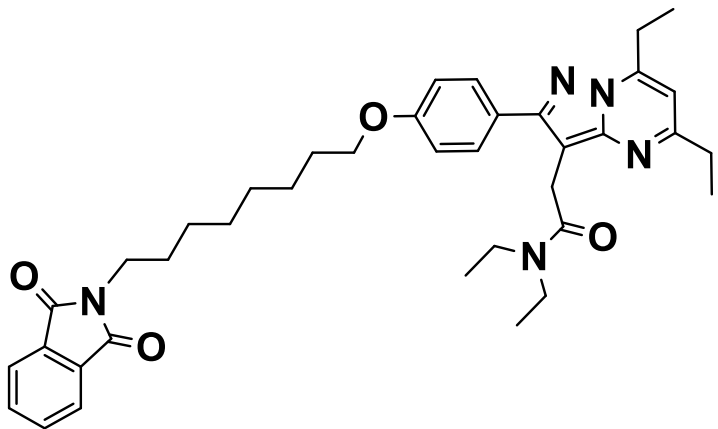




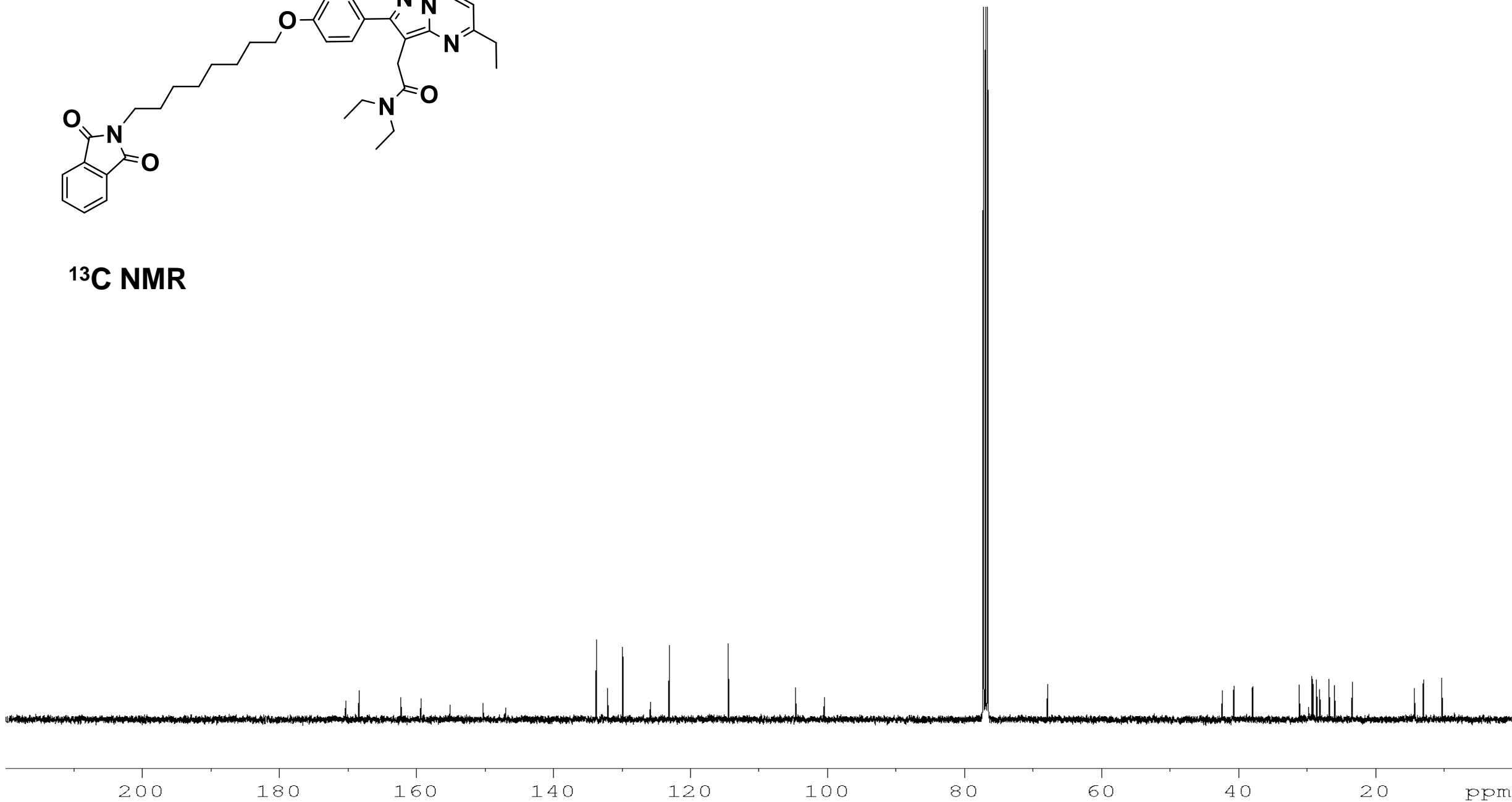


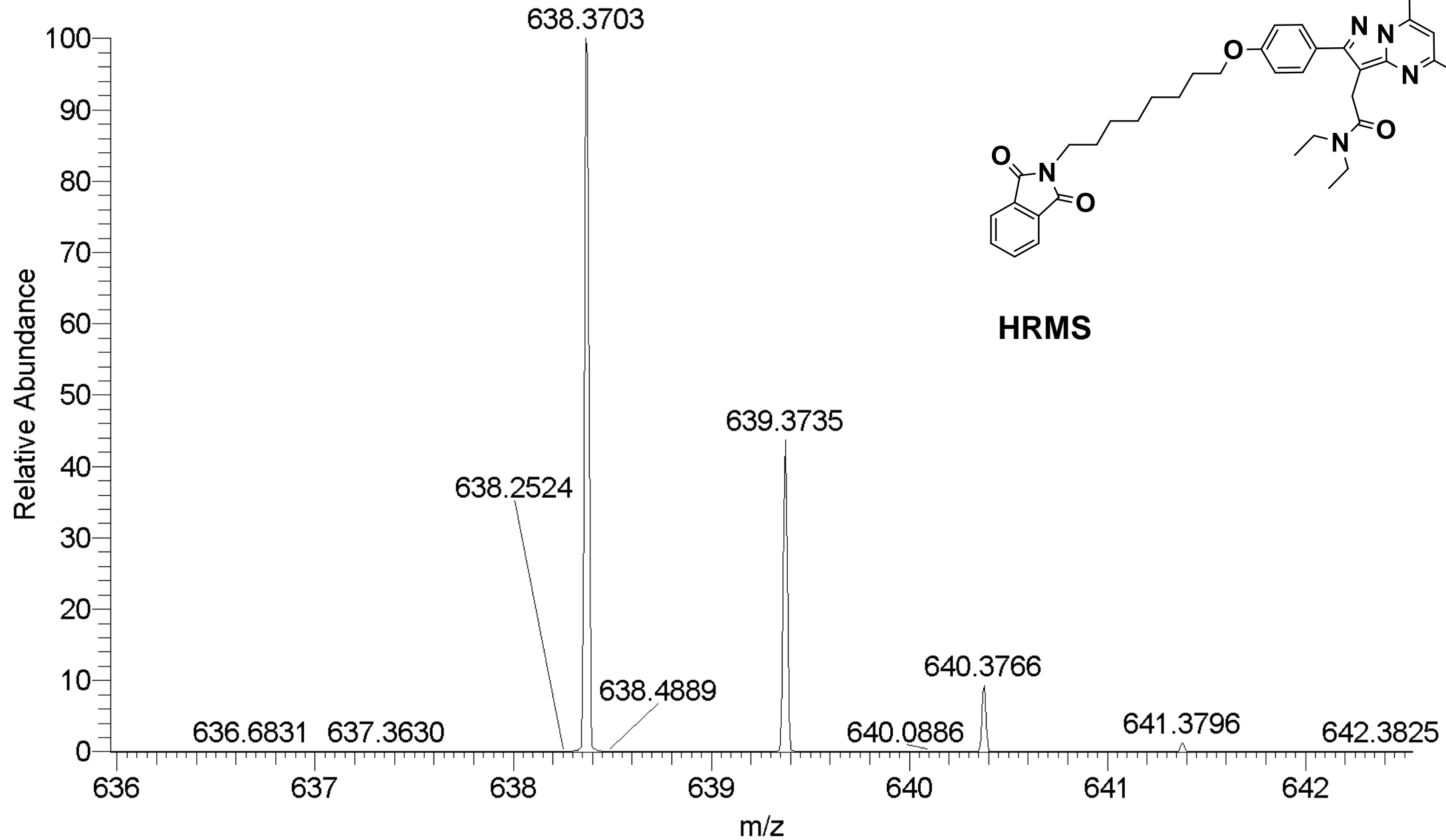
^1H NMR

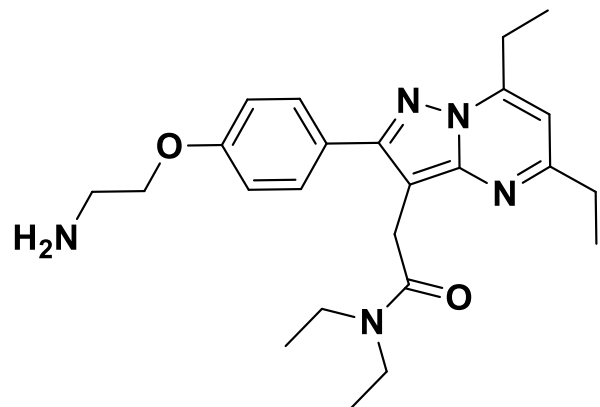




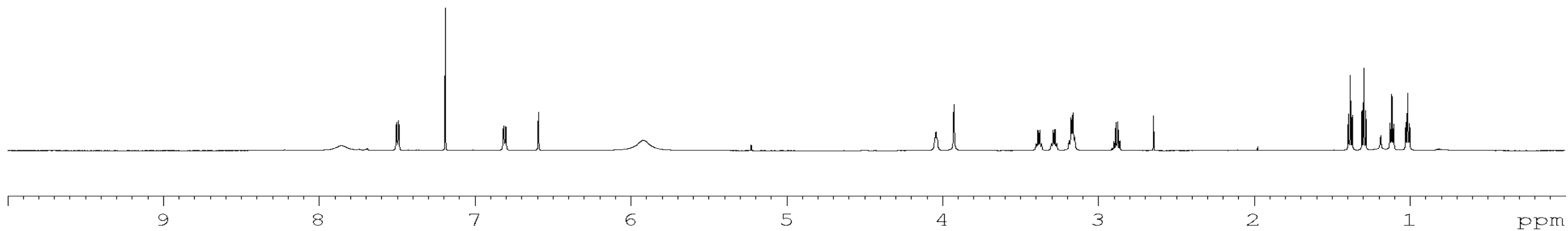
^{13}C NMR

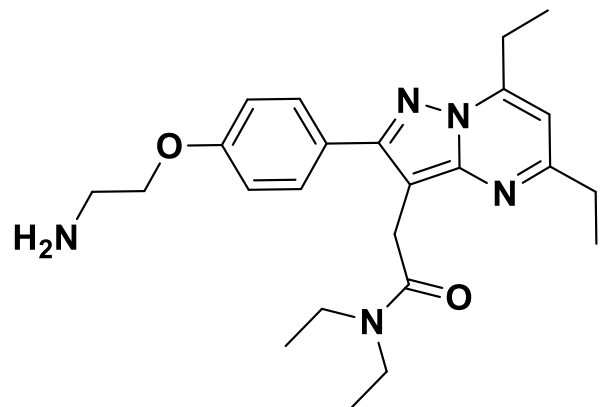




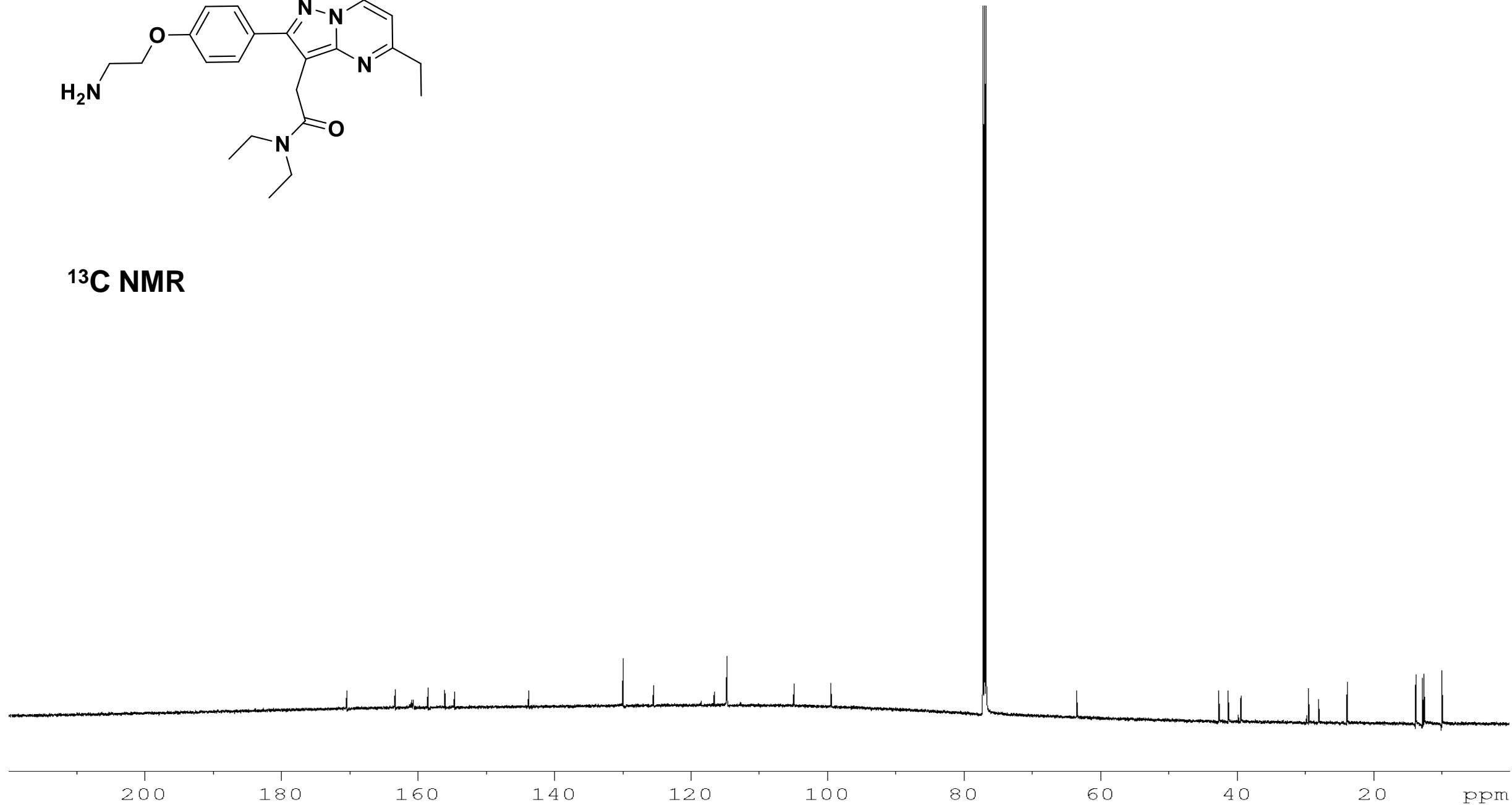


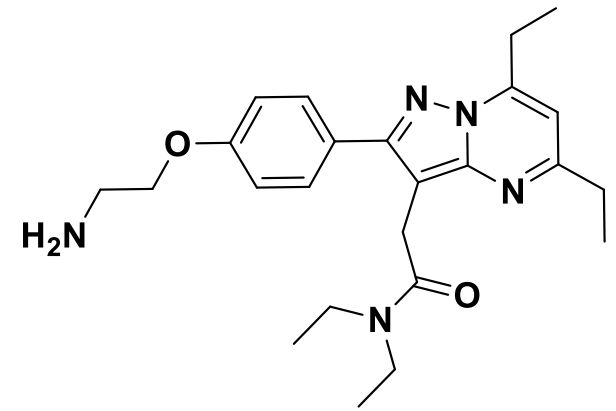
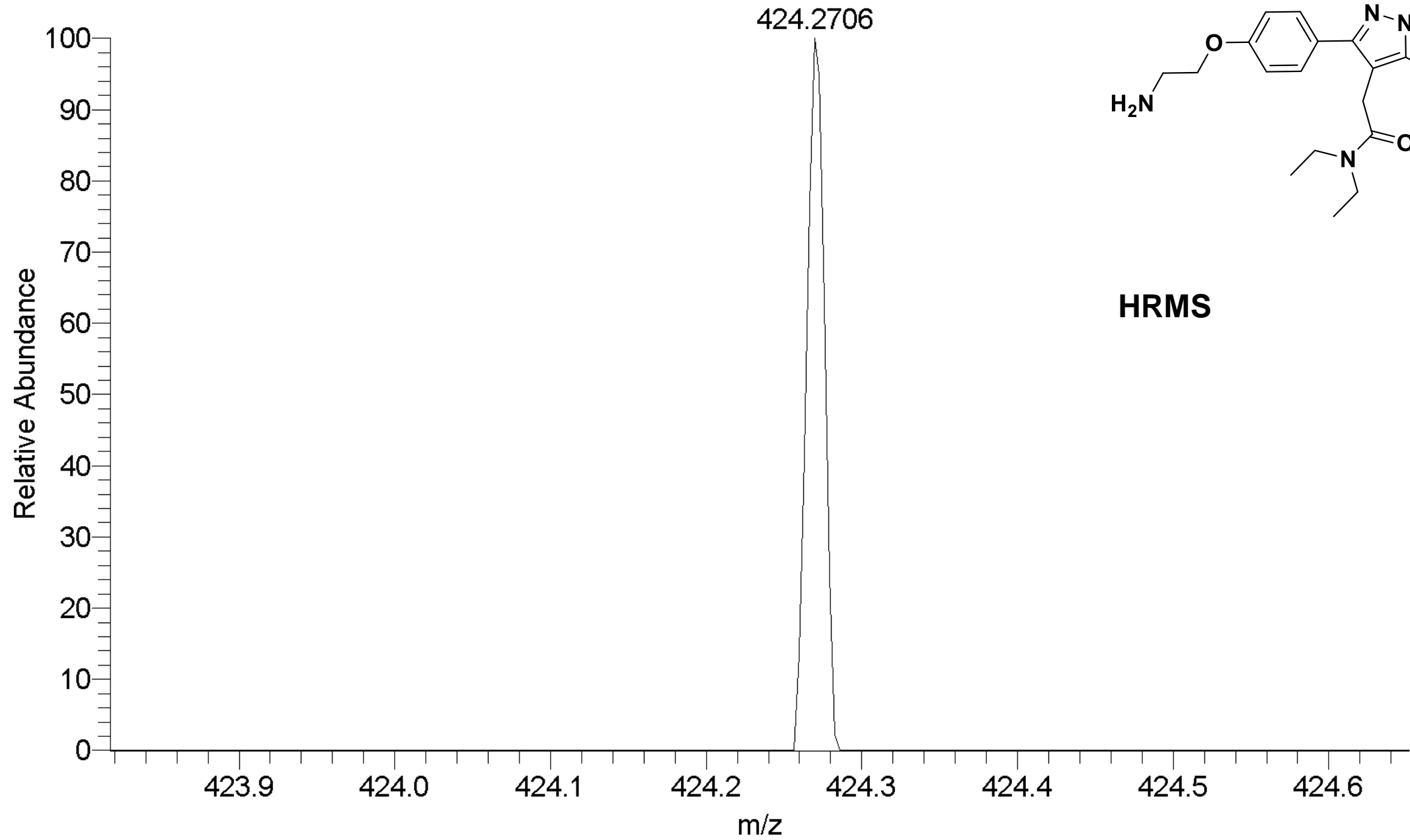
^1H NMR

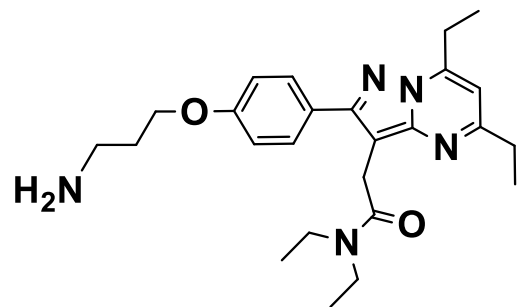




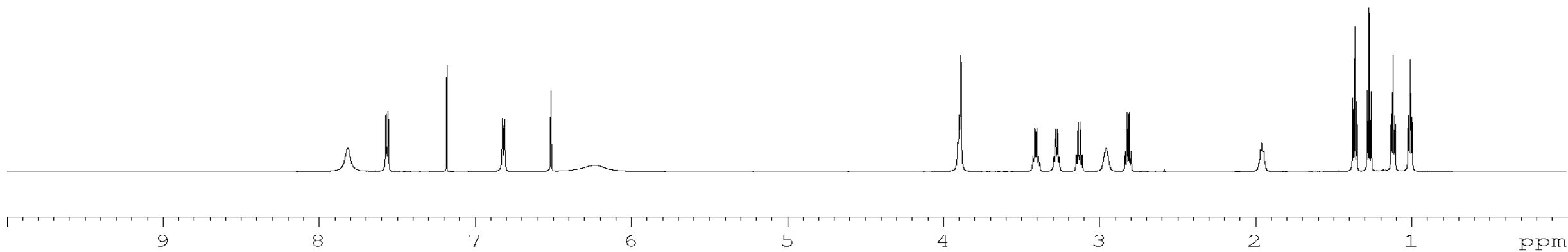
^{13}C NMR

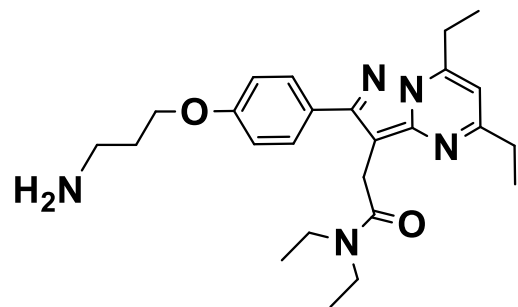




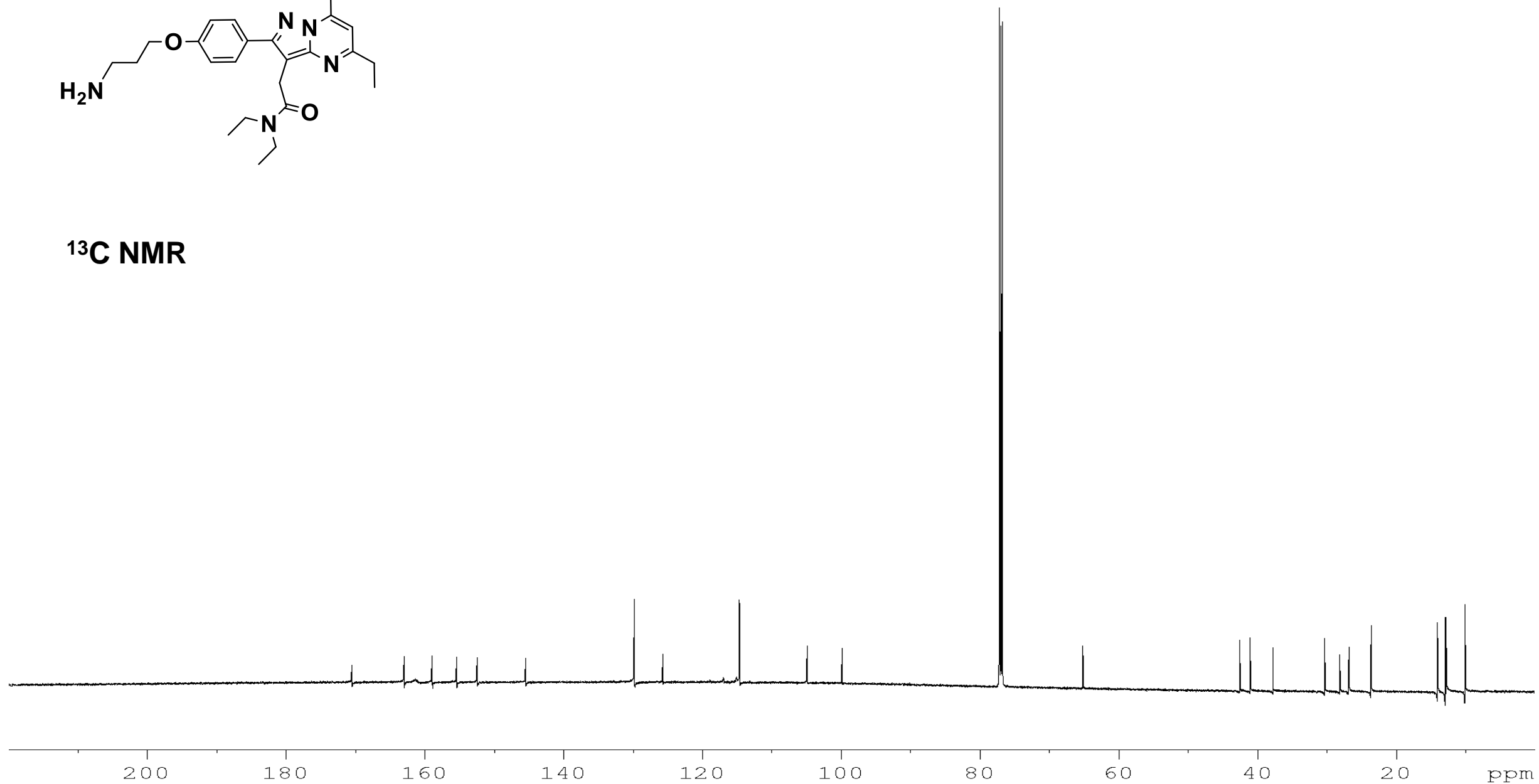


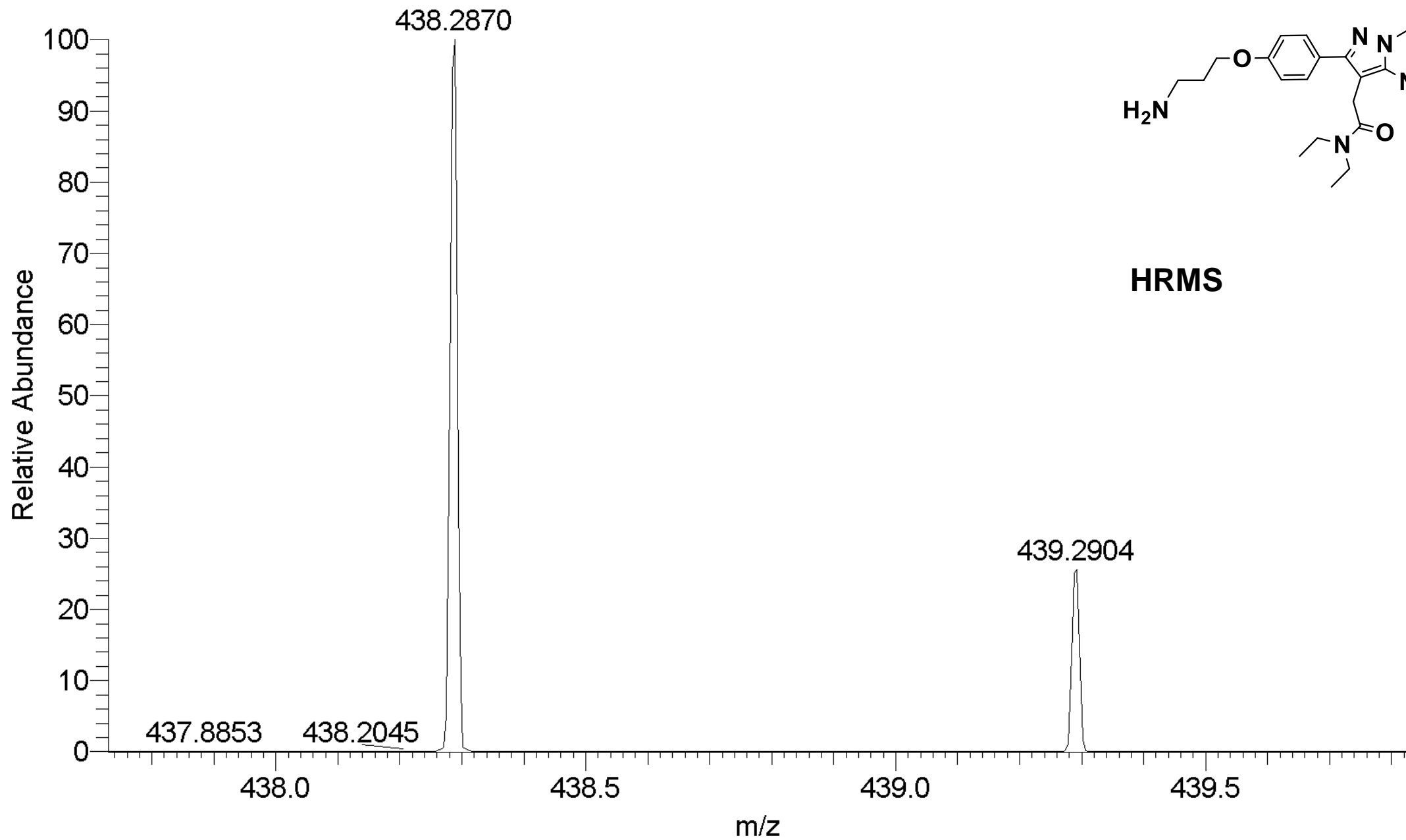
^1H NMR

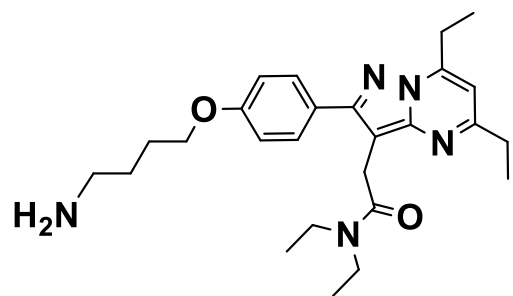




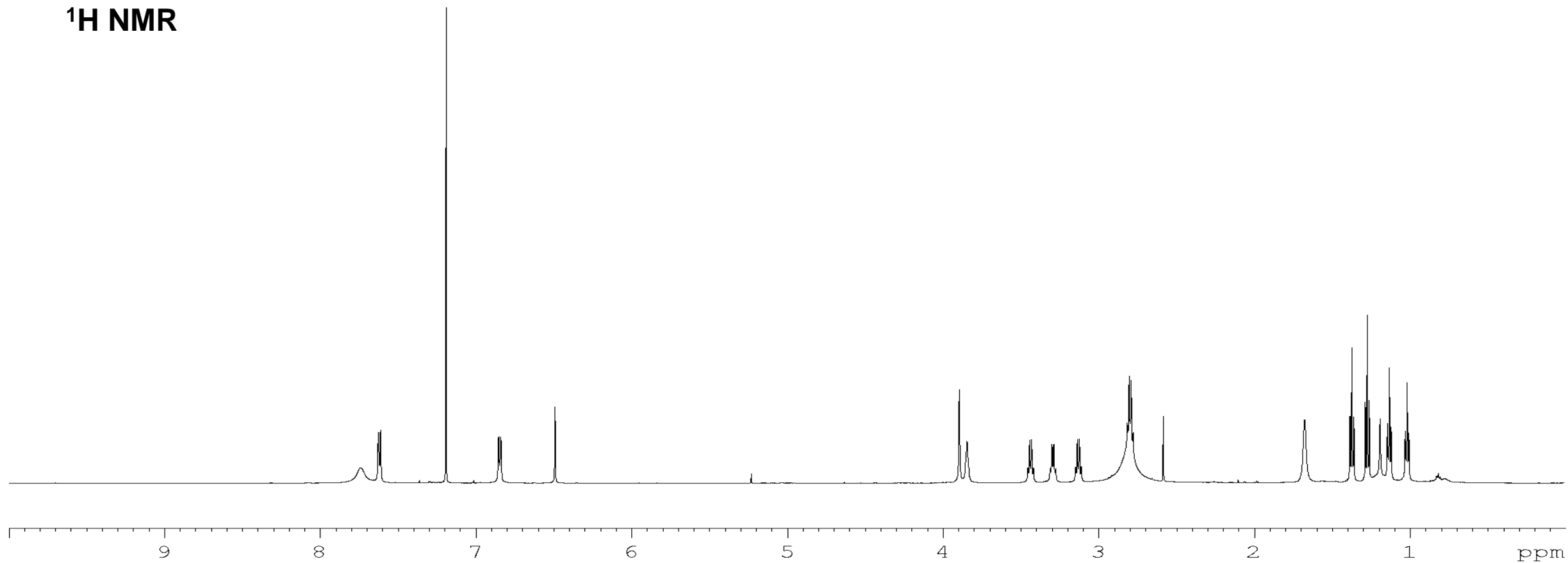
^{13}C NMR

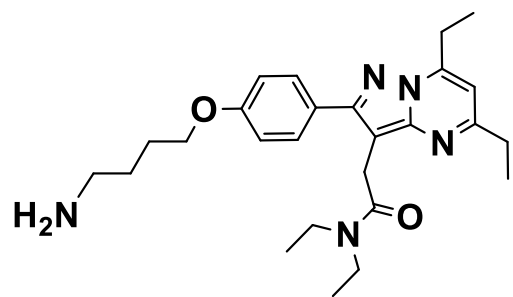




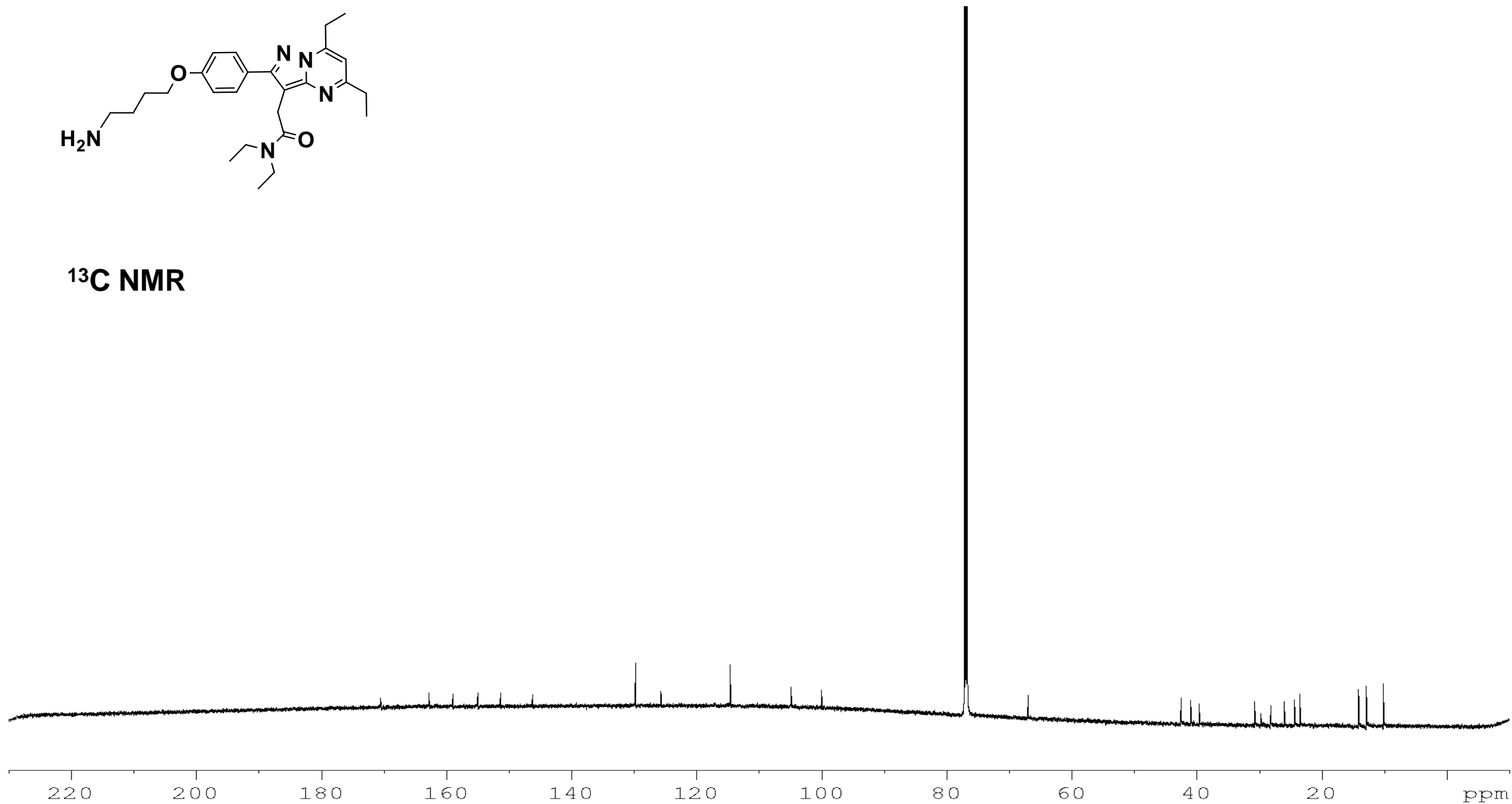


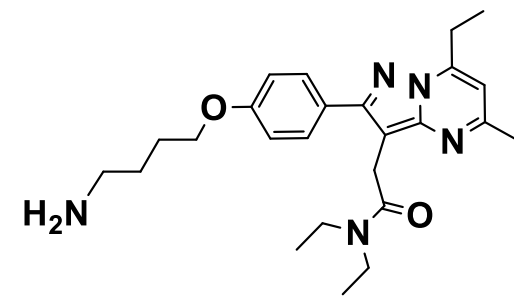
¹H NMR



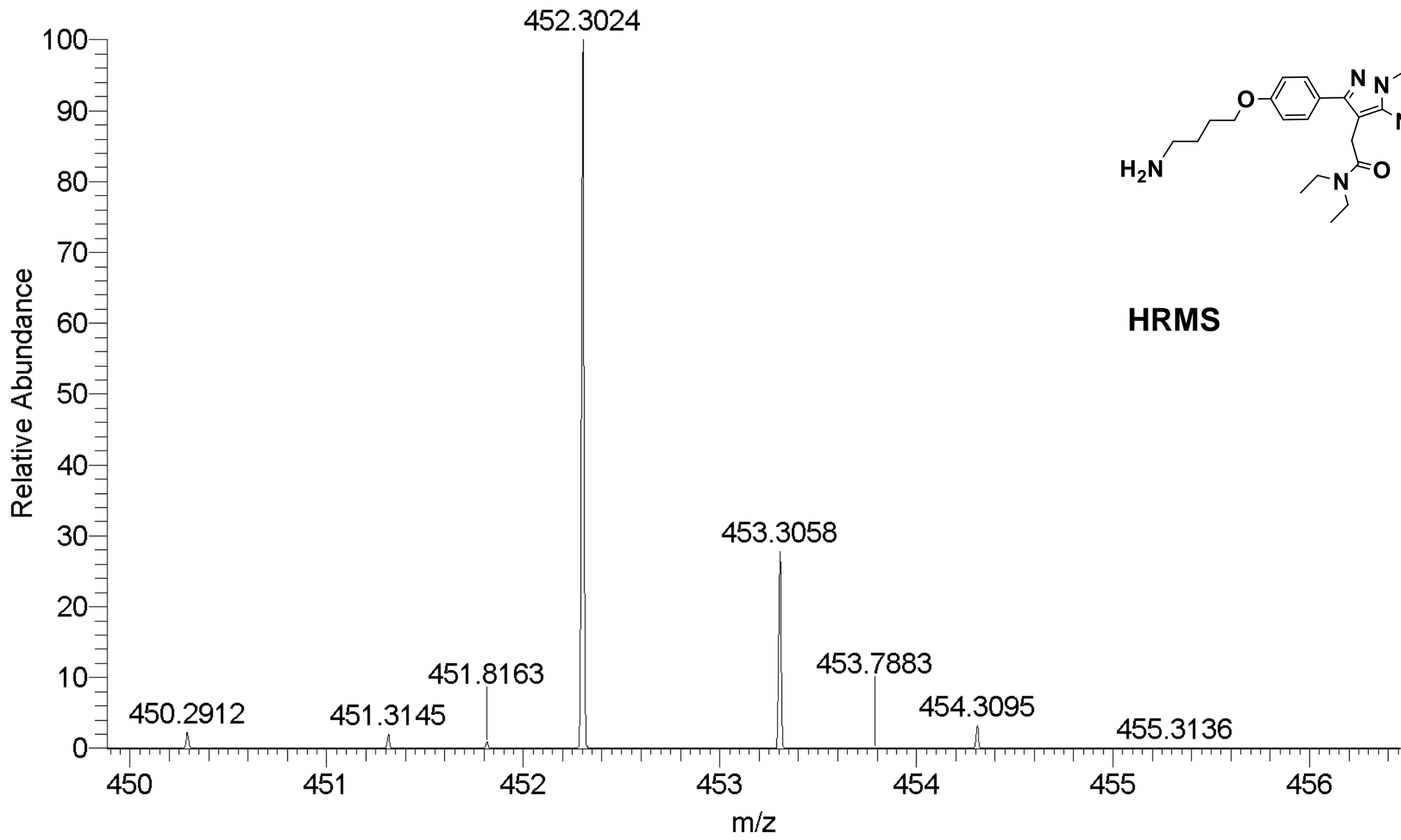


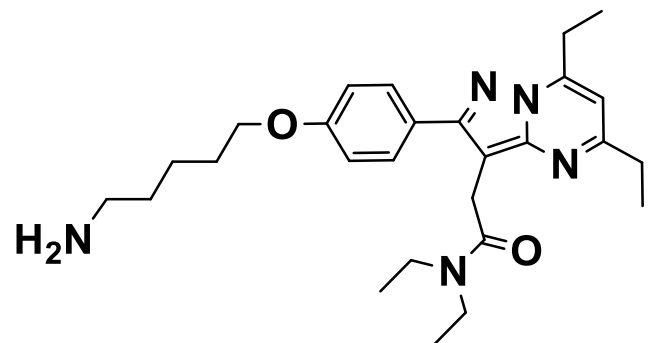
^{13}C NMR



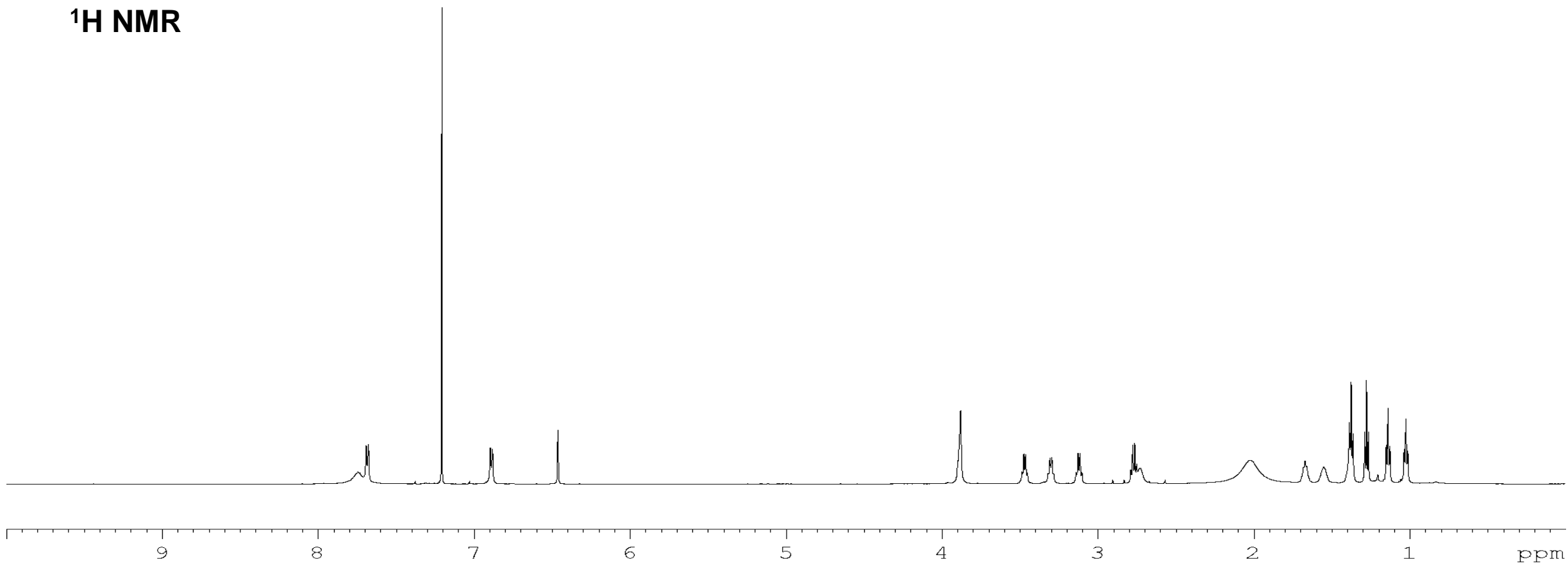


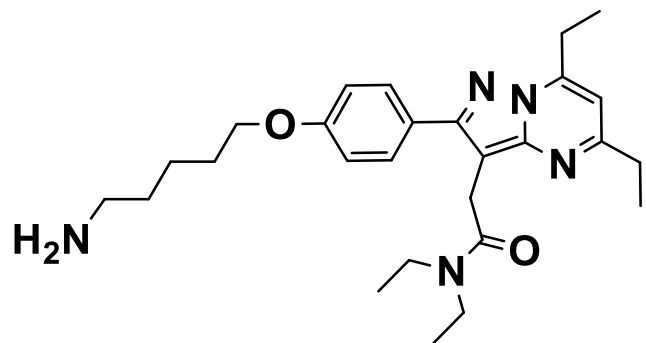
HRMS



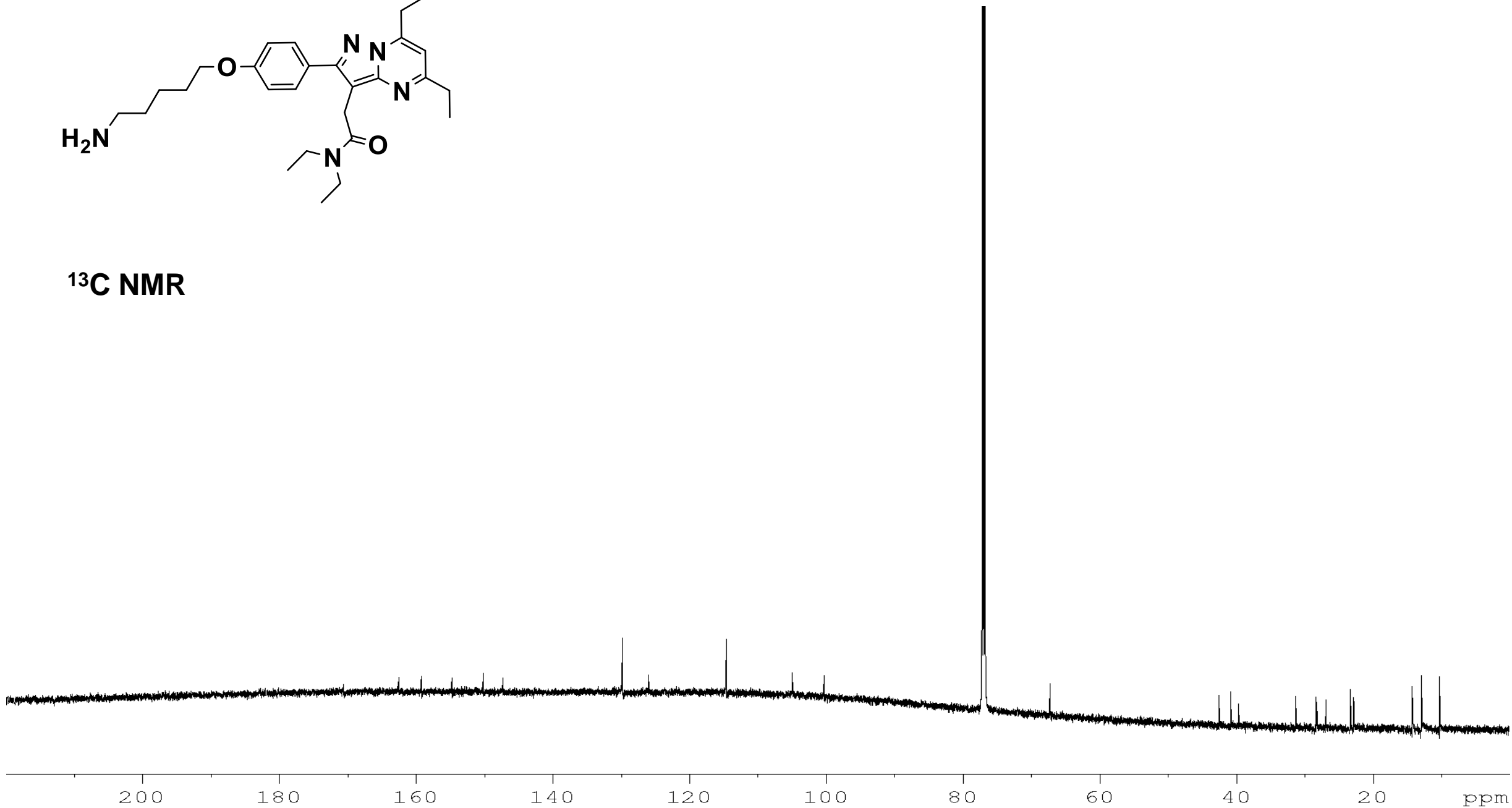


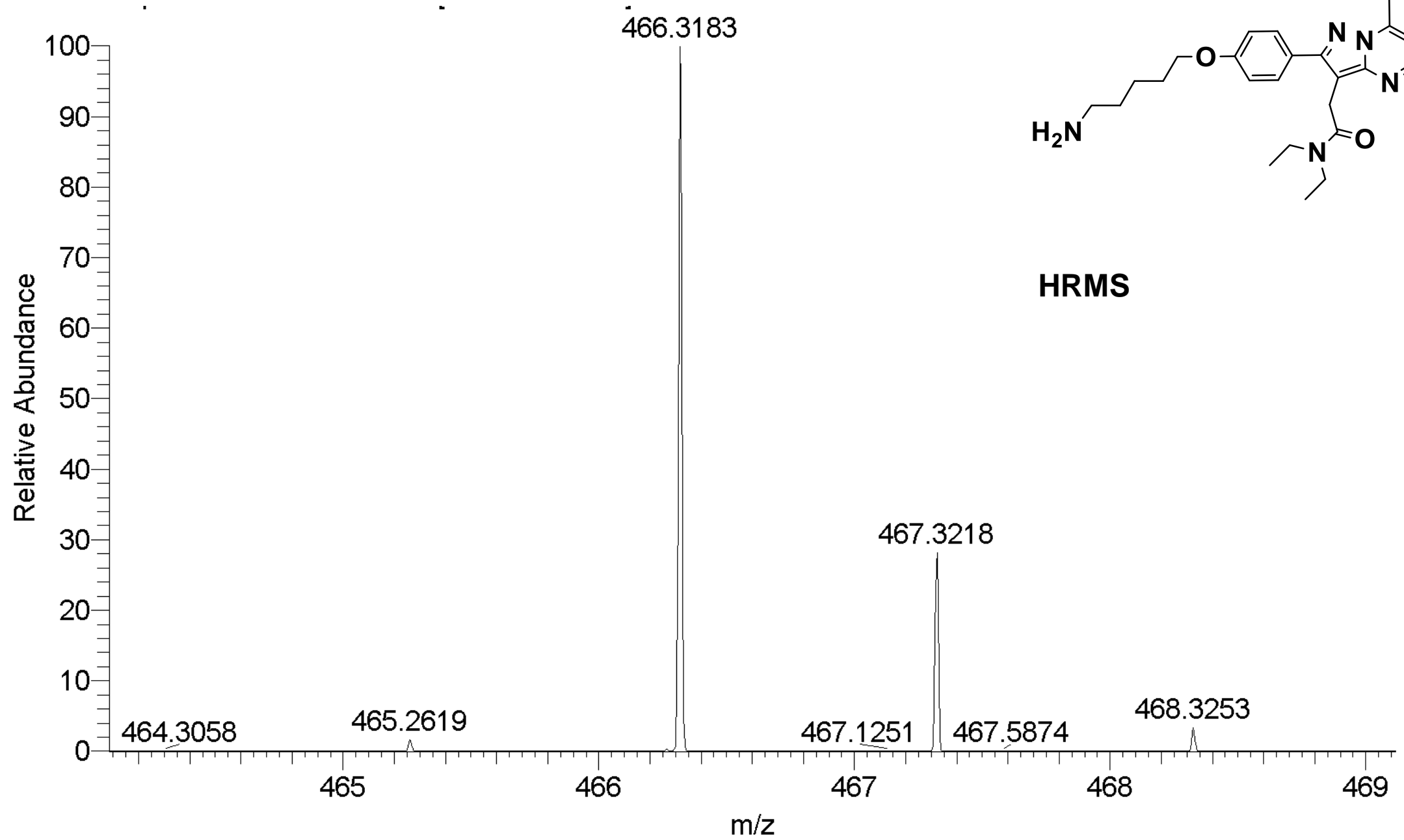
^1H NMR

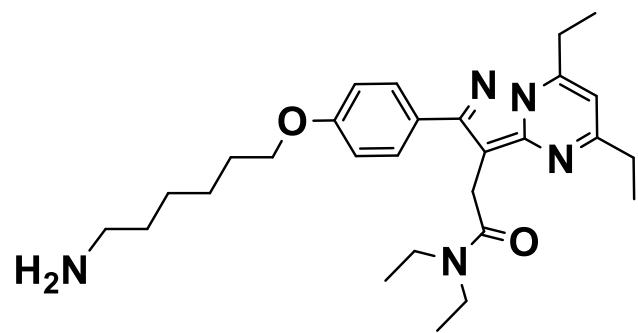




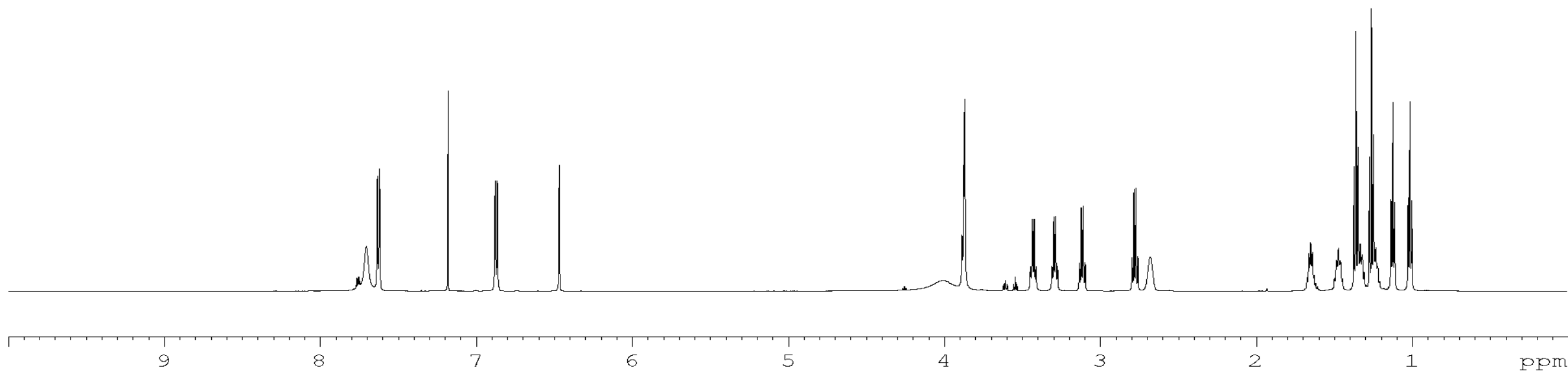
^{13}C NMR

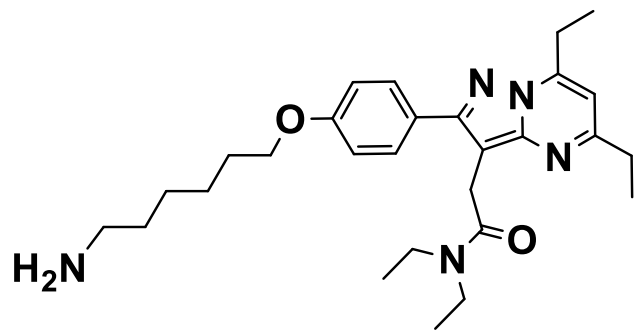




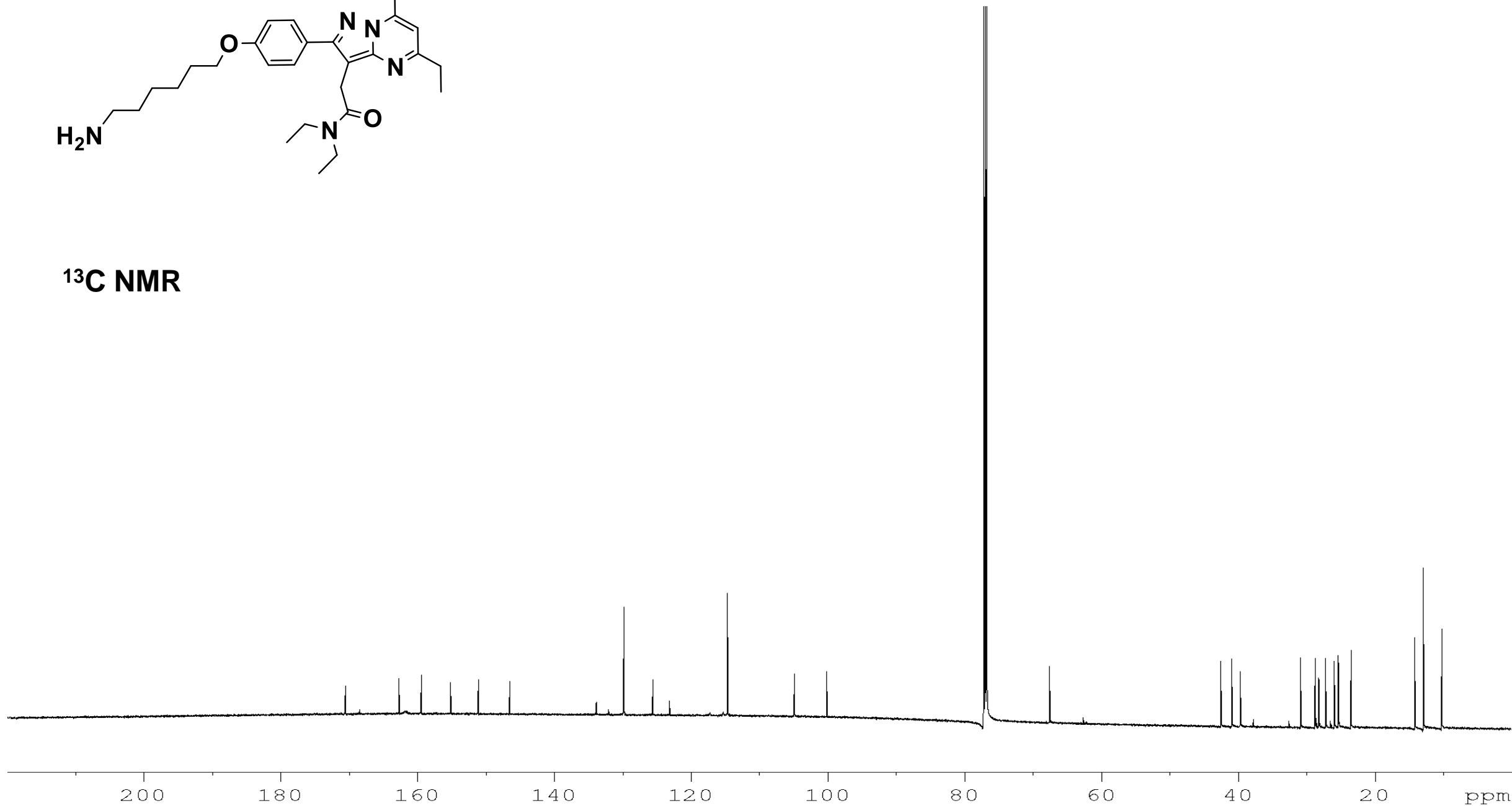


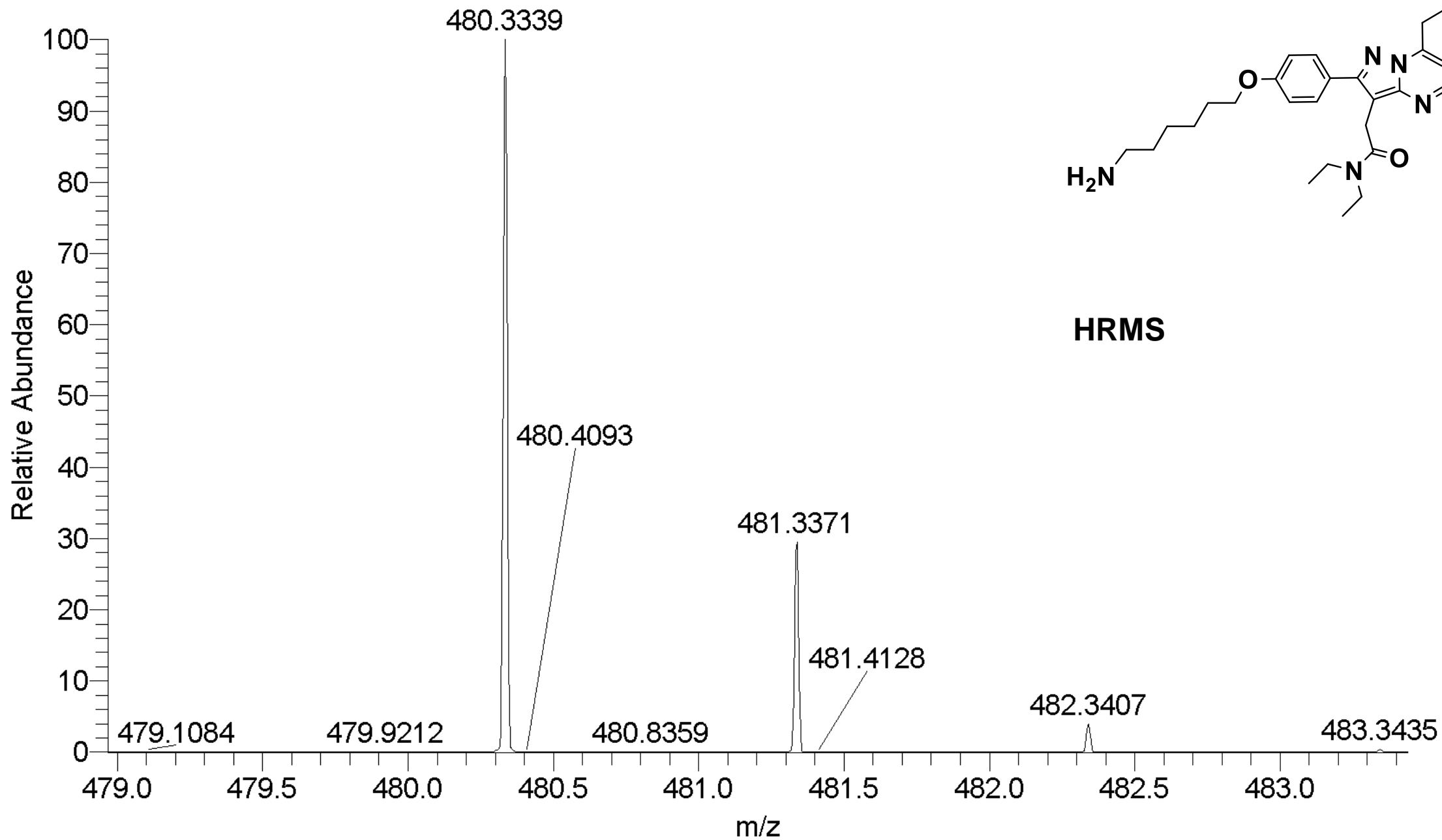
^1H NMR

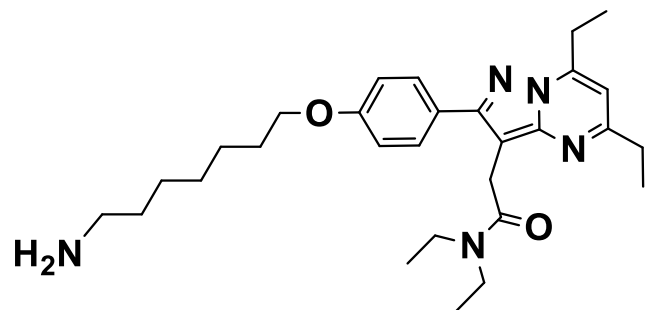




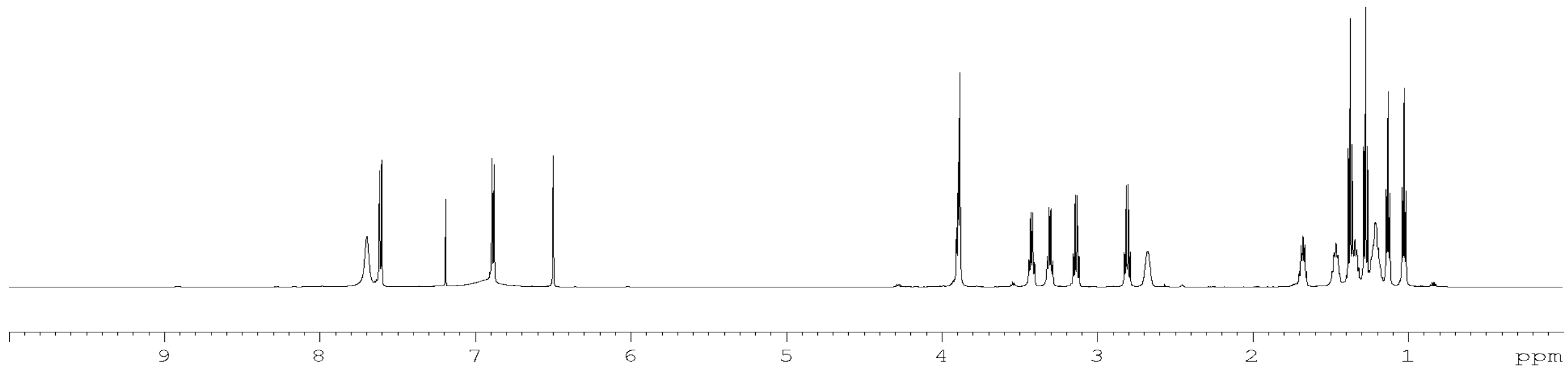
^{13}C NMR

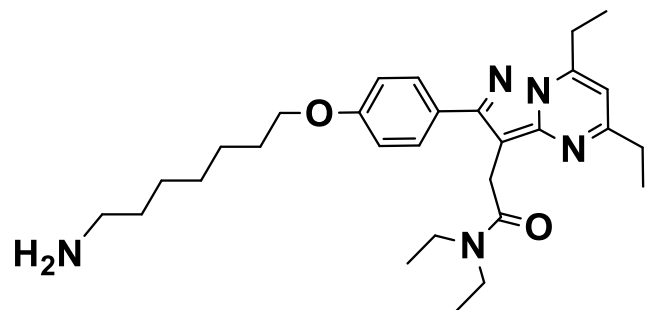




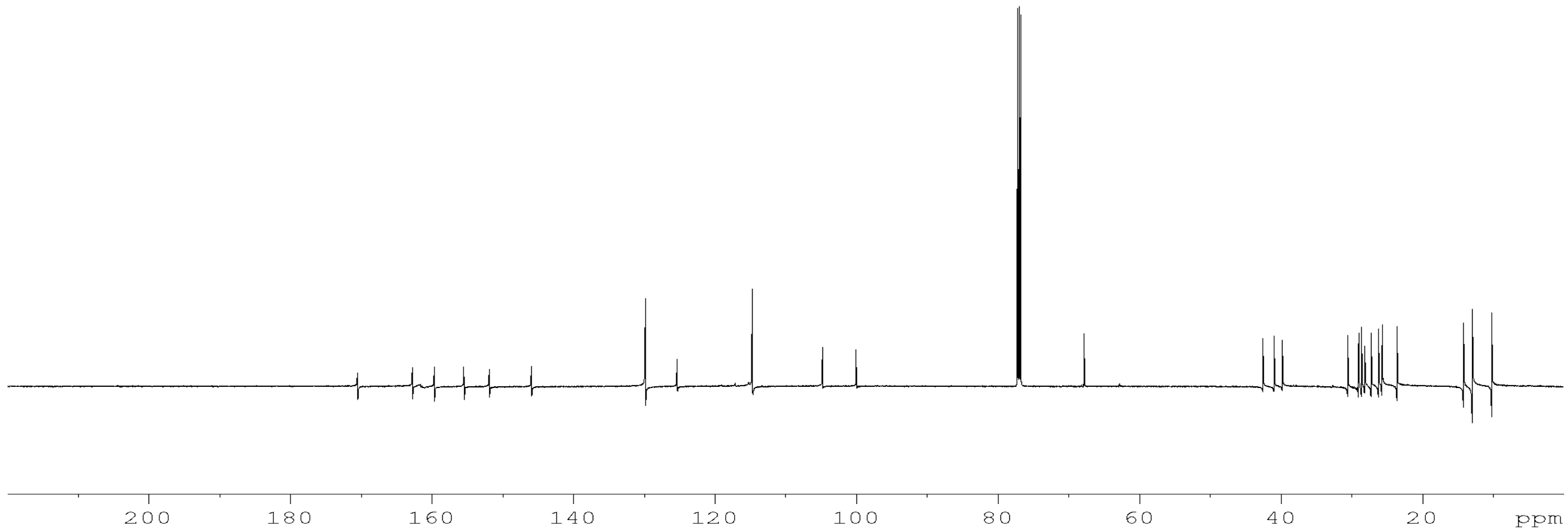


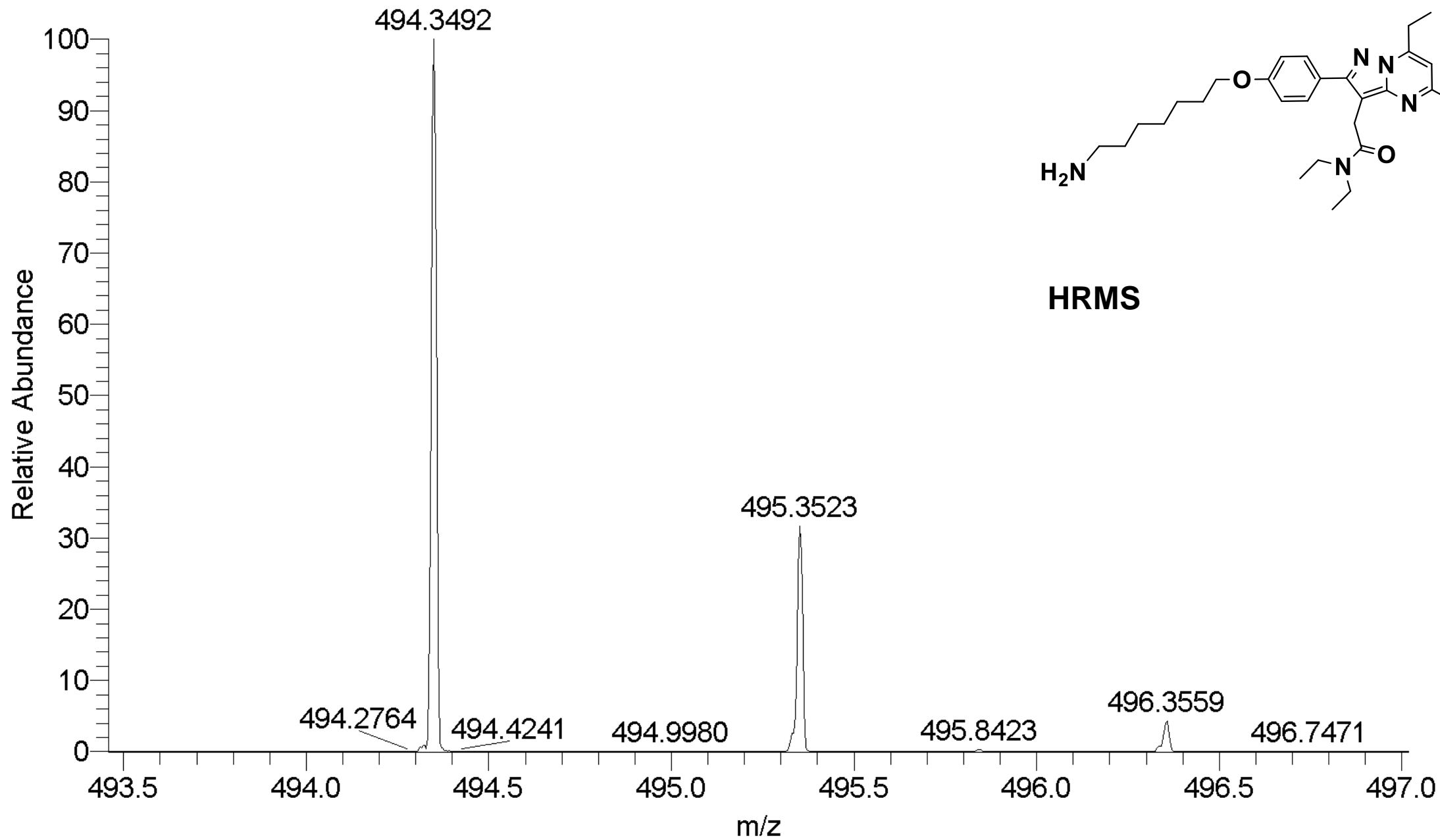
^1H NMR

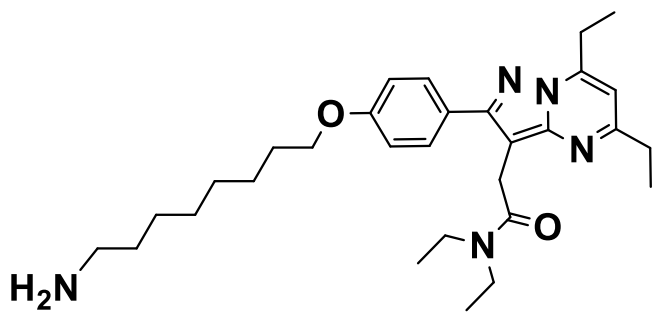




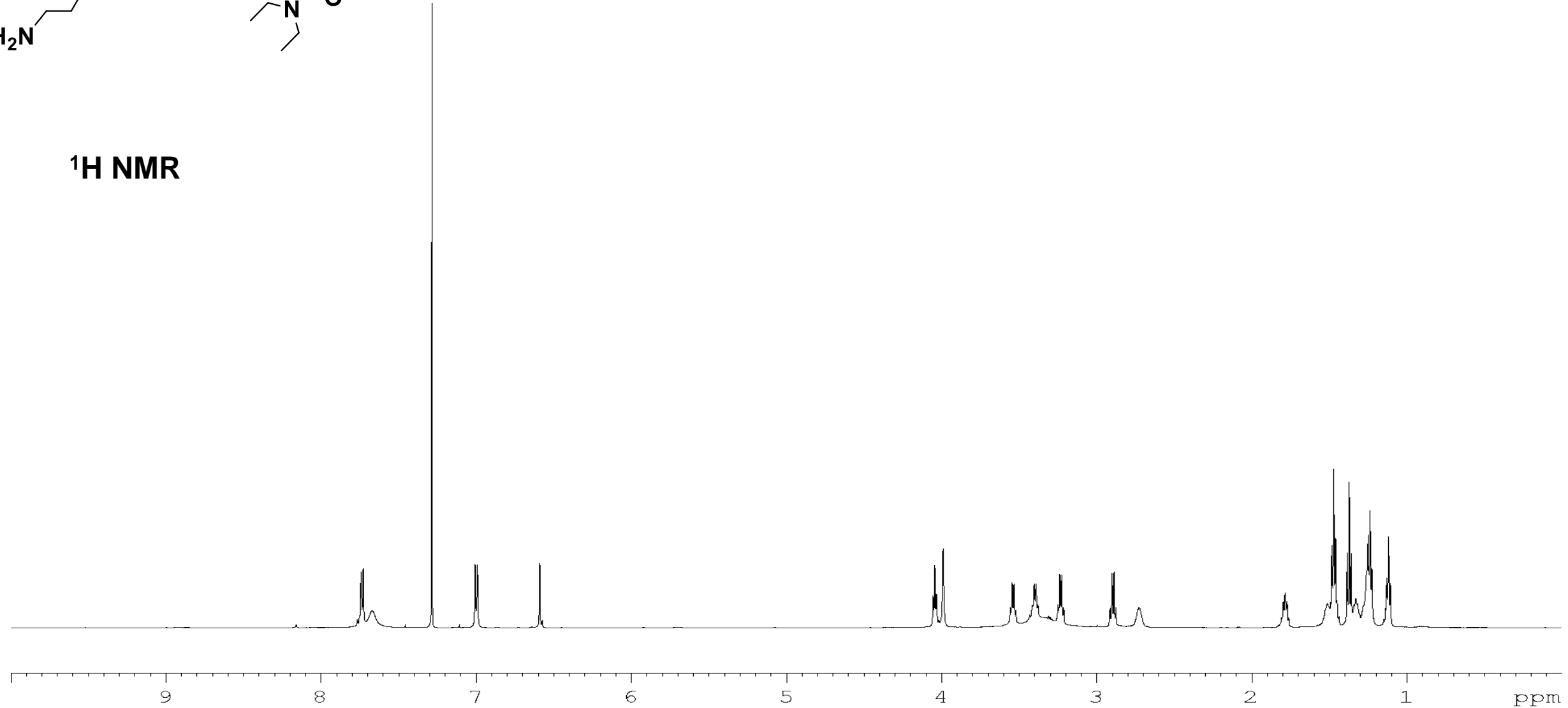
^{13}C NMR

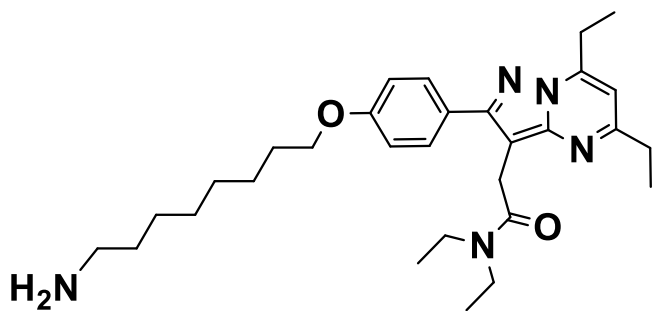




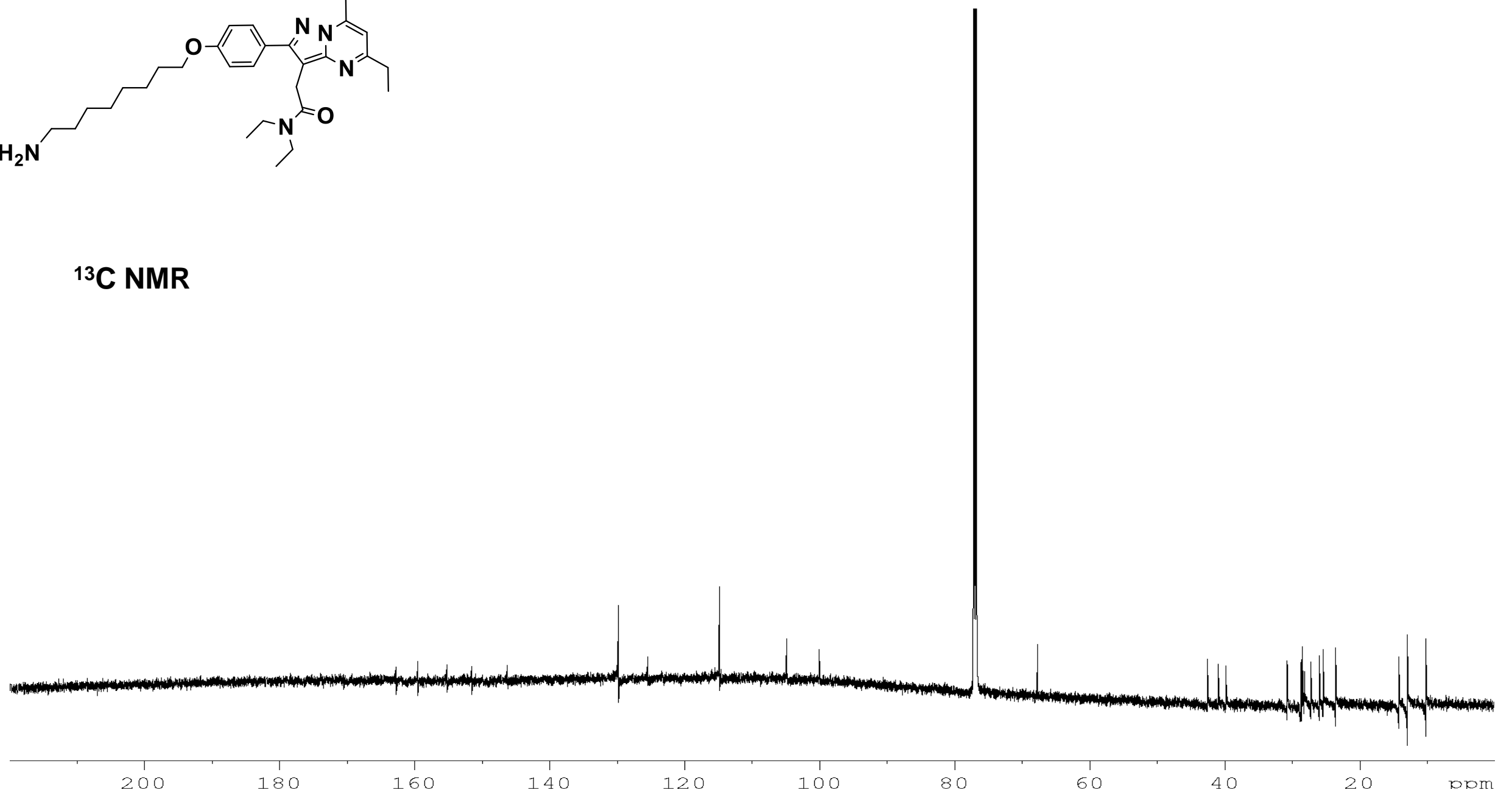


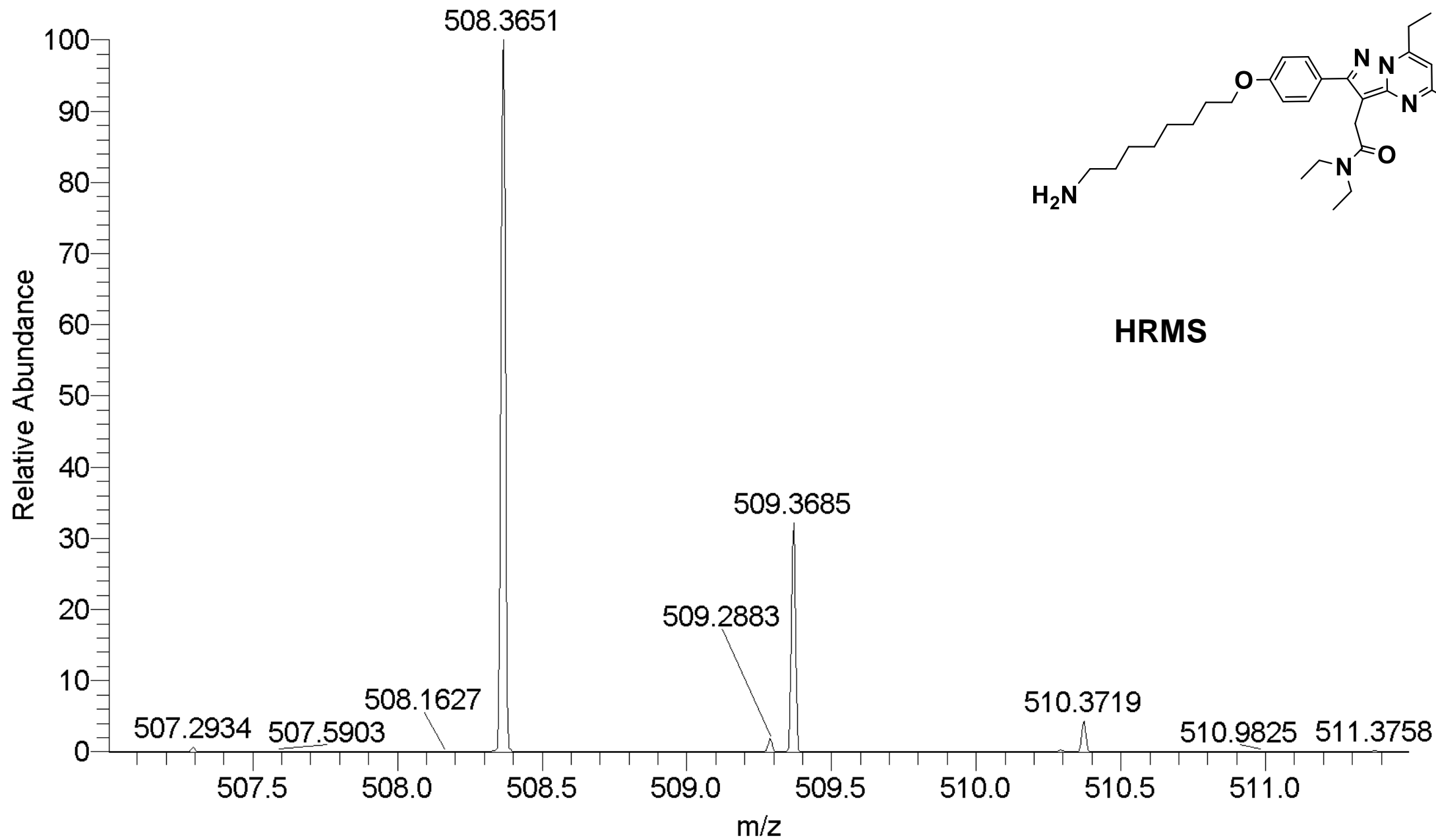
¹H NMR

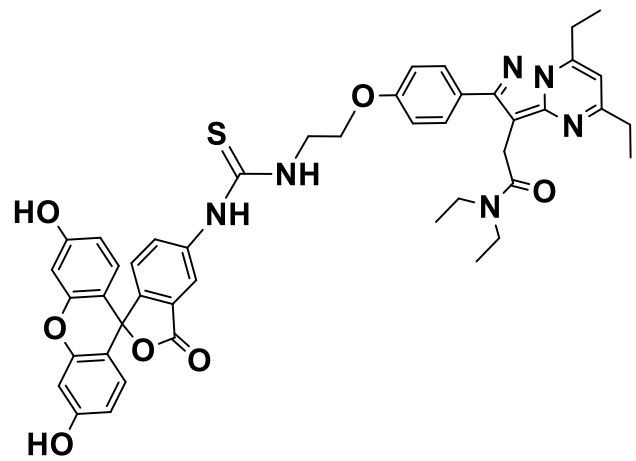




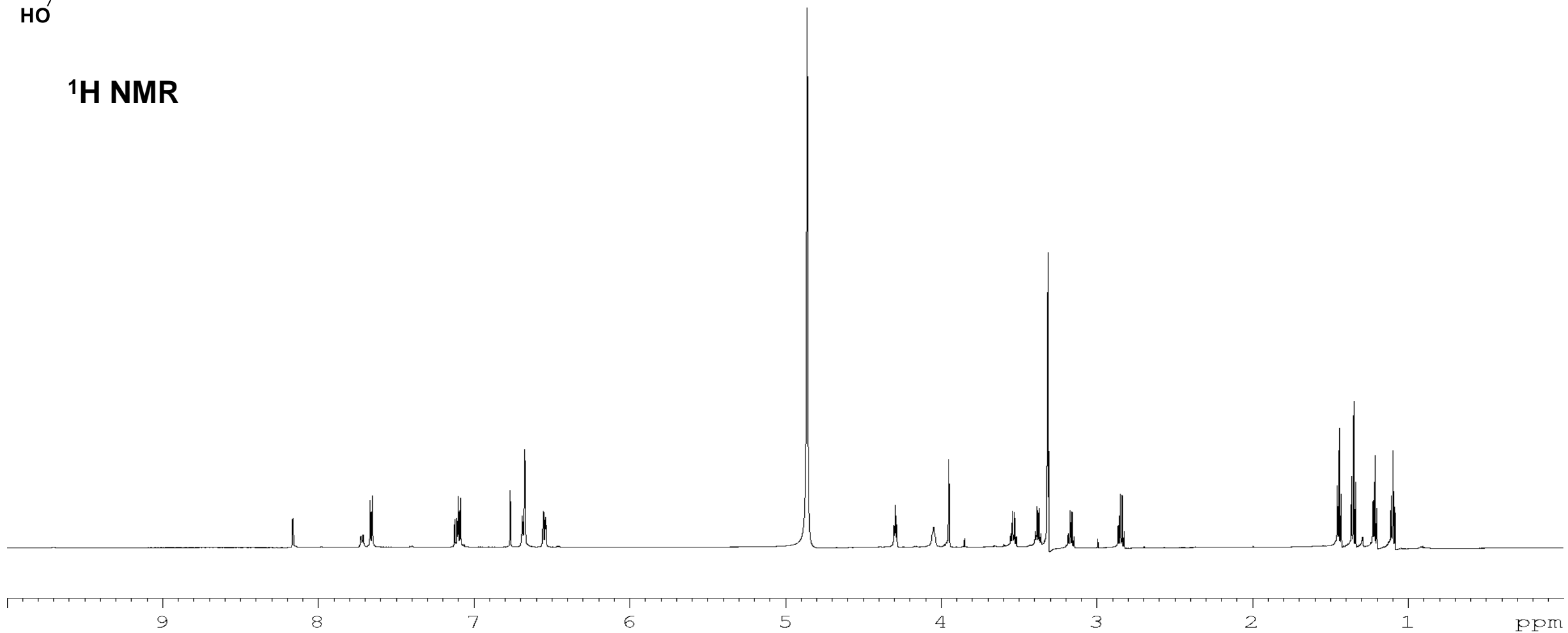
¹³C NMR

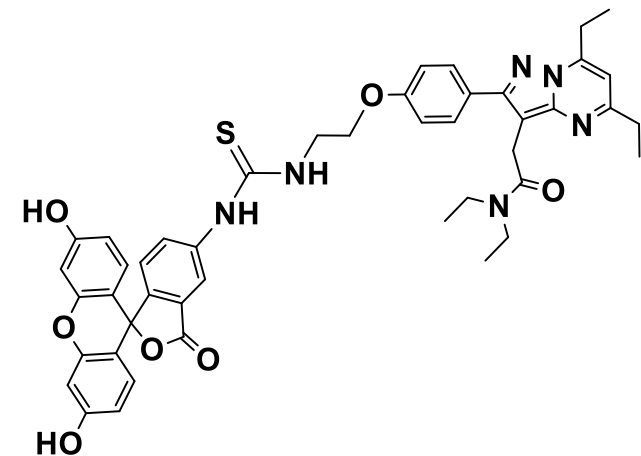
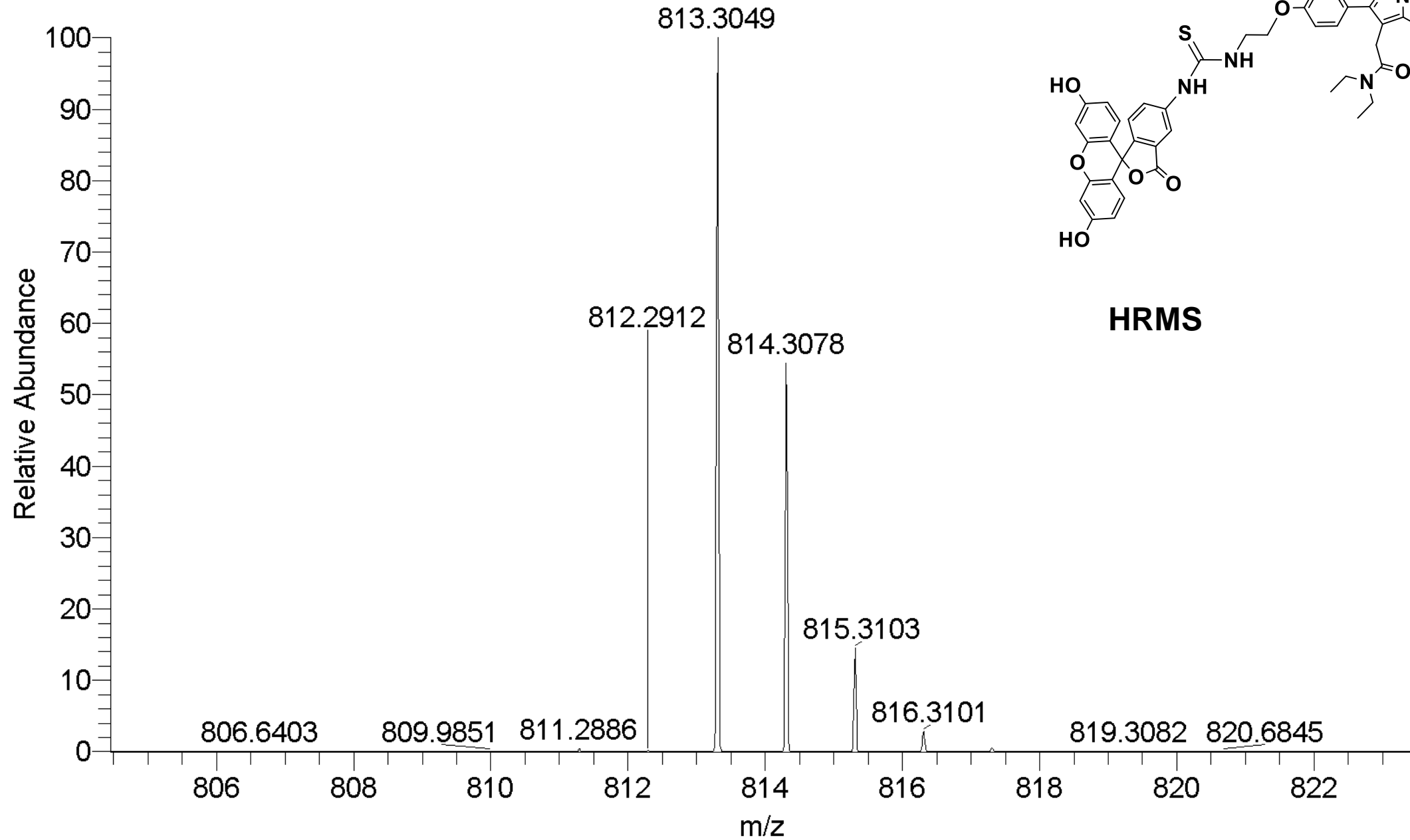


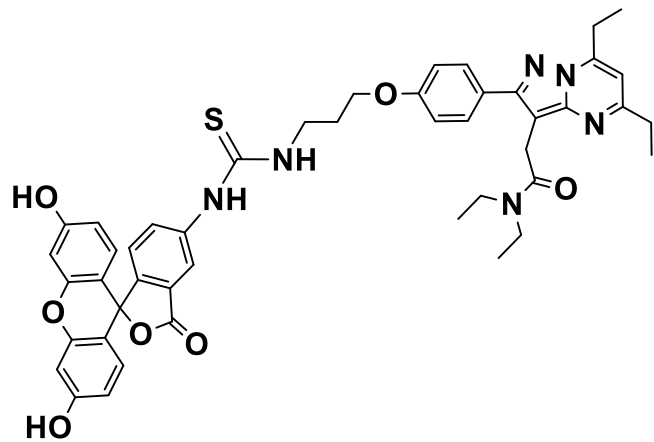




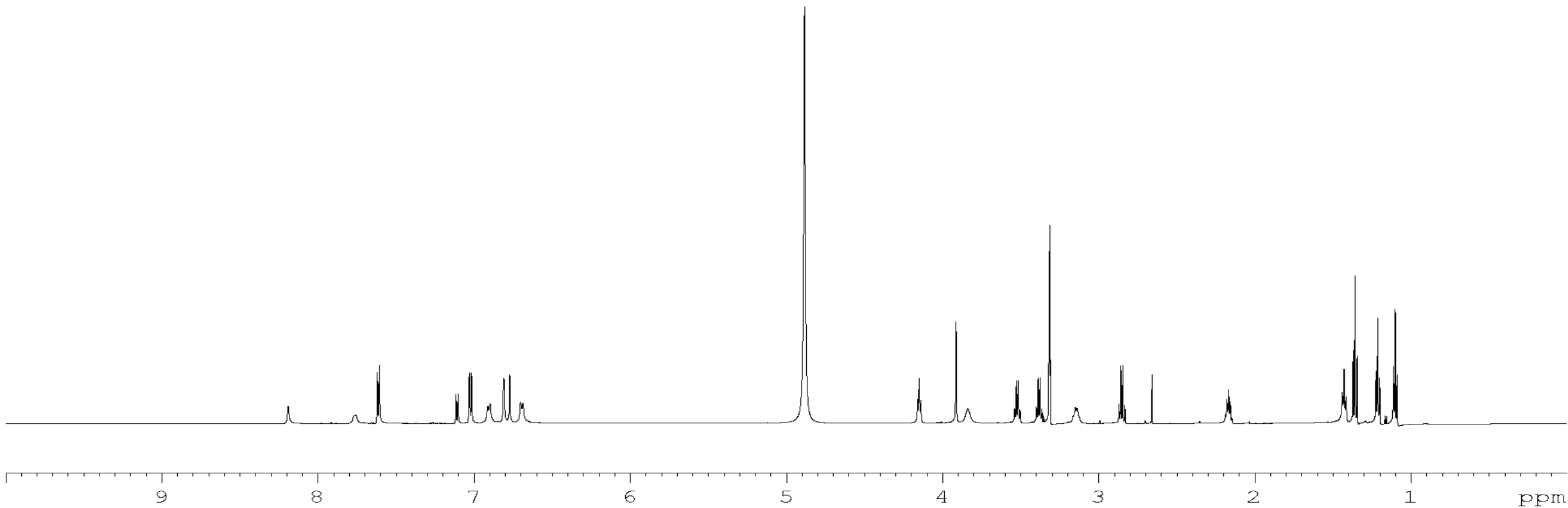
¹H NMR

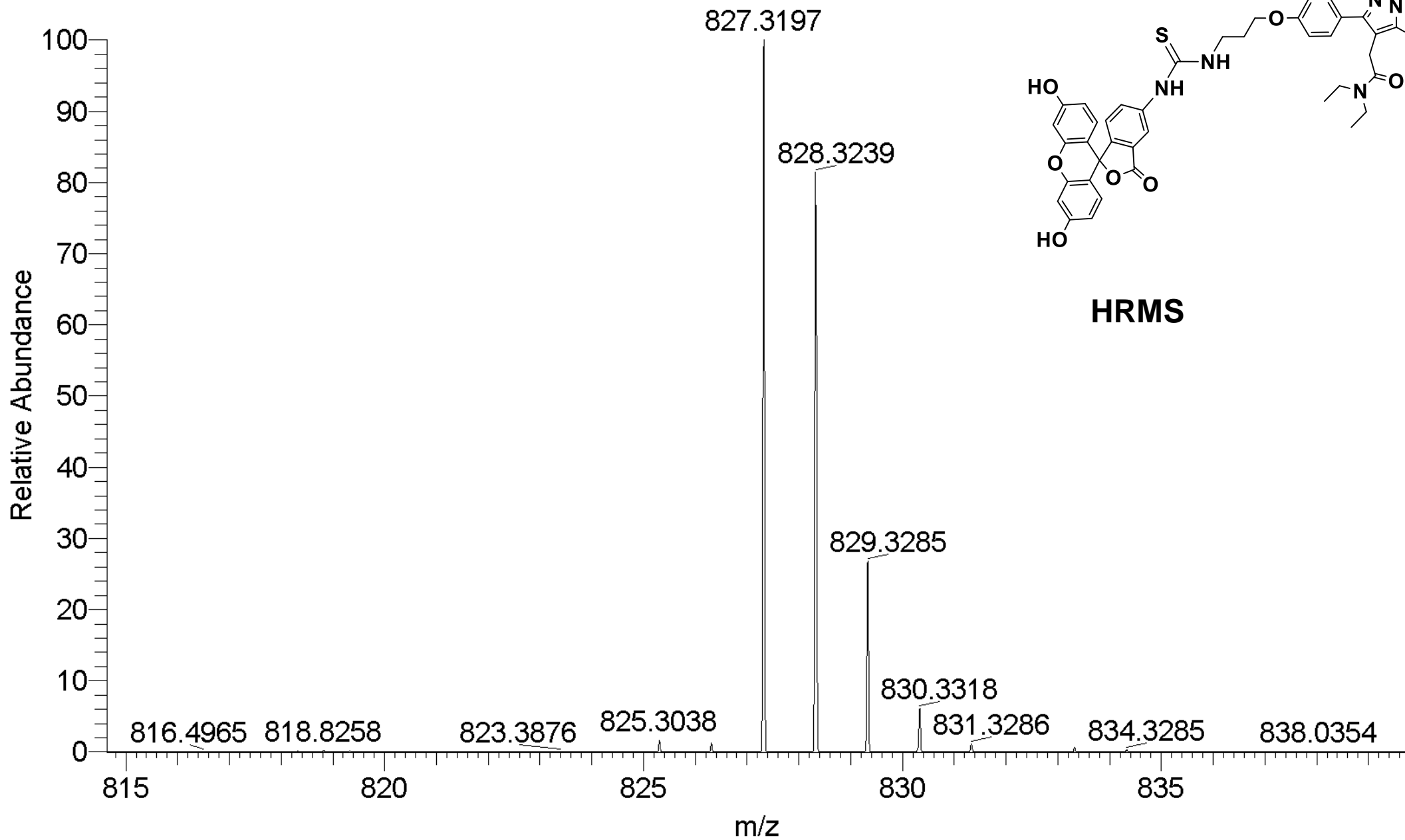


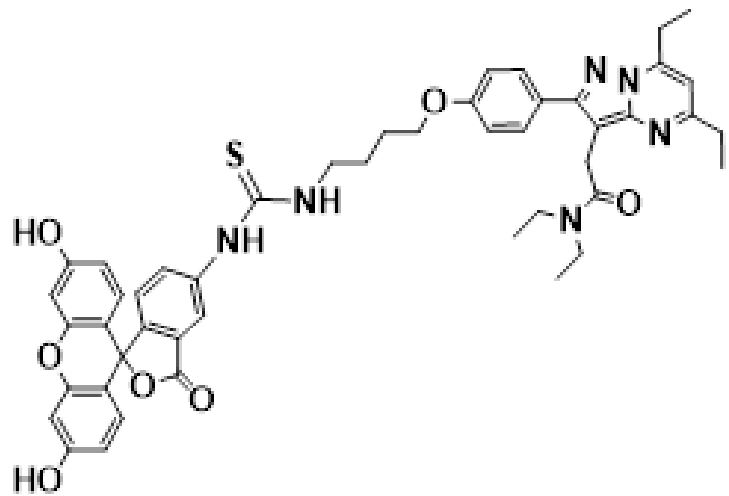




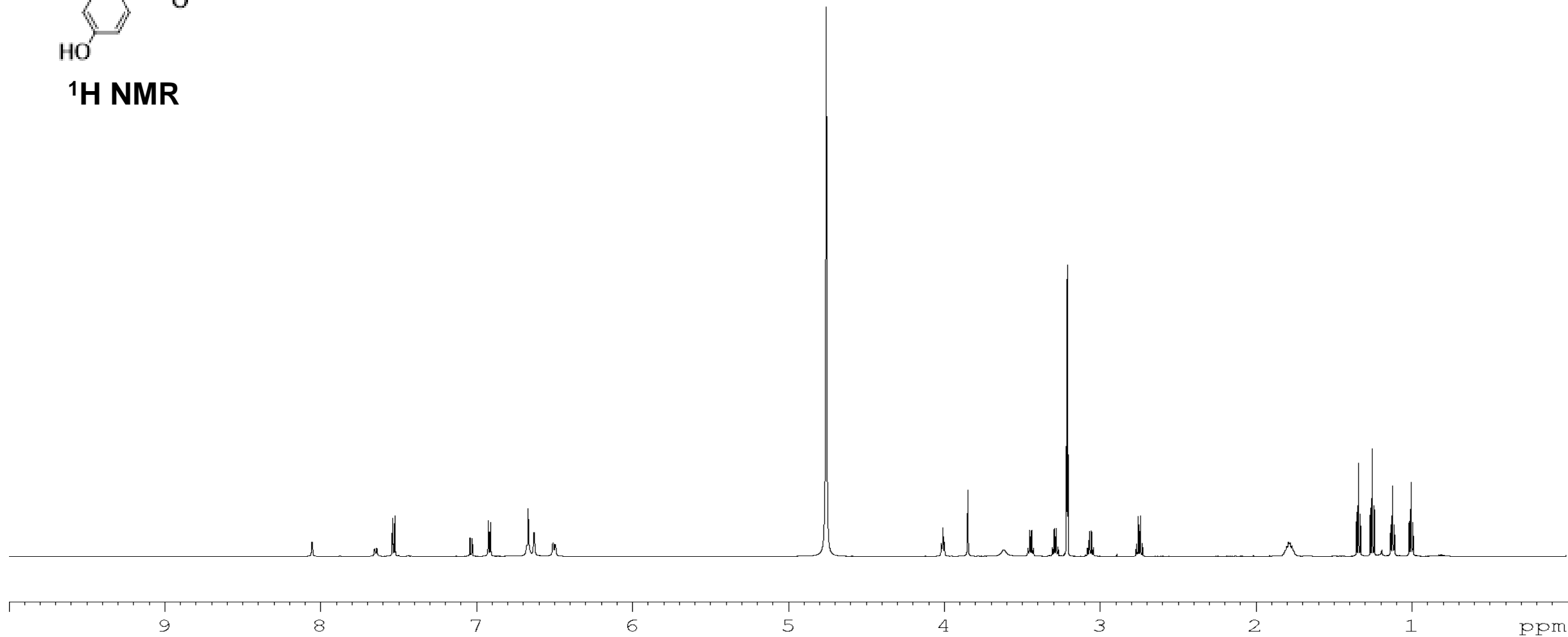
¹H NMR

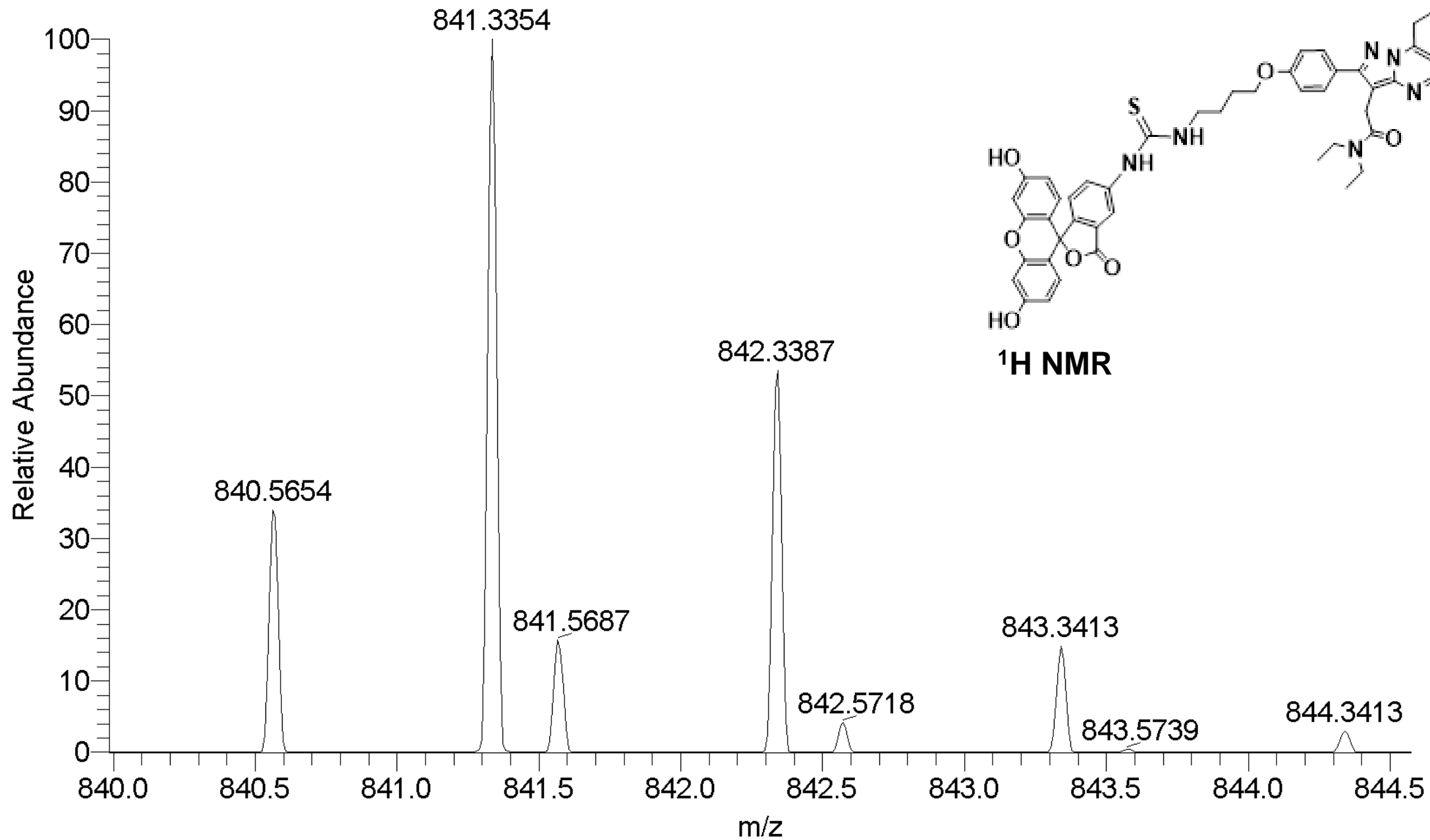


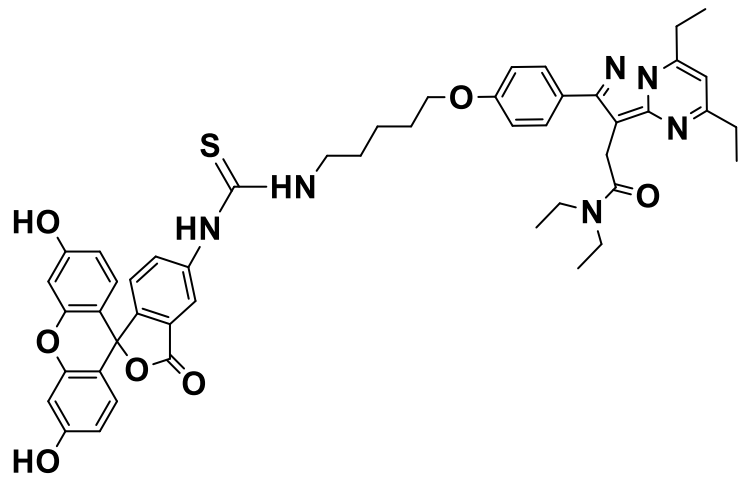




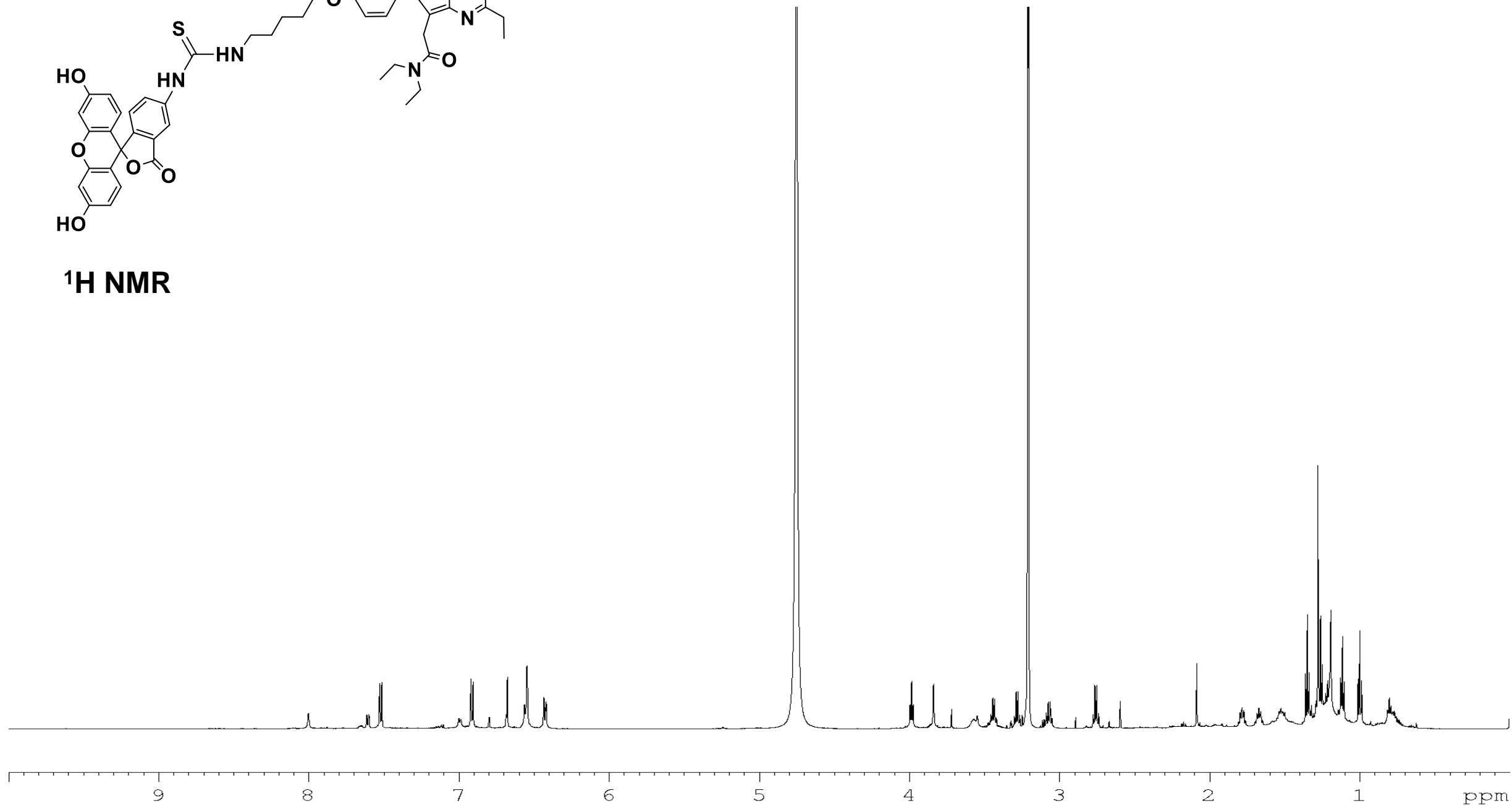
¹H NMR

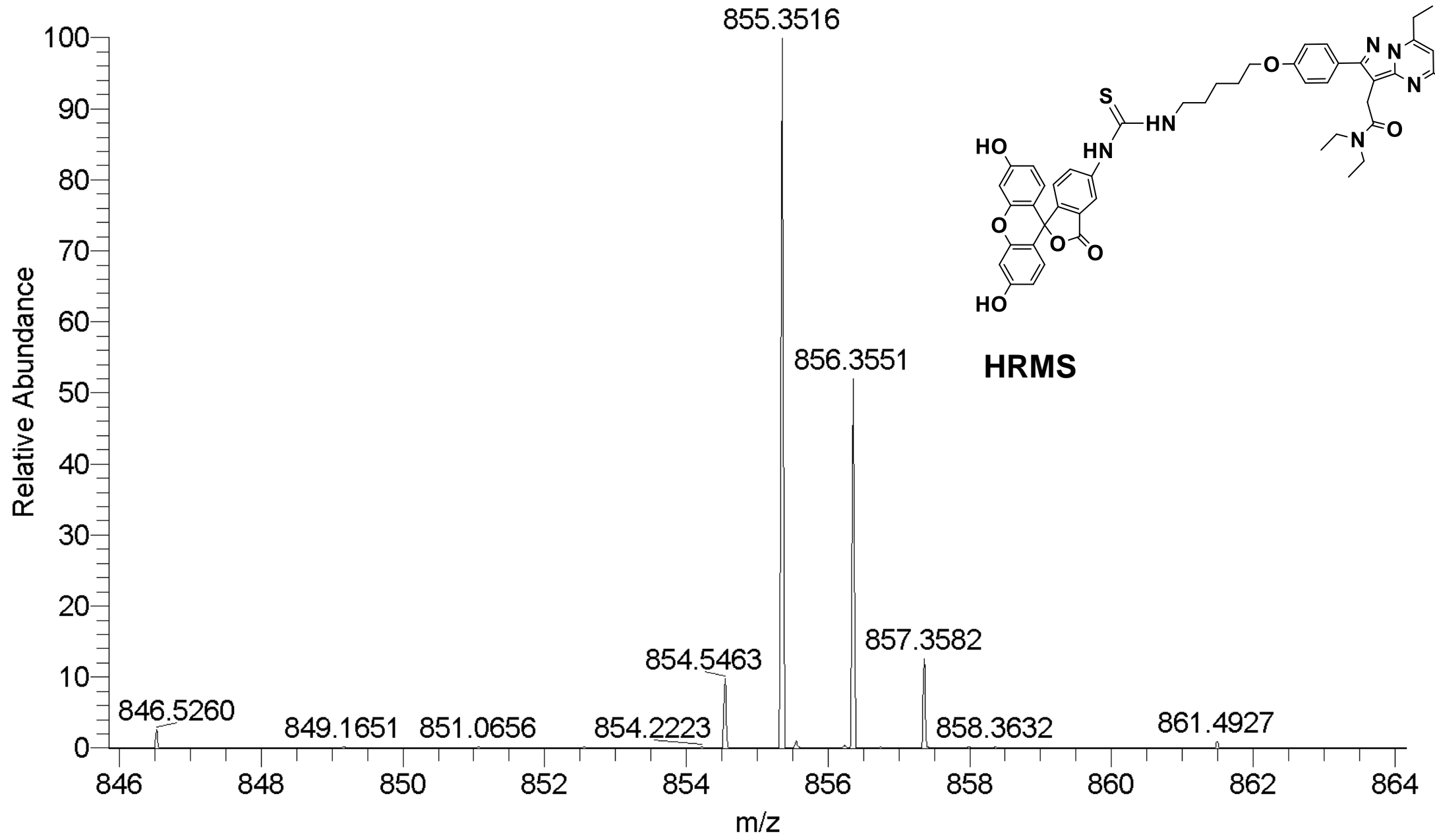


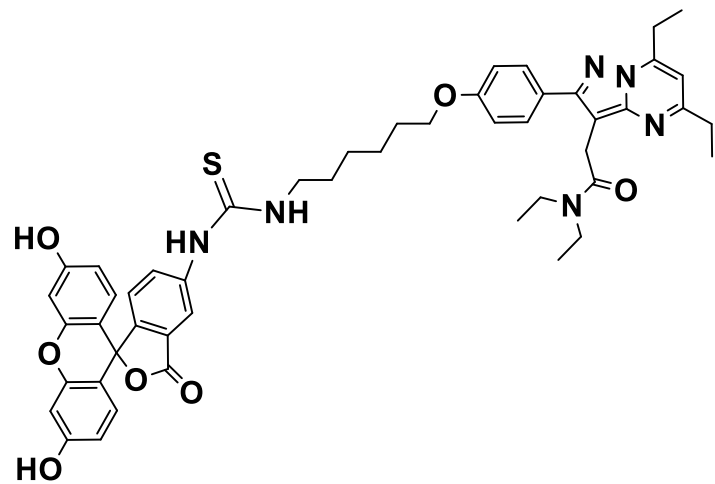




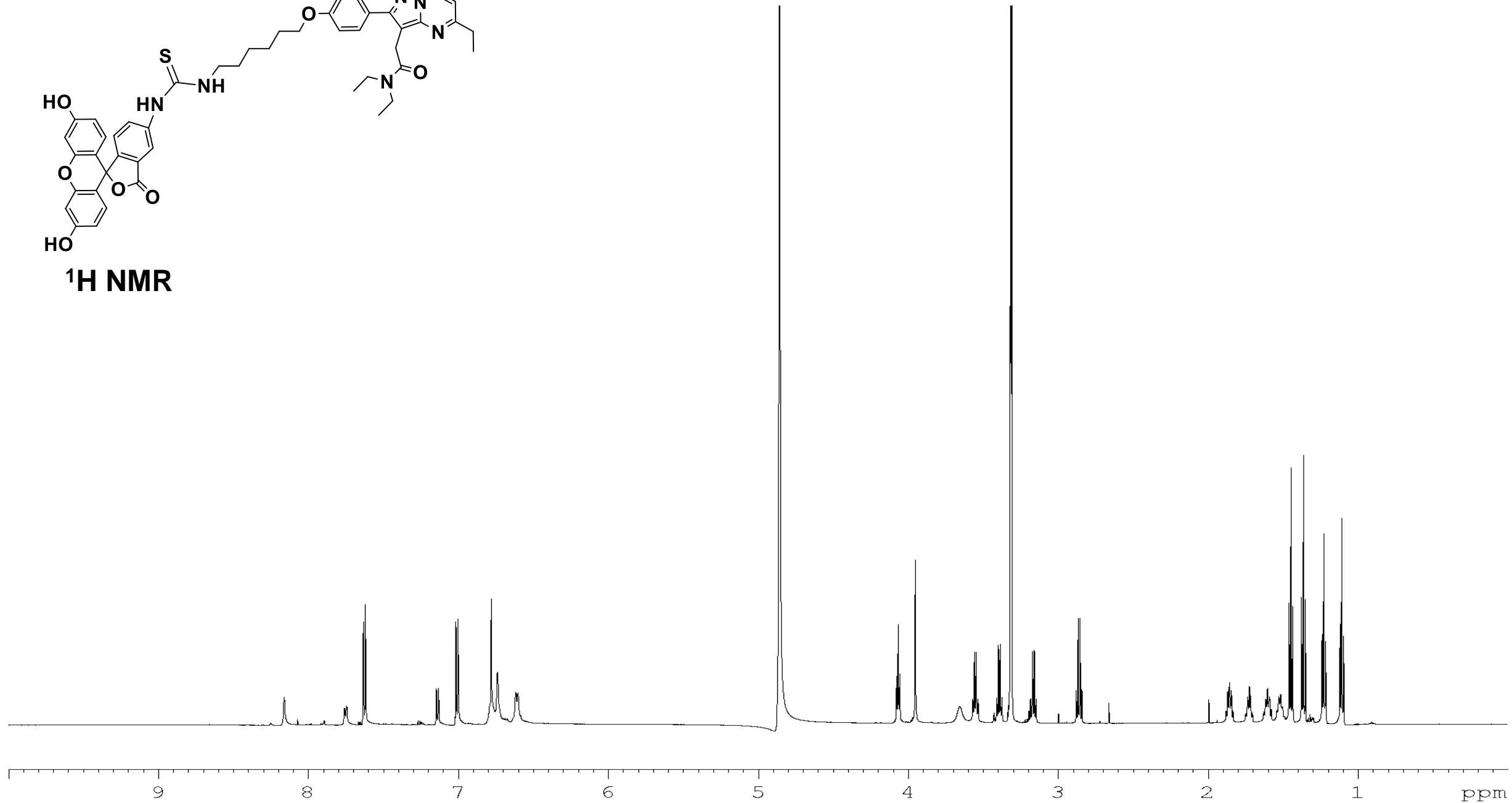
¹H NMR

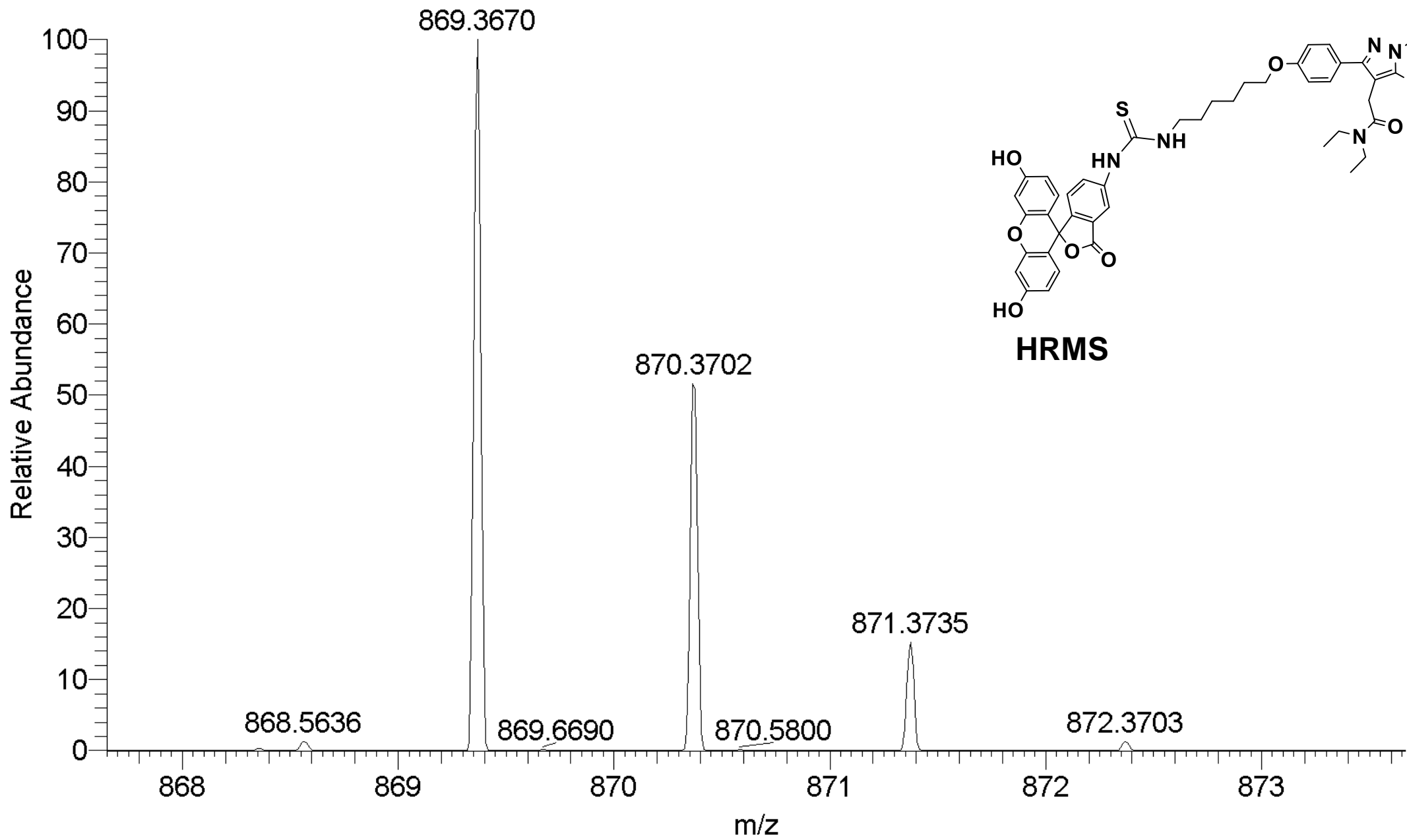


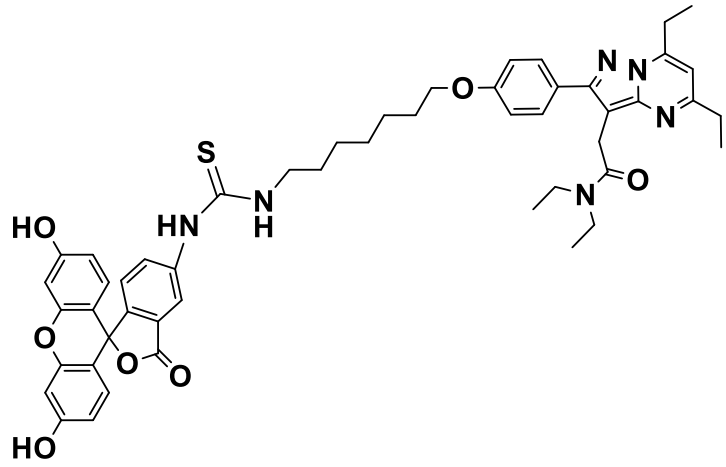




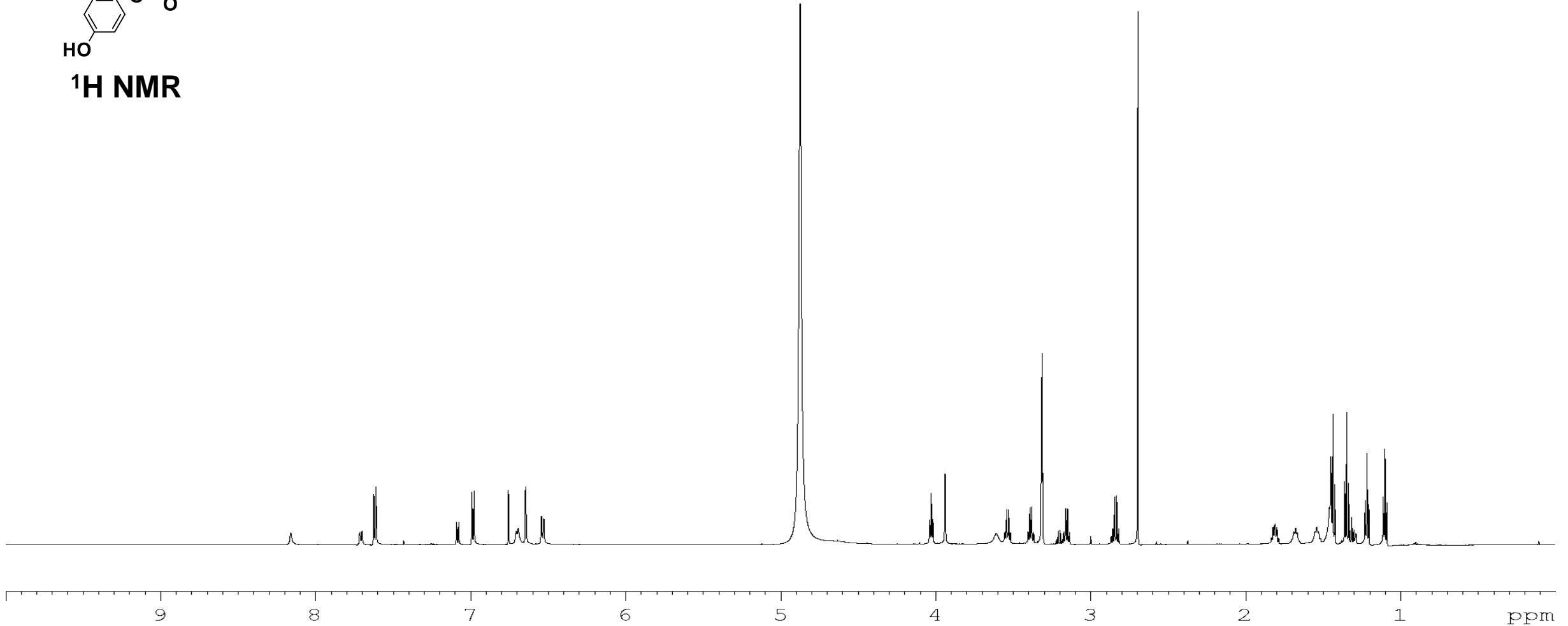
¹H NMR

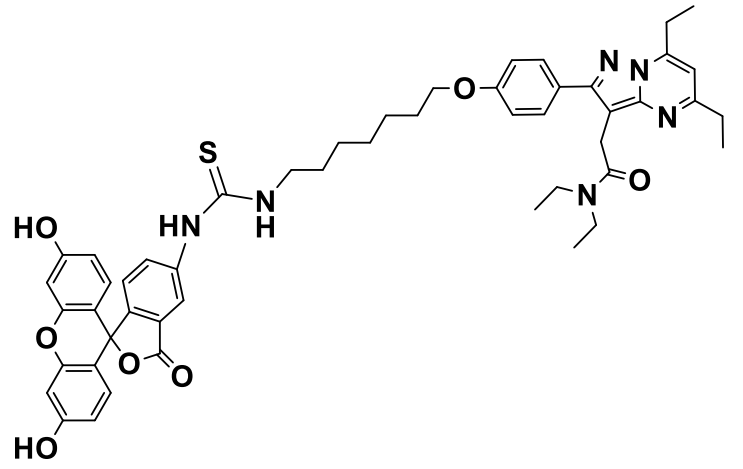
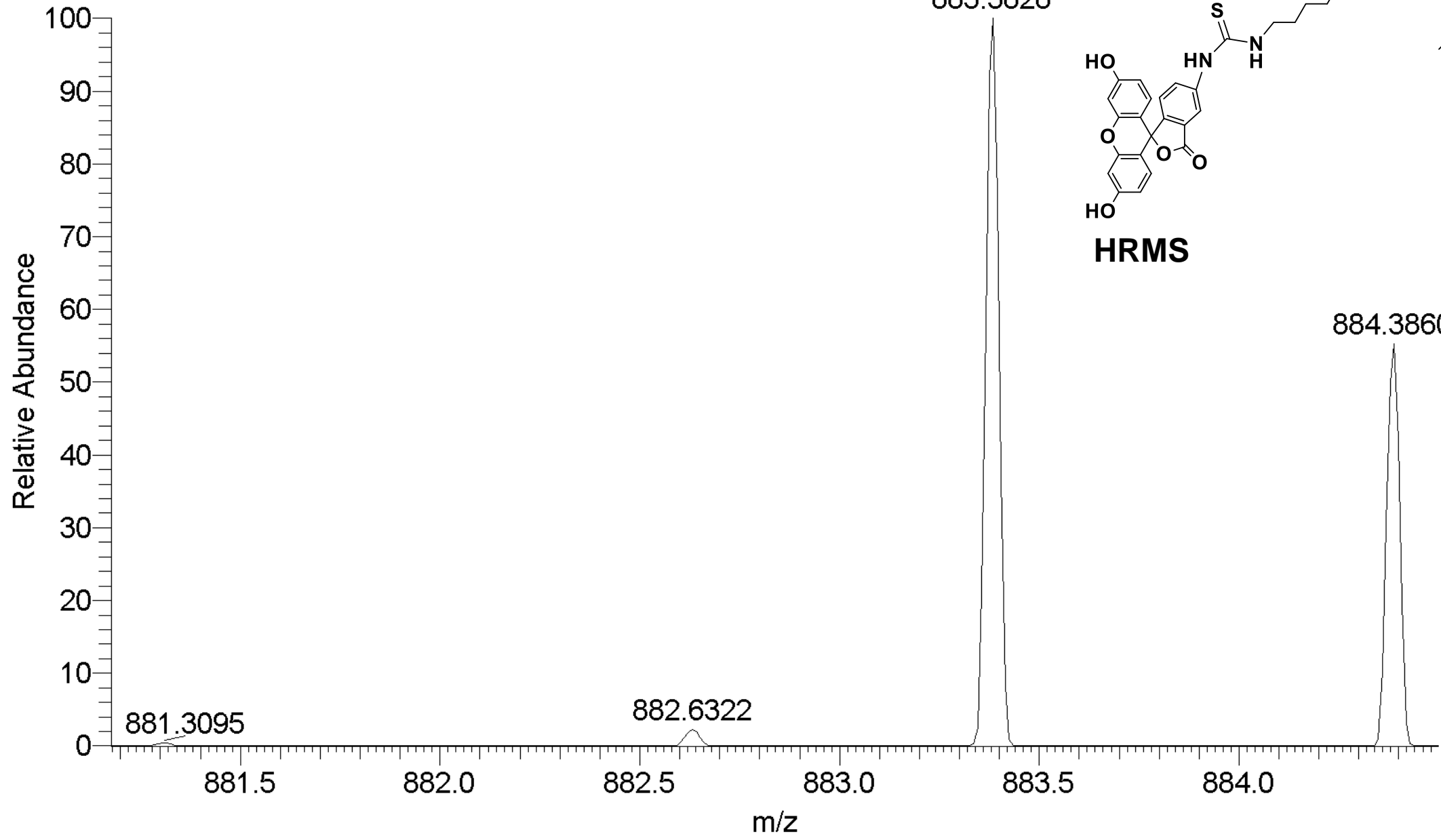




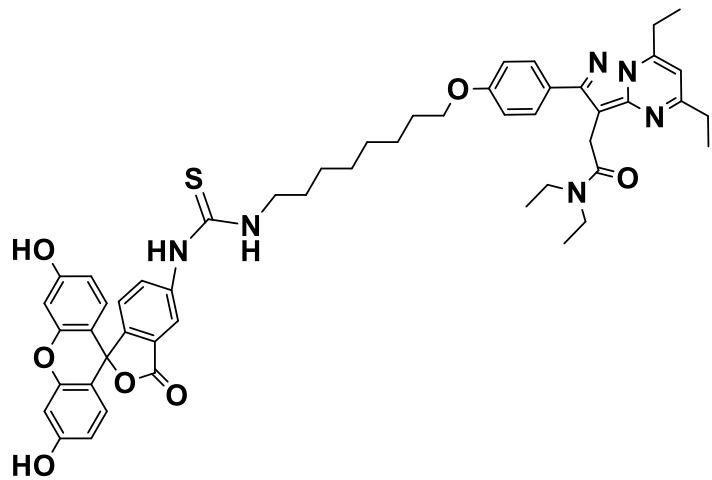


¹H NMR





HRMS



¹H NMR

